8-2023

Investigation of the Flow Field in the Jack Rabbit II Mock Urban Environment Field Tests Using a 1:50 Scale Wind Tunnel Model

Paulo Victor de Freitas Lopes
University of Arkansas-Fayetteville

Investigation of the Flow Field in the Jack Rabbit II Mock Urban Environment Field Tests Using a 1:50 Scale Wind Tunnel Model

A dissertation submitted in partial fulfillment
of the requirements for the degree of
Doctor of Philosophy in Chemical Engineering

by

Paulo Victor de Freitas Lopes
Universidade Federal Fluminense
Bachelor of Science in Chemical Engineering, 2017

August 2023
University of Arkansas

This dissertation is approved for recommendation to the Graduate Council.

_____
Tom O. Spicer III, Ph.D., P.E.
Dissertation Director

_____
Heather Walker, Ph.D.
Committee Member

_____
Karthik Nayani, Ph.D.
Committee Member

_____
Keith Walters, Ph.D.
Committee Member

_____
Jim Leylek, Ph.D.
Committee Member

Abstract

Accidental release of toxic chemicals can put workers and nearby populations at significant risk. Consequence assessment of accidents in urban environments is of particular interest. Urban geometries create wind channels between buildings, along with particularly dangerous areas downwind of buildings, where near-stagnant flow is present. Furthermore, recirculation zones can be formed between buildings, trapping high concentrations of toxic gases at ground level, particularly for denser-than-air gases.

In 2015, the Department of Homeland Security conducted the *Jack Rabbit II* Field Test (JR-II) at Dugway Proving Ground, UT. During JR-II, chlorine was released at the center of a Mock Urban Environment (MUE) and three types of data were collected: visual recordings of the releases, concentration measurements at specific locations, and wind velocity and direction. Due to the toxicity and corrosive nature of chlorine, some measurements could not be made during the JR-II trials. In a subsequent study called *Jack Rabbit II – Special Sonic Anemometer Study* (JRII-S), wind velocity and turbulence were measured at points of interest within the MUE.

Simulations of hazardous gas releases can be made in wind tunnel models, which provide for repeated tests with greater statistical analysis. Moreover, changes to test conditions can be made with relative ease and at lower costs. A 1:50 scale model of the JR-II MUE was constructed in the wind tunnel of the University of Arkansas. Laser Doppler Velocimetry (LDV) measurements show agreement between the approach wind characteristics in the tunnel model and field test. LDV velocity measurements within the MUE wind tunnel model also agree with the anemometry results obtained in JRII-S. Visualization of simulated chlorine releases in the wind tunnel shows good reproduction of release characteristics observed in the JR-II field tests.

Mathematical analysis investigated if it was possible to obtain accurate 3D velocity measurements from a simplified 2D LDV setup. Error quantification showed that the simplified setup yields valid approximations for the vertical velocity and turbulence directions depending on the flow field characteristics, but high error is observed in the velocity and turbulence in the cross-wind component.

After demonstrating that the wind tunnel models the JR-II and JRII-S field tests, Particle Image Velocimetry (PIV) experiments were conducted to provide velocity measurements that could not be obtained during JR-II. The wind tunnel model yields more comprehensive results than the pointwise measurements taken during JRII-S using sonic anemometers. Velocity measurements in a horizontal plane parallel to the ground were used to compare to computational fluid dynamics (CFD) simulations of the JRII-S field tests found in the literature. PIV measurements taken in the wind tunnel model pointed out concerns with those simulations.

Reproduction of the JR-II field tests showed the velocity field in a section of the MUE before and during the chlorine release. The effect of the added momentum of the release in the flow field and in the height of the dividing streamline at CONEX 11.4 was investigated, with bigger impact observed at lower atmospheric momentum.

Key Words: Wind tunnel modeling, gas release, Jack Rabbit II, Laser Doppler Velocimetry, Particle Image Velocimetry

Acknowledgments

First of all, I would like to thank my parents, Paulo Arthur and Flora Maria, my brothers, André Freitas, André Luiz, Arthur, and Alexandre; and other family members for their continuous support, even if separated by a few thousand kilometers and a couple of time zones.

I would also like to thank the professors in CHEG for their determination and teachings through my doctoral course. Special thanks to the principal investigator of this project, Dr. Tom Spicer, for sharing his knowledge in process safety and gas dispersion, and for his continuous patience and support. I would also like to thank Dr. Jamie Hestekin for the recruiting process and the initial push to get me to come to Arkansas for Grad School.

I would like to thank out post-doctoral fellow, Dr. Chad Smith. His experience with PIV and his mechanical insights were crucial for the progress of this work, along with taking his time to review and correct this dissertation. I would also like to thank my fellow grad students in the CHRC group, Samuel Gallimore and Sami Fares, for the cooperation in this work and the moments of fun.

I would also like to thank my different groups of friends for their support, companionship, friendship, and advice throughout this project. I would like to thank my CHEG friends in other groups (Juliana, Letícia, Shad, Jessica, Luis, etc.); my friends in other departments (Bakhtiyar, Whit, Vitor, Helen, Larissa, Thainá, Cristina, Elis, PJ, Maria Clara, etc.); and my friends in Brazil (Mateus Dias, Leo, Pedro Galvão, Pedro Medeiros, Paulo Fernando, Miranda, Marcelo, DDG, Bernie, Torresmo, and the F.O.L.E.S. group – Renas, Octavio, Gusta, Vieira, Jão, Yago, Bessa, Machado, Rodrigo, Vital, Rafa, Julião, Alê, Comac, Antônio, Nakamura, and Vitim) and other parts of the world (Gabriel, Bruno, Robson, Tharaka, Lucho, Ange, etc.).

Table of Contents

List of Figures

Appendices

List of Tables

Appendices

Chapter 1 – Introduction and Literature Review

1.1 Uses and Transportation of Chemicals by the Industry

Chlorine is used as raw material in the manufacture of paper and other chemical products. It is also used in water and sewage treatment. The United States produces 11 million metric tons of chlorine per year (American Chemistry Council, 2020); however, chlorine is produced in only approximately half of the American states (EPA, 2022). Therefore, large-scale transportation of chlorine is required. Chlorine transportation is regulated by the Pipeline and Hazardous Materials Safety Administration (PHMSA) and by the United States Department of Transportation (USDOT) (The Chlorine Institute, 2022). Between 2010 and 2016, a total of 32 chlorine rail accidents and incidents occurred in the US (The Chlorine Institute, 2022), representing a danger to rail yard workers and local populations. Releases of chlorine to the atmosphere produce a denser-than-air gas cloud due to the molecular weight of chlorine, as well as suspended aerosol droplets formed from liquefied, pressurized releases.

Accidents that involve the release of denser-than-air gases and/or aerosols are of particular interest since these chemicals tend to stay at ground level. The presence of dangerous clouds of toxic or flammable chemicals at ground level leads to additional risk to nearby populations.

1.2 Past Chemical Accidents

Transportation and storage of toxic chemicals carry an inherent risk for chemical plant workers and nearby populations. History has several examples of accidental releases that have caused high numbers of fatalities, such as Flixborough, UK, where an accidental release of cyclohexane and consequent explosion caused 28 deaths (Venart, 2004). Another major accident occurred in Bhopal, India, resulting in almost 20,000 deaths due to an accidental release of

methyl isocyanate (Varma, R. & Varma, D.R., 2005).

A transportation accident happened in Graniteville, SC, in 2005, where a train carrying chlorine (and other chemicals) derailed and one train car was punctured. Forty-five metric tons of chlorine aerosol were released, resulting in nine deaths and leaving over 500 injured (Buckley *et al.*, 2007). Figure 1 shows the wreckage of the Graniteville accident (Baum, 2013).

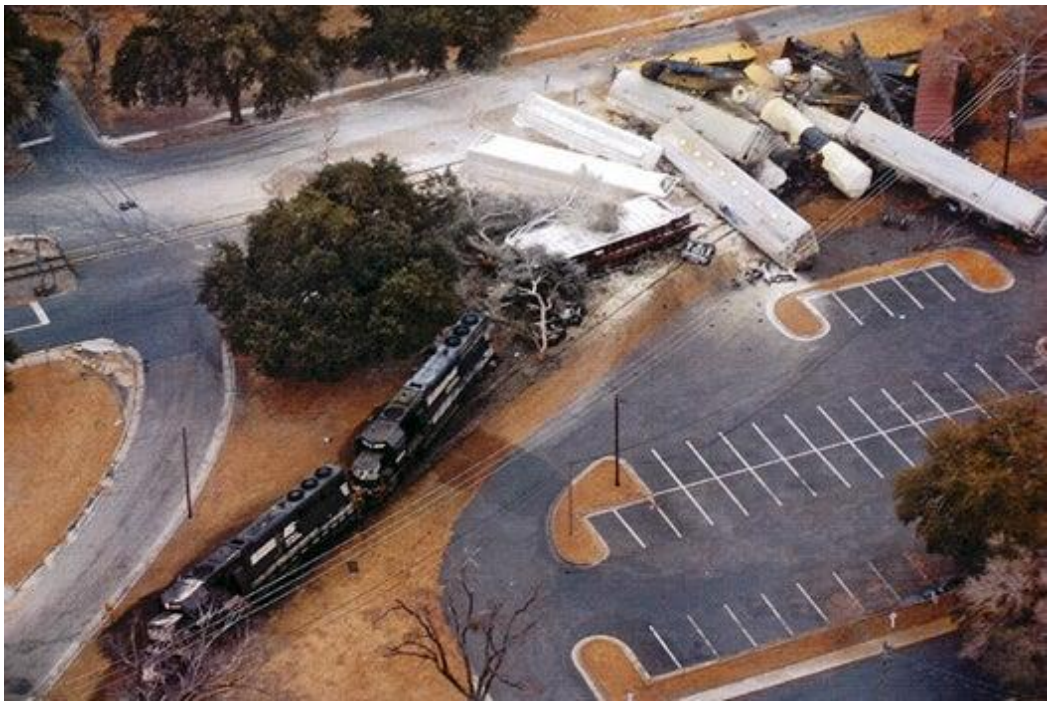

Figure 1- Wreckage consequent of the train collision at Graniteville, SC (Baum, 2013).

In 2007, a human error caused the release of 900 lbs. of chlorine in the port of Tacoma, WA (JEMS, 2008). Twenty-five people received medical attention, including a dozen first responders caught by surprise by a sudden change in wind direction. More recently, a crane malfunction caused a chlorine tank to drop onto the deck of a ship, releasing 25 metric tons of the gas in the port of Aqaba, Jordan, in June 2022. A total of 251 injuries and thirteen casualties were reported (Akour, 2022). Figure 2 shows two pictures of the incident, with the resultant chlorine cloud (Akour, 2022) in Figure 2a and the remains of the tank after the incident (Mazraawi, 2022) in Figure 2b.

Figure 2- (a) Frame capture of the Aqaba Port incident, taken seconds after the chlorine tank is accidentally dropped (Akour, 2022). (b) Forensic experts evaluate the tank after the accident (Photo by Mazraawi, 2022).

Apart from accidental releases, chlorine has also been weaponized by radical groups. Over a period of 46 days in 2007, at least half a dozen separate explosions of chlorine tanks by Iraqi radicals killed multiple people (Cave & Fadam, 2007; Parsons, 2007; Rubin, 2007; Semple, 2007). Multiple attacks using chlorine were also reported during the Syrian Civil War (BBC, 2021). However, compared to accidental industrial releases, terrorist attacks using chlorine are of little concern due to its lower fatality rate when compared to other terrorist methods, as most of the fatalities are caused by the explosions instead of exposure to chlorine.

The diverse geometry of urban layouts can aggravate the risk imposed by accidental industrial chemical releases, especially in the case of denser-than-air (DTA) gases. Buildings affect airflow and alter local wind velocities and turbulence levels (Belcher *et al.*, 2012; Britter & Hanna, 2003). Building geometries create recirculation zones that can trap DTA clouds on the lee side of buildings. Therefore, the release of a toxic, heavy gas in an urban environment has catastrophic potential. Simulations of DTA gases can lead to a better understanding of how the gas flows in an urban setting. These simulations allow for crucial improvements to consequence assessment in case of a release in an actual urban environment.

1.3 Simulation of Gas Releases in Field Tests

Methods of consequence assessment of hazardous material releases can be developed and validated using several approaches. Field tests provide data in real atmospheric conditions but are expensive and subject to changes in atmospheric conditions during the test. Physical models (such as wind tunnel and water tunnel models) of potential release scenarios have the advantage of precise control of parameters compared to field studies, which allows repeated experiments to establish proper ensemble behavior with a sufficient number of repeated experiments. However, such physical models may not fully reproduce the complexity of chemical releases, including release momentum and cloud density, and this can be particularly significant in aerosol releases. Therefore, care must be taken to identify the most critical scaling parameters and to compare important characteristics to those of field tests. Computational models are the least costly to use and are developed based on some combination of theory, field tests, and physical models. Hence, field tests and physical models are frequently used as validation tools when developing analytical methods and computational models. Simplified scenarios can be studied in a physical model and used effectively for computational model validation (Blackman *et al.*, 2015).

1.3.1 General Aspects of Field Tests

Full-scale field tests show how chemical dispersion is affected by actual atmospheric conditions, including wind speed, mechanical and thermally induced turbulence, air temperature, relative humidity, and local surface roughness. Full-scale field tests are necessary, but they are subject to uncontrolled real-world conditions at the moment of the release. Field tests are highly complex and have limitations, including high costs, variation of the approaching wind (such as meander and instantaneous changes in wind speed or wind gusts), and lack of repeatability. Statistical analysis is not possible in most field tests because the test usually consists of a single

release for each set of conditions. During a field test with a single repetition, it is possible to get one set of data that is not representative of the major characteristics of the situation (an outlier) due to the lack of control and unpredictability of certain conditions. Data collection during field tests can also be complex and challenging, which leads to gaps in knowledge and unanswered questions.

1.3.2 Previous Field Tests over Unobstructed Terrain

For a better understanding of the dispersion of potentially toxic chemicals, several field tests over no obstacles or over very few obstacles have been commissioned over the past 50 years. The Burro (Koopman *et al.*, 1982), Coyote (Goldwire, Jr. *et al.*, 1983), Falcon (Brown *et al.*, 1990), and Maplin Sands (Hist & Eyre, 1983) field tests investigated the dispersion of liquefied natural gas (LNG). These test series aimed at different properties regarding the flammability of the gas, respectively: dispersion over water, dispersion and burning of clouds, effectiveness of vapor fences in LNG containment, and combustion characteristics. Dispersion of liquefied petroleum gas (LPG) was also studied in the Coyote Field Test. Goldfish (Blewitt *et al.*, 1987) and Desert Tortoise (Goldwire, Jr. *et al.*, 1985) were conducted with identical setups, studying the dispersion of hydrogen fluoride (HF) and liquefied, pressurized ammonia, respectively. During the Goldfish Series, the release unexpectedly stayed at ground level. Soon after the start of the release, HF oligomerized into denser-than-air $(HF)_6$. The Eagle Test Series consisted of nitrogen tetroxide (N_2O_4) releases conducted over flat, unobstructed terrain (McRae *et al.*, 1987).

The Heavy Gas Dispersion Trials (HGDT, also referred to as “Thorney Island Experiments”) consisted of the instantaneous releases of large volumes (ranging from 1320 to 2100 m^3) of different mixtures of nitrogen and Freon™ 12 (CF_2Cl_2). In Phase I, the cloud was

released over a flat area, without obstacles (McQuaid, 1985). Phase II continued the study with releases aiming at three different kinds of obstacles: a dyke (5 m in height); a porous screen (10 m in height); and a building (9 m in height) (Davies & Singh, 1985). Figure 3 shows the cloud instant after the release in one of the Phase II trials (Health & Safety Laboratory, 1985).

Figure 3 - Freon-12 release during the Heavy Gas Dispersion Trials – Phase II (Health & Safety Laboratory, 1985).

Considering the dangers of releasing large-scale quantities of chlorine and anhydrous ammonia, the United States Department of Homeland Security (DHS) and the Transportation Security Administration (TSA) commissioned a field test study called *Project Jack Rabbit* (JR-I) conducted at US Army's Dugway Proving Grounds (DPG) in Utah. JR-I consisted of separate release trials of chlorine and liquefied, pressurized ammonia over flat, unobstructed terrain, serving as a baseline and proof-of-concept for future tests, mainly Jack Rabbit II (JR-II), which is explained in detail in Section 1.7. Figure 4 shows a chlorine release from the JR-I field test (Fox & Storwold, Jr., 2011).

Figure 4 - Downward chlorine release during the Jack Rabbit I Field Tests (Fox & Storwold, Jr., 2011).

1.4 Models of Field Tests over Unobstructed Terrain

Appropriate modeling is frequently used to fill-in gaps left by the full-scale field tests. Physical scale models allow for the control of wind conditions, including velocity, turbulence intensity, and wind direction. It is significantly easier and more cost-effective to make changes to a scale model experiment. Extensive repetition improves statistical representation and sampling. Models can be physical or computational. Physical models consist of scale reproduction of field tests in wind or water tunnels. As most gases used in field tests are hazardous (flammable, toxic, or both), the model release takes place with a non-hazardous simulant gas.

Wind tunnel models were made for several of the field tests mentioned in Section 1.3.2, such as Burro (König-Langlo & Schatzmann, 1991; Neff & Meroney, 1981), Maplin Sands (König, Schatzmann, & Lohmeyer, 1987; König-Langlo & Schatzmann, 1991), Goldfish (Petersen & Ratcliff, 1989), Falcon (Shin, Meroney, & Neff, 1991), and Thorney Island (König-Langlo & Schatzmann, 1991; Spicer & Havens, 1985).

Apart from open terrain, field tests can also be performed in mock urban environments, as was done in the Jack Rabbit II field test, which is explained in detail in Section 1.7. Studying a

release in an urban setting is of particular interest because the flow is very complex and poses risk to a larger number of people.

1.5 Flow in Urban Environments

The behavior of the wind in urban environments is significantly different than in open rural areas. This phenomenon can be quantified via surface roughness, the height at which the wind velocity profile no longer follows a logarithmic curve. Surface roughness is commonly used to parameterize the wind speed profile, and its values vary from 0.1 m in open country to 0.25 m in scattered buildings and up to 2 m in city centers (Britter & Hanna, 2003).

Flow patterns and the dispersion of passive contaminants in real or mock urban environments was investigated in several previous field tests, including: the Urban Dispersion Program (UDP) (Allwine & Flaherty, 2007), composed of the Madison Square Garden Dispersion Study (MSG05) (Reynolds, R.M., 2006) and the Midtown Manhattan Atmospheric Tracer Field Tests (MID05) (Reynolds, R.M., *et al.*, 2006); Urban 2000 (Allwine *et al.*, 2002), Mock Urban Setting Test (MUST) (Warner *et al.*, 2006), and the Joint Urban 2003 (Allwine & Flaherty, 2006).

Urban zones also cause changes in the wind direction, channeling flow in streets and creating low wind areas near buildings. Mixing and transport of pollutants are governed by turbulent mixing and mean transport through the streets (Belcher, 2005). In the simplest case, air moves along the streets, channeled in the spaces between buildings, usually referred to as “urban canyons”, as shown in Figure 5.

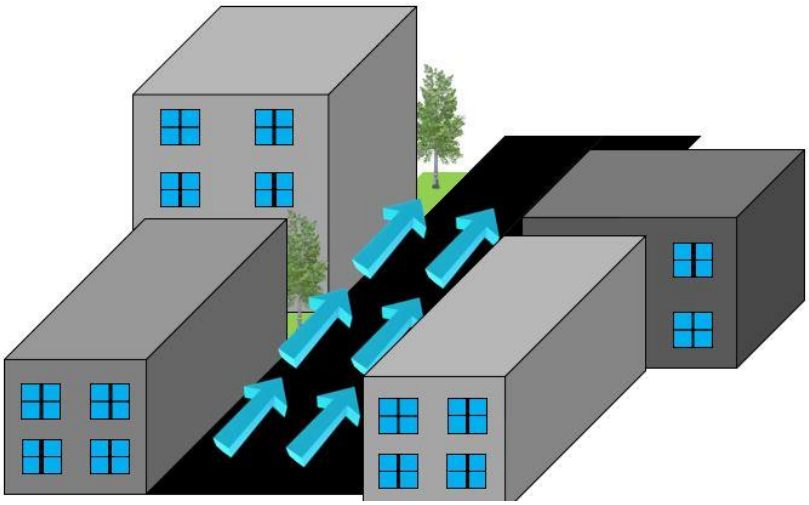

Figure 5 - Channeling effect of the wind (represented by the arrows) in an urban environment.

A particular concern is given to the wake region formed behind buildings. A recirculation zone is formed behind buildings, composed of slowly circulating air, lasting up to a distance equivalent to two or three building heights (Belcher, 2005). In the far wake, the wind speed returns to the upwind velocity after ten to 30 building heights (Belcher, 2005). A pollutant released upwind of a building can flow around it and then entrain into the recirculation zone. Meanwhile, the rest of the pollutant cloud is quickly mixed in the far wake region due to the increased turbulence generated by the building.

In contrast to the wake region behind buildings near ground level, the fast-moving air above the roof line sheds an unstable shear layer with high vorticity and turbulence, that oscillates (Louka, Belcher, & Harrison, 1999). When the fluctuations bring this shear layer down, the faster air from above the roof level moves down, approaching the next building downwind, creating an intermittent recirculation zone of air in the street between the buildings, reinforcing the effect of the wake region behind buildings. The depth and strength of the shear layer are affected by the distance between the buildings and the roof shape (Louka, Belcher, & Harrison, 1999; Xiaomin, Zhen, & Jiasong, 2006). At neighborhood level, vertical dispersion is

enhanced due to vertical transport out of the array of buildings as the wind adjusts to the urban environment (MacDonald, Griffiths, & Hall, 1998). Lateral displacement is also affected, as the plume is wider along the cross-wind direction than the spread observed over flat ground (Davidson *et al.*, 1996).

All those effects combined are crucial in the dispersion of pollutants in urban zones. Urban configurations like street canyons generate vortices that can increase the concentration of such pollutants. The type of flow regime in the canyon determines the exchange rate with clean air above the rooftop level and, consequently, the diffusion of the pollutant. Wider streets increase the effectiveness of pollutant dispersion, with larger vertical transfer to the flow of clean air at the rooftop level (Xiaomin, Zhen, & Jiasong, 2006).

Changes in the channel, such as T-junctions, create strong vertical and lateral dispersions (Boddy *et al.*, 2005). The flow of air has a dividing streamline as it approaches the building. The air above the dividing streamline is forced upwards, moving over the building. Winds on the sides of the dividing streamline are deflected to the side of the building and redirected to the side streets of the T-junction, leading to a stronger dispersion, as shown in Figure 6 (Belcher, 2005). Dividing streamlines end at a stagnation point upon contact with the building.

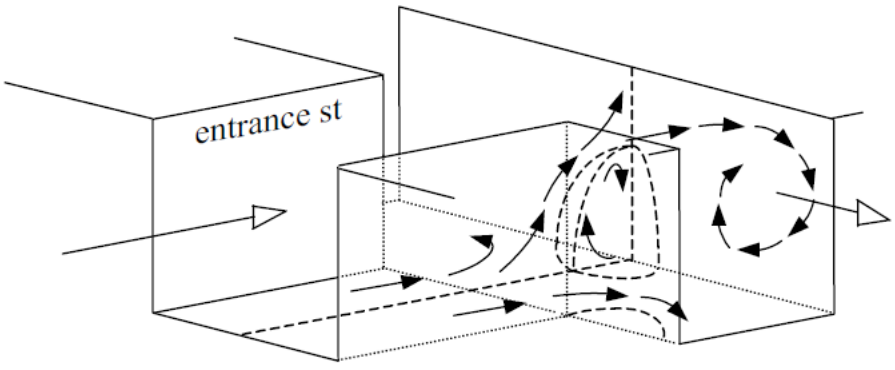

Figure 6 - Representation of the flow complexity at T-junctions (Belcher, 2005).

The concept of dividing streamline is defined as the streamline that, in a stably stratified

flow field over a three-dimensional obstacle, separates the streamlines that go over the obstacle from the ones that go around it. The height of the dividing streamline is affected by the shape and orientation of the obstacle, stability of the flow, upstream air density, and velocity profile shape (Snyder *et al.*, 1985). It was postulated that along a streamline, there is a conversion of kinetic to potential energy of a parcel of air as it rises over the obstacle (Sheppard, 1956). This transfer of energy can be expressed as shown in Equation 1 (Snyder *et al.*, 1985). The terms in Equation 1 are density (ρ), free-stream velocity (U_∞), height of the dividing streamline (H_S), acceleration of gravity (g), height of the top of the obstacle (h), and height (z) above the ground.

$$\frac{\rho U_\infty^2 H_S}{2} = g \int_{H_s}^{h} (h - z) \left(-\frac{\partial \rho}{\partial z} \right) dz \quad \textbf{(1)}$$

In Equation 1, the left-hand side represents the kinetic energy of the fluid parcel, and the right-hand side as the potential energy gained by the fluid parcel as it goes up from a height around the dividing streamline to the top of the obstacle. The density gradient term $\left(\frac{\partial \rho}{\partial z}\right)$ quantifies the stratification of the density of the incoming flow. In the case of a DTA gas dispersion in an urban environment, the height of a dividing streamline is crucial. A dividing streamline at a lower height means that more of the approaching wind is diverted over the top of the obstacle. DTA gases stay low to the ground and cause high contaminant concentrations near ground level. Therefore, the closer the dividing streamline is to ground level, the more contaminant is carried to the top of the obstacle by the upward flow above the dividing streamline. A higher concentration of DTA gases on top of a building poses an unplanned risk for the people inside, as most air intakes are present on the roofs of tall buildings. Relatively high concentrations of contaminant tracers have been reported at the top of skyscrapers, as vertical spread is enhanced by large eddies present nearby tall buildings (Hanna & Chang, 2015).

Additional studies of flow in urban environments are present in the literature (Aliabadi, Moradi, & Byerlay, 2021; Barlow *et al.*, 2015; Carlotti, 2015; Cermak, 1975; Dauxois *et al.*, 2021; Fernando *et al.*, 2001; and Song *et al.*, 2018)

1.6 Urban Modeling in Wind Tunnels

To better understand flow patterns in urban areas, multiple studies of the flow around models of buildings or groups of buildings can be found in the literature. These physical models are inserted in repeatable, controlled environments, like wind or water tunnels. Three main techniques are used for the velocity measurements: Hot Wire Anemometry (HWA), Laser Doppler Velocimetry (LDV), and Particle Image Velocimetry (PIV). LDV is a high-rate data acquisition technique but is limited to a single point in space. The PIV technique measures velocities over a planar area but is limited in data acquisition frequency. The HWA technique was not used in this dissertation.

1.6.1 Laser Doppler Velocimetry Measurements in Urban Models

Laser Doppler Velocimetry (also called Laser Doppler Anemometry – LDA – if measuring air velocity) is a technique widely used in physical models due to its non-intrusive nature. Depending on the setup, LDV can measure one, two, or three velocity components simultaneously, commonly called 1D, 2D, and 3D LDV, respectively.

Urban models can comprise scale models of real cities (Kaster-Klein & Rotach, 2004) or hypothetical groups of buildings. LDV results in such models show lower velocities below roof level near buildings and higher velocities in intersections, which indicates the presence of channeling effects. High values of turbulent kinetic energy just above rooftops point to vortex shedding from the top of the buildings (Kaster-Klein & Rotach, 2004). Additionally, models can also be made of generic objects, such as cubes, arranged to simulate urban areas (Castro, Cheng,

& Reynolds, R.T., 2006; Herpin *et al.*, 2018). LDV measurements at mid-cube height show high cross-wind components, as shown in Figure 7 (Herpin *et al.*, 2018), as the cubes redirect the flow, along with near-zero velocity in building wakes.

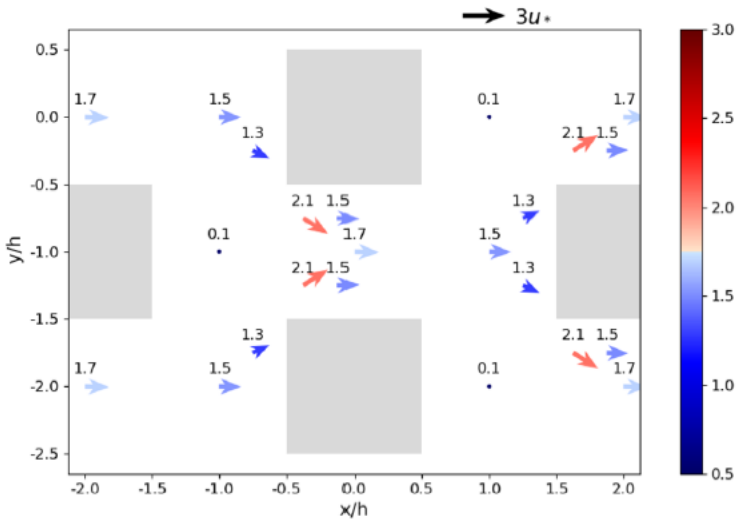

Figure 7 - LDV measurements at mid-model height show a redirection of the flow to serpentine around the model buildings. Near-zero velocity vectors behind the models are also shown (Herpin *et al.*, 2018).

1.6.2 Particle Image Velocimetry Measurements in Urban Models

Particle Image Velocimetry (PIV) is another technique widely used for velocity measurements in physical models. PIV measurements around a single building show a vortex in front of the object and a region of near-stagnant flow in the wake of the model (Reynolds, R.T. & Castro, 2008). PIV results were consistent with the previous LDV measurements (Castro, Cheng, & Reynolds, R.T., 2006) on the same setup (Reynolds, R.T. & Castro, 2008). PIV results show velocity data along a plane, while LDV results give detailed velocity data, like turbulence, at a few points within that plane.

Study of the spacing between buildings in the spanwise direction shows that sufficiently close buildings behave as a single buff body (i.e., vortex shedding was observed only in the outer part of the structures), and the flow complexity around the pair increases with the spacing

between them. As the space between the two buildings is increased, vortices form inside and outside the pair of buildings. Wind channeling between the buildings was also observed (Kim, B. *et al.*, 2019).

Multiple 2D PIV studies in urban models have been used to evaluate the flow in the urban canyons between buildings in the along-wind direction (Paterna, 2015; Sosnowski *et al.*, 2019; Takimoto *et al.*, 2011). 2D PIV measurements in these configurations show a reduction of the horizontal velocity component in the region between the buildings and in the wake of the downwind structure, as shown in Figure 8a (Sosnowski *et al.*, 2019). In the region between the buildings, there is a strong acceleration of the wind downward just in front of the downwind building that, combined with the increased flow upward just behind the upwind building, indicates the presence of a strong vortex in the region between buildings, illustrated in Figure 8b (Sosnowski *et al.*, 2019).

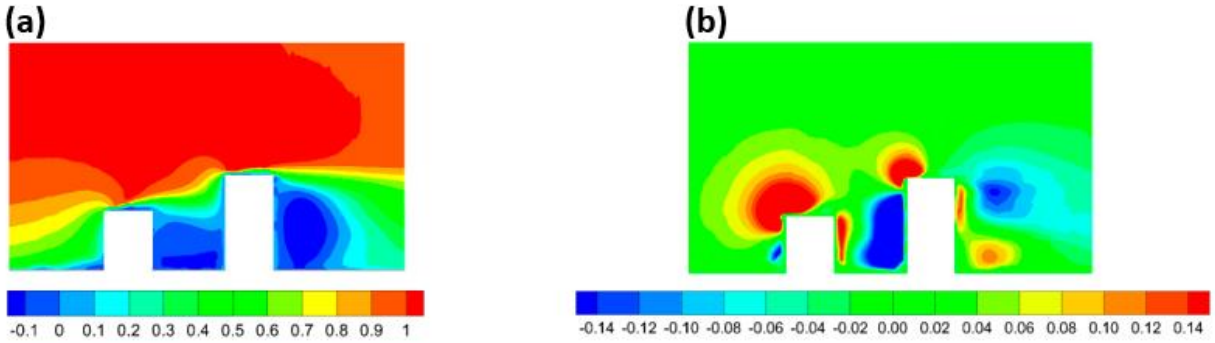

Figure 8 - PIV velocity measurements in a pair of scale buildings. (a) Horizontal velocity component; (b) Vertical velocity component. Both scales are normalized by the freestream horizontal velocity component (u_∞ = 5.5 m/s) (Sosnowski *et al.*, 2019).

Figure 8b shows an increase in the vertical component at the leading edge of each building, possibly resulting in vortex shedding. The formation of vortices from the leading edge of the upwind building was demonstrated in wind tunnel measurements taken by Paterna (2015). Vorticity measurements in the shear layer at roof level show high vorticity values caused by

strong velocity gradients in that area of the flow. The strongest gradients are observed when the recirculating flow between the buildings interacts with the approaching flow at roof level. Vorticity measurements along a group of identical mock buildings are shown in Figure 9 (Paterna, 2015).

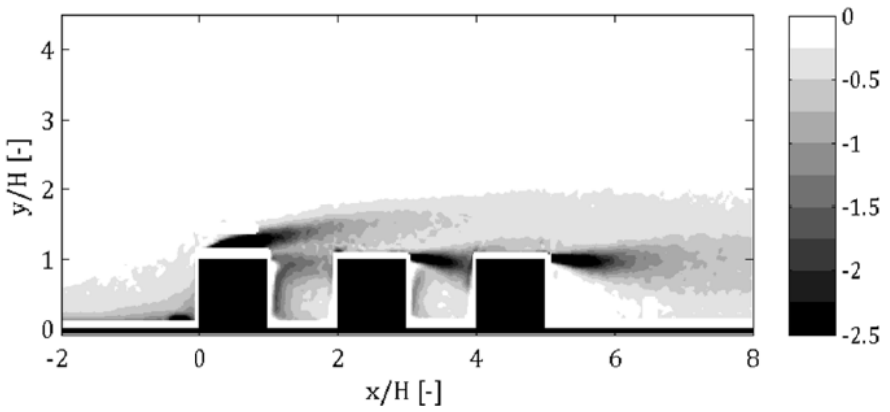

Figure 9 - Vorticity measurements around a group of scale buildings obtained via PIV (Paterna, 2015).

The cross-flow around a pair of wall-mounted cylinders along the same plane (called tandem configuration) can be considered analogous to the flow approaching a pair of buildings in an urban environment. PIV measurements have shown that if the cylinders are sufficiently close to one another, the shear layer generated by the free end of the upwind cylinder reattached on the surface of the downwind cylinder. However, for cylinders separated by a large distance, the shear layer reattached at ground level, while a second recirculation zone is formed behind the downwind cylinder, as shown in Figure 10 (Kim, T. & Christensen, 2018). In the case of cylinders of different heights, a phenomenon called “sheltering” is observed, where the downwind cylinder has limited interaction with the approaching flow because the upwind cylinder blocks part of the approaching flow (Essel, Balachandar, & Tachie, 2023). It was observed that sheltering increases with cylinder height ratio and decreases with the spacing between the cylinders (Hamed, Peterlein, & Randle, 2019). Higher sheltering also enlarges the

near-stagnant flow region between the cylinders (Essel, Balachandar, & Tachie, 2023).

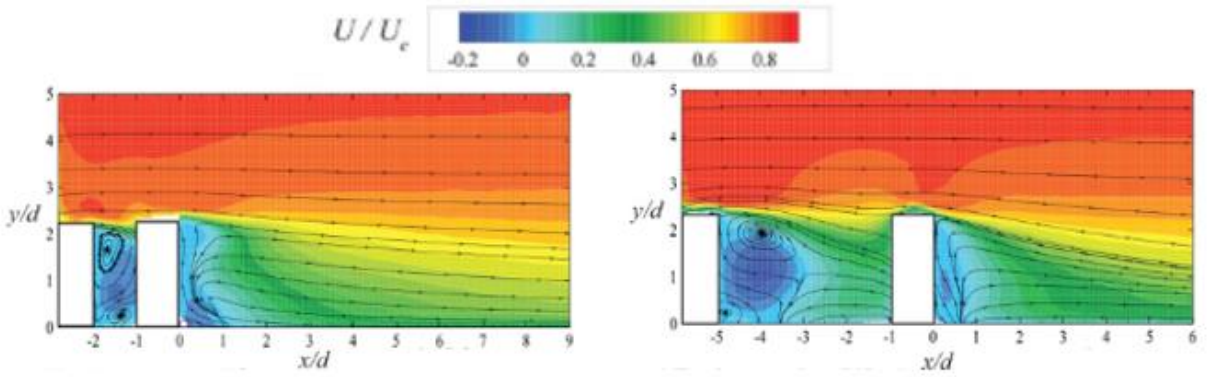

Figure 10 - Effect of separation of cylinders in tandem configuration to the wake region (Kim, T. & Christensen, 2018).

Additional wind tunnel studies of flow characteristics in urban models are present in the literature (Ahmad, Khare, & Chaudhry, 2005; Blackman, Perret, & Mathis, 2019; H'ng *et al.*, 2022; Shirzadi, Tominaga, & Mirzaei, 2019; Zhao *et al.*, 2021; and Zhixiang, L. *et al.*, 2020). The PIV studies mentioned above investigated only the wind flow in urban environments, which would also be sufficient to characterize the dispersion of a true neutrally buoyant gas typical of air pollution, but there has been no attempt to simulate any gas releases that would disrupt the ambient flow field. Any gas release of sufficient volume displaces the ambient flow regardless of density. However, in the specific case of a denser-than-air release in an urban environment, the flow complexity within the urban setting is enhanced. To that end, the Jack Rabbit II field test was undertaken to investigate the impact of a DTA gas release (chlorine) in a mock urban environment.

1.7 The Jack Rabbit II Field Test

The field tests mentioned in Section 1.3.2 were conducted over no obstacles or over very few obstacles. No test had been conducted with a DTA gas over a full urban environment. The Jack Rabbit II Field test was conducted to investigate the flow characteristics of a HTA gas in an

urban setting. The work presented in this dissertation consists of a physical model of the Jack Rabbit II field test.

The Jack Rabbit II field test was conducted at Dugway Proving Ground (DPG) in Utah, using a simulated urban environment, with the primary objective of investigating DTA releases in an urban setting. Expanding the study from JR-I, JR-II consisted of multiple chlorine releases in a complex mock urban environment (MUE). The MUE consisted of 83 CONEX shipping containers, representing buildings at roughly 1:10 scale. Those containers were distributed along 12 equally spaced rows. Each container was identified by a pair of numbers; the first indicated the row (numbered from south to north), and the second showed the position in that row from west to east. JR-II Phase 1 consisted of five trials between August 24th and September 3rd, 2015. In all trials, chlorine gas was released downward from the tank and spread outwards, as shown in Figure 11 (Fox, 2019; Vogel, 2015). Three types of data were collected: visual recordings of the releases using HD video cameras, chemical concentration measurements taken in multiple locations within the MUE, and meteorological data at multiple heights in a tower located south of the release point ("Meteorological Tower 3" or "Tower 3").

Figure 11 - Chlorine release during the Jack Rabbit II Field Tests (Fox 2019; Vogel, 2015).

Figure 12 shows a schematic of the CONEX containers and their relative position to the concrete pad and the release point at its center. Row 13 (shown in blue in Figure 12) was composed of seven vehicles. The MUE at DPG was oriented at 165° (i.e., rotated 15°

counterclockwise from the north), which is the historically prevailing wind direction for the test site during the time of the year planned for the tests. Wind direction is defined in meteorology as the direction from which the wind originates (e.g., a wind direction angle of 180° refers to the wind coming from the south).

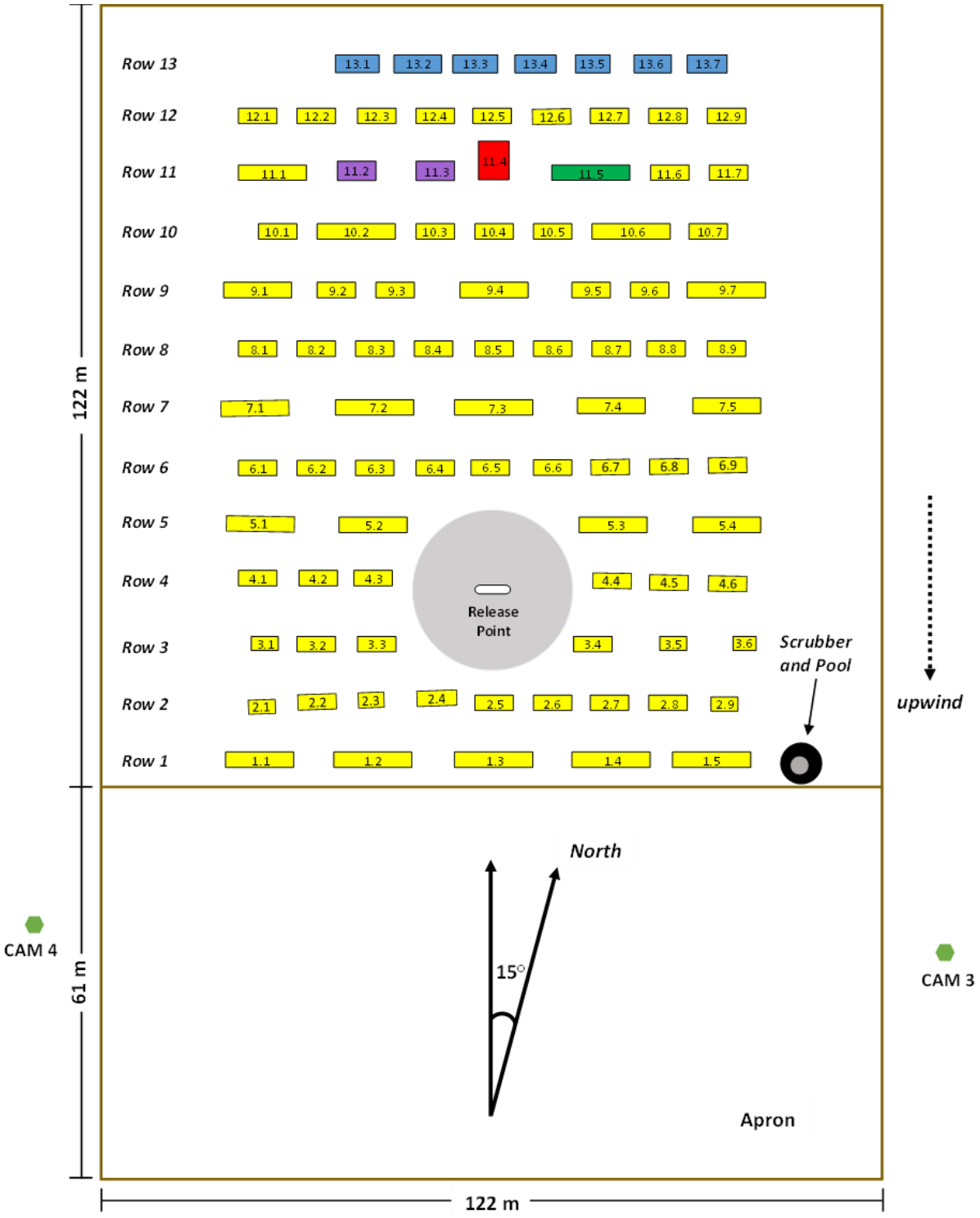

Figure 12 - Schematic of the CONEX layout from the Mock Urban Environment of the Jack Rabbit II Field Test (Fares, 2022).

Table 1 shows the main characteristics of the trials, including average wind direction and speed (Hanna, 2020) and chlorine release amount and duration (Spicer & Tickle, 2021). Table 1 shows that the prevailing wind direction was southerly, meaning the wind typically blew from the bottom of Figure 12, with some variation in wind angle (Hanna, 2020). Figure 13 illustrates the relative angles between the pad orientation and the average wind direction of JR-II Trials 2 and 4 as examples.

Table 1 - Main characteristics of the Jack Rabbit II Trials (Hanna, 2020; Spicer & Tickle, 2021).

Trial	Initial mass of Cl_2 (kg)	Primary release rate (kg/s)	Average Wind Direction	Wind Direction Relative to the MUE	Wind Speed (m/s) (at 4 m AGL)
1	4545	224	140°	-25°	2.78
2	8192	273	174°	9°	5.58
3	4568	275	166°	-1°	4.62
4	7017	271	187°	22°	2.35
5	8346	273	213°	48°	1.98

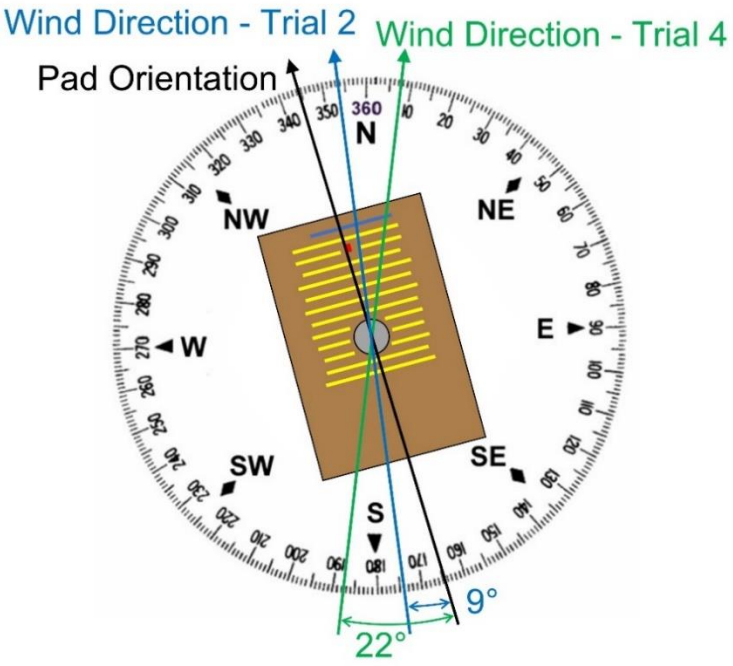

Figure 13 - Relative angles of the JR-II Field Test pad and the average wind direction of JR-II Trials 2 and 4.

1.7.1 Jack Rabbit II – Special Sonic Anemometer Study Field Test

During JR-II, no meteorological data was collected within the container array due to the highly corrosive nature of chlorine. Since it was still necessary to know the flow characteristics among the containers, a follow-up field test took place in the MUE, called JR-II Special Sonic Anemometer Study (JRII-S). No chlorine was released in JRII-S, and only metrological data was collected. A total of 30 three-dimensional sonic anemometers (Model 81,000, R.M. Young Company, Traverse City, MI) were placed at points of interest in the MUE: 13 around CONEX 9.4 (10.67 m wide, 2.44 m deep, 2.59 m tall) and 17 around CONEX 11.4, which simulated a tall building. CONEX 11.4 consisted of two adjacent stacks of three containers each to form a single obstacle, measuring 4.88 m wide, 6.05 m deep, 7.77 m tall. The relative position of the sonic anemometers to the CONEX containers is shown in the highlighted part of Figure 14.

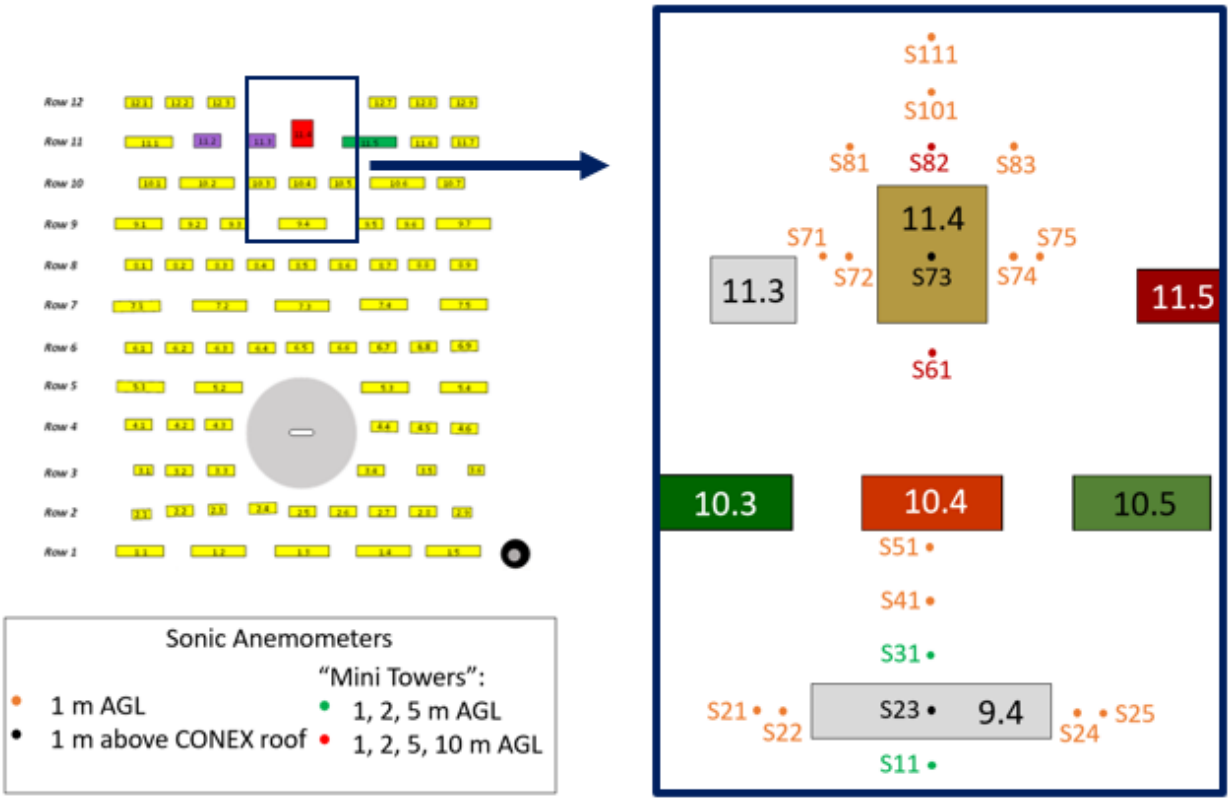

Figure 14 - Modified MUE for JRII-S tests, highlighting the locations of the Sonic Anemometers.

Fourteen individual sonic anemometers were placed at 1 m above ground level (AGL) (shown in orange in Figure 14) around CONEX containers 9.4 and 11.4. These included the sonic anemometers at the sides of CONEX 9.4 (S21, S22, S24, and S25) and CONEX 11.4 (S71, S72, S74, S75, S81, and S83), along with S41 and S51 north of CONEX 9.4; and S101 and S111 north of CONEX 11.4. At the other locations (all immediately in front of or behind the CONEX containers), the anemometers were placed in "mini-towers", i.e., groups of three or four sonic at different heights. These mini-towers allowed for an investigation into how the containers changed the flow as a function of elevation. The mini-towers close to CONEX 9.4 (S11 and S31) had anemometers at 1, 2, and 5 m AGL, while the ones close to CONEX 11.4 (S61 and S82) had an additional anemometer at 10 m AGL. In both cases, the tallest sonic anemometer in the mini-towers was placed above the adjacent container roof level. Finally, a sonic anemometer was placed on top of each CONEX 9.4 and 11.4, located 1 m above the roof level of the containers (S23 was 3.9 m AGL, and S73 was 9.7 m AGL). The anemometers were numbered from south to north (row 9 was skipped) and from west to east in the same row. For the mini-towers, the suffix L was added to the name to indicate anemometers at different levels, numbering by increasing height (e.g., S82L3 is the third highest anemometer in the second location in the eighth row). To accommodate the northernmost anemometers during the JRII-S study, three CONEX containers in Row 12 were removed (12.4, 12.5, and 12.6), plus the entirety of Row 13. Sonic anemometers placed in Tower 3 measured the approaching wind speed and turbulence at five heights (2, 4, 8, 16, and 32 m AGL).

In total, JRII-S recorded data continuously in two different windows, one spanning from October 11 to November 2, 2015, and the second from March 2 to 28, 2016. Velocity components and secondary statistical data were time-averaged in 30-minute intervals. Among all

the data collected, six of those 30-minute intervals were identified as significant because the wind in those Time Frames had similar characteristics to JR-II chlorine release trials. The main characteristics of these Time Frames are shown in Table 2. Time Frames A, C, and E consisted of approaching wind that traveled approximately along the MUE centerline, perpendicular to the long face of the CONEX containers.

Table 2 - Summary of meteorological conditions of the relevant Time Frames from JRII-S.

Time Frame	Date	Time (UTC)	Average Wind Direction	Wind Direction Relative to MUE	Wind Speed (m/s) (at 4 m AGL)
A	March 6, 2016	09:00	166°	1°	7.26
B	March 6, 2016	11:00	182°	17°	7.79
C	March 24, 2016	11:00	163°	-2°	3.79
D	March 24, 2016	13:30	172°	7°	4.65
E	March 27, 2016	07:00	166°	1°	4.96
F	March 27, 2016	08:00	153°	-12°	5.61

1.7.2 Previous Physical Modeling of the JR-II and JRII-S Field Tests

Two physical models (Owkes *et al*., 2020; Pirhalla *et al*., 2021) and one computational model (Carissimo, Trini Castelli, & Tinarelli, 2021) studied the wind field in the JR-II and JRII-S field tests. Wind tunnel tests in a 1:50 scale model of the MUE were performed by the Environmental Protection Agency (EPA) (Pirhalla *et al.*, 2021). In their tests, 2D Laser Doppler Velocimetry (LDV) was used to determine the velocity of the wind and turbulence intensity in the scaled MUE. LDV measurements were compared to JR-II results to determine the agreement between the model and full scale. Releases of a neutrally buoyant tracer gas (ethane) were conducted, and concentration was measured using Flame Ionization Detectors (FID). Direct comparison with Computational Fluid Dynamics (CFD) was made, applying fine scales Embedded Large Eddy Simulations (ELES) modeling. Gas releases were simulated using AERMOD and compared to the data acquired with the FID, showing excellent qualitative and

quantitative agreement for vertical and lateral concentration profiles (Pirhalla *et al.*, 2021). The researchers also experimented with modified MUE layouts, including adding more CONEX containers and moving CONEX 11.4 closer to the release point.

Water tunnel tests were conducted simulating the atmospheric conditions of JR-II Trial 5 at a 1:188 scale (Owkes *et al.*, 2020). Three-dimensional data was captured using Magnetic Resonance Velocimetry (MRV) and Concentration (MRC) – using a passive tracer. These results were also compared to Large-Eddy Simulations (LES), showing qualitative and quantitative agreement. Figure 15 compares the velocity measurements obtained via LES and MRV in a horizontal plane at a height equivalent to 90% of the standard CONEX container (Owkes *et al*., 2020).

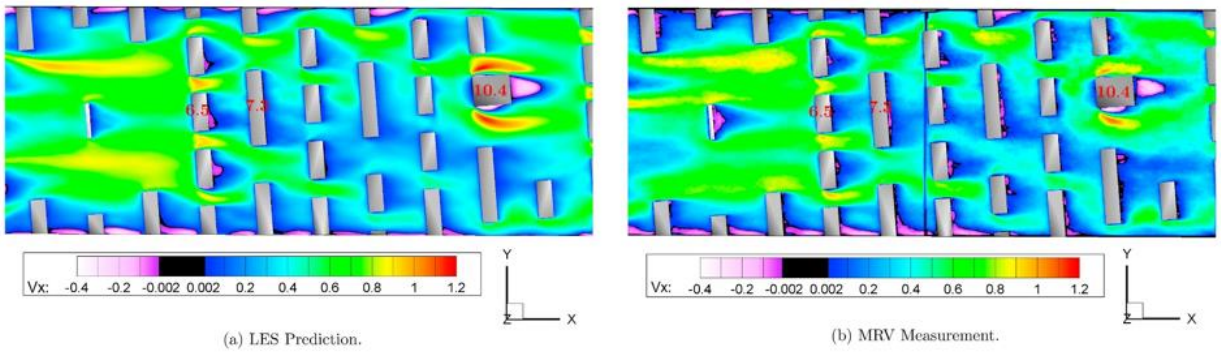

Figure 15 - Velocity measurements reproducing Trial 5 of JR-II obtained via (a) Large Eddy Simulation and (b) Magnetic Resonance Velocimetry in a water tunnel (Owkes *et al.*, 2020). Values are normalized by a reference velocity of 0.31 m/s.

Both modeling studies have limitations. The EPA study was limited to wind directions parallel to the orientation of the MUE due to size restrictions in their wind tunnel. The releases in that work consisted only of a tracer gas, and no simulation of chlorine releases was performed. Owkes and coworkers were able to obtain velocity measurements within the MUE but, due to scaling issues, limited their study to a section within the MUE, as shown in Figure 16 (Owkes *et al.*, 2020). The releases conducted in that study were also neutrally buoyant, inconsistent with the

DTA purpose of the JR-II tests. The upwind intrusion of the release chemical reported by Owkes and peers is significantly smaller and does not agree with the intrusion observed in the visual recordings of the JR-II trials. Additionally, by checking the references of the water tunnel study, it appears that the wind speed and release conditions for Trial 5 were used, but the researchers incorrectly used the relative wind direction of Trial 3 at 2 m AGL (4.5°) instead of the proper averaged relative wind direction (48°) of Trial 5.

Both studies also made computational simulations of the releases. However, in both works, the computational inputs were based on the physical models, instead of the field test. Lastly, neither of the studies compared velocity nor concentration measurements to data obtained during JR-II.

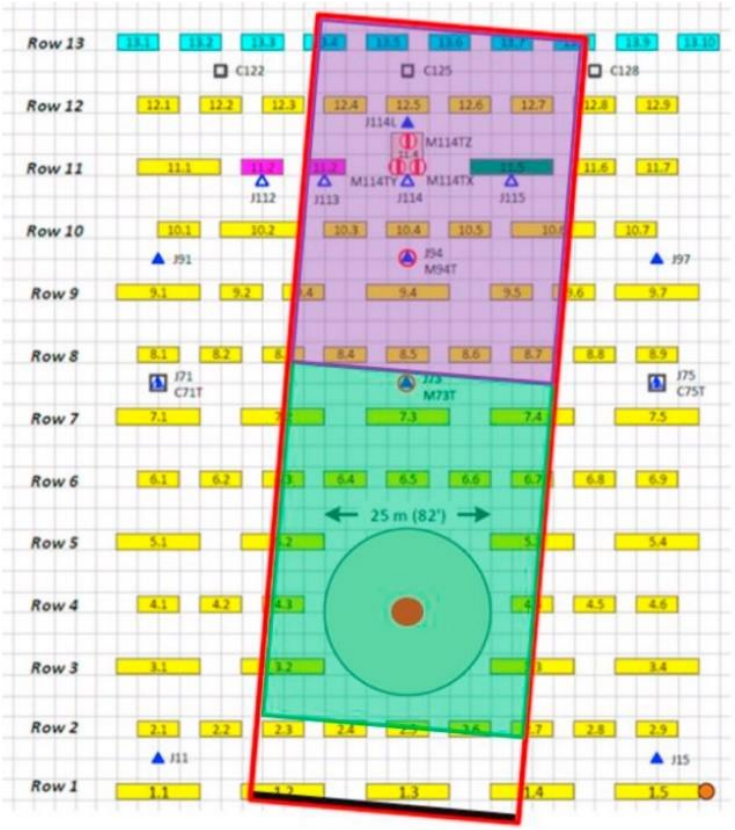

Figure 16 - Overlap of the MUE layout from JR-II to the water tunnel used by Owkes and peers. Concentration measurements were made in the green zone, while velocity measurements were taken in the green and pink zones (Owkes *et al.*, 2020).

1.7.3 Previous Computational Modeling of the JRII-S Field Test

Computational simulations are another method used to evaluate risk assessment in case of a hazardous release. Validated computational models are extremely valuable for risk assessment due to their setup and lower cost. In the study by Carissimo, Trini Castelli, and Tinarelli, two different CFD models, *Code_Saturne* (CS) – applied in Reynolds-Averaged Navier-Stokes (RANS) model and a k-ε turbulence closure – and Parallel Micro-Swift-Spray (PMSS) were used to simulate the flow field in the MUE in JRII-S Time Frames C and D wind conditions. The researchers simulated the entire flow field of JRII-S. Pointwise velocity measurements at the 1 m AGL Sonic Anemometer locations were extracted and compared to the velocity data obtained during JRII-S, showing an overall good agreement, as shown in Figure 17 (Carissimo, Trini Castelli, & Tinarelli, 2021). The CS model showed an improved prediction of flow direction in the channels (Sonic anemometers S21, S22, S24, S25, S71, S72, S74, and S75), with more significant differences in wind direction observed in the recirculation region in the lee side of the buildings (S31, S41, S51, S82, S101, and S111).

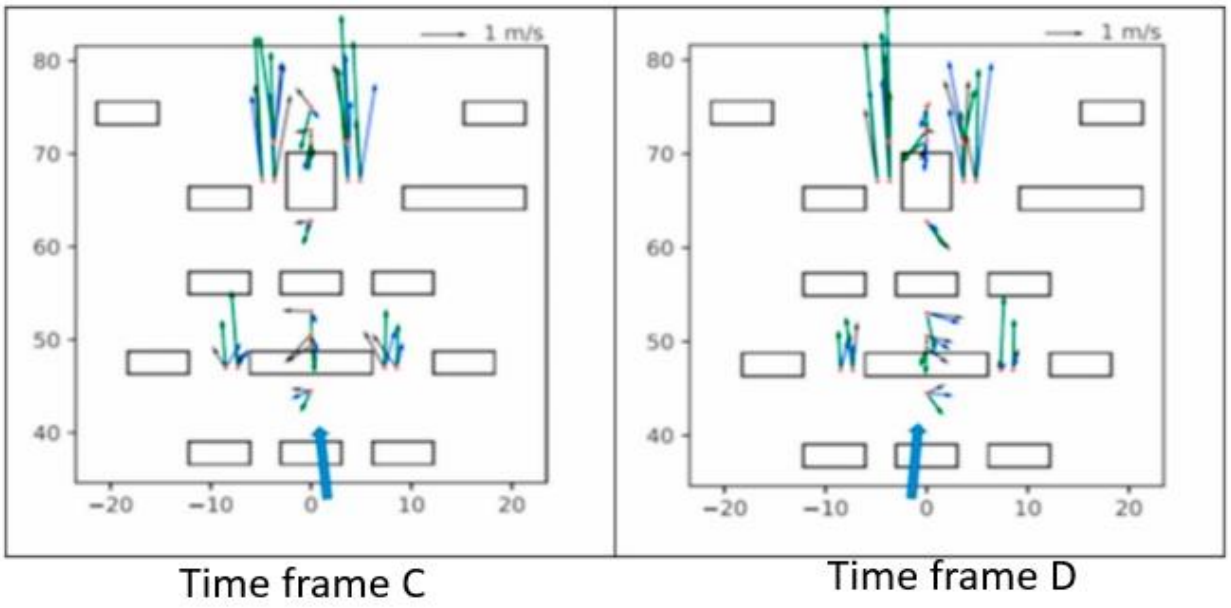

Figure 17 - Pointwise velocity comparisons at the Sonic Anemometer locations from JRII-S Time Frames C and D between Field (black vectors), CS model (blue), and PMSS model (green) (Carissimo, Trini Castelli, & Tinerelli, 2021).

The velocity flow field obtained in simulations of Time Frame C conditions is shown in Figures 18a (CS) and 18b (PMSS), while the results of simulations in Time Frame D conditions are shown in Figures 18c (CS) and 18d (PMSS) (Carissimo, Trini Castelli, & Tinarelli, 2021). Comparison of the velocity fields shows disagreement between simulations. In Time Frame C, the PMSS model yields faster velocities in the channels (especially the center-left channel, which starts at X = 5 m). Additional differences in the velocity magnitudes in front of CONEX 11.4 (located in Figure 18 at X = 0, Y = 65 m) and in the extent of the higher velocity zones downwind of Row 11 are also observed. The authors attributed the disagreement to the asymmetric geometry of the MUE while also highlighting that the agreement is better in the central area of the simulations (-10 m < X < 10 m) (Carissimo, Trini Castelli, & Tinarelli, 2021).

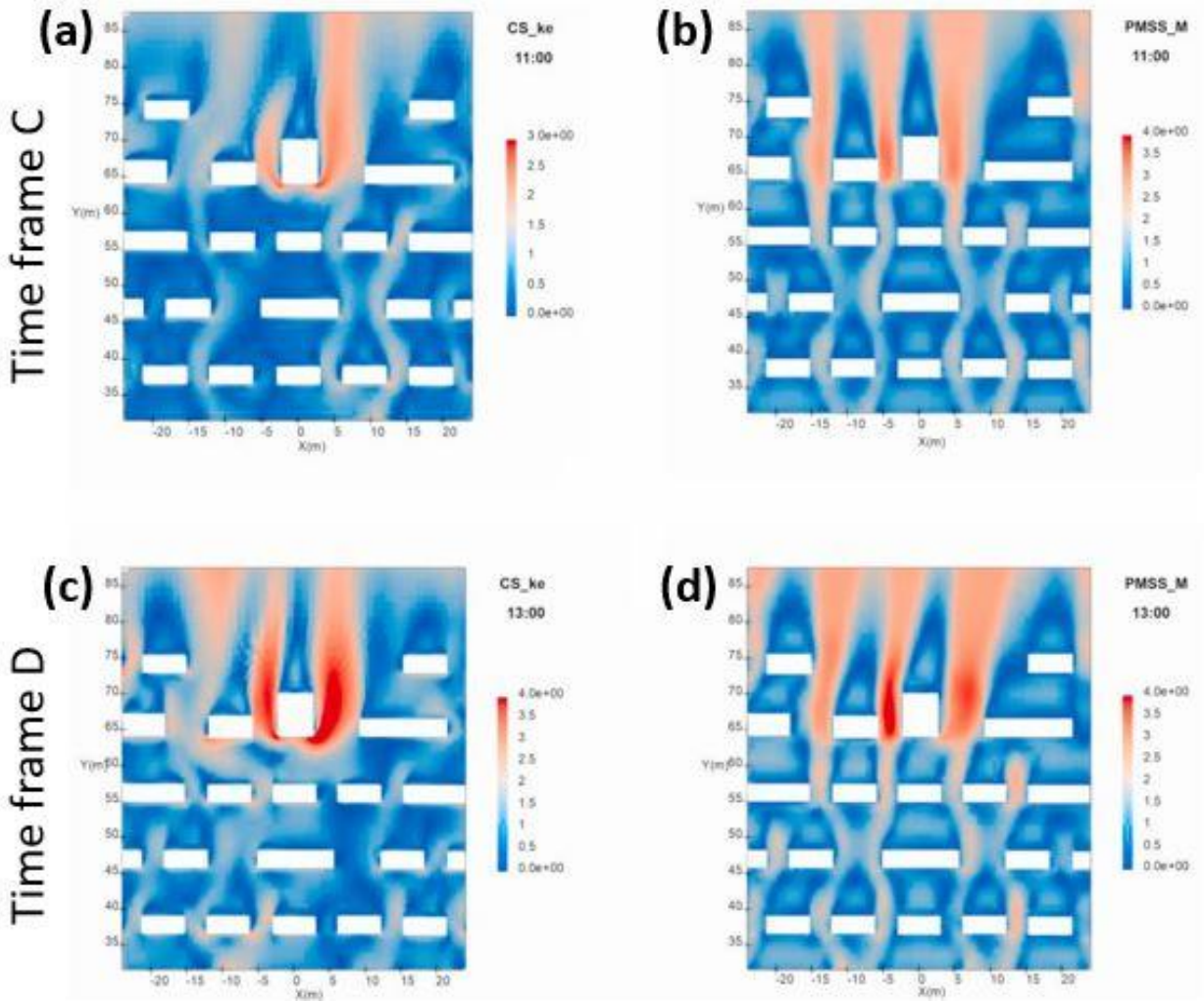

Figure 18 - Simulations of a section of the MUE from JRII-S in (a) Time Frame C wind conditions using the CS model; (b) and the PMSS model; (c) Time Frame D wind conditions using the CS model; and (d) the PMSS model (Carissimo, Trini Castelli, & Tinarelli, 2021).

The computational modeling by Carissimo and peers lacks physical validation against a physical model of the JRII-S field test. The simulations have only been evaluated against field data at the sonic anemometer locations. Additionally, the simulations of releases (originated at fictional sources within the MUE) in the simulations do not agree across the different models used, as shown in Figure 19 (Carissimo, Trini Castelli, & Tinarelli, 2021).

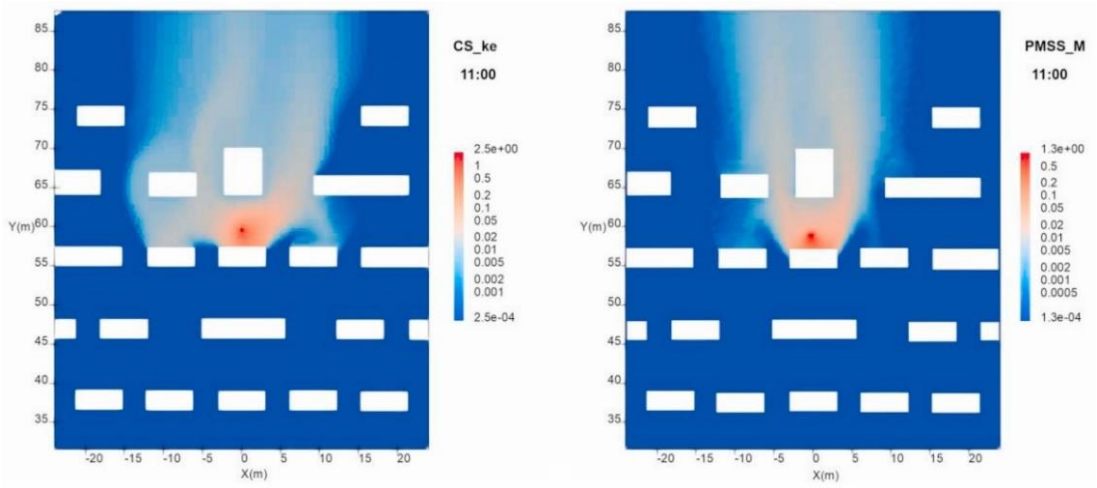

Figure 19 - Release simulations from fictional sources in Time Frame C wind conditions from JRII-S (Carissimo, Trini Castelli, & Tinarelli, 2021).

1.8 Research Objectives

All the studies mentioned previously are significantly important to the field. However, further studies are required for better comprehension of the dispersion of DTA gases in urban environments for consequence assessment. As discussed previously, all of the previous studies have limitations, with no actual reproduction of the conditions of the JR-II field test. These limitations include scaling issues, not releasing DTA gas, or lack of validation. The velocity measurements in physical models are significant for understanding velocity and vorticity patterns in urban environments. However, PIV measurements of a simulated field test with DTA gas release do not currently exist in the literature. PIV measurements during gas releases within a valid scale model would quantify how the added momentum from the releases affects the velocity, vorticity, and height of the dividing streamline. Since it was impossible to make velocity measurements during the JR-II field tests due to the corrosive nature of chlorine, a release of a chlorine simulant on a scale model can fill this gap. Furthermore, using a side view of CONEX 11.4, PIV can show the velocity field beyond previous pointwise measurements, thus identifying the dividing streamline and recirculation zones near the tall CONEX container.

The CFD model referenced here (Carissimo, Trini Castelli, & Tinarelli, 2021) investigated the flow through the entire MUE. However, this CFD model is yet to be compared to any measurements taken in physical models of JR-II. PIV experiments encompassing the last few rows of the model MUE (around CONEX 11.4) can be compared to CFD studies and can identify complex flow phenomena, providing information about the dispersion of a contaminant in an urban environment.

In order to fill in these knowledge gaps, the following research objectives are proposed:

- Obtain LDV measurements in the scale model of the JR-II field test in a wind tunnel.
    - Compare to DPG approach wind to assure agreement between wind tunnel and field tests atmospheric conditions.
    - Compare LDV measurements to sonic anemometers data from JRII-S.
    - Investigate potential errors from generating three-component velocities from extrapolated two-dimensional LDV data measurements.
- Conduct PIV measurements within the MUE model in the CHRC wind tunnel by projecting a vertical laser sheet in the centerline of the MUE. These PIV measurements consist of a side view of CONEX 11.4, with the following objectives:
    - Measure the entire flow field directly in front of, above, and behind CONEX 11.4.
    - Simulate a chlorine release and show the effect of added momentum from the release, including any change in the height of the dividing streamline.
- Conduct PIV measurements using a top view of the area around CONEX 11.4, with the laser sheet in the XY plane at 2 cm above the MUE pad. Compare these measurements of the overall flow around CONEX 11.4 to CFD data available in the literature for a horizontal plane at 1 m above the full-scale MUE.

Chapter 2 – The Wind Tunnel Facility at the Chemical Hazards Research Center

An experimental plan using the ultra-low speed wind tunnel at the Chemical Hazards Research Center was created to fulfill the objectives of this work. This chapter describes the facility and its capabilities, instrumentation, and the MUE model.

2.1 The Wind Tunnel

The ultra-low speed wind tunnel located in the Chemical Hazards Research Center was built to model the dispersion of hazardous gases in the atmosphere while reproducing turbulence levels similar to those found in the atmospheric boundary layer (ABL). The tunnel has a working section of 24 m long and a cross-section measuring 6 m x 2.1 m (W x H). The tunnel is in the center of an isolated room. Control and observations are made from an adjacent control room to avoid major disruptions to the tunnel flow. A schematic of the wind tunnel and the control room is shown in Figure 20 (Havens, Spicer, & Walker, 1996). The coordinate system referenced throughout this work places the x coordinate along the tunnel (positive direction towards the exit of the tunnel), the y coordinate across the tunnel (positive direction pointing away from the control room), and the positive z coordinate direction pointed vertically upwards.

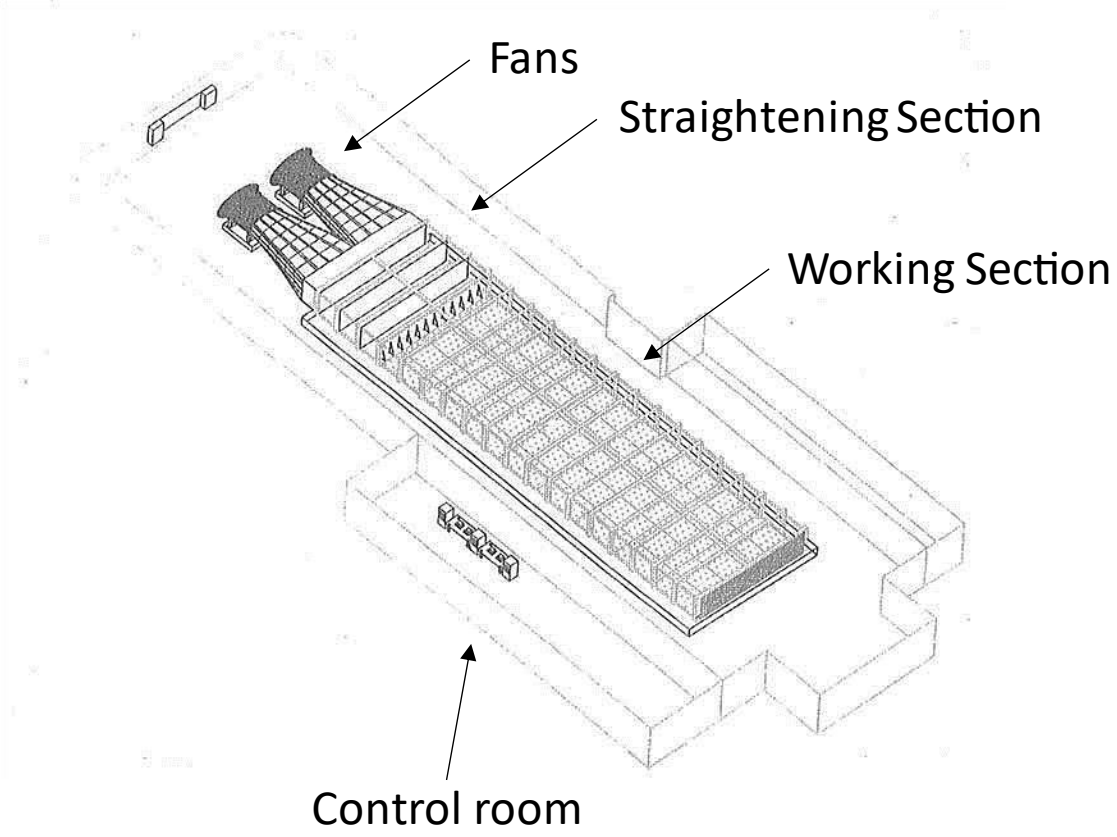

Figure 20 - Schematic of the Wind Tunnel Facility at the CHRC (Adapted from Havens, Spicer, & Walker, 1996).

The tunnel is a push-through type wind tunnel, powered by two 75 hp fans (Buffalo Forge Company Model 72D5 ADJUSTAX), measuring 1.8 m in diameter. Between the fans and the working section of the tunnel, the flow passes through a flow-straightening section. At the beginning of the working section, turbulence is generated using a row of Irwin Spires, custom-made from acrylic, measuring 93 cm tall and 13.5 cm wide at the base. Turbulence is maintained throughout the tunnel via surface roughness elements made of aluminum angles, measuring 1.5 in x 1.5 in (3.8 cm x 3.8 cm). The spires generate a fully developed boundary layer with a height of approximately 60 cm. The Irwin spires and the surface roughness elements are shown in Figure 21, along with the area source, which is explained in Section 2.4.

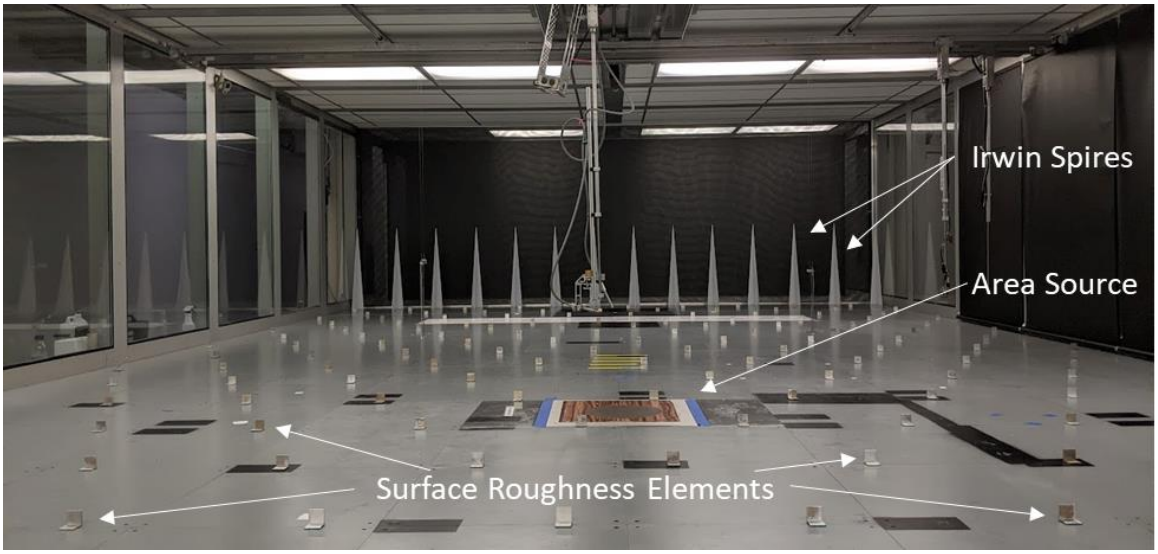

Figure 21 - Turbulence generating pieces in the Wind Tunnel.

2.2 Instrumentation

The CHRC wind tunnel facility is equipped with two different laser-based velocity measurement systems: Laser Doppler Velocimetry and Particle Image Velocimetry.

2.2.1 Laser Doppler Velocimetry

Laser Doppler Velocimetry (LDV) is a relatively non-intrusive technique that measures the velocity and turbulence intensity at a single point in a flow field. LDV consists of the projection of pairs of monochromatic, coherent laser beams, in which one of the beams has its frequency shifted. The pair of beams is projected and converges into a crossing region. Shifted and unshifted beams interfere with each other, forming fringes (bands of light and dark) in a small measurement volume. When particles within the flow pass through this measurement volume, they scatter light in a frequency proportional to their velocity.

2.2.1.1 The Three-dimensional LDV System

The LDV technique requires the presence of neutrally buoyant seed particles that travel with the flow (accurately tracking the flow) and have the same velocity and turbulence characteristics as the flow. For LDV tests in the CHRC wind tunnel, the seed particles are

produced using fog fluid, injected into the tunnel using a commercially available fog machine (Rosco Vapour™). A previous study indicated that a homemade 50% v/v glycerin and water solution remained airborne considerably longer than commercially available fog fluids (Morris, 2018).

The LDV system in the CHRC has four components: a Coherent Innova 70C Argon laser, a TSI ColorBurst beam splitter, two fiber optic transmitting and receiving probes (a TR210 and a TR110-13, equipped with converging lenses of 110.3 mm and 60 mm of focal length, respectively), and a TSI FSA 4000-3 signal processor. The laser light generated by the Coherent system is sent to the ColorBurst beam splitter, which separates the incoming light into three different wavelengths: green (514.4 nm), blue (488 nm), and violet (476.5 nm). The ColorBurst system also creates the shifted and unshifted beams in each color, for a total of six beams. The green and blue pairs travel via fiber optics to the TR210 probe, while the violet pair travels through the TR110-13 probe. All beams are then projected in the tunnel for velocity and turbulence measurements. The same probes receive the light scattered by the fog particles. The light signal (indicating flow velocity) travels through parallel fiber optics to the signal processor, which converts light intensity to an electronic signal using a photomultiplier tube. The electronic signal is processed using software (TSI FlowSizer 64™) that performs statistical analysis to determine the flow velocity. The software also allows the user to optimize settings, improving the acquired data quality.

2.2.1.2 Three-dimensional LDV alignment

The TSI software acquires data only when each particle has detected movement in all three channels simultaneously. Therefore, beam alignment is necessary to ensure that all beams cross within the same measurement volume. A common alignment procedure is to use a small

pinhole (100 μm in this work) to locate the exact intersection of a pair of beams. Complete beam intersection is assured by adjusting the position of the probes until all six beams pass through a pinhole. A schematic showing the beam crossing and the fringes pattern is presented in Figure 22a. A picture of the crossing of the six beams is shown in Figure 22b.

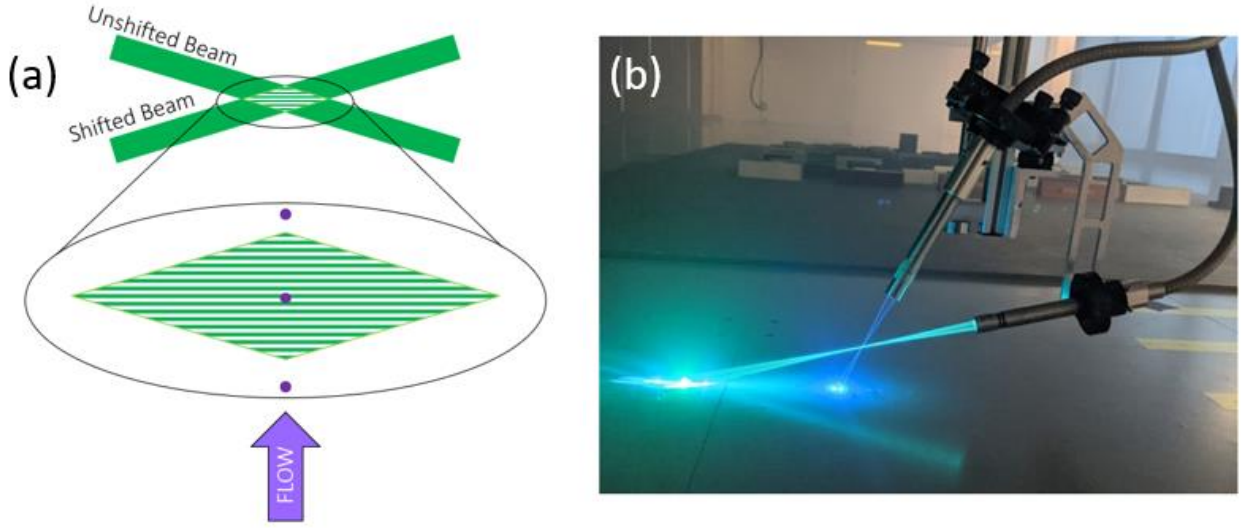

Figure 22 - Schematic of the fringes pattern for one-dimensional LDV measurements. The crossing of the six beams in the current CHRC LDV system is on the right.

In the setup for this work, the green/blue probe (which projects the green and blue beams) was attached to a mount (Newport RM25A) with roll adjustment. The violet probe was placed into a six-axis mount (ThorLabs K6XS) with pitch, roll, yaw, and three-dimensional directional adjustment. In this work, both mounts were attached to a custom-made aluminum bracket, which is also attached to a rotation stage (Newport RS40), providing yaw adjustment for both probes simultaneously. A 300 g brass cylinder served as a counterweight to keep the probe apparatus level. This apparatus was attached to the tunnel traverse system, which allows for movement in the x, y, and z directions remotely from the control room. A numerical display is calibrated and monitored from the control room, making it possible to position the measurement volume created by the probes without disturbing the tunnel flow.

2.2.2 Particle Image Velocimetry

Particle Image Velocimetry (PIV) is a non-intrusive measurement technique that measures velocity vectors in a planar region within the seeded flow. Velocities are measured at multiple locations (vector field) in a planar section of the flow, making this technique very different than pointwise LDV measurements. For PIV, two consecutive laser pulses (separated by a time interval, ΔT) illuminate the desired measurement plane. Synchronously, a camera captures one picture for each laser pulse. Software processing divides the images into subregions and uses statistical analysis to determine the average particle motion in each subregion in the field of view. The vector field is calculated based on the displacement of the particles and the known time interval between the pulses, with one vector determined for each subregion. A simple schematic of a PIV system is shown in Figure 23 (Raffel *et al.*, 1998).

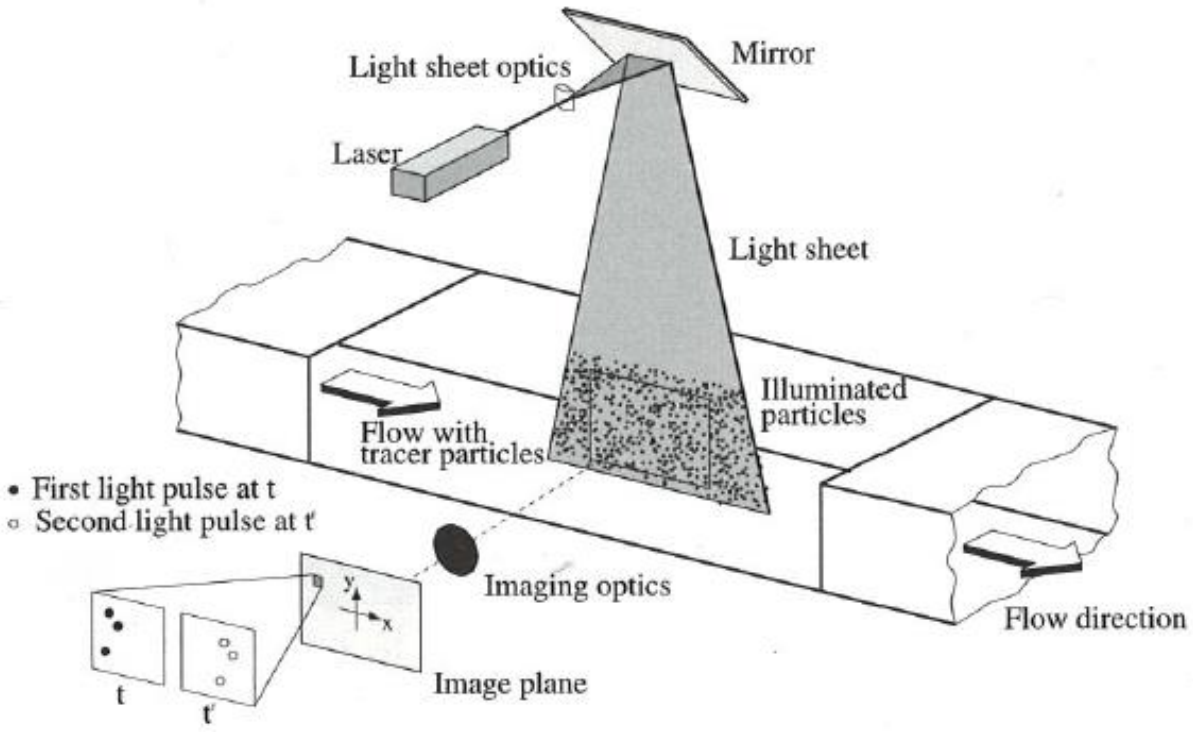

Figure 23 - Schematic of a Particle Image Velocimetry system (Raffel *et al.*, 1998. Reproduced with permission).

The PIV system in the CHRC has four components: a Quantel EverGreen HP double-pulse Nd:YAG laser (532 nm wavelength); a sheet-forming optical train composed of two spherical (f = 50 and -50 mm) lenses, and one cylindrical (f = -15 mm for tests in the XZ plane and f = -25 mm for tests in the XY plane) lens; a TSI PowerView™ 25MP-72 CMOS Camera (35 mm diagonal active area, 4.5 μm x 4.5 μm pixel size), equipped with Nikon AF Nikkor 50 mm, f1.8 lenses; and a TSI LaserPulse 610036 synchronizer. User interface and processing take place in TSI Insight 4G™ software. The PIV system uses the same seeding system described previously for LDV measurements.

2.3 The Mock Urban Environment Model

A physical scale model of the Mock Urban Environment (MUE) present in JR-II was built in the Wind Tunnel to reproduce the field-scale tests. The 1:50 model was scaled according to Froude similarity (Hall & Walker, 1996). Equation 2 shows the Froude number, where U represents a characteristic speed, g is the gravity acceleration, and L represents a characteristic length.

$$Fr = \frac{U^2}{gL} \quad \textbf{(2)}$$

Froude number scaling was originally used successfully to study atmospheric flows around buildings (Cook, 1985). A wind tunnel modeling study of atmospheric dispersion based on Froude number scale showed that the flow was independent of Reynolds number. The use of Froude number scaling effectively establishes the time scale factor since the velocity scale is the ratio of the characteristic length to time scales (Snyder, 1981). In contrast, Reynolds numbering scaling would imply that the time scale at wind tunnel and field scales are identical. Hall and Waters (1985) demonstrated that Froude scaling is appropriate for modeling transient releases of DTA gases.

Three plywood boards were used to represent the gravel pad from the JR-II field tests, each measuring 8 ft x 4 ft x 3/8 in (2.44 m x 1.22 m x 9.52 mm), for a total pad size of 8 ft x 12 ft (2.44 m x 3.66 m). A 50 cm diameter hole was cut in the middle board to simulate the release area (concrete pad) from JR-II. It was not possible to replicate in the model the pointwise, downward release conducted in the field test. Instead, gas flow is injected upwards into the tunnel at ground level. A polycarbonate disk redirects the vertical flow from the area source outwards, simulating the release as it crosses the boundary of the concrete pad. The disk is placed to create a 7 mm gap above the plywood boards. Effectively, the disk redirects the vertical flow from the area source outwards, simulating the release as it crosses the boundary of the concrete pad. Figure 24 shows the model MUE setup with a second disk, used only for LDV experiments and represents the concrete pad by filling the 50 cm hole, as this disk has the same thickness as the plywood boards. In both cases, a custom 3D-printed scaled chlorine tank (representing the field scale tank) was placed on top of the polycarbonate disk. The CONEX array was modeled using a mix of custom-made aluminum blocks and commercially available O-Scale miniature train containers. Toy cars represented the vehicles in Row 13. This setup was chosen so that the entire pad can be moved easily, allowing rotation to successfully reproduce the wind direction relative to the gravel pad, as reported from DPG. The model was placed at a distance equivalent to seven spire heights from the start of the tunnel test section.

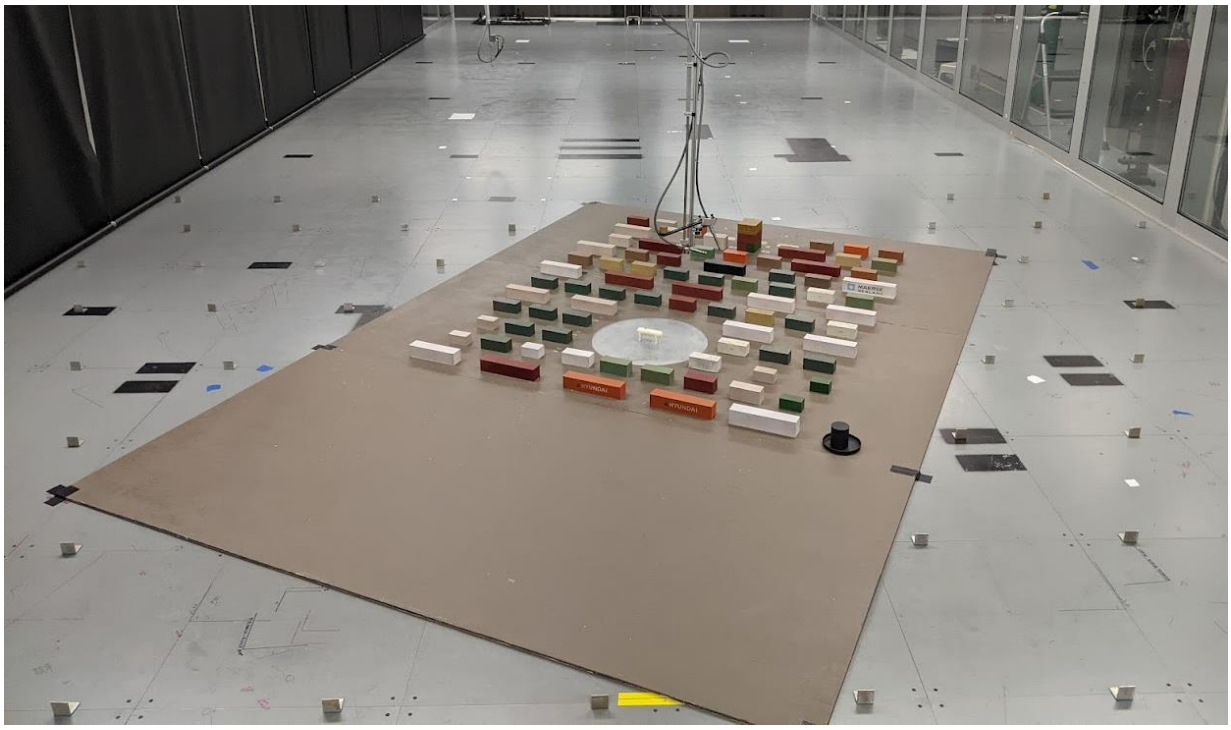

Figure 24 - 1-to-50 scale model of the MUE.

2.4 Simulation of the Chlorine Releases from JR-II

Flow visualization experiments were conducted in the MUE model to ensure visual agreement between the video record of the JR-II field tests and wind tunnel simulated gas releases (Gallimore, 2023). As mentioned previously, the releases were simulated by creating a gap between the polycarbonate disc and the tunnel floor. The gas mixture flowed through the gap and simulated the field-scale aerosol/gas flow as it crossed the edge of the concrete pad. Chlorine releases from JR-II were simulated in the MUE model using a mixture of air, sulfur hexafluoride, carbon dioxide, and theatrical fog (the last added with the purpose of making the release gas mixture visible). The releases in the model do not simulate the flow inside the concrete pad boundary. The physical model is only applicable outside of the circle representing the concrete pad.

Results from the release simulations indicated that the optimal gas mixture flow rate was

680 L/min, including 304 L/min of air, 76 L/min of SF_6, and 300 L/min of CO_2 (Gallimore, 2023). This proportion yields a gas mixture with a molar mass of 48.7 g/mol, the equivalent of a mixture of 46.9% of Cl_2 in (dry) air. Fog fluid is added to the gas mixture at 21.4 mL/min, which increases the density of the simulated release mixture to the equivalent of a mixture of 49% of Cl_2 in air. The continuous flow of these gases was controlled via multiple MKS Mass Flow Controllers (IE500A, 1559A) and then delivered to the output of the fog machine, as indicated by the blue arrow on the lower right side of Figure 25 (Gallimore, 2023).

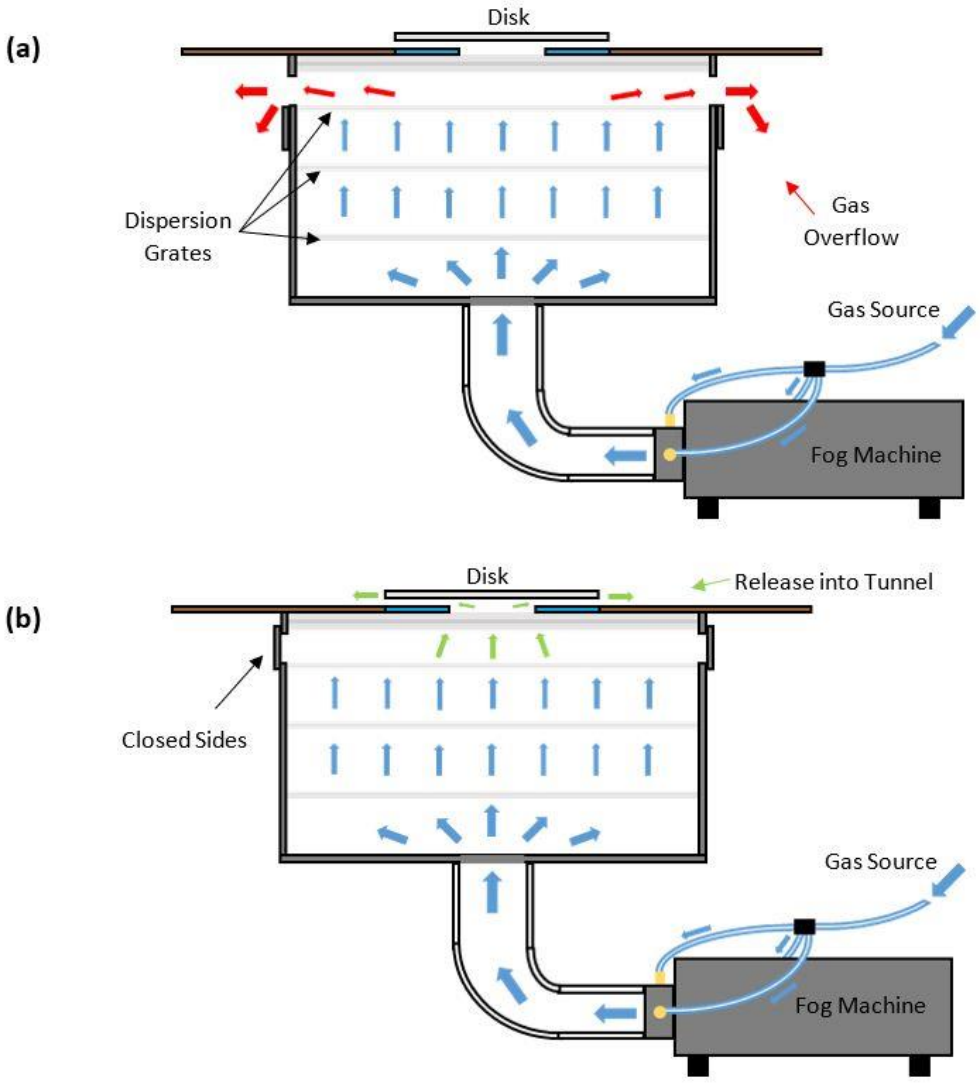

Figure 25 - Schematic showing a cross-section of the area source, including the gas delivery system to the tunnel (Gallimore, 2023).

To simulate the field releases, the source gas flow must start and stop promptly, which would not be possible using only the mass flow controllers. The area source has two configurations, open to the tunnel, as shown in Figure 25b, or closed, as shown in Figure 25a, which is the normal default configuration. Solenoid valves simultaneously close the flow to the sides of the area source and open the top, which causes the mixture of gases and fog to flow into the tunnel at ground level. The solenoid valves are operated remotely from the control room via an Arduino Uno and a relay board (Morris, 2018). The polycarbonate disk redirects the gas flow sideways, therefore modeling the flow of chlorine in the JR-II as it crosses the edge of the concrete pad. The duration for which the area source is open is programmable and changes according to the JR-II Trial condition. The full-scale discharge period (Spicer & Tickle, 2021) for each of the Trials 1-5 is shown in Appendix C. For the simulations in the wind tunnel, the discharge periods were scaled according to Froude similarity (Hall & Walker, 1997).

$$\frac{U_F * T_F}{L_F} = \frac{U_T * T_T}{L_T} \rightarrow \frac{\sqrt{50} * U_T * T_F}{50 * L_T} = \frac{U_T * T_T}{L_T} \therefore T_F = \sqrt{50} * T_T \quad \textbf{(3)}$$

Equation 3 shows the proper scaling rule for time (T), starting from dimensionless time (Hall & Walker, 1997). In Equation 3, U and L represent velocity and length, respectively, while subscripts F and T refer to Field Test and Wind Tunnel (*i.e.*, $L_F = 50L_T$). The relation between U_F and U_T is shown in Section 2.5.1. For the actual duration in which the area source was open for releases in the tunnel, 0.3 sec were added to the scaled-down value to account for the delay between the opening of the area source and the actual flow of source gas in the tunnel (Gallimore, 2023). The tunnel scale discharge period is also shown in Appendix C.

2.5 Velocity Characterization of Scale Model vs. JR-II and JRII-S Field Tests

Several experiments were conducted to demonstrate the agreement between the JR-II and JRII-S field tests results and wind tunnel data. The first step was to make comparisons of wind

velocity data between the wind tunnel model and the field tests.

2.5.1 Setup of Tunnel Characterization Measurements

In the JR-II and JRII-S field tests, a 32 m tall meteorological tower ("Tower 3") was placed 100 m upwind of the urban test grid. The wind velocity was measured via Sonic Anemometers and Portable Weather Information Data Systems (PWIDS) placed at 2, 4, 8, 16, and 32 m AGL. The results at 32 m AGL were deemed unreliable and were not used for comparison to tunnel data. For the tunnel tests, LDV measurements were taken at the corresponding location of Tower 3. To better characterize the velocity profile, measurements were taken at additional heights, which did not have a corresponding equivalent in the JR-II measurements. The model velocity profile consisted of measurements at 4, 8, 12, 16, 20, 32, and 50 cm AGL, averaging 200,000 instantaneous velocity measurements at each height.

LDV measurements at 8 cm AGL were taken at multiple fan speeds to verify a correlation between along-wind wind velocity (m/s) and fan speed (rpm). A correlation was established and is presented in Appendix A.

Further LDV measurements were made to compare the tunnel and the trials of JR-II field tests, as well as the Time Frames of the JRII-S field test. Both wind velocity and turbulence, quantified using friction velocity (u_*), were compared. According to Equation 4, since length factors scale by a factor of 50, the velocities must scale by a factor of $\sqrt{50}$ to fulfill the Froude scaling condition (Hall & Walker, 1997).

$$Fr_F = Fr_T \rightarrow \frac{{U_F}^2}{gL_F} = \frac{{U_T}^2}{gL_T} \rightarrow \frac{{U_F}^2}{50L_T} = \frac{{U_T}^2}{L_T} \therefore U_T = \frac{U_F}{\sqrt{50}} \quad \textbf{(4)}$$

2.5.2 Agreement with Tower 3 Velocity Measurements

Velocity profiles were measured at the equivalent location of the Meteorological Tower 3 at DPG. The agreement between along-wind velocity measurements in the wind tunnel and field

data for JR-II Trials 2 and 4 is shown in Figure 26. Along-wind and vertical velocity values for all JR-II Trials are shown in Appendix B1. Agreement plots for JR-II Trials 3 and 5 are shown in Appendix B2, since those Trials were not modeled in the study of this dissertation. Wind data from JR-II Trial 1 (Hanna, 2020) showed a velocity profile that was very different from the remaining trials, and it was found that the CHRC wind tunnel was not capable of recreating the wind profile from Trial 1. Therefore, Trial 1 was not used in wind tunnel modeling.

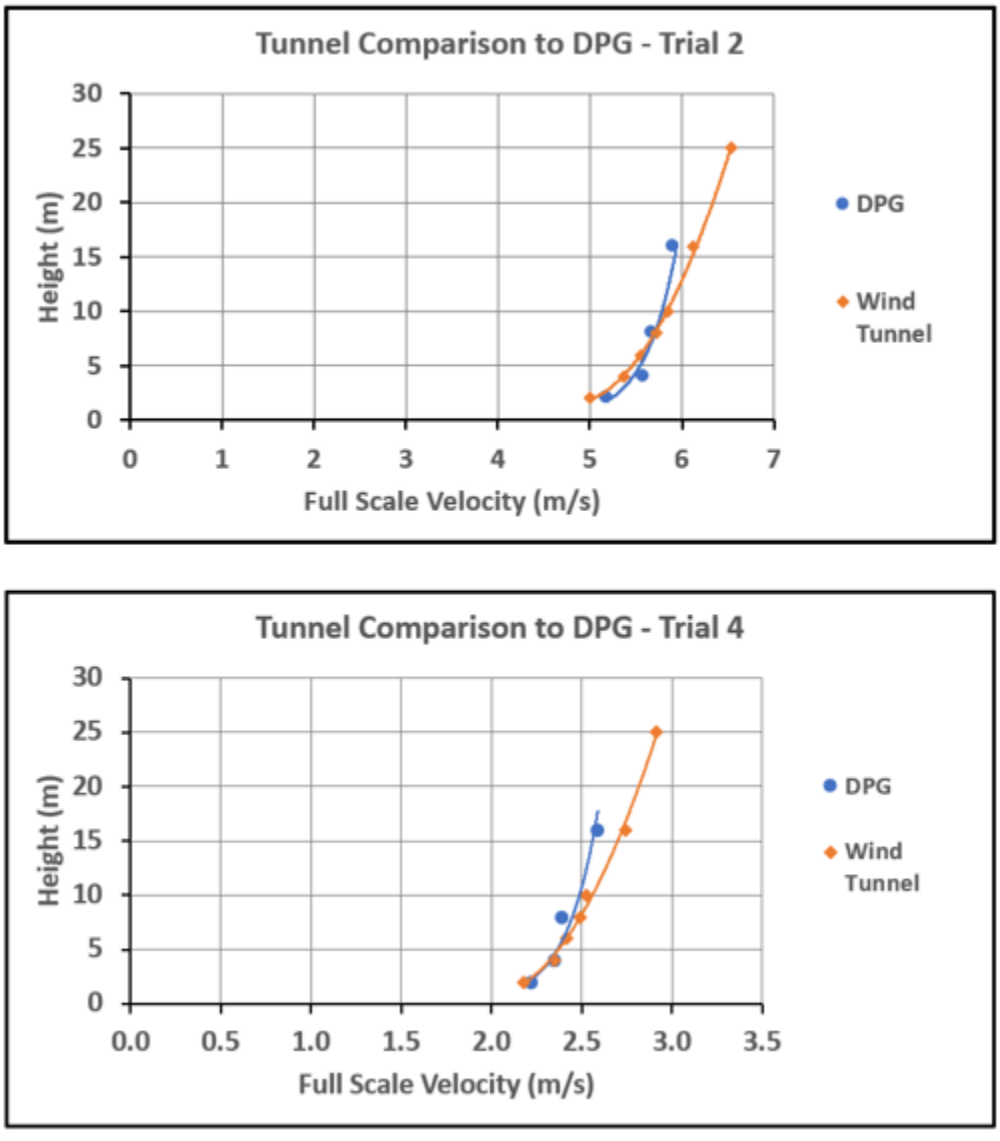

Figure 26 - Velocity Profile comparisons between field and scale models for JR-II Trials 2 and 4.

In the subsequent tests in the MUE, priority was given to Time Frames C and E because of lower speed (more consistent with the JR-II conditions) and coincidental direction with the pad orientation (*i.e.*, the approaching wind direction is parallel to the long axis of the MUE) in those Time Frames. Figure 27 compares velocity data between DPG and wind tunnel data (at full-scale) for Time Frames C and E and shows excellent agreement between the measurements. Along-wind and vertical velocity values for all Time Frames are shown in Appendix B3. Comparison plots for the remaining Time Frames can be found in Appendix B4.

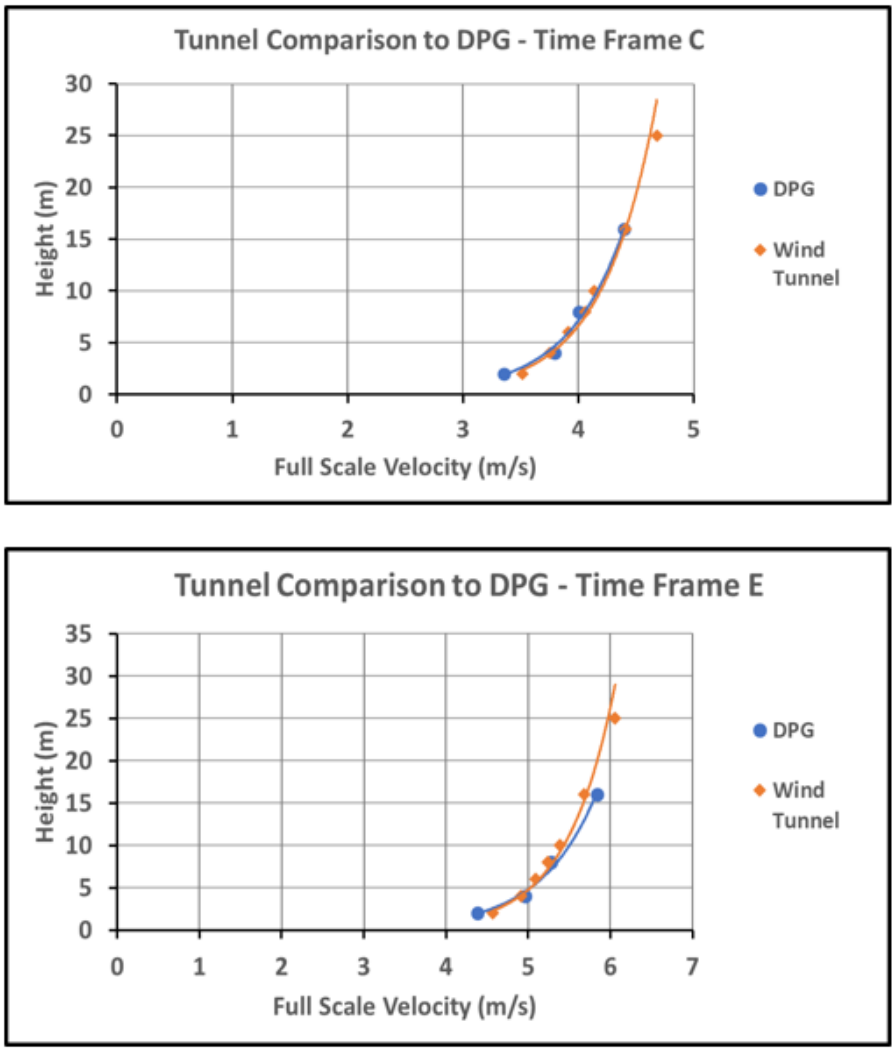

Figure 27 - Velocity Profile comparisons between field and scale models for JRII-S Time Frames C and E.

Turbulence agreement between field and tunnel was verified by comparing friction velocity data. Close to ground level, the flow is determined by the shear stress and the density of air. The shear stress on the ground is due entirely to viscous effects (no-slip condition). The square root of the ratio of the shear stress on the floor to the air density generates a relevant velocity scale called friction velocity (Pope, 2000). In practical terms, friction velocity can be defined based on the covariance of the velocity components, as shown in Equation 5, in which $\overline{u'w'}$ and $\overline{v'w'}$ represent the Reynolds stresses. The Reynolds stresses are defined as the covariance between velocity components in x and z directions and y and z directions, respectively. Figure 28 compares friction velocity data between DPG and wind tunnel data (at full scale) for Time Frames C and E, showing good agreement between wind tunnel and field tests. The values for friction velocity in field and tunnel scales are tabulated in Appendix B5. As shown in Figure 28, the average value of friction velocity measured in the wind tunnel agrees with the average friction velocity values measured during the JRII-S field tests.

$$u_* = \sqrt[4]{\left(\overline{u'w'}\right)^2 + \left(\overline{v'w'}\right)^2} = \sqrt[4]{\left(cov(u,w)\right)^2 + \left(cov(v,w)\right)^2} \quad \textbf{(5)}$$

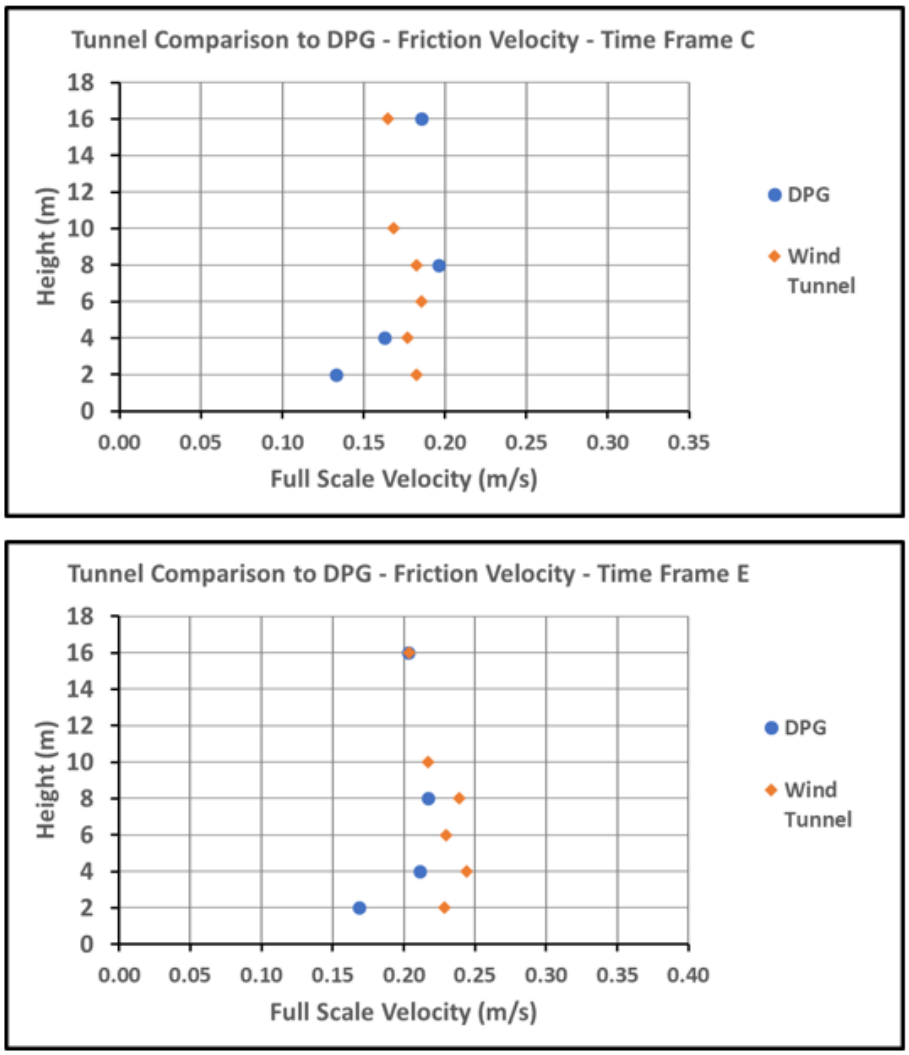

Figure 28 - Friction velocity comparison between field and scale model for Time Frames C and E.

2.5.3 Characterization of Visual Data vs. JR-II Field Tests

After demonstrating the approach wind velocity agreement between the wind tunnel model and the field tests, the wind tunnel can be used for modeling the chlorine releases of JR-II.

Flow visualization experiments were performed in the wind tunnel to establish an approach to model the chlorine releases in the field (Gallimore, 2023). As previously stated, the chlorine cloud was simulated using a mixture of air, SF_6, and CO_2, with added theatrical fog for visualization. An HD Camera (Canon VIXIA HF G10 Full HD Camcorder with HD CMOS Pro)

was placed around the model at analogous positions to the HD cameras in the field test. Trials 4 and 5 were reproduced in the wind tunnel and compared to the JR-II data from Cameras 4 and 5. Figure 29 exemplifies the setup, showing the relative placement of Camera 3 and the pad set up for a simulation of the Trial 5 release. As mentioned before, the duration of the releases was scaled down according to scaling theory. Additionally, time scaling was also applied in the video processing, as the recorded releases in the tunnel were slowed down by a factor of $\sqrt{50}$ (Gallimore, 2023).

Figure 29 - Camera setup for flow visualization experiments in the MUE model, replicating Trial 5 from the JR-II field test.

The flow visualization experiments also demonstrated the agreement between tunnel releases and JR-II field test releases. Figure 30 shows timelapse comparisons between the chlorine cloud in the JR-II field tests (Trial 4, Camera 4) and the simulant chlorine cloud in the physical model (Gallimore, 2023). In the field test, chlorine is released in liquid phase, which rapidly forms an aerosol. The chlorine aerosol can be seen as an opaque yellow cloud in the recordings. Part of the chemical evaporates, and the gas part of the cloud is transparent and is visible at high concentrations. To better compare the model to the field test, images from JR-II had the chlorine cloud enhanced on MATLAB, shown in Figure 30 in a bright green color

(Gallimore, 2023). The sequence in Figure 30 shows an excellent agreement between model and field, another indicator of tunnel capabilities in successfully reproducing the JR-II releases.

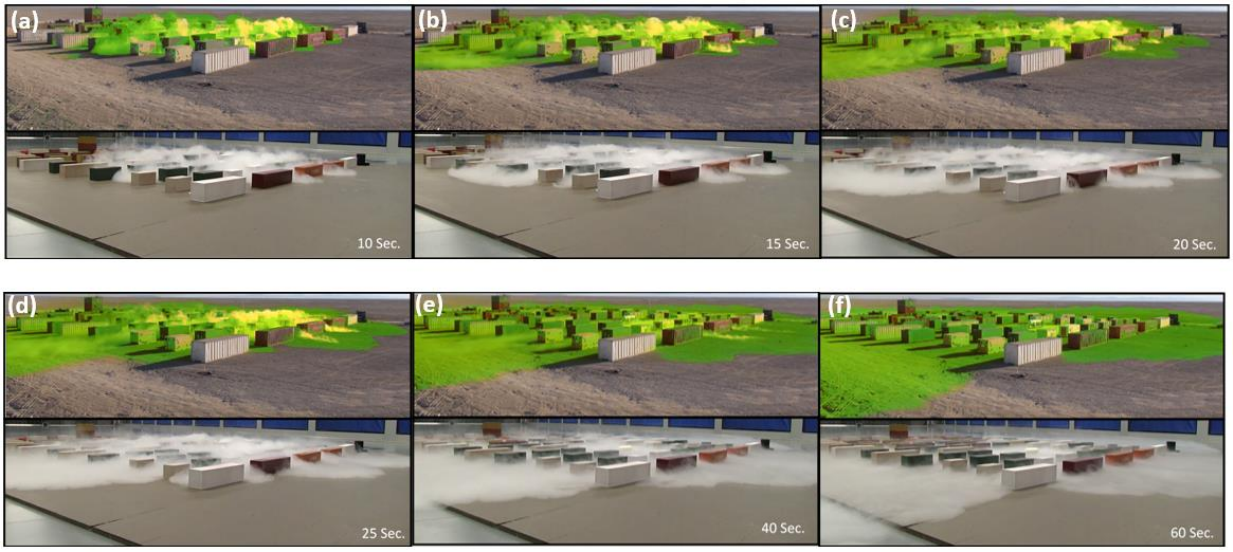

Figure 30 - Timelapse of chlorine release in JR-II Trial 4 (top) compared to the model in the CHRC wind tunnel (Bottom). Captures show (a) 10 sec; (b) 15 sec; (c) 20 sec; (d) 25 sec; (e) 40 sec; and (f) 60 sec after the release (Gallimore, 2023).

Throughout this chapter, the wind tunnel facility at the Chemical Hazards Research Center was described, along with the instrumentation present at the facility. The model MUE was also described. LDV velocity and turbulence data taken in the model at the equivalent Tower 3 location, along with the flow visualization experiments conducted in the model (Gallimore, 2023), all show that the CHRC wind tunnel is capable of reproducing the JR-II field tests.

Chapter 3 – Three-dimensional vs. Two-dimensional Laser Doppler Velocimetry Setup Study

This chapter addresses the question: “Is it possible to obtain accurate 3D velocity and turbulence measurements by using only one LDV probe (2D measurements) placed at an angle?” Quantification of errors in velocity and turbulence measurements obtained using the simplified 2D setup are investigated by extrapolation of the 2D data and comparisons to measurements obtained via the LDV setup with two probes (3D measurements).

3.1 Background

The crossing of a pair of LDV laser beams creates a fringe pattern in a small “measurement volume”. Measurements are conducted when the seeded particles within the flow scatter light as they pass through the measurement volume, with only one direction measured per pair of beams. Therefore, crossing different pairs of beams is crucial for three-dimensional LDV, as these measurements depend on the coincidence of the measurement volumes created by each pair of beams. The most common method used to assure beam crossing is using a method by which all beams pass through a pinhole, and the method guarantees that all beams are coincident within the diameter of the pinhole (100 μm in this work). Ideally, the probes would be placed orthogonally so that each pair of beams would directly measure one velocity component. However, it is not possible to align orthogonal beam pairs through a pinhole, and therefore the intersection of all such beam pairs (within the same volume) cannot be assured. An alternative method for LDV alignment consists of projecting beams onto a charge-coupled device (CCD) sensor. However, it does not eliminate the geometric constraint present in the pinhole method. Therefore, for 3D LDV measurements, it is necessary to place the probes at an angle from the vertical axis so that one of the pairs of beams measures one velocity component directly while

the other two pairs work together to measure the remaining two components. A mathematical process transforms the "raw" velocities (i.e., off-axis, as measured by the probes – V1, V2, and V3) into customary orthogonal components (u, v, and w).

An example LDV setup is shown in Figure 31, which consists of a schematic of the probes, the relative angles between the probes and the vertical Z-axis, and the angles between V2 and V3 with v and w velocity components. Vectors V1 and u are pointed in opposite directions, with the u velocity component pointing into the page. The magnitude of V1 and u are equal because, in this arrangement, the green beams of the probe measure the u velocity component directly. The angle α is defined as the angle between the primary probe (green/blue beams) and the positive z-direction. Likewise, β is the angle between the secondary probe (violet beams) and the positive z-direction. The angles θ and σ are the complements of α and β, respectively.

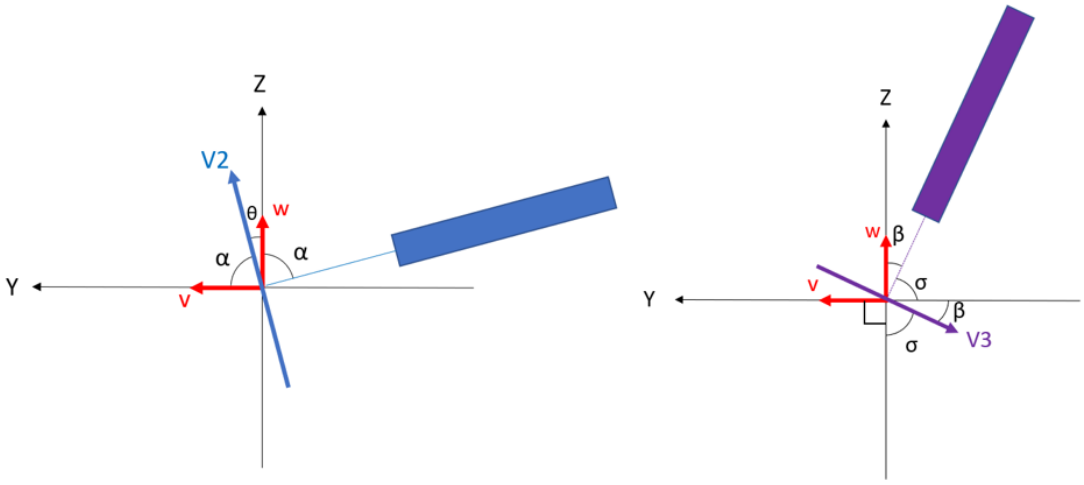

Figure 31 - Relative position of the LDV probes to the tunnel axis, with the relative positions of the measured velocity vectors V2 and V3 and the wind tunnel orthogonal vectors v and w.

Three-dimensional, two-probe LDV systems are significantly more complex and expensive than two-dimensional, one-probe systems. The alignment procedure through a pinhole is also cumbersome and time-consuming. Those factors can tempt scientists to use only the primary probe placed at an angle to measure the velocity of the wind and then extrapolate the 2D

LDV measurements to produce three-component velocity vectors. Such a 2D LDV setup is adequate to measure one velocity component, but accurate measurements of the other two velocity components (and their respective turbulence levels) are not assured. Placing the primary probe orthogonal to two velocity components of the flow (aligned with the experimental coordinate system) is also adequate if it is most important to measure only those two components. In this case, two velocity components are directly measured, while the third component is not measured at all.

When the probes are placed at a fixed angle, they measure the projection of the velocity vector. The average magnitude of the velocity vectors is measured correctly. However, the measurement fails to detect instantaneous fluctuations in magnitude and direction due to the changes in relative angles (between the velocity vector and probe) caused by the instantaneous changes in the flow. Significant errors in turbulence measurements can occur depending on the flow characteristics, as there is no independent contribution from the perspective of a second LDV probe.

3.2 Experimental Setup

Mathematical analyses were performed to quantify the error resulting from the extrapolation of 3D velocity components from an angled 2D LDV setup. Two different wind velocities were studied, a lower velocity and a higher velocity case, with measurements obtained using a 3D LDV setup at the Tower 3 location for Time Frames C (93 rpm, u_∞ = 0.67 m/s) and E conditions (118 rpm, u_∞ = 0.88 m/s), respectively. Data processing of the 3D results was used as a baseline and compared to "3D" data obtained from extrapolation of 2D data from the primary probe. For reasonable comparisons, the same 3D dataset was used twice, once to calculate the actual three velocity components; and once to create a 2D dataset by completely ignoring data

measured by the violet probe. In this second processing, it was assumed that only the primary probe was available. The extrapolated 3D results were calculated based on the angle of the probe. Afterwards, the extrapolated "3D" results (from the 2D dataset) were compared to the baseline 3D results to determine errors in the magnitude of the velocity components and turbulence.

The study presented in this section used the specific flow field of the CHRC wind tunnel, characterized by a dominant u component and significantly smaller v and w components. This method for error quantification might not be suited for investigating flows with vastly different magnitudes of the velocity components.

3.3 Results

In the LDV data processing, it is necessary to convert the velocity vectors measured by the probes (V1, V2, V3 – as measured by the green, blue, and violet beams, respectively) into useful, cartesian coordinate velocity components (u, v, w). Equation 6 shows the Transformation Matrix used for said conversion. Angle α is the angle between the blue/green (primary) probe and the vertical axis, while β is the angle between the violet (secondary) probe and the vertical axis. For this experimental work, α ≈ 75° and β ≈ 25°. Throughout this section, 3D LDV velocity components are accompanied by the subscript "act" (for actual), while 3D velocity components obtained from 2D setup extrapolation are accompanied by the subscript "ext" (for extrapolated).

$$\begin{bmatrix} V1 \\ V2 \\ V3 \end{bmatrix} = \begin{bmatrix} -1 & 0 & 0 \\ 0 & \cos\alpha & \sin\alpha \\ 0 & -\cos\beta & -\sin\beta \end{bmatrix} * \begin{bmatrix} u_{act} \\ v_{act} \\ w_{act} \end{bmatrix} \quad \textbf{(6)}$$

Equation 6 can be written in the system form, as shown in Equation 7.

$$V1 = -u_{act} \quad \textbf{(7a)}$$

$$V2 = v_{act} * \cos\alpha + w_{act} * \sin\alpha \quad \textbf{(7b)}$$

$$V3 = -v_{act} * \cos\beta - w_{act} * \sin\beta \quad \textbf{(7c)}$$

A scatter plot of the instantaneous velocity data measured by the blue beams (V2) and the actual vertical velocity component (w_{act}) show a linear correlation between the variables, as shown in Figure 32, in which data from Tower 3 at 8 cm for lower wind speed was used as an example. Notice that the angular coefficient of the regression line is approximately equal to sin (75°), the same angle between the probe and the vertical axis (α), indicating that the error in the velocity measurements is related to α. Notice also that due to the geometric positions of V2 and w, this relation is expected, as the projection of V2 onto w is proportional to sin (α).

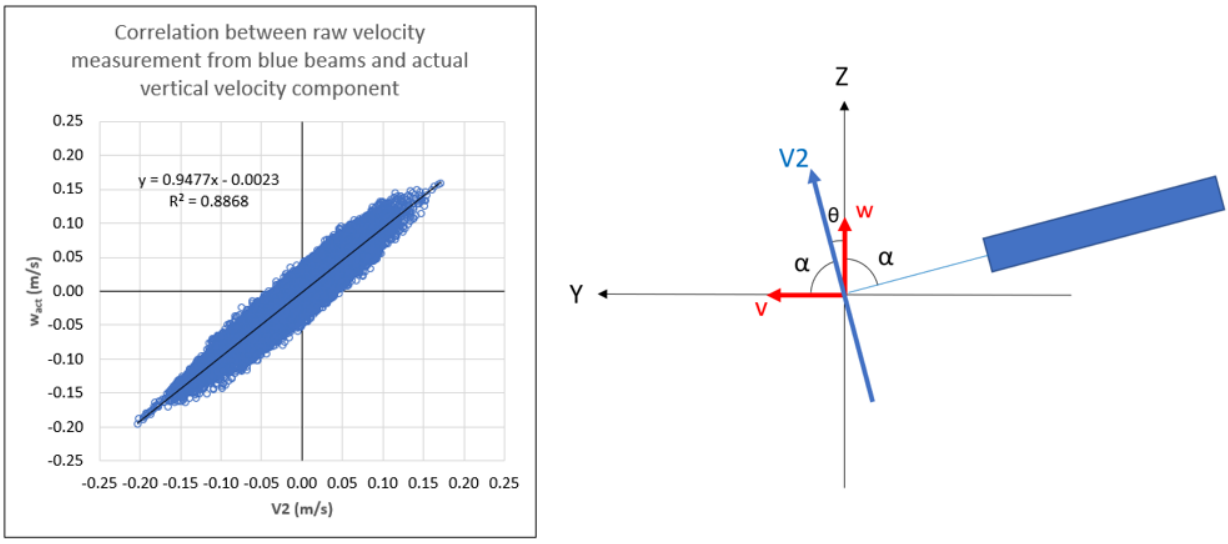

Figure 32 - Correlation between the velocity measured by the blue beams pair of the LDV and the actual vertical velocity component in the wind tunnel.

On the other hand, a similar scatter plot between V2 and the actual cross-tunnel component (v_{act}) shows no correlation, indicating that the 2D LDV setup is incapable of accurately measuring the cross-tunnel velocity component, as shown in Figure 33.

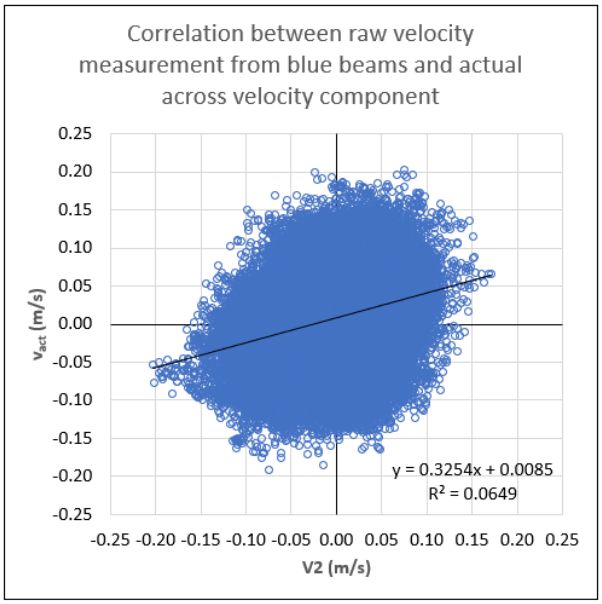

Figure 33 - Correlation between the velocity measured by the blue beams pair of the LDV and the actual crosswind velocity component in the wind tunnel.

To illustrate the point further, Figure 34 shows a scatter plot of the instantaneous velocity data measured by the violet beams (V3) and v_{act} shows a similar linear correlation as that of V2 and w_{act} shown previously.

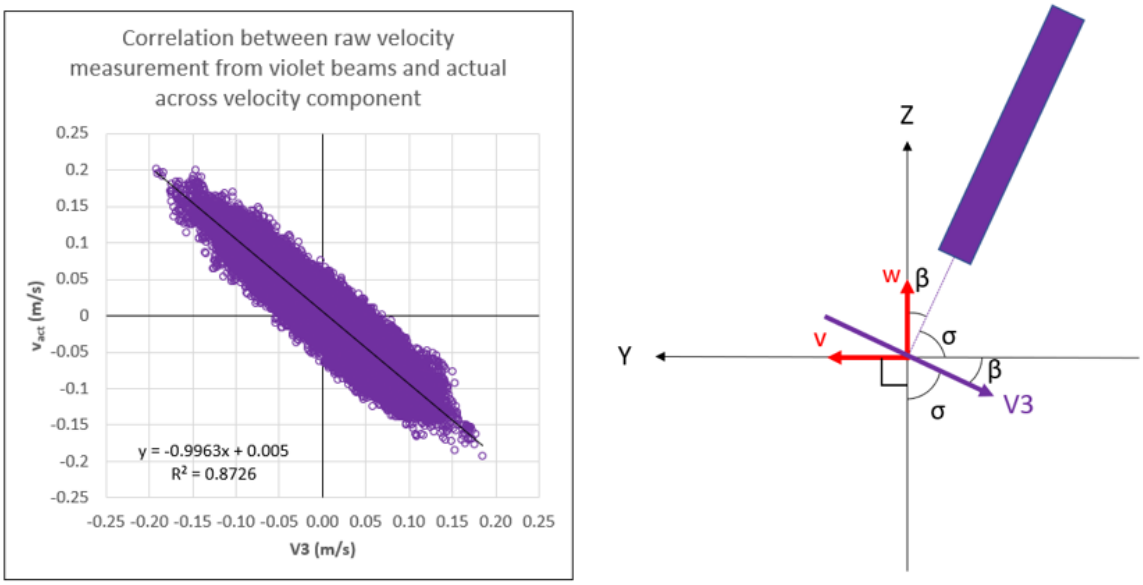

Figure 34 - Correlation between the velocity measured by the violet beams pair of the LDV and the actual crosswind velocity component in the wind tunnel.

Therefore, both blue and violet probes work together to measure the v_{act} and w_{act} velocity components. In this particular 3D LDV setup (with $\alpha = 75°$ and $\beta = 25°$), the blue beam pair is the major contributor for measuring the actual value for the vertical component, with V3 providing additional information that is missed by the blue beams due to perspective distortion. If the blue beams of the primary probe were placed orthogonally to the z-axis (i.e., $\alpha = 90°$), then the w velocity component would be measured directly. As there is some distortion due to the angle of the blue probe, both blue and violet beams must work together to obtain the correct w_{act} value.

Equation 8 was used to extrapolate the V2 measurements (assuming a 2D setup) to the 3D velocity components v_{ext} and w_{ext}. Due to the coincidental orientation of the green beams and the along axis (x-direction) of the tunnel, measured components V1 and the actual along-wind component (u_{act}) are equal, as shown in Equation 7. Therefore, the u component is invariant to the relative angle of the probe.

$$u_{ext} = u_{act} = -V1 \quad \textbf{(8a)}$$

$$v_{ext} = V2 * \cos\alpha \quad \textbf{(8b)}$$

$$w_{ext} = V2 * \sin\alpha \quad \textbf{(8c)}$$

Values of the extrapolated vertical and cross-wind components obtained via Equation 8 can be compared to the actual values of those components, obtained from the full 3D LDV setup and Equation 7. The comparison between the velocity components in the low wind case is shown in Figure 35. A similar comparison for the higher wind case is shown in Figure 36. Tabulated values of actual and extrapolated velocity components are shown in Appendix G4.

Figure 35 shows that the simplified 2D setup can yield a valid approximation for the vertical velocity component in certain circumstances. At lower heights, in both wind cases, the

extrapolated vertical velocity diverges significantly from the actual value, with errors around 40%. As height increases, the extrapolated values and actual values get closer to one another but are still significantly apart in the lower wind case (averaging at 13% in the lower wind case and 5% in the higher wind case), as the perspective from the secondary probe is necessary to calculate the actual value of the vertical component. The absence of the violet beams' contribution also explains why the extrapolated value always has a smaller (or approximately equal) magnitude than the actual component.

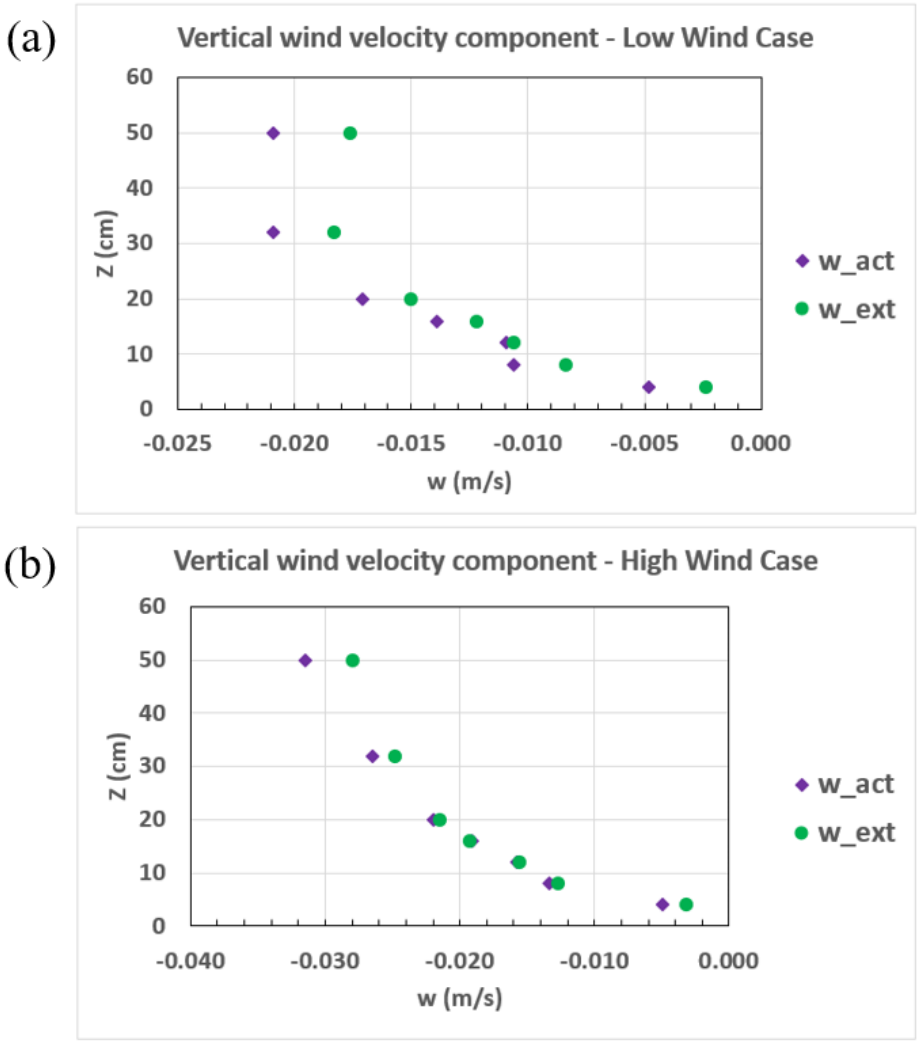

Figure 35 - Comparison between extrapolated 2D and actual 3D LDV measurements of the vertical velocity component (w) in (a) Time Frame C and (b) Time Frame E conditions.

When comparing the cross-wind direction, extremely high errors are found, as shown in Figure 36, with the error magnitudes averaging 160% in the lower velocity and 310% in the high velocity case. A higher discrepancy is observed in the higher wind case due to higher turbulence. This indicates that the violet probe measures most of this velocity component of the wind. Additionally, only negative values of v_{ext} were generated. Therefore, this 2D setup is inadequate to measure the cross-wind velocity component. In this 2D setup, the blue probe is biased to measure the vertical component due to its relative angle positioning in respect of the vertical axis. Similar results are observed in the results of the vertical and cross-wind velocity directions, shown in Appendix G1.

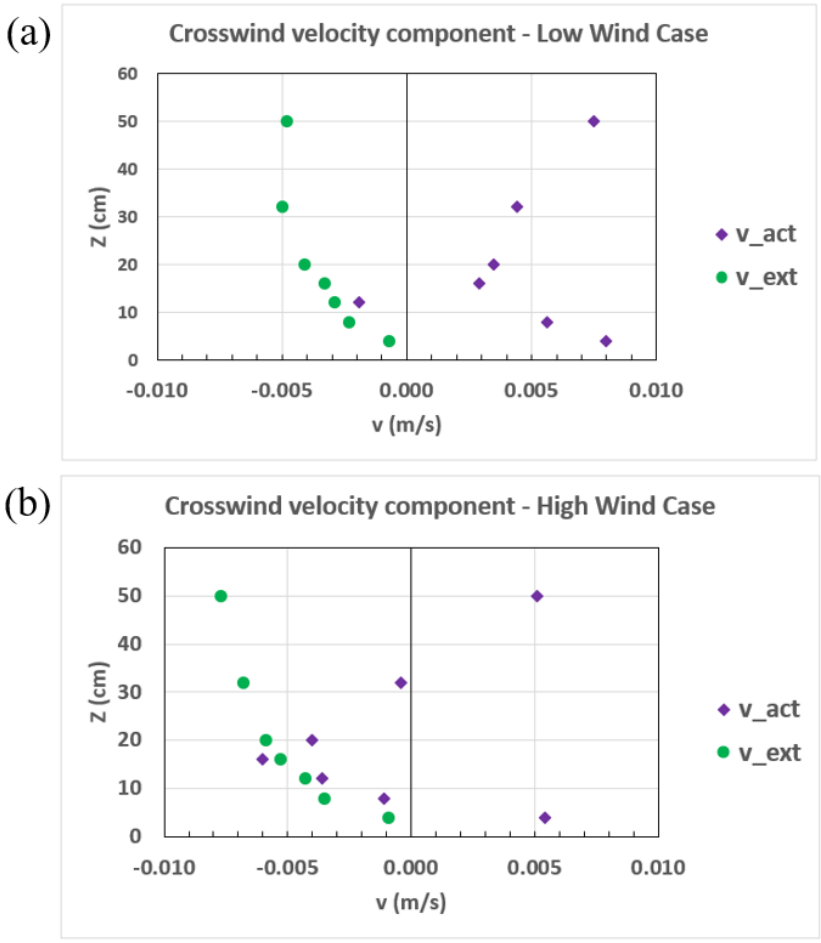

Figure 36 - Comparison between extrapolated 2D and actual 3D LDV measurements of the cross-wind velocity component (v) in (a) Time Frame C and (b) Time Frame E conditions.

The overall turbulence was quantified using the values of turbulent kinetic energy, used to determine the error magnitude on the turbulence levels when the simplified setup is used. Turbulent kinetic energy (TKE) is defined in Equation 9.

$$TKE_{act} = \frac{1}{2}\left(\overline{(u_{act}{}')^2} + \overline{(v_{act}{}')^2} + \overline{(w_{act}{}')^2}\right) \quad \textbf{(9)}$$

For the extrapolated case, the new TKE equation is defined in Equation 10.

$$TKE_{ext} = \frac{1}{2}\left(\overline{(u_{ext}{}')^2} + \overline{(v_{ext}{}')^2} + \overline{(w_{ext}{}')^2}\right) \quad \textbf{(10)}$$

Based on the definitions established for v_{ext} and w_{ext} in Equation 8, Equation 10 can be rewritten in terms of V1, V2, and α, as shown in Equation 11. Equation 11c shows that the instantaneous fluctuations in velocity measured by the blue beams are a result of combining fluctuations in the cross-wind and vertical directions. The results for the TKE values for the lower and higher wind cases are shown in Figure 37. Tables of actual and extrapolated values of TKE are shown in Appendix G5.

$$TKE_{ext} = \frac{1}{2}\left(\overline{(V1')^2} + \overline{(V2')^2} * \cos^2(\alpha) + \overline{(V2')^2} * \sin^2(\alpha)\right) \quad \textbf{(11a)}$$

$$TKE_{ext} = \frac{1}{2}\left[\overline{(V1')^2} + \overline{(V2')^2} * (\cos^2(\alpha) + \sin^2(\alpha))\right] \quad \textbf{(11b)}$$

$$TKE_{ext} = \frac{1}{2}\left(\overline{(V_1{}')^2} + \overline{(V_2{}')^2}\right) \quad \textbf{(11c)}$$

The error magnitude in the TKE values was approximately invariant when the wind speed increased, around 34%, averaging across all heights, with a slight decrease in error with height. The extrapolated values underpredicted the value of TKE in all heights in both wind cases, as shown in Figure 37. The missing contribution from the violet probe causes the large difference in TKE measurements shown in Figure 37. Since the velocity fluctuations in all three directions are the same order of magnitude, and the perspective from one of the probes is

missing, the underprediction of TKE_{ext} measurements by about a third of the value of TKE_{act} is expected.

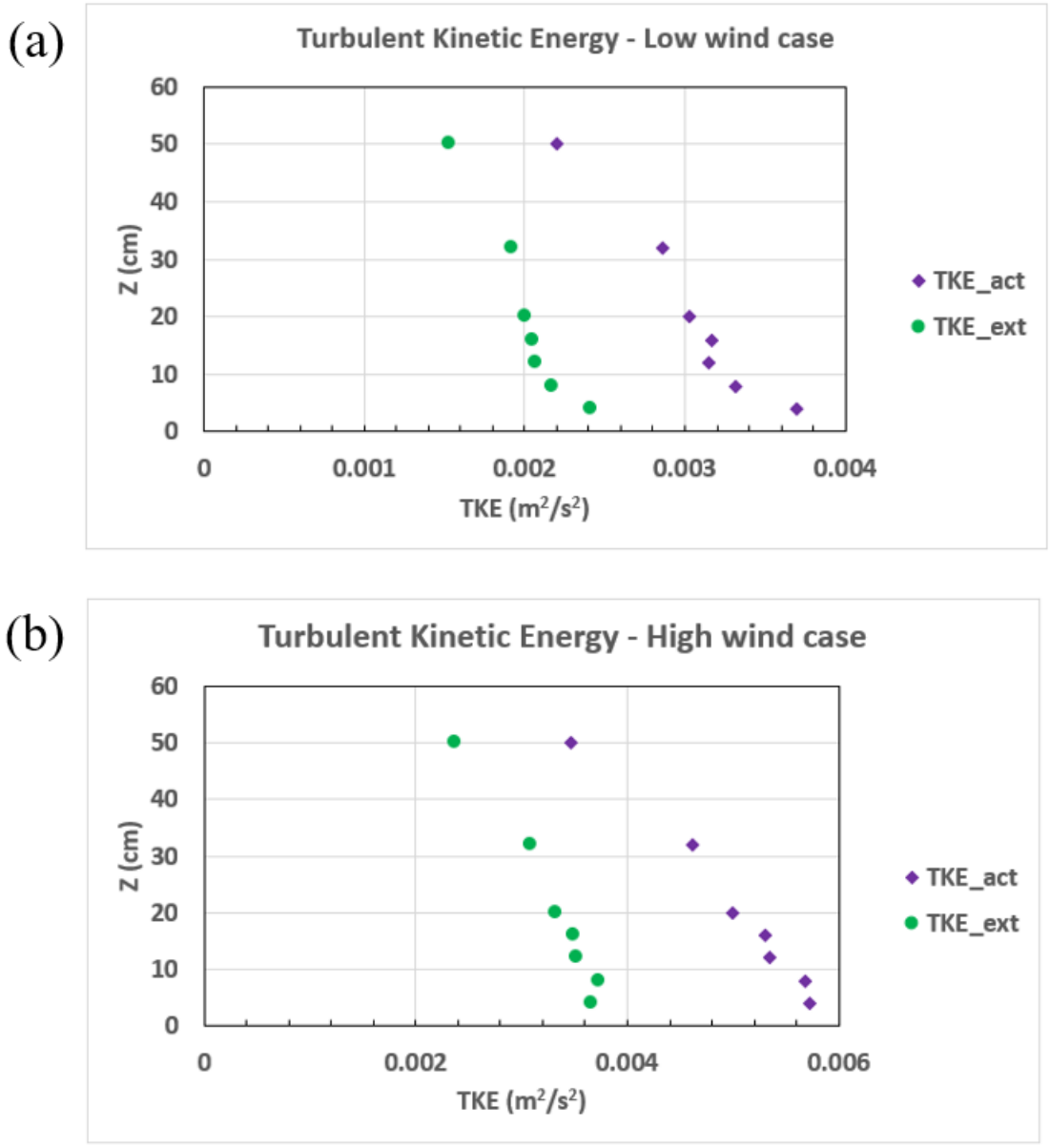

Figure 37 - Comparison between extrapolated 2D and actual 3D LDV measurements of Turbulent Kinetic Energy in (a) Time Frame C and (b) Time Frame E conditions.

The previous results indicate that the presence of the secondary probe is deemed necessary for accurate measurement of the velocity components and turbulence intensities. However, if one of the velocity components is significantly less important than the other two,

using the sophisticated and expensive 3D setup becomes unnecessarily cumbersome. Placing the probe perpendicularly to the axis formed by the two (more) important directions is enough to accurately measure those two velocity components and turbulence intensities, even without applying the transformation matrix. This configuration has been used before in the CHRC wind tunnel, as shown in Figure 38. In Figure 38a, the primary probe was placed horizontally, parallel to the tunnel floor. In that setup, velocity components u and w were measured directly, while v was not measured. In Figure 38b, the probe was placed vertically, perpendicular to the tunnel floor. This time, u and v were measured directly, while w was not measured. A second alternative setup is proposed in Appendix G3.

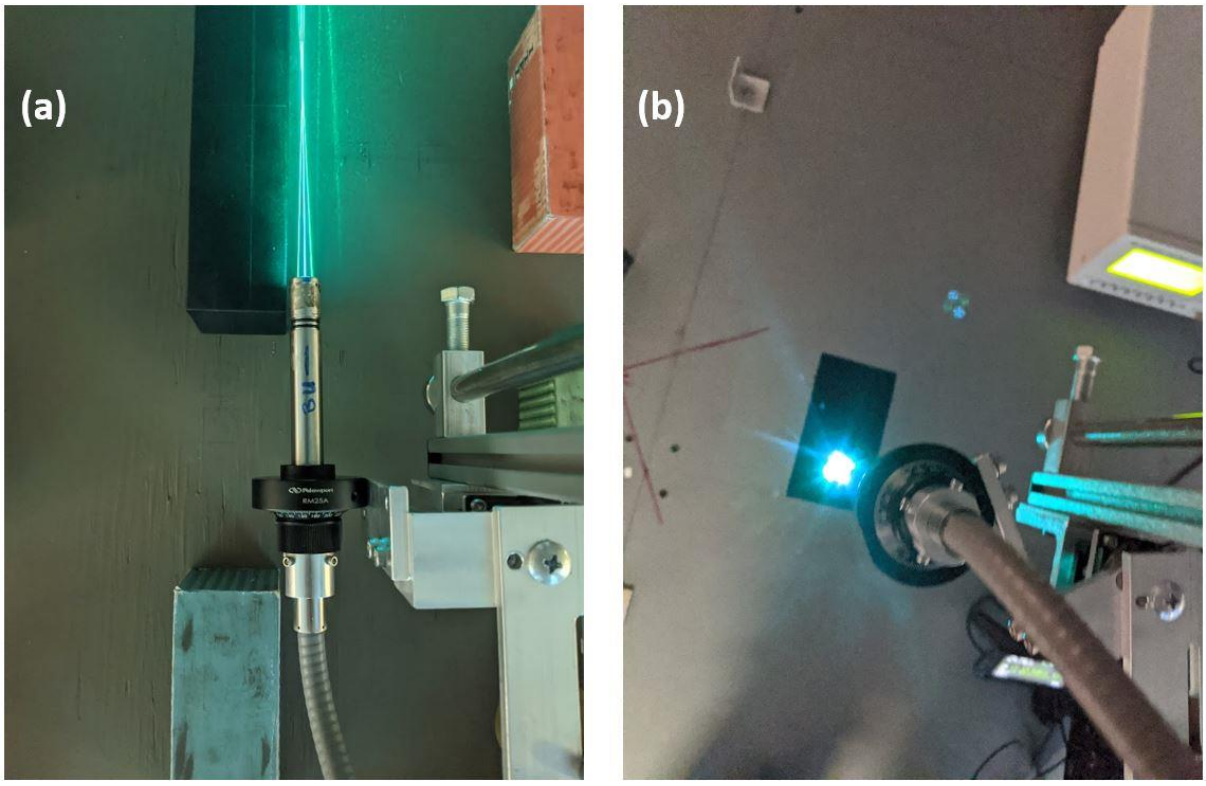

Figure 38 - Simplified LDV setup with the primary probe placed: (a) horizontally and (b) vertically.

3.4 Conclusions

Throughout this section, the possibility of obtaining reliable LDV data using a simplified 2D setup, in lieu of using a more complex 3D setup was discussed. To make a valid comparison, the same raw 3D LDV data (V1, V2, V3) was used twice, first to calculate the actual velocity components (u_{act}, v_{act}, w_{act}) via the transformation matrix; and second to obtain the extrapolated velocity components (u_{ext}, v_{ext}, w_{ext}), using the relative geometric position of the probe to the vertical and cross-wind directions. In the setup used, the relative angle between the primary probe and the vertical axis was $\alpha \approx 75°$; and the relative angle between the secondary probe and the vertical axis was $\beta \approx 25°$.

Analysis of the error magnitudes shows that the extrapolation process provides a fairly good approximation of the vertical (w) velocity component but fails to provide a good approximation of the cross-wind (v) component. Additionally, the simplified LDV setup always underestimates the value of the overall turbulence measurements (TKE) by about a third, due to the missing measurements of the fluctuations in the cross-wind direction.

Because of the inherent limitation of extrapolating 3D velocity results from a 2D (single probe) setup, it was determined that the full 3D LDV setup is crucial for obtaining accurate velocity measurements at Tower 3 location and at the sonic anemometer locations among the containers in the JRII-S field test. All LDV data shown in the remainder of this work was acquired using the full 3D LDV setup with two LDV probes. Alternative setups are proposed if the full 3D configuration is not available.

Chapter 4 – Experimental Setup

This section describes in detail the experimental setups used in this work. Velocity measurements were taken in the CHRC wind tunnel using two different measurement techniques, LDV and PIV.

4.1 Laser Doppler Velocimetry Experiments

The LDV portion of this work focused on measurements at the sonic anemometers from the JRII-S field test. With the agreement between wind tunnel and field tests established based on approaching wind measurements (as shown in Section 2.5.2), the next experimentation phase consisted of using the wind tunnel to make measurements at the corresponding locations in the Sonic Anemometers of the JRII-S study, focusing on Time Frames C and E, as in those tests the approaching wind was at an approximate 0°, aligned with the centerline of the pad. 3D LDV was used to collect data for all 30 sonic anemometers locations. Figure 39 illustrates the LDV probes at the equivalent location of sonic anemometer S61L2 as an example. Repeatability of the velocity was evaluated by performing three sets of measurements at each location. Repeatability was confirmed, as the velocities were statistically equivalent when these measurements were compared. Approximately 200,000 instantaneous LDV velocity acquisitions in each set (for a total of 600,000 acquisitions) were used to calculate velocity averages and secondary statistics for each repeat at a given location.

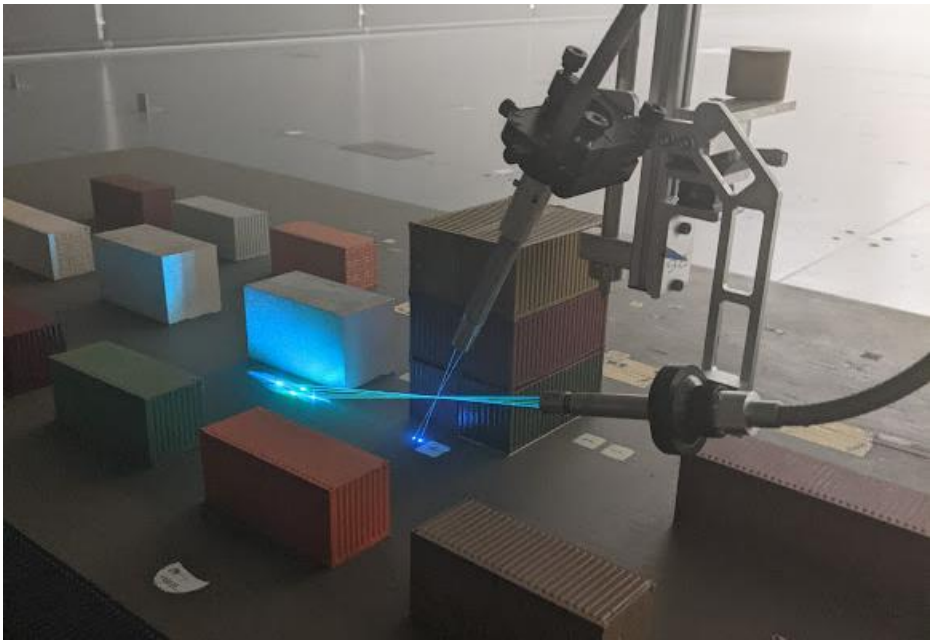

Figure 39 - Laser Doppler Velocimetry on the MUE model at Sonic Anemometer S61L2.

4.2 Particle Image Velocimetry Experiments

The PIV experiments were conducted in two different setups. In the first set, the laser sheet was projected vertically, aligned with the XZ plane of the tunnel, with the camera placed on the side of the pad. In the second set, the laser sheet was projected horizontally, aligned with the XY plane of the tunnel, with the camera placed above the pad. In both cases, the camera was targeted to capture the area surrounding CONEX 11.4.

4.2.1 Laser Sheet in the XZ plane (Side view)

Figure 40 shows the relative setup of the laser, camera, and CONEX 11.4 for the vertical laser sheet tests. As shown, the laser projected the light from above the pad, aligned with the centerline of the tunnel (which is also the centerline of the pad). The camera was placed on the side, approximately 1.2 m from the centerline of the tunnel. This positioning resulted in a field of view of approximately 450 mm x 450 mm, which is the maximum field of view possible with complete overlap of the laser sheets in the vertical configuration. The camera focus was adjusted daily to ensure the best quality in the raw images.

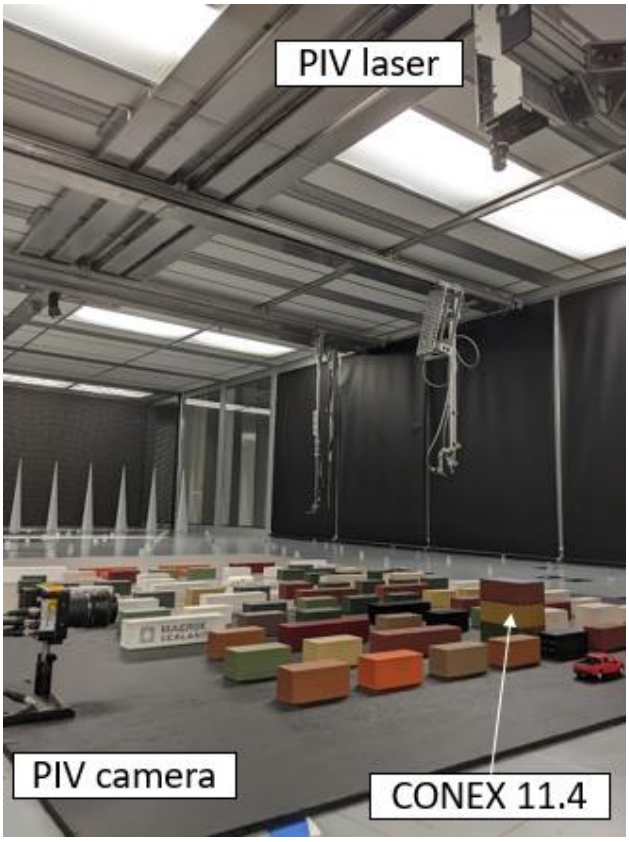

Figure 40 - Setup for the PIV experiments using a vertical laser sheet.

Table 3 summarizes the experiments performed using this setup. Four wind conditions from the field tests were replicated, two from JR-II (Trials 2 and 4) and two from JRII-S (Time Frames C and E). Trials 2 and 4 were chosen for modeling because Trial 2 has the highest approaching wind speed among all trials, and Trial 4 has a significantly lower speed, therefore forming a "low speed/high speed" pair. As previously discussed, it was not feasible to model Trial 1 conditions. Furthermore, Trials 3 and 5 were not considered for wind tunnel modeling because Trial 3 had unreliable atmospheric data (only the PWIDS set of wind velocity data from Tower 3 was available), and the wind speed in Trial 5 was very low, while the wind angle was very large (48°) relative to the MUE. Time Frames C and E were chosen because the wind angle aligned with the pad. Despite also having a near-zero relative wind direction, Time Frame A was not simulated due to its extremely high wind velocity.

Table 3 - Conditions from JR-II and JRII-S reproduced in the wind tunnel for the PIV in the XZ plane tests.

JR-II/JRII-S condition	Fan Speed (RPM)	Wind angle (°) [Relative to the pad]	Simulated release?
Time Frame C	93	0	No
Time Frame E	118	0	No
Trial 4	60	0†	No
Trial 4	60	0†	Yes (Neutrally Buoyant)
Trial 4	60	0†	Yes (Cl_2 simulant)
Trial 2	128	0‡	No
Trial 2	128	0‡	Yes (Cl_2 simulant)
†The actual relative wind angle in the field test was 22°. The pad was placed at 0° to minimize through-sheet particle motion.			
‡The actual relative wind angle in the field test was 9°. The pad was placed at 0° to minimize through-sheet particle motion.			

For the modeling of Trial 2 of JR-II, two different tests were performed: one baseline, before simulated chlorine releases ("pre-release"), and one with simulated releases. Three conditions were simulated for modeling Trial 4 of JR-II: pre-release, simulated chlorine release, and a simulated neutrally buoyant release. This last test was performed to study the effect of the velocity of the release separately from the effect of the higher density. No release was simulated for the tests based on JRII-S since no chlorine was released in this field test.

Additionally, to optimize PIV quality data, it was necessary to minimize the through-sheet particle motion (further explained in Section 4.2.3). This minimization was achieved by aligning the pad with the tunnel for Trials 2 and 4 conditions, yielding a 0° relative angle between wind and pad instead of the proper relative wind angles that were measured at Tower 3 in JR-II, 9° and 22° respectively. In practical terms, the wind angle only affects the lateral motion (y-direction) of the cloud. For the vertical PIV measurements, it was more important to investigate flow changes in the XZ plane.

The tests in JRII-S conditions and JR-II pre-release conditions were composed of 2,000

image captures, subdivided into four runs of 500 captures each. For the simulated chlorine releases, it was ensured that the PIV image capture was coincidental with the instant that the area source opened. Data acquisition of the simulated releases (both dense and neutrally buoyant) was subdivided into three types:

a. Seeded release (Gas mixture and fog) – 70 image captures per release repeat. Five repeats.
b. Unseeded release (Gas mixture only) - Short captures (100 captures per repeat). 20 repeats.
c. Unseeded release (Gas mixture only) - Long captures (200 captures per repeat). Five repeats.

Preliminary experiments indicated that seeding the release (i.e., turning the simulated chlorine cloud visible, as it was done in the flow visualization experiments) was improper for PIV data, as the fog particles tended to stay together. The PIV processing software (TSI Insight 4G™) was unable to identify the particles and perform correlations in the densely seeded cloud, as shown in Figure 41. Note that Figure 41 clearly shows some concentration of source gas on top of CONEX 11.4. The seeded releases were only used to determine the average time of arrival of the simulated chlorine cloud at the CONEX 11.4 location, along with the duration of the steady state phase of the releases. Those images were not processed in TSI Insight 4G™. The short-duration captures were used to evaluate the effect of the steady state phase (first fraction of the release, where the chlorine concentration is maximum) of the release in the flow. The long-duration captures were used to evaluate the impact of the final phase (i.e., secondary releases, which take place after the steady state phase of the release has passed into the flow field).

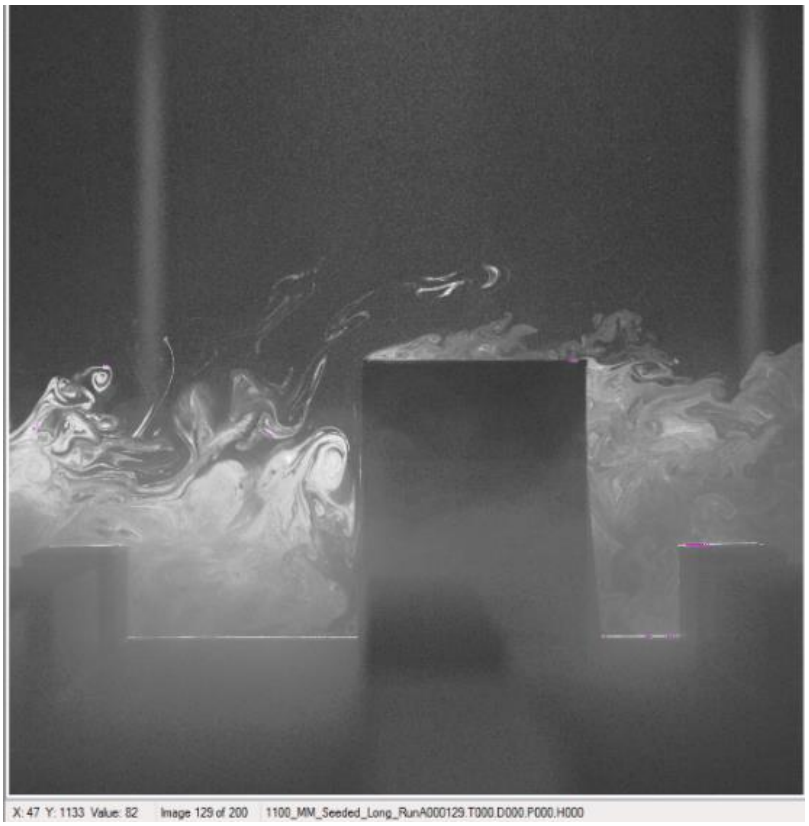

Figure 41 – Side view of a simulation of a chlorine release in the model with seed particles, used to determine the time interval between release and arrival at CONEX 11.4.

Vector field averages and vorticity intensities were calculated in Tecplot® Focus 2013R1. Vorticity (ω) was calculated using finite differences, comparing the velocities in the four adjacent subregions around the edges of the subregion in which vorticity is being calculated. This method for determining vorticity is shown in Equation 12, in which X and Z represent distances (mm), U and W represent velocity components (m/s), and i and j are dummy variables representing steps (neighboring subregions) in the horizontal and vertical directions, respectively. The relative positions of the neighboring subregions used in Equation 12 are better shown in the schematic of Figure 42. Since standard 2D PIV only yields velocity components within the laser sheet plane, only the vorticity component normal to the laser sheet can be obtained. Shearing and extensional strains in the measurement plane can also be calculated from PIV data (Raffel *et al.*, 1998).

$$\omega = 1000\left[\frac{W(i+1,j)-W(i-1,j)}{X(i+1,j)-X(i-1,j)} - \frac{U(i,j+1)-U(i,j-1)}{Z(i,j+1)-Z(i,j-1)}\right] = 1000\left[\left.\frac{\Delta W}{\Delta X}\right|_i - \left.\frac{\Delta U}{\Delta Z}\right|_j\right] \quad \textbf{(12)}$$

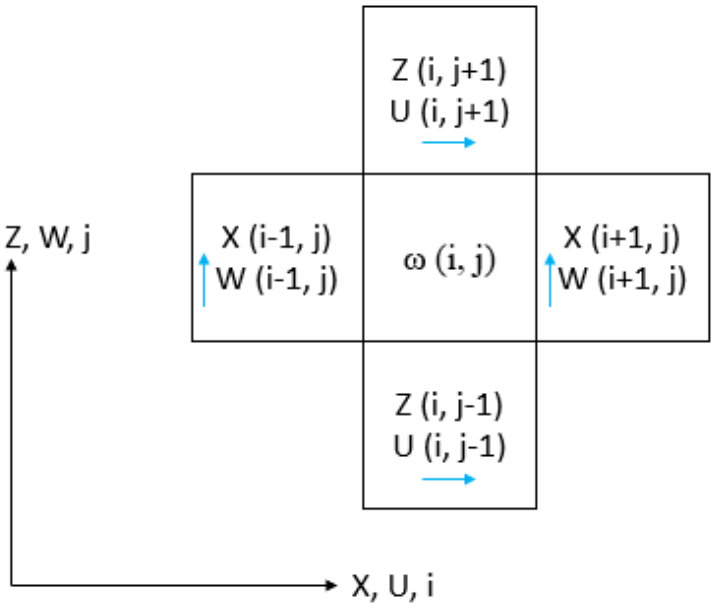

Figure 42 - The vorticity in the region (i, j) is calculated via finite differences of the vertical velocity component (W) in the horizontal direction (X) and the horizontal velocity component (U) in the vertical direction (Z).

4.2.2 Laser Sheet in the XY plane (Top view)

Figure 43 shows the relative setup of the laser, camera, and CONEX 11.4 for the horizontal laser sheet tests. As shown, the laser light was projected from downwind of the pad. The laser sheet was projected at 2 cm above the pad (equivalent to 1 m above the pad in field scale), the height of ten sonic anemometers located around CONEX 11.4. Two Nd:YAG mirrors (ThorLabs NB1-K12) were added to the optical train in a periscope assembly to redirect the laser sheet and ensure that it was projected at 2 cm above the pad. The camera was placed approximately 145 cm above the pad. This positioning generates a field of view of approximately 600 mm x 600 mm, which is the maximum field of view achievable with complete overlap of the laser sheets in the horizontal configuration. The camera focus was adjusted daily to ensure the best quality in the raw images.

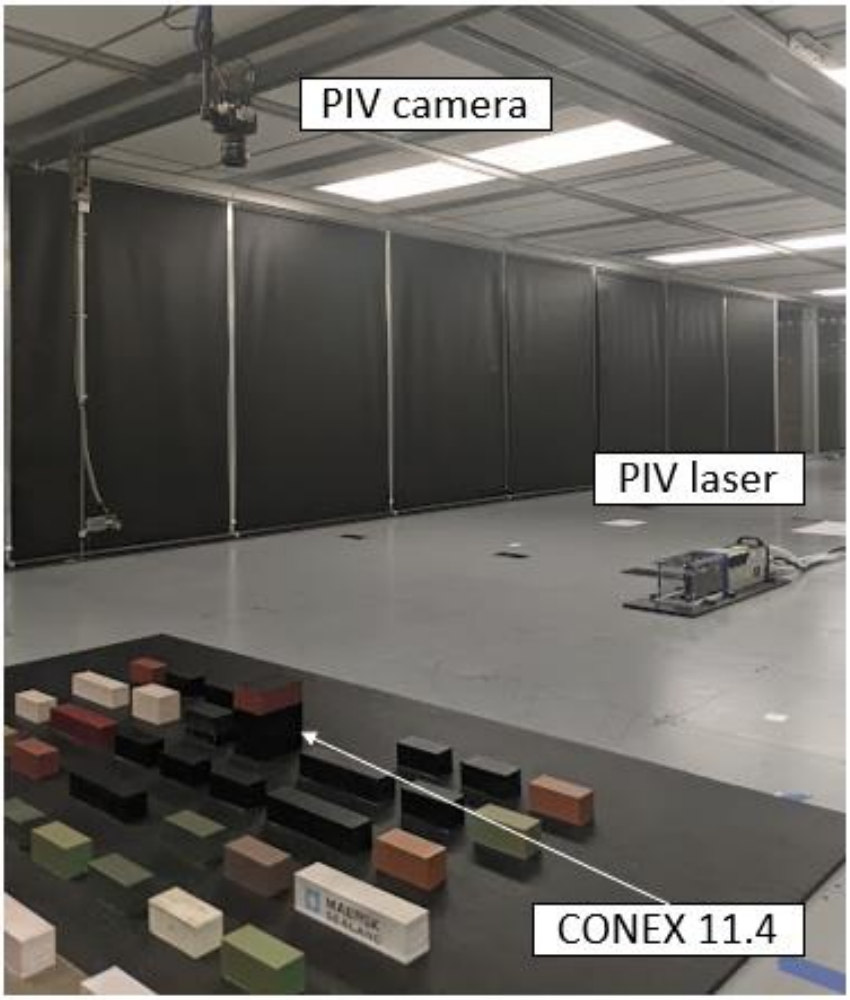

Figure 43 - Setup for the PIV experiments using a horizontal laser sheet.

Table 4 summarizes the experiments performed. Three wind conditions from the field tests were replicated, one from JR-II (Trial 4) and two from JRII-S (Time Frames C and D). Trial 4 was chosen over Trial 2 due to its lower freestream velocity and wider wind direction relative to the pad. Time Frames C and D were chosen for modeling as comparisons between PIV data from this work can be made with CFD simulations found in the literature (Carissimo, Trini Castelli & Tinarelli, 2021). For the Trial 4 reproduction, two tests were conducted: a pre-release (without simulated chlorine releases) case and a simulated chlorine release. No release was simulated for the tests based on JRII-S since no chlorine was released in this field test.

Table 4 - Conditions from JR-II and JRII-S reproduced in the wind tunnel for the PIV in the XY plane study.

JR-II/JRII-S condition	Fan Speed (RPM)	Wind direction (°) [Relative to the pad]	Simulated Cl_2 release?
Time Frame C	93	0	No
Time Frame D	112	7	No
Trial 4	60	22	No
Trial 4	60	22	Yes

For the tests in the XY plane, a few of the opaque containers in the model were replaced with model containers with a transparent layer of clear casting epoxy. Hence, it was possible to project the laser light upwind of those containers and obtain PIV measurements at those locations. The opaque models of CONEX containers 11.3 and 11.4 were replaced in both JR-II and JRII-S models, as shown in Figure 44. The laser sheet passing through the layers of transparent clear casting epoxy in both CONEX containers is also shown in Figure 44. Additionally, in the modeling of the JR-II test, opaque CONEX containers 12.4, 12.5, and 12.6 were replaced by the models with the transparent layer, and the cars of row 13 were removed completely; while in the modeling of the JRII-S tests, the opaque CONEX containers 10.3, 10.4, and 10.5 were replaced by the models with the transparent layer. Note that CONEX containers 12.4, 12.5, and 12.6, plus the entirety of row 13 (cars) were removed in the setup of the JRII-S field test and consequently were not placed in the wind tunnel model.

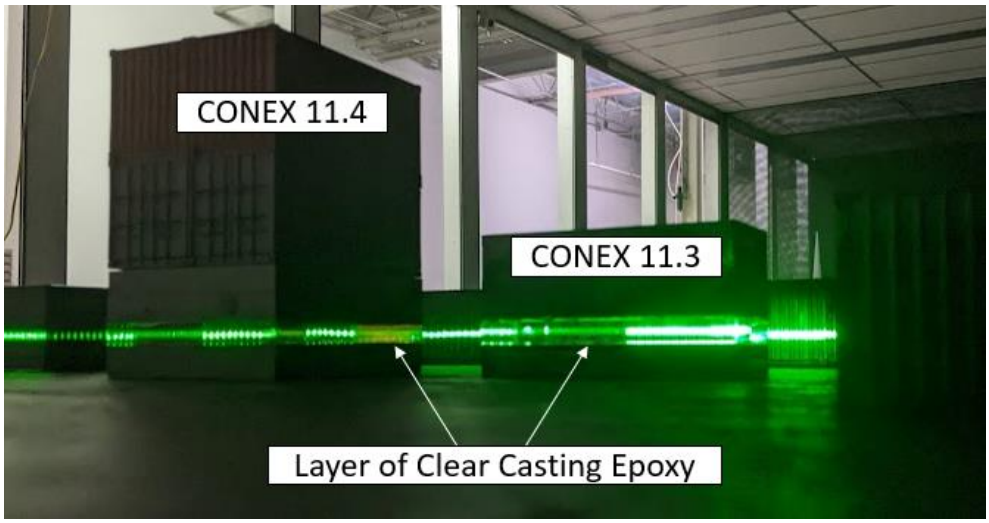

Figure 44 - Layer of transparent clear casting epoxy at 2 cm AGL in CONEX containers 11.3 and 11.4.

The tests in JRII-S conditions and JR-II pre-release conditions were composed of 2,000 image captures, subdivided into four runs of 500 captures each. For the simulated releases, it was ensured that the PIV image capture was coincidental with the instant that the area source opened. The simulated releases were subdivided into two types:

a. Seeded release (Gas mixture and fog) – 120 image captures per release repeat. Three repeats.
b. Unseeded release (Gas mixture only) – 120 image captures per repeat. 20 repeats.

Once again, the denser release kept the fog particles too close during the seeded release, as shown in Figure 45. TSI Insight 4G™ is incapable of determining particle motion in extremely high seed density like the one in the seeded releases. Instead, the seeded releases were only used to determine the average time of arrival of the simulated chlorine cloud at the channels in the last rows of the MUE, along with the duration of the steady state phase of the releases. Those images were not processed in TSI Insight 4G™. Note the shadows in the laser sheet upwind of CONEX containers caused by the corners of the layers of clear casting epoxy.

Figure 45 - Top view of a simulation of a chlorine release in the model with seed particles, used to determine the time interval between release and arrival at the channels in the last rows of the MUE.

Vector field averages and vorticity intensities were calculated in Tecplot® Focus 2013R1. Vorticity (ω) was calculated using finite differences, comparing the velocities in the four adjacent subregions around the edges of the subregion in which vorticity is being calculated, as shown in Equation 13. Equation 13 is analogous to Equation 12 but considering the cross-wind (V) and along-wind (U) velocity changes over the X and Y directions.

$$\omega = 1000\left[\frac{V(i+1,j)-V(i-1,j)}{X(i+1,j)-X(i-1,j)} - \frac{U(i,j+1)-U(i,j-1)}{Y(i,j+1)-Y(i,j-1)}\right] = 1000\left[\left.\frac{\Delta V}{\Delta X}\right|_i - \left.\frac{\Delta U}{\Delta Y}\right|_j\right] \qquad \textbf{(13)}$$

4.2.3 The PIV Processing Pipeline

The PIV software is equipped with algorithms and image adjustment tools to process the captured images and determine vectors across the camera's field of view. The best results from PIV experimentation are achieved when specific parameters are optimized: camera focus, time

between laser pulses (ΔT), interrogation subregion size, light sheet thickness, and seeding amount and concentration. For any PIV application, six rules-of-thumb were established to ensure that PIV measurements (particle images) have the highest possible quality (Keane & Adrian, 1990):

A. The size of the interrogation subregion should be small enough so that one vector describes the flow in that subregion.
B. Each interrogation subregion should contain more than ten particles.
C. Maximum in-plane particle displacement should be less than 25% of the interrogation subregion size.
D. Maximum through-plane displacement should be less than 25% of the light sheet thickness.
E. Minimum in-plane particle displacement should be at least two particle diameters.
F. Camera exposure must be long enough to show the particles clearly.

The rules-of-thumb were created so that the acquired PIV images would yield vector field results (from the correlation of particles) with a high degree of confidence. Rule A refers to resolution, as a large subregion would fail to generate one vector that sufficiently describes the complexities of the flow (e.g., flow redirection and vortices) in that region. The other rules-of-thumb are related to seeding. Rule B gives the software the best chance to find the average particle displacement in the subregion and obtain a strong correlation peak. Rule C was written to ensure that most particles stay within the same subregion for both laser pulses. Rule D is to prevent particles from entering or leaving the field of view in the direction perpendicular to the plane. Rule E regards the accuracy of PIV measurements. Each seed particle occupies more than one pixel. When light is scattered by each particle, the software can identify the light intensity

and find the centroid of each particle with sub-pixel accuracy. Consequently, typical PIV measurements yield errors in the order of 0.1 of a pixel (Adrian & Westerweel, 2011). By assuring that the particle displacement is greater than two particle diameters, the relative error of the calculated particle displacement is minimized, improving the accuracy of the velocity measurements. And finally, Rule F ensures the best quality image for the particles so that the displacements can be calculated.

Modern PIV software packages have additional processing tools that allow more flexibility on the rules-of-thumb without loss of data. Additionally, many of the software packages set their default settings to the values of the rules-of-thumb but can be altered somewhat to achieve good vector results from less-than-perfect PIV data.

The values of ΔT for each wind condition used in this work are shown in Appendix D. The image processing takes place in five steps: calibration, preprocessing, masking, processing, and postprocessing. This sequence is referred to as the "processing pipeline" in the TSI Insight 4G software.

For 2D PIV, calibration consists of placing an object of known size in the measurement plane. An image of this object is taken and used to establish a conversion between image pixels and physical distance in the plane.

Image preprocessing improves the quality of the raw images before actual PIV processing to generate velocity vectors. Several preprocessors are available in TSI Insight 4G™, with the following two relevant for this work: image generator and image calculator, which together work as a background image subtractor. Background subtraction is a very common preprocessor for PIV measurements. Images frequently have fixed parts, such as objects, boundary walls, and stationary laser reflections. Removing the fixed parts highlights the moving particles (which

carry the relevant velocity information in PIV measurements), improving the signal-to-noise ratio of the images. Based on a list of images, the image generator calculates the pixel-wise (minimum or average, as chosen by the user) intensity of all images that list. The result is a background image, which can be subtracted from each of the original images using the image calculator preprocessing. Figure 46 is a side-by-side comparison of a raw PIV image (left) and the result of the preprocessing after background subtraction (right).

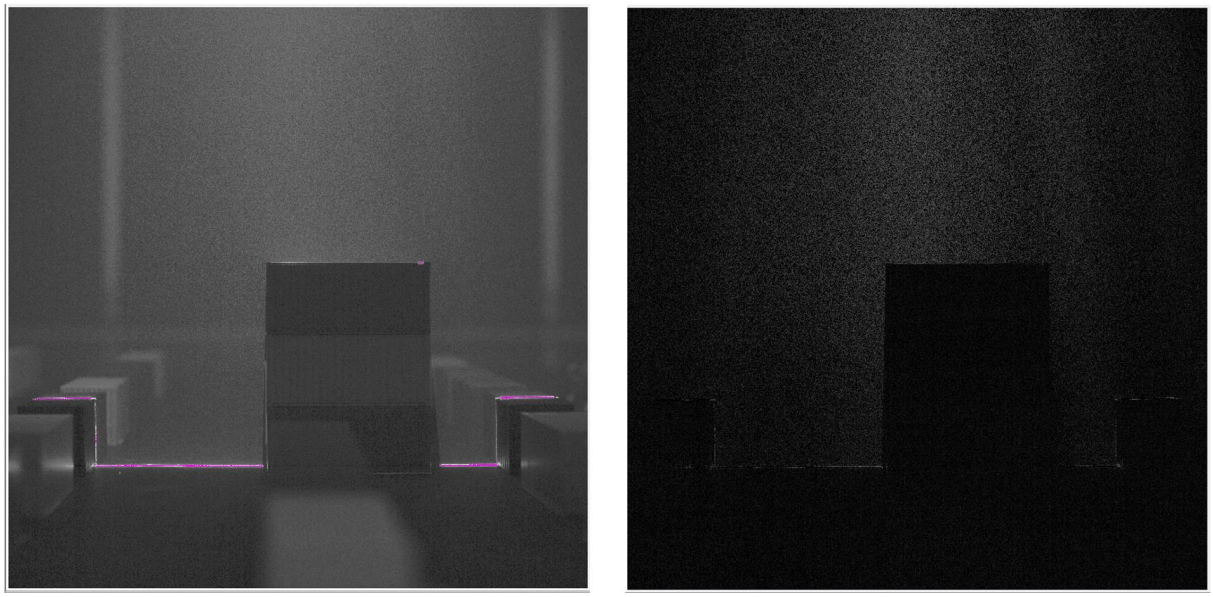

Figure 46 - PIV image before and after applying the background subtraction preprocessing.

Figure 46 also shows regions in the flow that are not illuminated by the laser sheet, such as the pad and the side of CONEX 11.4. A processing mask can be applied to a list of images to hide areas in the field of view from the processing algorithm. Applying the processing mask directs the processing algorithm to look for particles (i.e., calculate vector displacements) in only certain areas of the image, therefore saving computational time and file size, and preventing incorrect vectors from being created in areas where there are no particles. Applications of masking in this work in both vertical and horizontal sheet PIV are shown in Figure 47. Processing only takes place in areas in dark grey. Areas in light grey are "masked out" and

hidden from the processing algorithm.

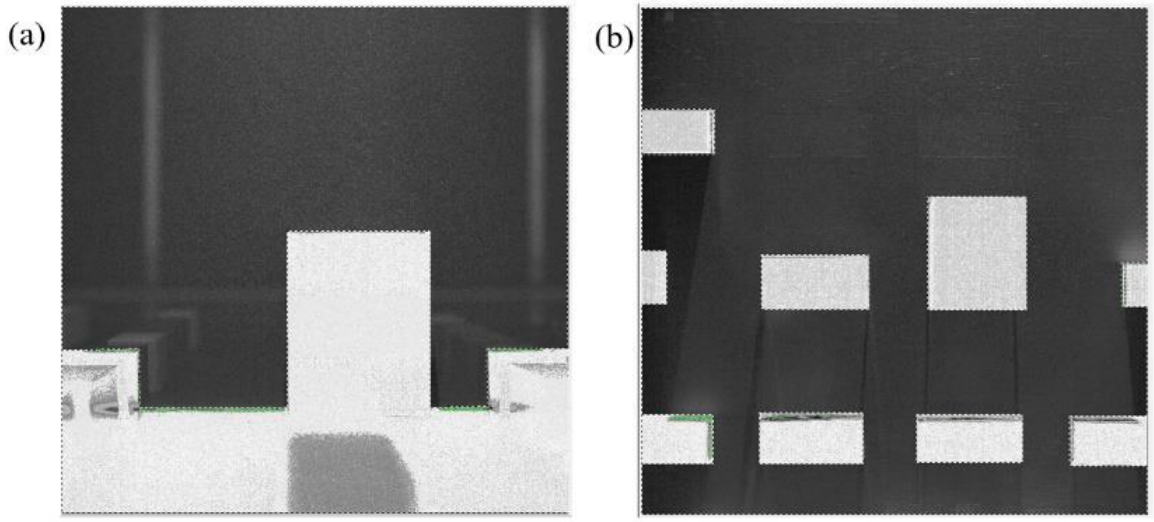

Figure 47 - Application of masking in PIV measurements from (a) side view and (b) top view.

After preprocessing and masking, the actual velocity vector processing can take place. The PIV processing algorithm is implemented using grid engines that subdivide the images into smaller subregions. The grid engine processes the particle field in either a single ("Nyquist Grid") pass or multiple ("Recursive Nyquist Grid") passes. Nyquist grid is the simplest and fastest method because it consists of a single pass. It generates a vector field with 50% subregion overlap. During processing, only the particles that are present in a subregion in both frames are used to calculate the velocity vector of that region. This means that particles that leave or arrive in that subregion in between the laser pulses are not considered. Nyquist grid fixes this problem by creating an intermediary region, overlapping 50% of two neighboring subregions, with the objective of including valid velocity information from particles that moved from one subregion to another between the laser pulses.

Recurse Nyquist Grid yields results with increased accuracy and higher spatial resolution. It consists of multiple passes. The first pass is similar to the Nyquist Grid, with 50% overlap grid spacing. Afterward, the vector field is verified using pass validation, in a similar process to the

postprocessing method that is explained later. The subregions in the first pass are larger and give a rough estimate of the flow field. The subregions of the second pass are smaller than the ones in the first pass. The calculated particle displacements in the first pass are used as starting points for the second pass. This method yields higher matched particles and decreases noise (Raffel et al., 1998). An example of multi-pass interrogation is shown in Figure 48 (Raffel et al., 1998). The grey squares in the lower left corner of each image represent the interrogation windows sizes used in each pass. As the subregions get smaller with each pass, the accuracy and resolution of the flow field increase significantly.

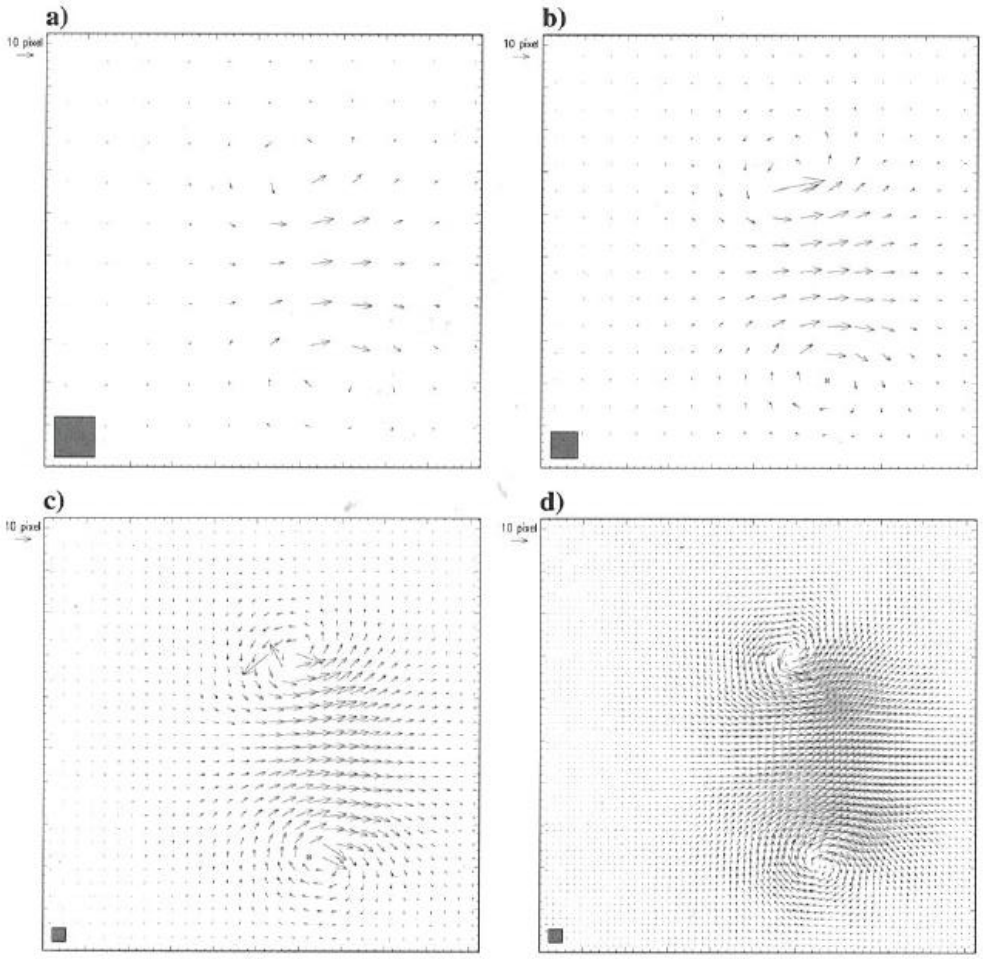

Figure 48 - Four-step multi-pass interrogation processing. (Raffel et al., 1998. Reproduced with permission).

PIV processing determines if a vector is valid based on the height of the correlation peak in comparison with the height of the noise peaks. If the rules of thumb are appropriately followed, PIV images processing generates over 95% correct velocity measurements (TSI Incorporated, 2020). Spurious correlations can still be found due to through-plane motion, low seeding, correlations with reflection that could not be masked, or from too many seed particles in the flow. Postprocessing is a method that analyzes all vectors and identifies the spurious ones based on several available filters. Global validation filters eliminate any vectors with a component measured above a threshold set by the user (i.e., unreasonably fast calculated vectors). Other available postprocessing filters compare vectors to their neighbors, in a method called local validation. Local validation compares each vector to its close neighbors by placing each vector in the center of a grid of a specified size (e.g., 3x3, 5x5, 7x7, etc.). If the vector in question differs from the median or mean (as specified by the user) of neighboring vectors by a factor over a user-defined tolerance, the vector is deemed invalid and removed. Postprocessing can also fill the removed vectors via interpolation.

The processing pipeline settings chosen for the PIV section of this dissertation are summarized in Table 5. The complete list of global validation velocity limits per trial is shown in Appendix D.

Table 5 - PIV processing pipeline settings applied in this work.

Processing Pipeline Step	Processing Pipeline Sub Step	Tests in the XZ plane (Vertical laser sheet)	Tests in the XY plane (Horizontal laser sheet)
Calibration	N/A	Ruler placed in measurement plane prior to the tests	
Pre-processing	Generate Background (Minimum or Average)	Background subtraction (Minimum Intensity)	Background subtraction (Average Intensity)
Processing Mask	N/A	MUE pad and Side of CONEX 10.4, 11.4 (JR-II and JRII-S) Additional mask: CONEX 12.5 (JR-II release trials)	Roof of CONEX 10.2, 10.3, 10.4, 10.5, 11.2, 11.3, 11.4, 11.5, 12.2 (JR-II and JRII-S) Additional mask: Roof of CONEX 12.3, 12.4, 12.5 (JR-II release trials)
Processing	Scheme	Recursive Nyquist Grid	
	First pass interrogation subregion size	64 x 64 pixels	
	Pass Validation	Local Validation (Median of 5x5 grid)	Local Validation (Mean of 3x3 grid)
	Second pass interrogation subregion size	32 x 32 pixels	
	Maximum allowed particle displacement	25% of subregion size on first pass (16 px)	37% of subregion size on first pass (23.68 px) – JRII-S 35% of subregion size on first pass (22.4 px) – JR-II release trials
Postprocessing	Global Validation	Varied with wind speed†	
		Ranged from 6000 to 13000 px/sec	Ranged from 4250 to 6800 px/sec
	Local Validation	Not used	Local Validation (Mean of 3x3 grid)
	Vector Filling	Not used	
	†Full list of global validation thresholds per wind speed is shown in Appendix D		

Chapter 5 – Results and Discussion

The results of LDV and PIV measurements in the MUE model are analyzed in this chapter.

5.1 Laser Doppler Velocimetry Results

Comparison between JRII-S sonic anemometer data and measurements taken with the LDV system in the tunnel model shows an overall good agreement between model and field data for vector direction and magnitude, as shown in Figures 49 and 50. Figure 49 shows the comparison of sonic anemometers (S11, S23, S31, S41, S51, S61, S73, S82, S101, S111) from a side perspective in Time Frames C (Figure 49b) and E (Figure 49c). The locations of the sonic anemometers (relative to the CONEX containers) in the centerline of the MUE are shown in Figure 49a. There is excellent agreement with respect to wind direction, especially for sonic anemometers in front of (Mini-towers S11 and S61) and above (S23, S31L3, S73, and S82L4) the rooftop level of CONEX containers 9.4 and 11.4. Tabulated data of the sonic anemometer data obtained during the JRII-S Field tests are shown in Appendix E, and tabulated LDV measurements data obtained in the Wind Tunnel model are shown in Appendix F. Note that there was no data collected in JRII-S Time Frame E in sonic anemometers S41 and S51, which is why there are only (orange) wind tunnel velocity arrows at those locations in Figure 49b. Data from sonic anemometers S31L3 and S82L2 were discarded in both Time Frames because those velocity measurements were unreasonably high.

Figure 50 compares the 1 m AGL sonic anemometers (S11L1, S21, S22, S24, S25, S31L1, S41, S51, S61L1, S71, S72, S74, S75, S81, S82L1, S83, S101, S111) from a top view in Time Frames C (Figure 50a) and E (Figure 50b). The locations of the sonic anemometers (relative to the CONEX containers) at 1 m AGL are shown in Figure 50c. Good agreement was achieved as the magnitude and direction of the vectors were consistent between field test and

wind tunnel. The agreement within the MUE further shows that the wind tunnel is capable of reproducing the field tests. Differences in the vector direction between the tunnel and field in Figure 50 can be explained by high variability in the (mean) wind direction observed in the field over the 30-min averaging interval. A region of near-stagnant flow is formed in the wake of CONEX containers 9.4 and 11.4. High variability in vector direction is observed in this region. Flow measurements fluctuate between relatively small positive and relatively small negative values, yielding a near-zero average velocity. Furthermore, in these regions, velocity direction changes over small distances. Hence, a slight difference between the locations of the LDV probe in the wind tunnel and the sonic anemometer in the field can cause a significant difference in the measured velocity. Note that there was no data collected in JRII-S Time Frame E for sonic anemometers S22, S41, S51, S71, S72, and S83.

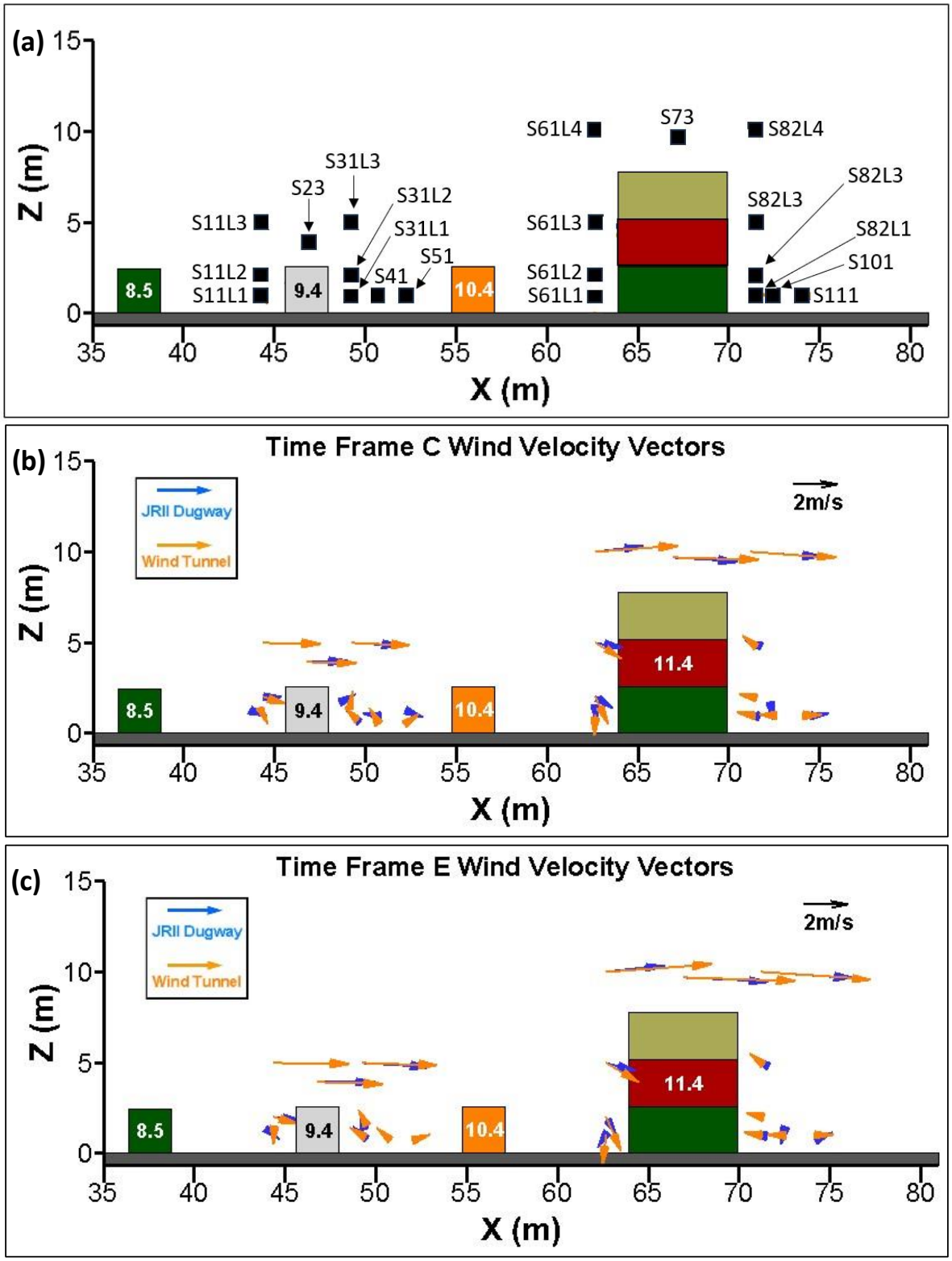

Figure 49 - Comparisons of along-wind and vertical velocity components between sonic anemometer measurements on the field and LDV measurements in the model in (a) Time Frame C and (b) Time Frame E conditions. (c) Locations of the Sonic Anemometers.

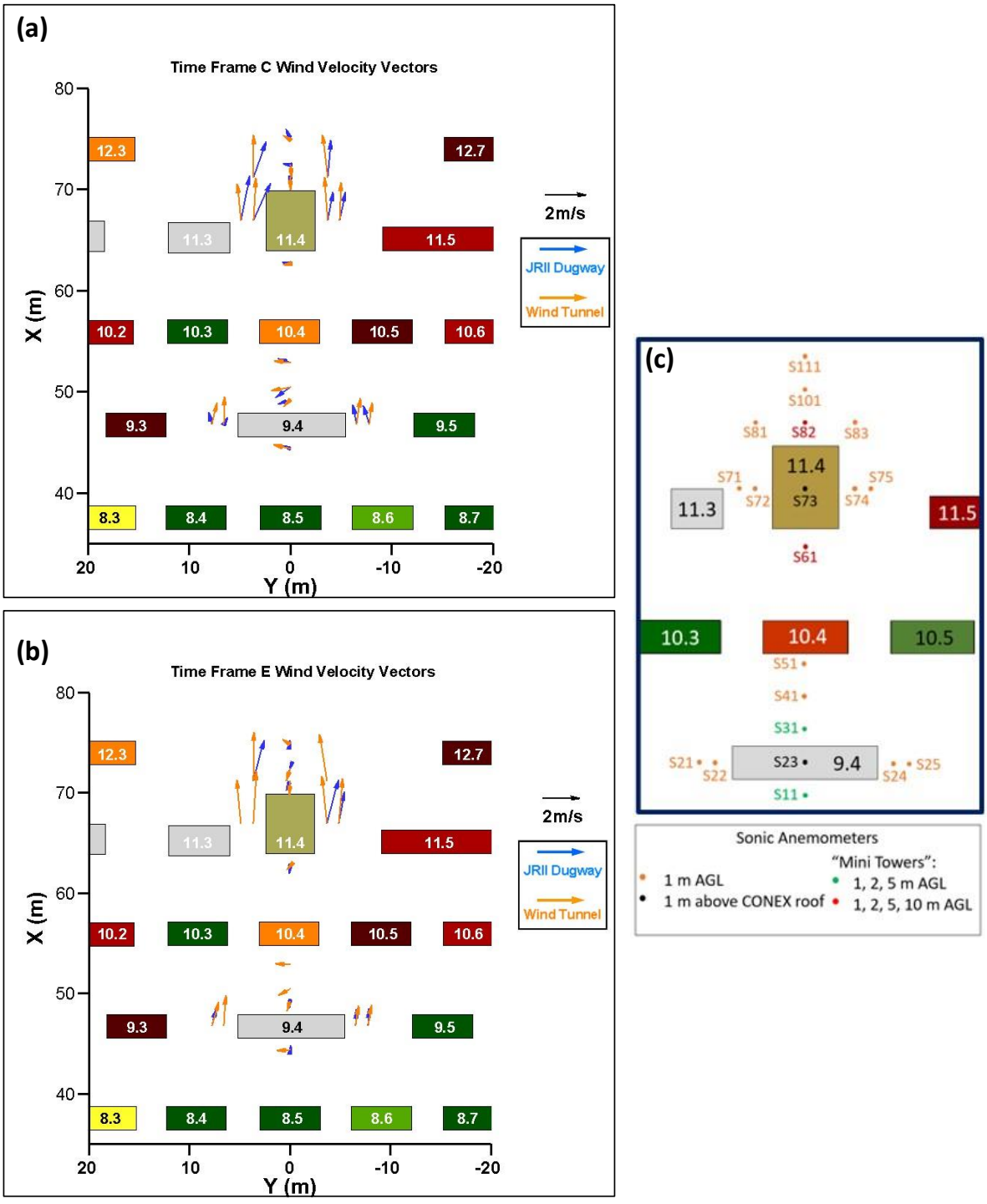

Figure 50 - Comparisons of along and cross-wind velocity components between field and model for 1 m AGL sonic anemometers in (a) Time Frame C and (b) Time Frame E conditions; (c) Locations of the Sonic Anemometers.

5.2 Particle Image Velocimetry Results

PIV results for models of the JR-II and JRII-S field tests are shown and discussed in this section. Unless explicitly stated, all velocity measurements are shown at field scale, that is, wind tunnel velocity measurements were scaled up to field scale values using Froude number similarity. All vorticity results are shown at tunnel scale, in s^{-1}.

The axis titles Xf, Yf, and Zf, respectively, refer to distances in the along-wind, cross-wind and vertical directions in the field scale, while axis titles X, Y, and Z do the same in tunnel scale. The number of instantaneous velocity measurements that contributed to an averaged result for each test condition is shown in Appendix D. In general, more than 50% of the instantaneous vector results contributed to the average velocity field, being close to 100% for the vast majority of the subregions. Plots of the instantaneous measurements that contributed to the averaged result for each subregion in Time Frame C conditions are shown in Figure 51 as an example. Results in the XZ plane are shown in Figure 51a and in the XY plane in Figure 51b. Colors from orange to red indicate that over 80% of instantaneous measurements contributed to the average in those locations. Similar plots for all other test conditions are shown in Appendix H7.

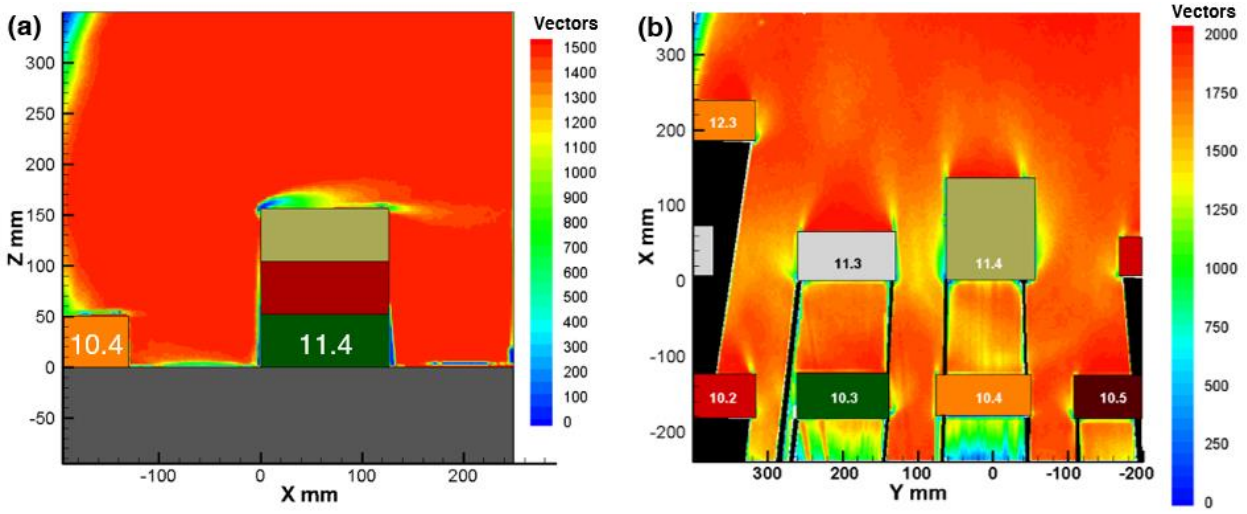

Figure 51 – Plot of Vector count per subregion in JRII-S Time Frame C conditions in the (a) XZ plane and (b) XY plane.

5.2.1 Modeling the JRII-S Field Test

Results of modeling the JRII-S field test are shown in this section. PIV results in the XZ plane (vertical laser sheet) include tests of Time Frames C and E. PIV measurements in the XY plane (horizontal laser sheet) of the model at a (field scale) height of 2 m AGL were conducted for Time Frames C and D.

5.2.1.1 Velocity Measurements in the XZ Plane

PIV measurements were taken in the surroundings of the tall container CONEX 11.4. The approaching wind in this field of view enters the frame on the left-hand side, moving in the positive x-direction. In the plots of average velocity in the XZ plane with streamlines, all the streamlines in black are equally spaced at 1 m apart. The dividing streamline is shown separately in pink.

As discussed before, only pointwise velocity measurements (sonic anemometers) were taken during the JRII-S field tests. PIV measurements in the scale model show the entire flow complexity in that section of the MUE. The average two-dimensional velocity magnitude in the XZ plane for Time Frame C is shown in Figure 52a. The average velocity vectors are shown separately in Figure 52b, along with the dividing streamline. Figure 52c shows a magnified view around CONEX 11.4 only, with the locations of the sonic anemometers (Mini-towers S61 and S82, plus S73, S101, S111) marked by black crosses. Finally, the extracted velocity vectors at the equivalent location of the sonic anemometers are shown in Figure 52d, with PIV, LDV, and field test results shown by the green, orange, and blue arrows, respectively. The velocity magnitude results shown in Figure 52 are expected and show the flow behavior similar to what was found in the literature in terms of PIV measurements in urban models (Essel, Balachandar, & Tachie, 2023; Kim, T. & Christensen, 2018; Takimoto *et al.*, 2011).

The slower velocity average (dark blue contour) at the rooftop level of CONEX 11.4 is a serious hazard, as lower velocities decrease the dispersion of gases. The risk is increased because most ventilation intakes of buildings are located on the rooftop. An increase in contaminant concentration at the rooftop can unexpectedly put people inside buildings at risk. Finally, the lower velocity at the rooftop explains the high concentrations of gases at that height, as reported in the literature (Hanna & Chang, 2015).

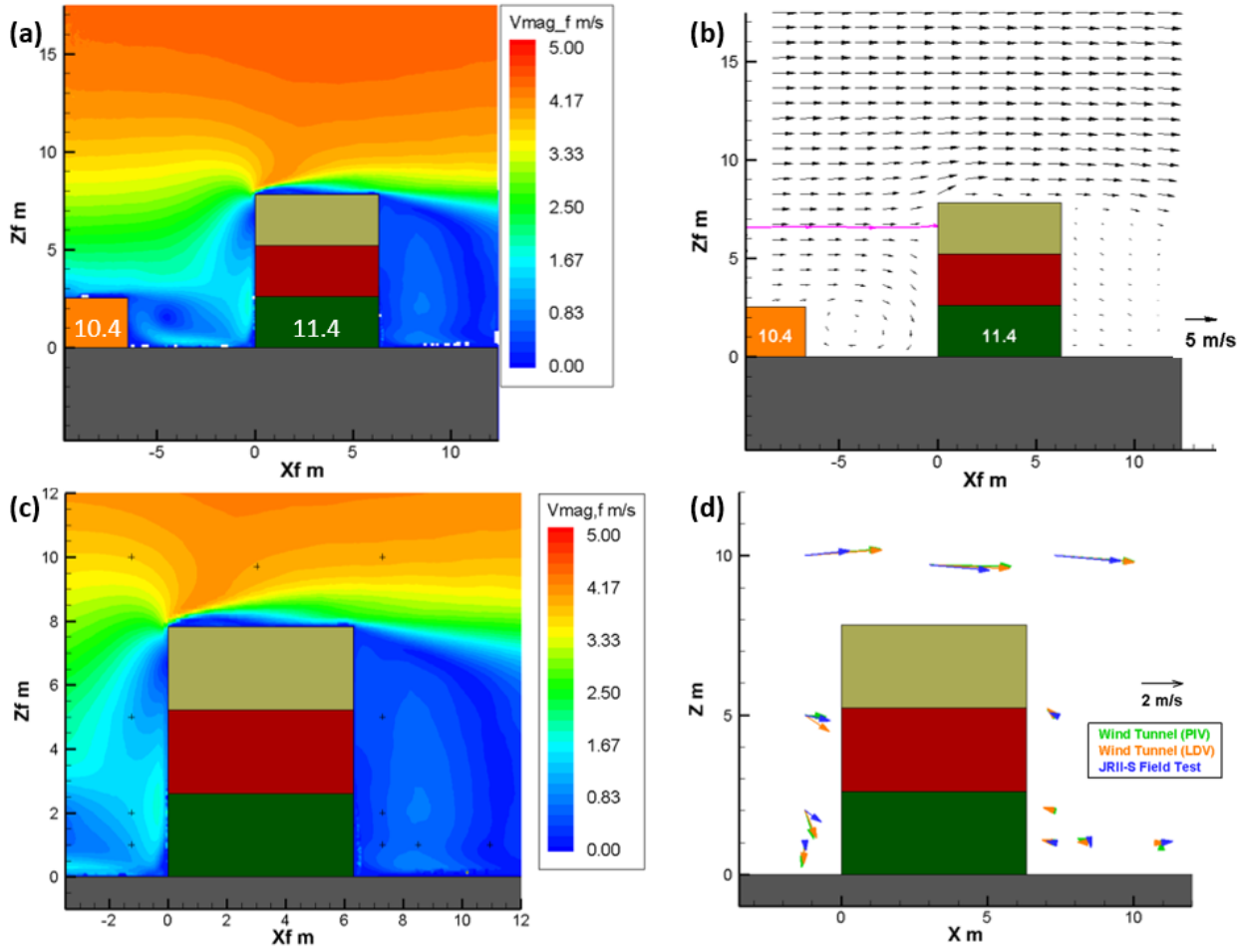

Figure 52 - PIV results in Time Frame C wind conditions. (a) Average velocity magnitude in the XZ plane, (b) Average velocity magnitude vectors, with the dividing streamline, (c) Sonic Anemometers locations around CONEX 11.4 are marked by the crosses, (d) Extracted velocity vectors at the Sonic Anemometer locations around CONEX 11.4.

Similar plots in Time Frame E conditions are shown in Figure 53. Figures 52 and 53 are not on the same scale. Extremely low flow is observed on the lee side of CONEX 10.4 and

CONEX 11.4. The presence of a region of slower flow in the canyon between CONEX 10.4 and 11.4, surrounded by slightly faster flow, indicates the presence of a recirculation region in this canyon. Regions of extremely slow velocities are present on the lee side of CONEX 11.4 in both wind cases, as was expected and was already identified by the point-wise measurements in the field test and by the LDV measurements in the model. The region of near-stagnant flow extends further downwind, out of the field of view of the camera. Extremely low average velocities on the roof of CONEX 11.4 are also observed.

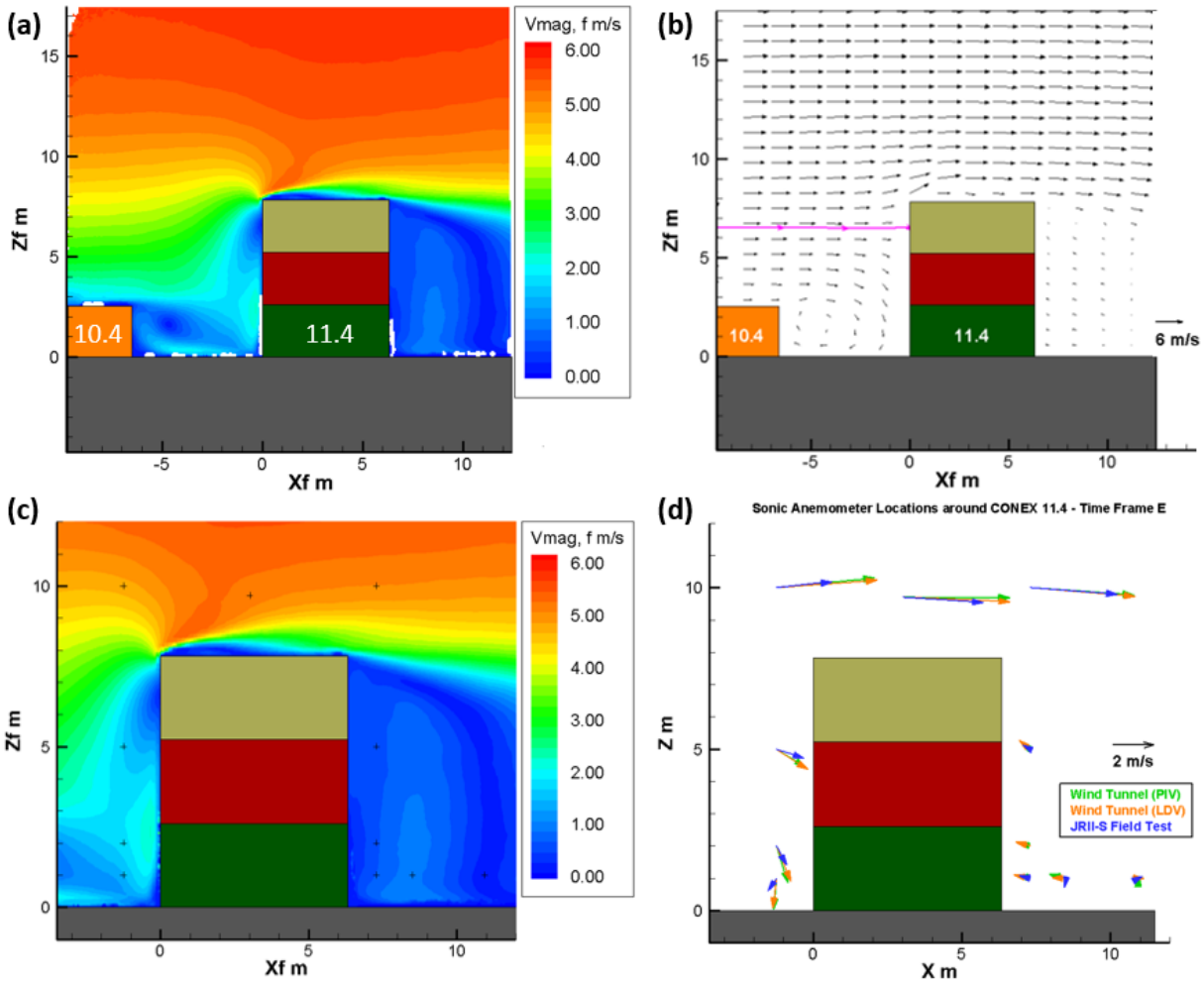

Figure 53 - PIV results in Time Frame E wind conditions. (a) Average velocity magnitude in the XZ plane, (b) Average velocity magnitude vectors, with the dividing streamline, (c) Sonic Anemometers locations around CONEX 11.4 are marked by the crosses, (d) Extracted velocity vectors at the Sonic Anemometer locations around CONEX 11.4.

Pointwise velocity results extracted from the average flowfield can be used to not only compare the PIV results with velocity data obtained in JRII-S, but can also be used to compare velocities obtained via the PIV and LDV techniques. The extracted vectors from the flowfield obtained in the PIV measurements are shown in Figures 52d and 53d in green vectors. Figures 52d and 53d show nearly identical results when comparing the LDV with the PIV techniques, which indicates that PIV measurements capture the characteristics of the flow and further demonstrate the capability of the wind tunnel to succesfully model the field test. Minor differences between the two techniques can be attributed to the difference in sample sizes inherent to the techniques. When comparing to JRII-S, Figures 52d and 53d show the same general results as Figure 49, indicating excellent agreement with respect to vector direction, especially for sonic anemometers in front of (Mini-tower S61) and above (S73 and S82L4) the rooftop level of CONEX 11.4. Tabulated extracted velocity values in the locations of the Sonic Anemometers are shown in Appendix H1.

The effect of the leading edge of CONEX 11.4 in the flow can also be observed in the PIV results. The average velocity plots in Figures 52a and 53a show a region of extremely low average velocity at rooftop level, near the leading edge of CONEX 11.4, which indicates a flow detachment from the CONEX rooftop. Timelapse (sequential PIV results) of instantaneous velocity magnitude measurements shows that the thickness of the detachment region changes constantly, as shown in Figure 54 as an example in Time Frame C wind conditions. Each panel in Figure 54 shows instantaneous velocity measurements at 0.1s increments.

Vortices are formed when slow upward flow traveling on the front face of CONEX 11.4 interacts with the fast flow approaching the model building at rooftop level. Vortices grow as they move across the roof and shed from the trailing edge of CONEX 11.4. Analysis of

sequences of instantaneous measurements shows that the time for a typical full cycle from the formation of the vortex to full shedding at the back edge of CONEX 11.4 is between 0.5 to 1 second (in tunnel scale). The frequency of the formation of vortices is irregular due to the nature of the turbulent flow.

Figure 54 shows the shedding cycle of two vortices formed in quick sequence. The first vortex ("Vortex 1") starts to form in Figure 54a, growing quickly as it moves along the roof of CONEX 11.4. While Vortex 1 approaches the back edge of the tall building, as shown in Figure 54e, the second vortex ("Vortex 2") starts to form at the leading edge. Vortex 2 then remains approximately the same size throughout Figures 54f, 54g, and 54h while it moves along the rooftop of CONEX 11.4. Meanwhile, Vortex 1 completely detaches from the back edge of CONEX 11.4 and finally sheds, as seen in Figure 54h, 0.7 seconds after its formation.

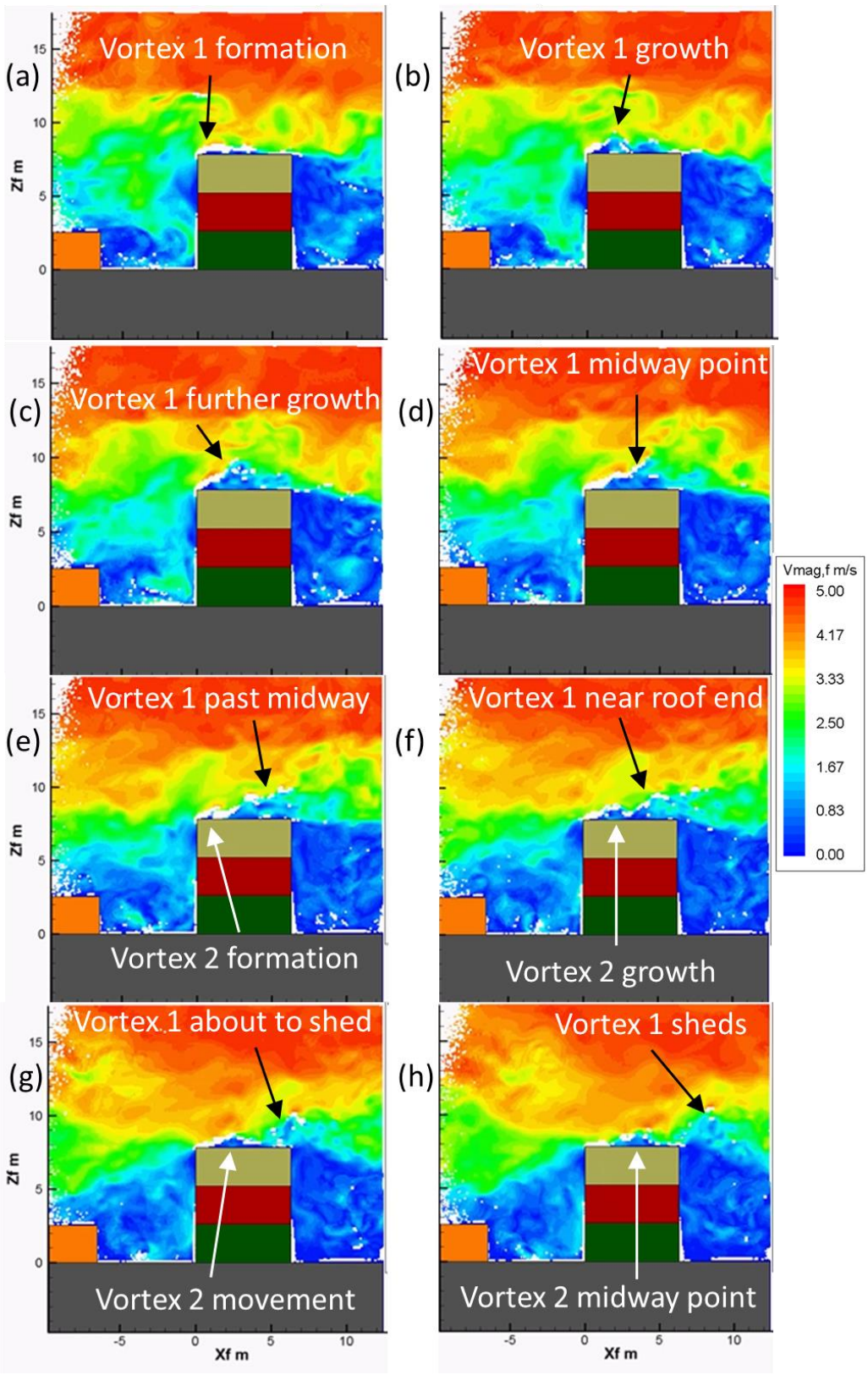

Figure 54 - Instantaneous sequential velocity measurements at 0.1 second intervals showing the cycle of two consecutive vortices formed at the leading edge of CONEX 11.4.

Further analysis of the PIV results shows streamlines, vorticity, and the along-wind and vertical velocity components in the region of interest. The streamlines in Time Frames C and E are shown in Figures 55 and 56, respectively. Note that the plots are not presented using the same color scale for velocity because Time Frame E is a faster wind case. The streamlines confirm the presence of a recirculation region in the canyon between the CONEX containers 10.4 and 11.4, which was indicated in the discussion of Figures 52 and 53.

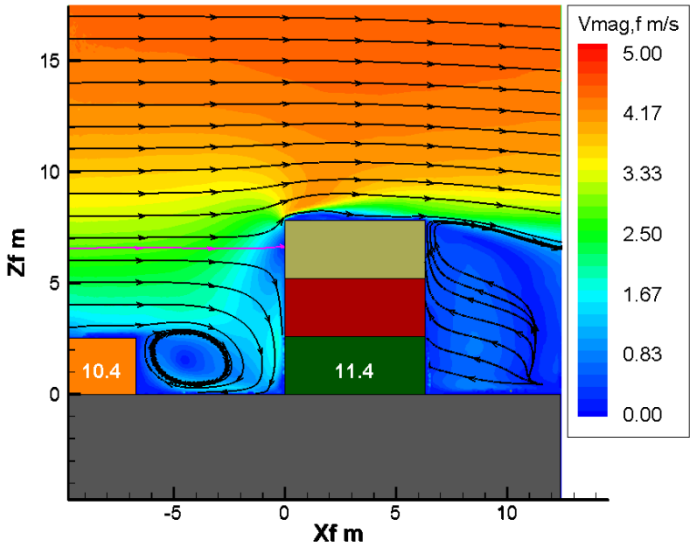

Figure 55 – Streamlines in the XZ plane in Time Frame C conditions.

The section of the approaching flow that recirculates in the canyon can be separated from the section that travels above CONEX 11.4 at the dividing streamline, present in Figures 55 and 56 slightly above the half-height line of the top CONEX (tan color) in the CONEX 11.4 assembly, at 6.59 m and 6.57 m AGL for Time Frames C and E, respectively, a negligible difference. The only major change between the two figures is the free-stream velocity (4.7 m/s and 6.2 m/s for Time Frames C and E, respectively), which indicates very little relation between free-stream velocity and height of the dividing streamline for the considered velocity interval.

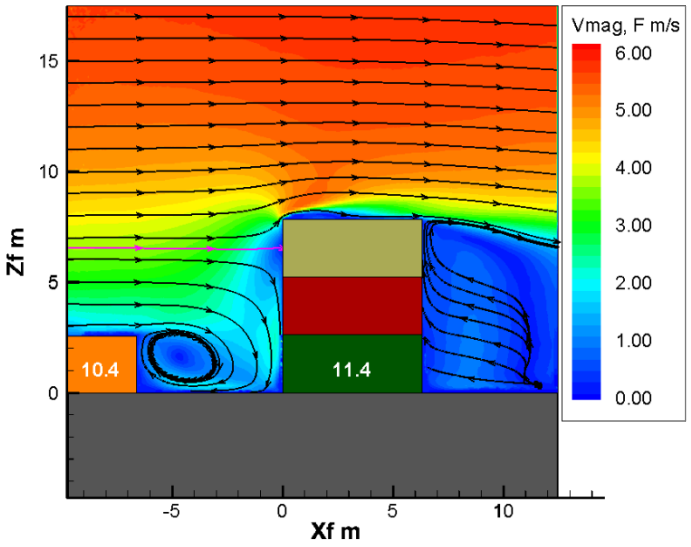

Figure 56 - Streamlines in the XZ plane in Time Frame E conditions.

The effect of the urban layout in the along-wind (u) and vertical (w) velocity components can be analyzed separately. Figures 57a and 57b show the average u and w components, respectively, for Time Frame C conditions, while Figures 58a and 58b are similar but for Time Frame E conditions. Figures 57 and 58 are not on the same color scale for velocity. Figures 57a and 58a show the presence of a fast reverse flow (towards negative x-direction) at ground level in the canyon between CONEX containers 10.4 and 11.4, which combines with the positive direction approaching flow that spills over to form the recirculation zone mentioned in the previous plots. The proximity of flow in different directions is also observed at rooftop level of CONEX 11.4, forming a moving recirculation zone as a consequence of the vortex shedding. Additionally, a reduction in horizontal velocity as the flow impinges onto CONEX 11.4 is also present, along with extremely low flow on the lee side of CONEX 11.4.

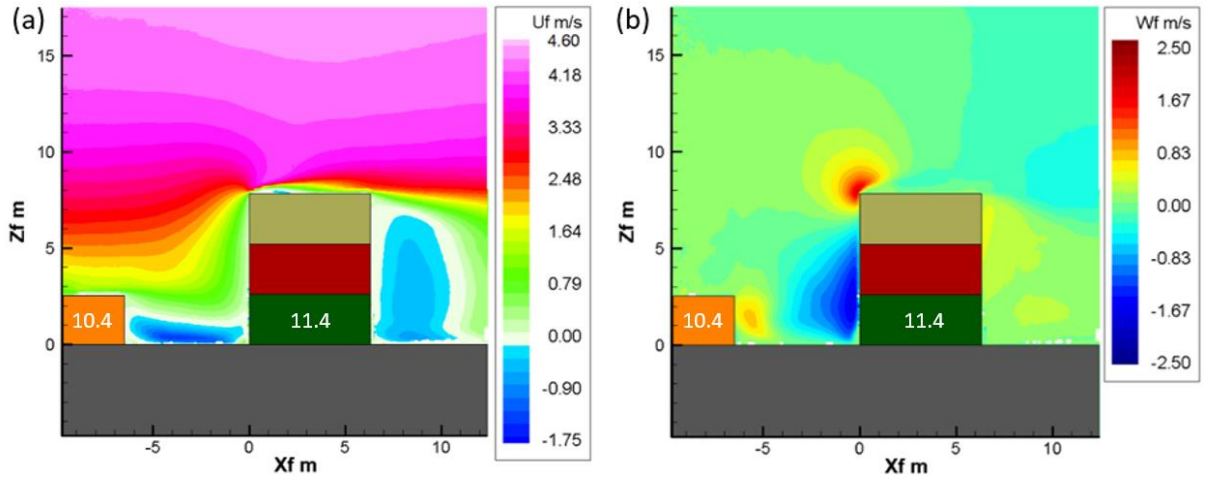

Figure 57 - Average (a) horizontal and (b) vertical velocity components in Time Frame C conditions.

Figures 57b and 58b show that the flow in the canyon region between CONEX containers 10.4 and 11.4 is split in the positive and negative directions, to either move up and around CONEX 11.4 or to recirculate in the canyon region, as it was already shown using the dividing streamline. Moreover, the vortex shedding on the leading edge of CONEX 11.4 is further demonstrated by the presence of a high upward flow over the top front edge of the tall CONEX. Plots in Figures 57 and 58 are consistent with a similar PIV result in an urban model (Sosnowski *et al.*, 2019).

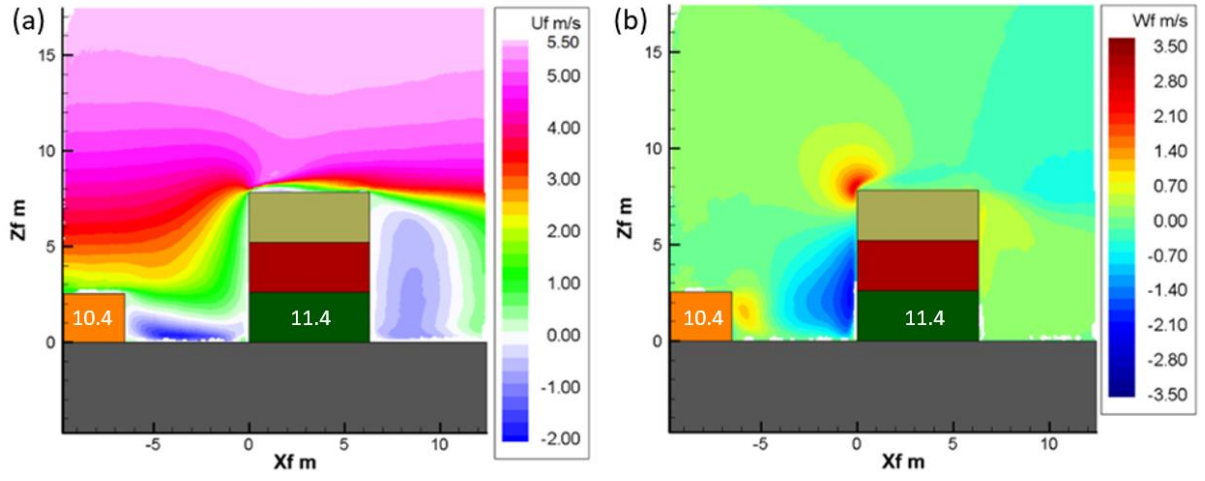

Figure 58 - Average (a) horizontal and (b) vertical velocity components in Time Frame E conditions.

Finally, the average vorticity (measured in s^{-1}) in the region around CONEX 11.4 is shown in Figures 59a and 59b for Time Frames C and E conditions, respectively. Figure 59 also clearly shows the recirculation region in the canyon between CONEX 10.4 and 11.4. A direct comparison of the vorticity profiles in Figure 59 shows a much stronger negative (clockwise) vorticity in the canyon region for Time Frame E conditions. Higher recirculation causes increased trapping of DTA contaminants at ground level, sustaining exposure risks for an extended time. The vortex shedding at the leading edge of CONEX 11.4 is also clearly shown, with higher rotation at the higher velocity (Time Frame E) case in Figure 59b.

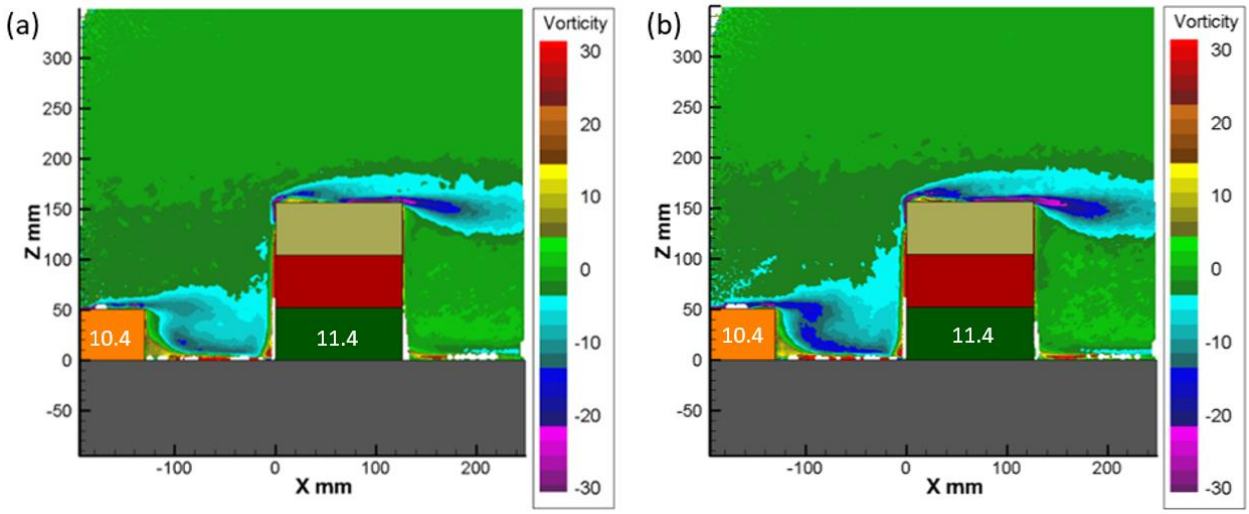

Figure 59 - Average vorticity (s^{-1}) in (a) Time Frame C and (b) Time Frame E conditions.

The shedding is a consequence of the interaction between the slower flow that is directed upward from the front face of CONEX 11.4 and the faster freestream approaching wind. The average vorticity plots are consistent with similar measurements taken with PIV in physical urban models (Paterna, 2015).

5.2.1.2 Velocity Measurements in the XY Plane

PIV measurements were taken in the area surrounding CONEX 11.4. For all figures in this section, the approaching wind enters the field of view from the bottom, moving in the

positive x-direction (upwards in the figures). Note that the horizontal axis shows the y-direction of the tunnel, with the positive direction pointing to the left of the image, in accordance with a normal right-handed coordinate system with the vertical (z) axis pointing up. For model containers that have a clear casting epoxy layer (as discussed in section 4.2.1.2), the corners of the clear layers interfered with the laser light, generating small shadow areas with low light intensity. Consequently, particles in these shadow areas were not adequately illuminated, and this led to no usable PIV data in those areas. There was no data collection in the areas upwind of CONEX containers 10.2, 11.2, 11.5, and 12.3 (zones in black in the figures in this section), as those containers were opaque (i.e., the laser light was not projected in the areas upwind of them).

Figure 60 shows the PIV results in the XY plane for Time Frame C conditions in the area around CONEX 11.4 at 1 m AGL. Figure 60a shows the average two-dimensional velocity magnitude in the XY plane, with the average velocity vectors displayed in Figure 60b. Figure 60c shows a close-up view of the average velocity magnitude around CONEX containers 11.3 and 11.4, with the corresponding average vectors displayed in Figure 60d. The relative direction of the approaching wind is shown in the lower left corner.

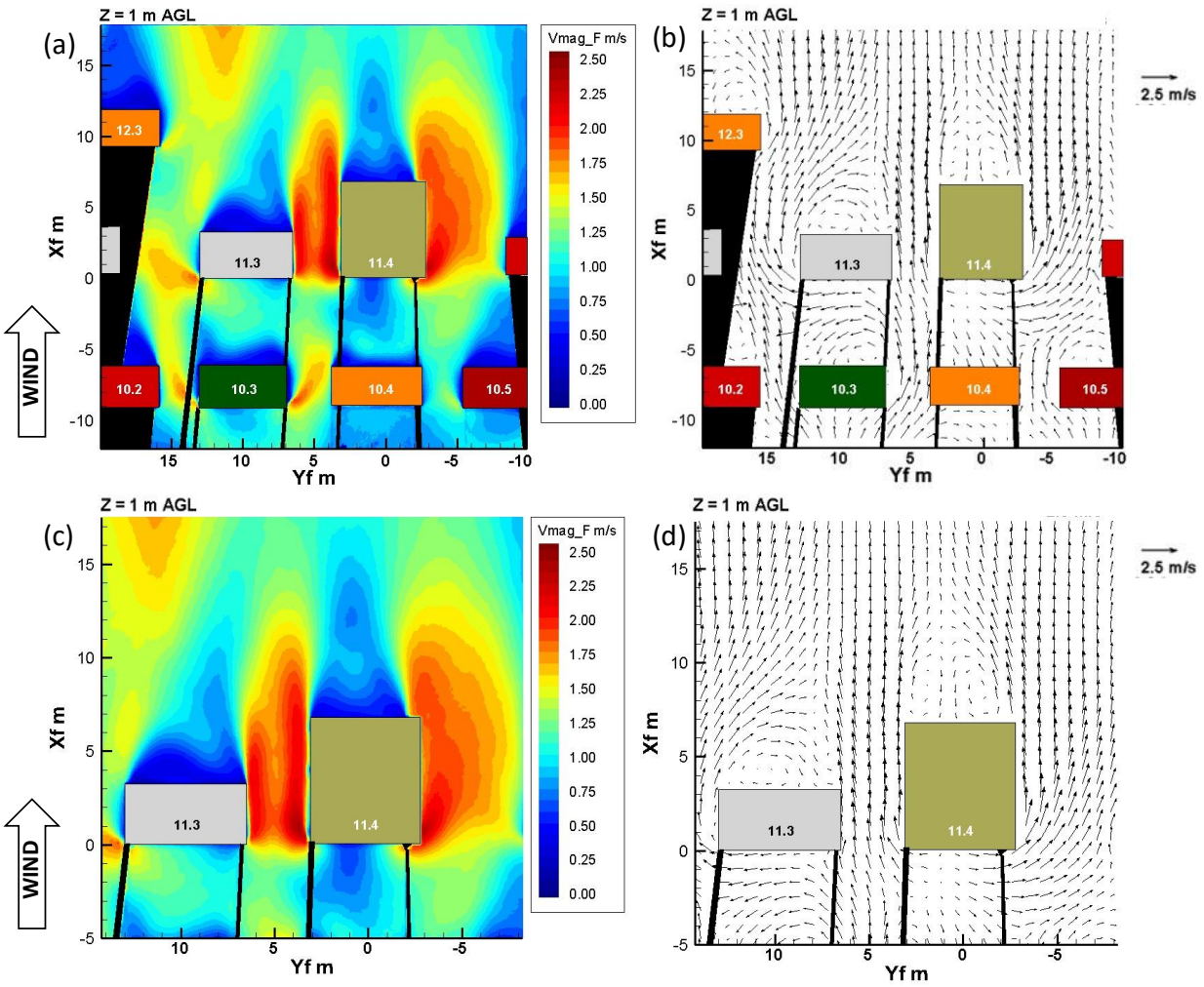

Figure 60 - PIV results in Time Frame C wind conditions. (a) Average velocity magnitude in the XY plane at 1 m AGL (b) Magnified plot of the average velocity magnitude in the XY plane around CONEX containers 11.3 and 11.4.

Figure 60 shows expected characteristics of the flow field, with slower recirculating flow on the lee side of CONEX containers, increased velocity in the channels between the containers, and strong lateral flow in the canyons between the rows. The difference in channel width on either side of CONEX 11.4 explains the different lateral extents of the high velocity zones along those channels, with a wider spread in the larger channel, to the right of tall CONEX 11.4 (between 11.4 and 11.5). The flow is higher beside CONEX 11.4 when compared to the other model buildings due to its size, three times taller than most CONEX containers. Sections of the flow that are below the dividing streamline travel downward and around the sides of CONEX

11.4, which increases the wind velocity in the channels beside the model building.

Figure 60c shows a close-up view of the average velocity magnitude around CONEX containers 11.3 and 11.4. On the lee side of CONEX 11.4, there are two (nearly) equal size, counter-rotating vortices, each originating from either side of the model building. A pair of counter-rotating vortices is also present immediately downwind of CONEX 11.3. However, in this case, the clockwise vortex is much wider than the counterclockwise one. The flow upwind of CONEX 11.3 (in the canyon between 10.3 and 11.3) is dominated by lateral motion to the left, towards the biggest channel (between CONEX containers 11.2 and 11.3) in lieu of the smaller channel (between 11.3 and 11.4). As this bigger flow parcel enters the channel between CONEX containers 11.2 and 11.3, vortex shedding along the left edge of CONEX 11.3 occurs, causing the recirculation region just downwind of the model building to be much wider than the recirculation present on the right side of CONEX 11.3.

Figure 60d also shows that the flow upwind of CONEX 11.4 (in the canyon between 10.4 and 11.4) moves slightly downward (i.e., in the negative x-direction). This result is consistent with the reversal observed in the results in the XZ plane shown in Figures 55 and 57a, as the parcel of fluid that arrives at CONEX 11.4 below the dividing streamline recirculates in the canyon.

Similar plots for Time Frame D conditions are shown in Figure 61. Figures 60 and 61 are not on the same color scale for velocity. The approaching wind in Time Frame D was oriented 7° clockwise relative to the pad, shown in the lower left of the image. Consequently, as shown in Figure 61a, the lateral motion is dominated by movement to the right (negative y-direction) in the figure. As a clear example, the average wind velocity on the channel to the right of CONEX 11.4 is much faster than the average flow in the left channel, due to the direction of the

approaching wind. Large areas of slow flow downwind of the model buildings (wakes) are observed, as expected.

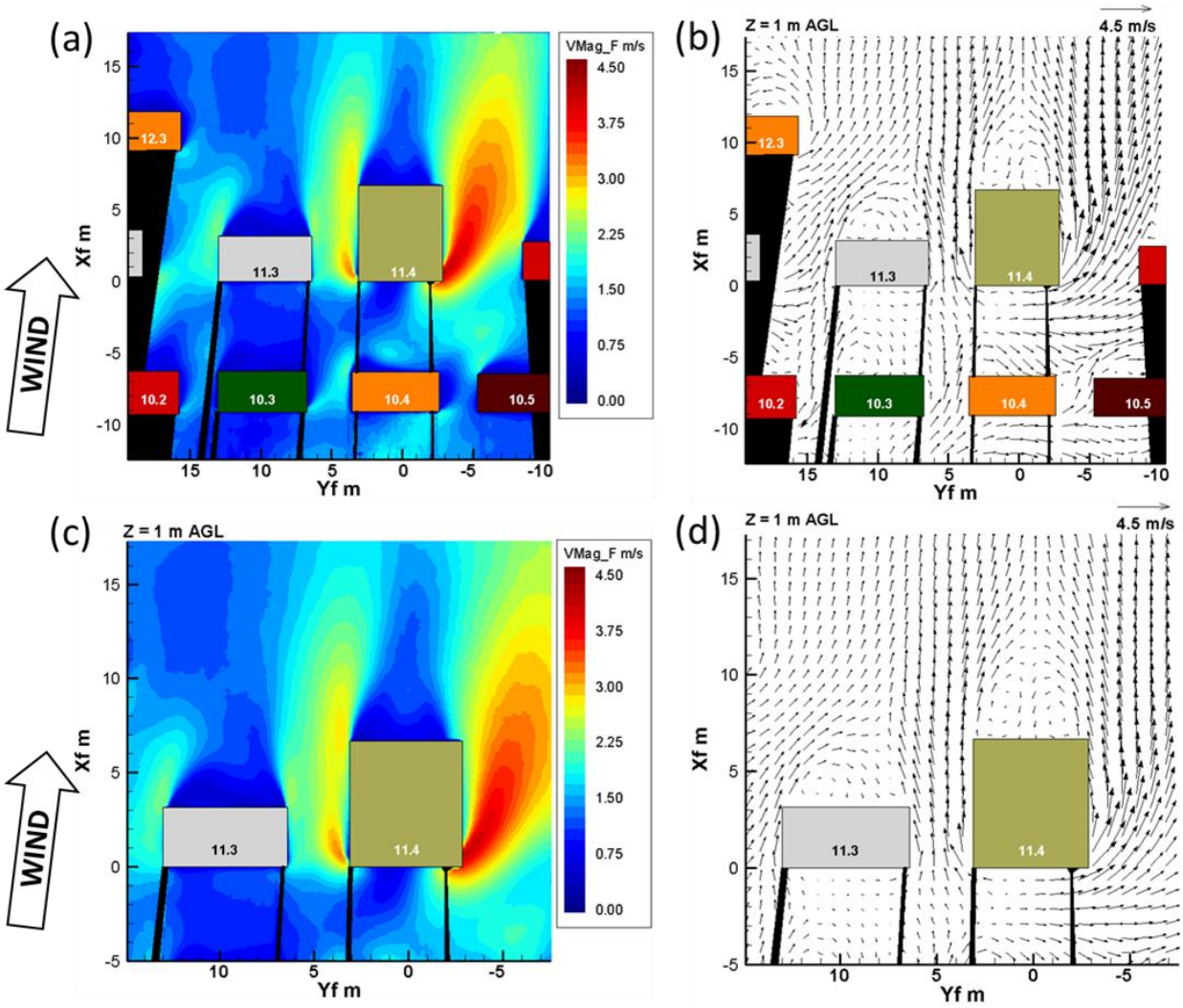

Figure 61 - PIV results in Time Frame D wind conditions. (a) Average velocity magnitude in the XY plane at 1 m AGL (b) Magnified plot of the average velocity magnitude in the XY plane around CONEX containers 11.3 and 11.4.

The dominant flow in the negative y-direction in Time Frame D conditions is also well observed in the canyons between the rows of CONEX containers (especially between CONEX contains 10.3 and 11.3). Figure 61c shows a close-up view of the average velocity magnitude around CONEX containers 11.3 and 11.4. Similar to the straight wind direction in Time Frame C, there is a pair of counter-rotating vortices on the lee side of CONEX 11.4. The approaching

wind direction creates an asymmetry in the vortex pair, as the clockwise vortex is now the bigger of the pair. The flow downwind of CONEX 11.3 is similar to the 0° angle, with the clockwise vortex dominating due to the different widths of the channels to either side of CONEX 11.3.

Figure 62 shows the average cross-wind velocity direction in Time Frame C conditions, with the approaching wind direction shown in the lower left corner. As shown in Figure 62, a slight majority of the approaching flow onto CONEX 11.4 is diverted to the right side (indicated by the yellow and orange color contours) into the channel between CONEX containers 11.4 and 11.5. The blue color contours in the lower left of CONEX 11.4 indicates the flow moving to the left into the narrower channel (between 11.3 and 11.4). This flow behavior is also attributed to the wider channel to the right of CONEX 11.4, when compared to the gap between CONEX containers 11.3 and 11.4 and contributes to the faster velocity mentioned in the discussion of Figure 60.

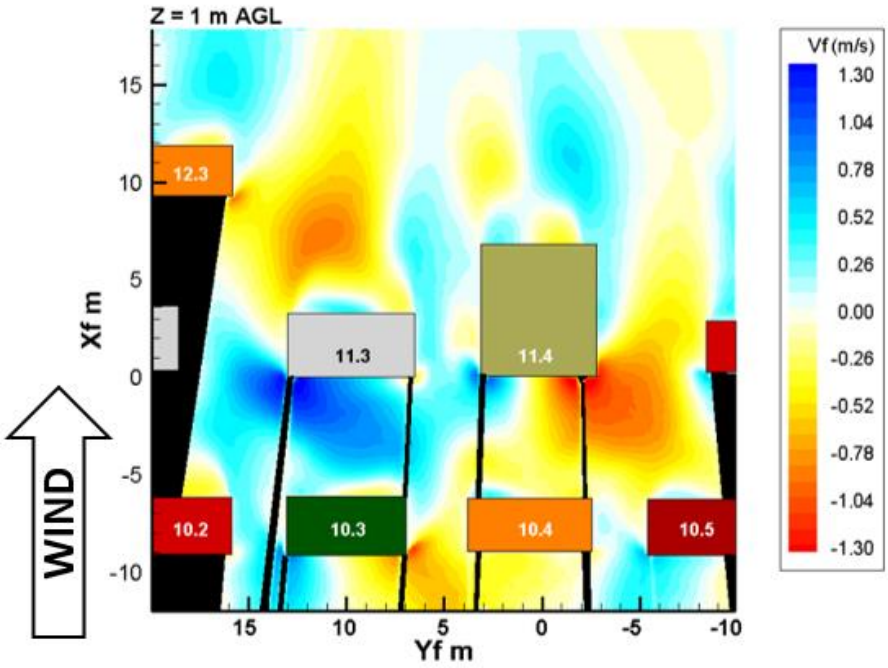

Figure 62 - Average cross-wind velocity component at 1 m AGL in Time Frame C conditions.

The flow pattern in the wake of CONEX 11.4 shows that the counterclockwise vortex is slightly more dominant, an effect also attributed to the wider channel. Analysis of the flow pattern around CONEX 11.3 reaffirms the results presented in the discussion of Figure 60. Figure 62 shows an average dominant positive flow in the cross-wind direction in front of CONEX 11.3, as it moves to the wider gap to the left of the model building. The flow reverses direction after passing by CONEX 11.3, generating the wider vortex in the counter-rotating pair present downwind of the model building. Counter-rotating vortices are a major concern in the case of a release of a DTA gas, as the vortices increase the residence time of the contaminant and, therefore, the concentration is elevated in the region between the vortices. Furthermore, the mean wind velocity in this thin region is extremely low, which suppresses the dispersion of the gas and maintains the risk of exposure for a longer time.

Figure 63 shows the average cross-wind velocity direction in Time Frame D conditions. Figures 62 and 63 are not on the same color scale. High intensity lateral flow to the right is observed mainly at the right front edge of CONEX 11.4 as a combined effect of the direction of the approaching wind and the wider channel to the right of the model building, which directs more flow to the right of the building. Average cross-wind velocities in the positive y-direction are uncommon, being only present at the front left edge of CONEX containers 11.3 and 11.4 and in the wake of CONEX containers 11.3, 11.4, and 12.3, as the flow leaves the MUE back onto unobstructed terrain.

Finally, the inclined wind direction of Time Frame D redirects the flow in the canyon between rows 10 and 11 to the right. Contrary to what Figure 61 indicated for a direct wind direction case, for this case of 7° approach wind, the flow in the canyon between CONEX containers 10.3 and 11.3 is no longer dominated by a strong positive direction cross-wind

component.

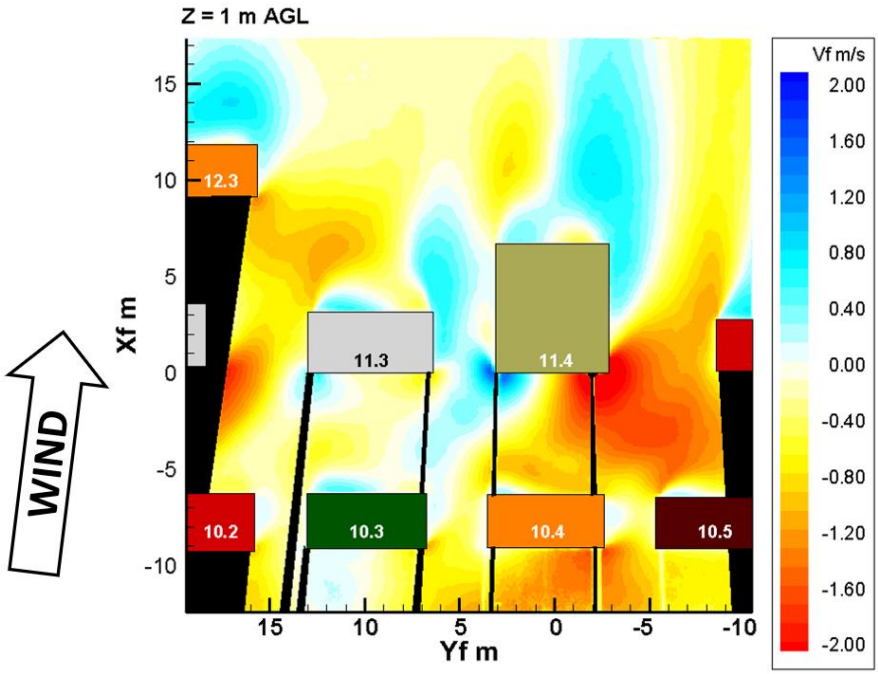

Figure 63 - Average cross-wind velocity component at 1 m AGL in Time Frame D conditions.

Similar to what was done with PIV results in the XZ plane, velocity data can be extracted from the PIV results in the XY plane at the locations of the sonic anemometers placed near CONEX 11.4. Hence, extracting the pointwise data allows for comparisons between PIV data and data obtained during the JRII-S field test but can also be used to compare velocities obtained via the LDV and PIV techniques. Figure 64b shows the velocity vectors in the XY plane for the JRII-S field test (blue vectors) and wind tunnel measurements using the LDV (orange) and PIV (green) techniques. The crosses in Figure 64a indicate the locations of the sonic anemometers (S61L1, S71, S72, S74, S75, S81, S82L1, S83, S101, and S111) at 1 m AGL around CONEX 11.4.

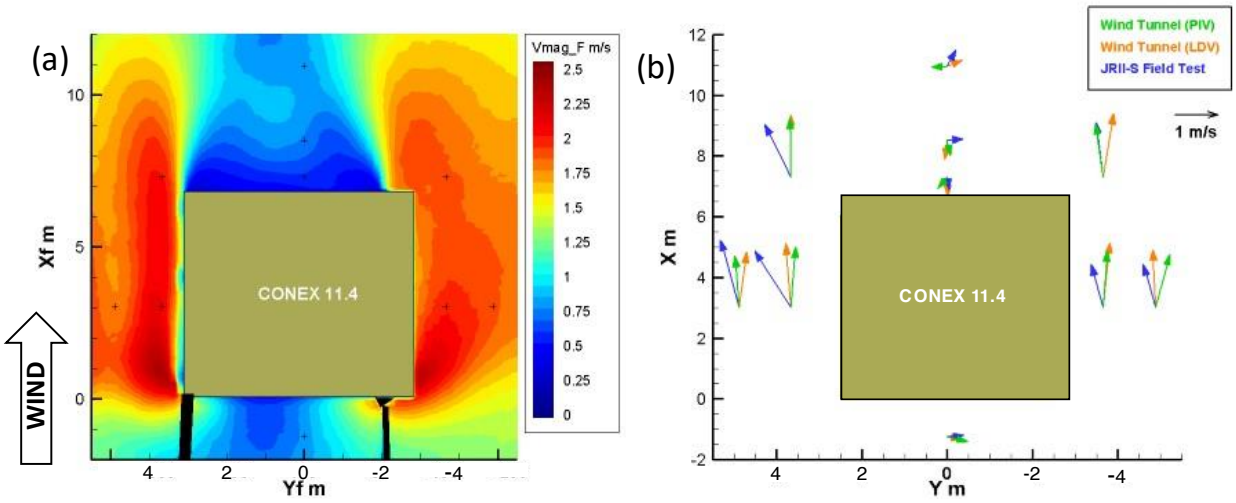

Figure 64 - (a) Sonic Anemometers locations around CONEX 11.4 are marked by the crosses (b) Extracted velocity vectors at the Sonic Anemometer locations around CONEX 11.4 at 1 m AGL.

Figure 64 shows close results between field measurements and the two techniques applied in the wind tunnel model, with extremely close velocity magnitudes and slightly different velocity directions considering all sonic anemometers. Disagreements in the wind direction are present at the three centerline sonic anemometers in the wake of CONEX 11.4 (S82L1, S101, and S111). As shown previously, a pair of slow, counter-rotating vortices is present in this area, causing significant changes in instantaneous measurements of velocity within the wake area. Flow measurements fluctuate between relatively small positive and negative values, yielding a near-zero velocity average. The disagreement in wind direction at S61L1 (in front of CONEX 11.4) as measured by PIV is also attributed to high wind direction variability with a near-zero average flow, as in this section the flow splits to go to either side of CONEX 11.4. High wind direction variability in the channels explains the slight disagreement shown at sonic anemometer locations S71, S72, S74, S75 (located beside CONEX 11.4, at Xf = 3 m); S81, and S83 (located to the downwind diagonals of CONEX 11.4, at Xf = 7.3 m). Extracted numerical velocity values in the locations of the Sonic Anemometers are shown in Appendix H1.

The average vorticity in that section of the MUE is shown in Figure 65, with Time Frame C conditions shown in Figure 65a and Time Frame D conditions shown in Figure 65b. Once again, the PIV results show the similarity of the counter-rotating vortices present in the wake of CONEX 11.4; and the major difference in magnitude in the vortices located downwind of CONEX 11.3 in both wind cases. Figure 65a also shows asymmetric vortices downwind of CONEX containers 10.3 and 10.4.

Differences in the rotation of fluid elements across the different Time Frames are attributed to a combined effect of the higher velocity of Time Frame D and the different directions of the approaching wind. These factors cause a strengthening of the rotation intensities of the negative (clockwise) vortices and suppress the intensities of the positive (counterclockwise) vortices. The difference in wind magnitude and direction is enough to balance the counter-rotating vortices downwind of CONEX 10.3 and to noticeably enhance the vorticity in the channels on either side of CONEX 11.4 in Time Frame D.

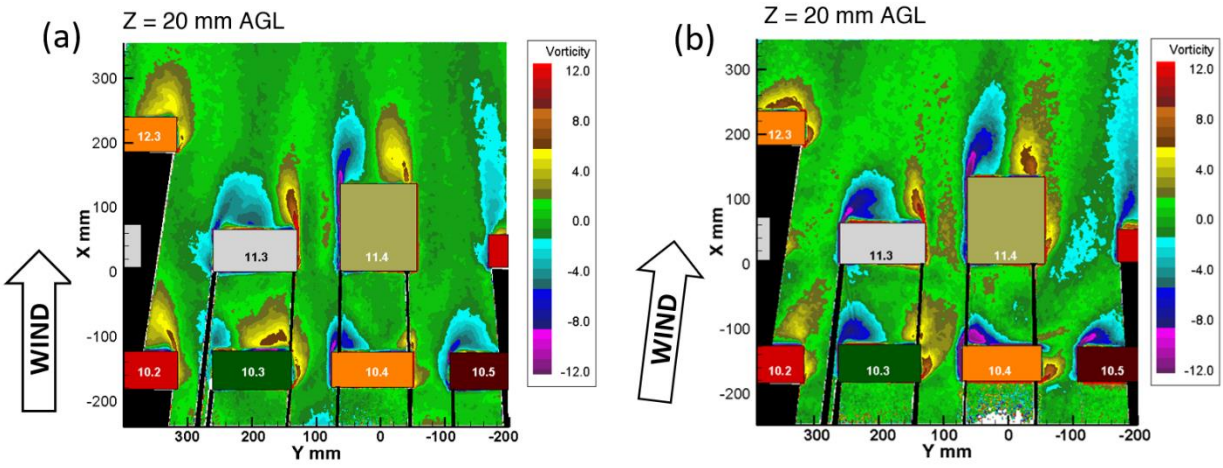

Figure 65 - Average vorticity (s^{-1}) in (a) Time Frame C and (b) Time Frame D conditions.

PIV results in a horizontal plane can be compared to CFD simulations found in the literature (Carissimo, Trini Castelli, & Tinarelli, 2021). Comparisons between PIV and computational data will focus on the CS model because it was deemed by the authors of the

paper that it agreed better with the sonic anemometers data from the JRII-S field test. The comparison between simulation and PIV in Time Frame C conditions is shown in Figure 66. The velocity data shown in Figure 66a was previously published (Carissimo, Trini Castelli, & Tinarelli, 2021), but a different color scheme has been used here to better visualize the extent of the velocity data. Access to the CS simulation results was granted by the first author (Carissimo, personal communication, May 18, 2022), and the data for the entire MUE is reproduced in Figure 66a. Figure 66b shows an enhanced, close-up view of the simulations, focusing on the centerline of the pad between rows 10 and 12. Figure 66c shows the average velocity in the XY plane as measured by the PIV technique in the MUE model located in the CHRC Wind Tunnel. Figure 66c is the same as Figure 60a but with a different color scheme. Figures 66b and 66c show the same field of view.

Comparison between the CS simulation results done by Carissimo and the PIV results indicates some large differences for Time Frame C (direct approach wind) conditions. The simulation overestimates the velocity in the gap between CONEX containers 11.4 and 11.5 by approximately 40%. Additionally, the extent of the high velocity area in the channel on the right side of CONEX 11.4 persists for much longer downwind in the CS simulation compared to the PIV measurements, being about 70% faster as this section of the flow leaves the field of view. The simulation also slightly overpredicts the velocity in the channel to the left of CONEX 11.4 by around 20%. The flow along the channel in the simulation seems to be the result of the shedding of flow around the front left edge of CONEX 11.4 only, while the PIV results show two parallel high velocity sections, each originating from the inner edges of CONEX containers 11.3 and 11.4.

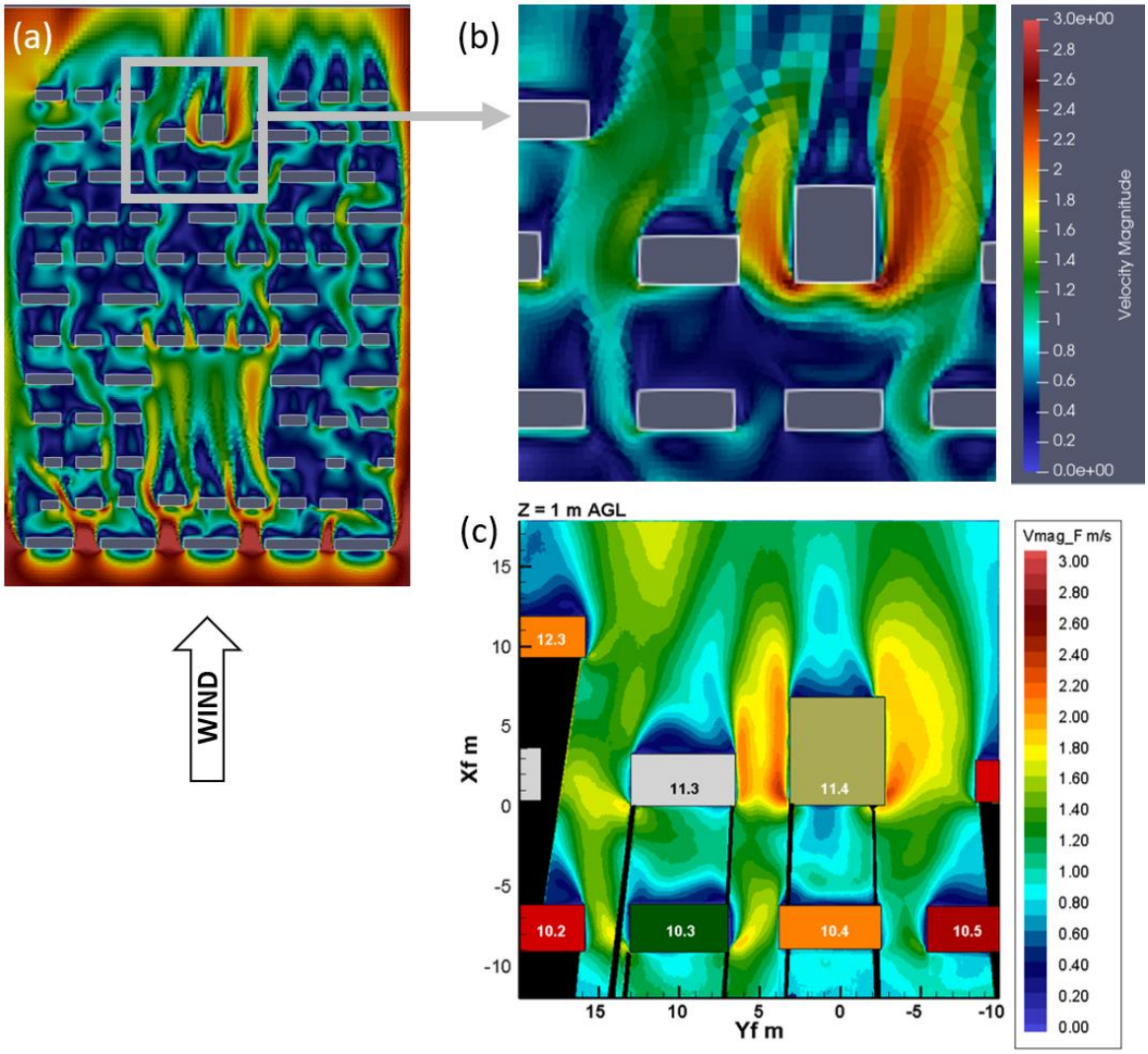

Figure 66 - (a) CS simulation of the flow in the MUE performed by Carissimo. (b) Enlarged detail of the simulation around CONEX 11.4. (c) PIV measurements of the average velocity magnitude in the XY plane at 1 m AGL in Time Frame C conditions.

The simulation underpredicts the flow on the channels beside CONEX 10.3 by approximately 55% and 30% on the right and left channels, respectively. The velocity in the canyon between CONEX containers 10.3 and 11.3 is underpredicted by about 60% and in the wake of CONEX 11.4 by around 50%. The flow on the left channel and immediately downwind of CONEX 11.3 are similar in the simulation and PIV. Other differences are observed upwind of row 10.

The comparison between CS simulation and PIV in Time Frame D conditions is shown in

Figure 67. The velocity data shown in Figure 67a was previously published (Carissimo, Trini Castelli, & Tinarelli, 2021), but a different color scheme has been used here to better visualize the extent of the velocity data. Access to the CS simulation results was granted by the first author (Carissimo, personal communication, March 3, 2023), and the data for the entire MUE is reproduced in Figure 67a. Figure 67b shows a close-up view of the simulations, focusing on the centerline of the pad between rows 10 and 12. Figure 67c shows the average velocity in the XY plane as measured by the PIV technique in the MUE model located in the CHRC Wind Tunnel. Figure 67c is the same as Figure 61a but using a different color scheme. Figures 67b and 67c show the same field of view.

In Time Frame D conditions, the computational and PIV measurements in the physical model are much closer. The extent of the high velocity zones on either side of CONEX 11.4 is approximately equal. The simulation predicts the velocity magnitudes along these channels well, with a slight underprediction (around 10%) in the channel between CONEX containers 11.4 and 11.5; and a slight overprediction (around 7%) in the channel between CONEX containers 11.3 and 11.4. The simulation also provides a good approximation for the flow velocity in the channel between CONEX containers 11.2 and 11.3, but the higher speed flow (dark green contours) persists further downwind in the simulation than was observed in the PIV results.

However, several sections of the computer simulation performed by Carissimo underpredict the wind velocity. Noticeable differences are observed between CONEX containers 10.4, 10.5, 11.4, and 11.5, slower by around 30% in the simulation. In the wake of CONEX 11.4, the simulation underpredicts the velocity by around 60%. In the far wake of CONEX 11.3 (past row 12), the CS simulation underpredicted the velocity by approximately 60%. Other differences are observed upwind of row 10 and in the wake of CONEX 12.3.

Carissimo and peers had identified that the approaching wind velocity agreement of their computational models was satisfactory. However, the authors were not confident in their turbulence agreement within the urban array, recognizing that the models used needed improvements in order to describe more accurately the flow between the containers. The PIV measurements taken in a valid model of the JRII-S Field Test presented int his work can improve the inputs of further computational studies, improving the flow simulation within the urban model.

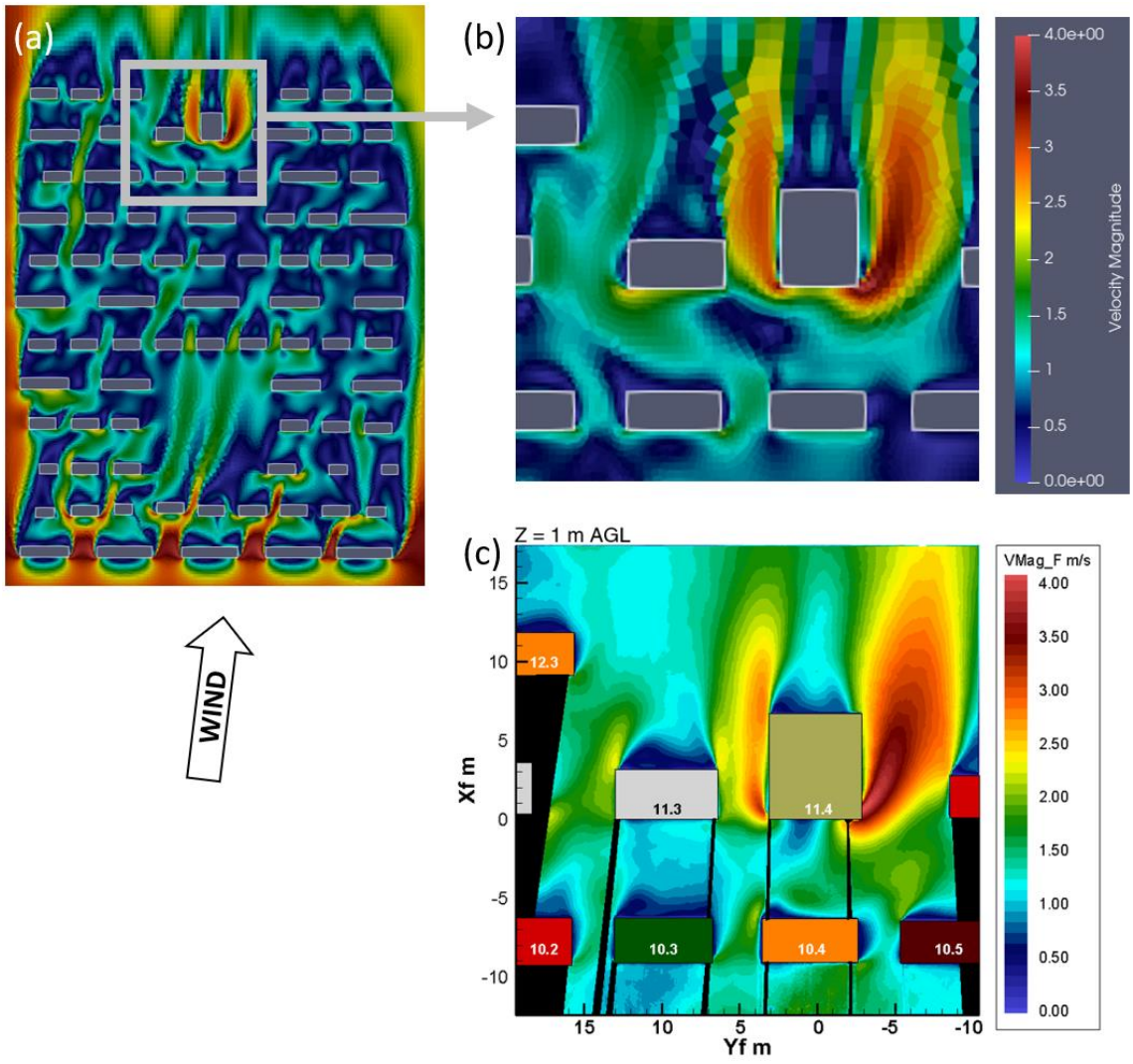

Figure 67 - (a) CS simulation of the flow in the MUE performed by Carissimo. (b) Enlarged detail of the simulation around CONEX 11.4. (c) PIV measurements of the average velocity magnitude in the XY plane at 1 m AGL in Time Frame D conditions.

5.2.2 Modeling the JR-II Field Test

Results of the simulation of the JR-II field test are shown in this section. The results in the XZ plane (vertical laser sheet) include simulations of Trials 2 and 4. The results in the XY plane include simulations of Trial 4 only. This section focuses on the effects of DTA releases in the urban flow field. Different flow properties are evaluated, comparing pre-release conditions with release situations.

In the plots of average velocity in the XZ plane with streamlines, all the streamlines in black are equally spaced at 1 m apart. The dividing streamline is shown separately in pink. The white line marks the height at which the dividing streamline hits CONEX 11.4 in the pre-release case and is placed in the height AGL along the same figure for reference.

Analysis of the seeded releases shows the average time interval after the release that the front edge of the simulated chlorine cloud arrives at CONEX 11.4, which is referred to as the steady state phase of the release (initial fraction of the gas release, with maximum chlorine concentration). After a few more seconds, the flow is dominated by secondary pockets of less dense gas that either entrained upwind shortly after the release or were trapped in urban canyons located between rows of the MUE.

Figure 68 shows PIV images in Trial 2 conditions as an example. Figure 68a shows the flow just before the time of arrival at CONEX 11.4, with fog wisps near the tall building, slightly ahead of the front edge of the released cloud. The start of the steady state phase is defined by the arrival of the front edge of the cloud at CONEX 11.4, as shown in Figure 68b. The duration of the steady state phase was determined by the release durations (4.54 sec and 3.96 sec in Trials 2 and 4, respectively), adding 0.5 sec in Trial 2 (faster wind condition) for cloud stretching effects. Figure 68c shows a representative capture of the flow during the steady state phase, with occasional fog wisps at higher locations. Figure 68d shows a typical state of the seeded release in

the post steady state phase, with the majority of the flow at ground level.

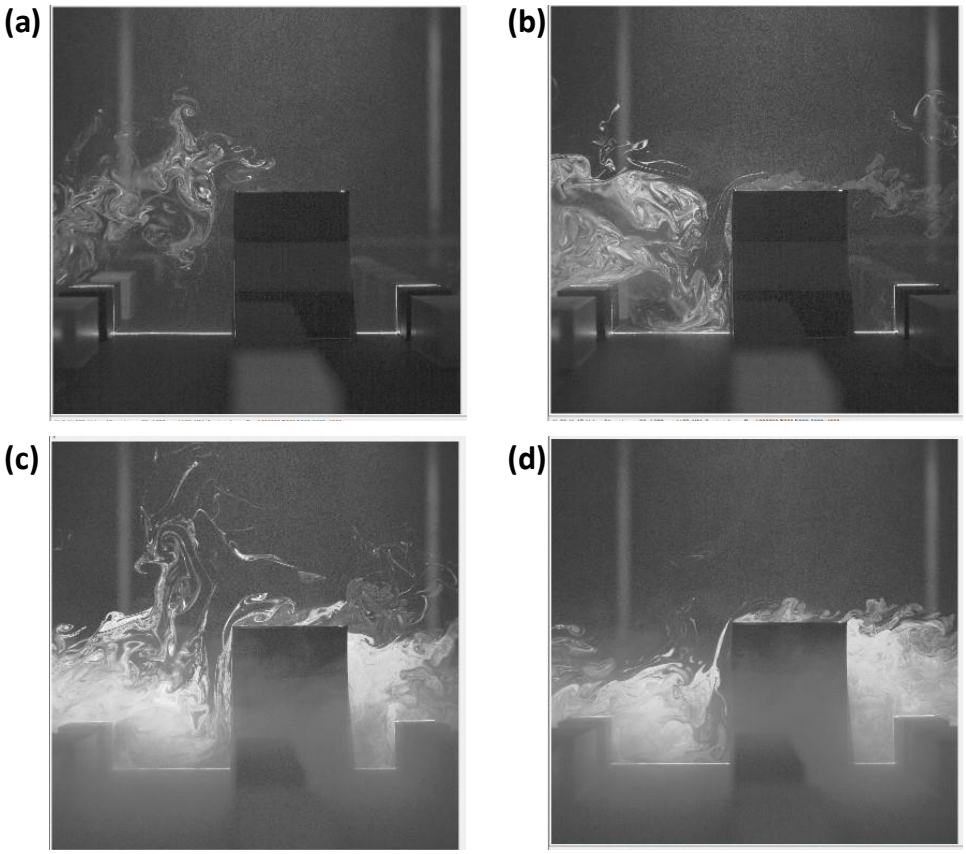

Figure 68 – PIV capture images of seeded releases in Trial 2 conditions at CONEX 11.4 (a) Just before the arrival, (b) time of arrival, (c) end of the steady state phase, (d) post steady state phase.

The times of arrival and departure of the steady state phase of the release in both wind conditions are summarized in Table 6.

Table 6 – Time intervals after the release for the arrival and departure of the steady state phase of the release at CONEX 11.4, as obtained from the seeded simulated chlorine releases.

JR-II Condition	Time of Arrival of Simulated Cl_2 cloud		Duration of the Release		Time of Departure of Simulated Cl_2 cloud	
	Tunnel Scale	Field Scale	Tunnel Scale	Field Scale	Tunnel Scale	Field Scale
Trial 2	3.0 sec	21.2 sec	4.54 sec	30.0 sec	8.0 sec	56.6 sec
Trial 4	4.0 sec	28.3 sec	3.96 sec	25.9 sec	8.0 sec	56.6 sec

5.2.2.1 Velocity Measurements in the XZ plane

Simulations of Trials 2 and 4 from JR-II were conducted in this PIV setup with a vertical laser sheet in the XZ plane along the centerline of the MUE model. The chlorine releases were simulated using a mixture of 304 L/min of air, 76 L/min of SF_6, and 300 L/min of CO_2, for a total of 680 L/min. The free stream velocity in the field tests was 2.80 m/s for Trial 4 and 6.50 m/s for Trial 2. In both cases, the simulation took place with a 0° relative wind direction relative to the pad instead of the measured wind directions during the JR-II Field Test (9° and 22° for Trials 2 and 4, respectively) in order to minimize through-sheet particle motion and optimize the PIV input images.

5.2.2.1.1 Trial 2 Simulations

The effect of the release on the overall velocity field can be evaluated. Figure 69 shows the average velocity magnitude, with the pre-release case (before the DTA cloud arrives) shown in Figure 69a and the DTA release (steady state) case shown in Figure 69b.

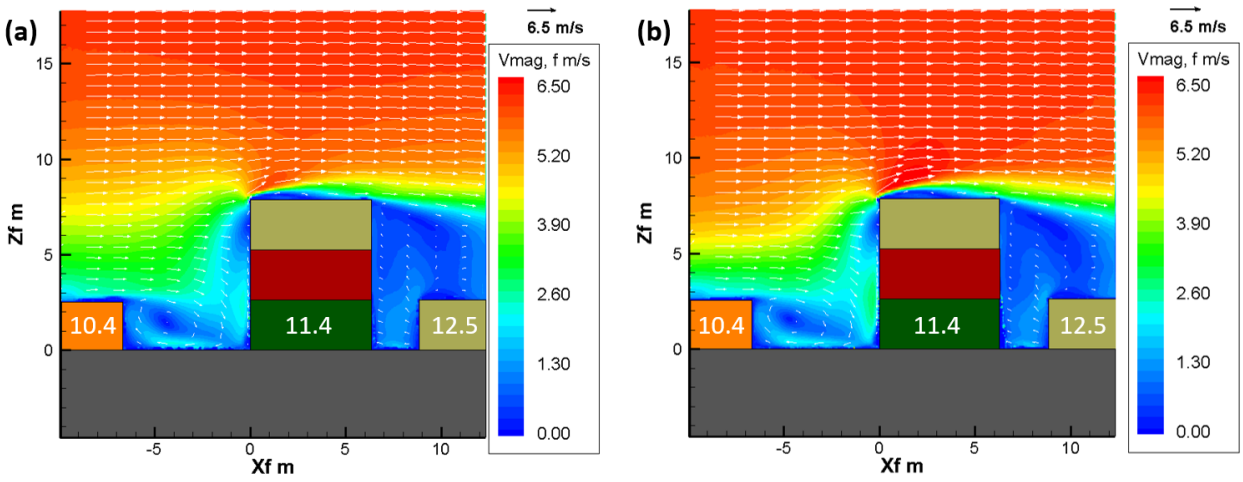

Figure 69 - Average velocity magnitude in the XZ plane in Trial 2 conditions for (a) Pre-Release and (b) Simulated chlorine release.

Two main differences can be observed. Mainly, the flow just upwind of CONEX 11.4 at lower level (Zf < 4 m) is faster in the release case, indicating a major change in velocity due to

the presence of the DTA release. Additionally, the flow in the free stream region above the front half of CONEX 11.4 is significantly faster in the release case. Extraction of velocity data in this region shows that the velocity in the release case increases by around 12% when compared to pre-release. Comparison between the figures also shows a shift of mid-high velocity values (yellow and orange contours) downward in the release case.

The effects of the release on the height of the dividing streamline can also be studied. Figure 70 compares streamlines in pre-release (Figure 70a) and release (Figure 70b) situations. Figure 70 shows a minimal effect of the release on the height of the dividing streamline. The height variation is negligible, moving from 6.53 m in the pre-release case to 6.6 m during the steady state phase of the release. It is important to note that this negligible difference in the height of the dividing streamline occurred in the faster wind conditions characteristic of Trial 2. The average velocity plots in Figures 69 and 70 show flow patterns that are consistent with PIV studies taken in previous urban models. Plots of the along-wind and vertical velocity components are shown in Appendix H2.

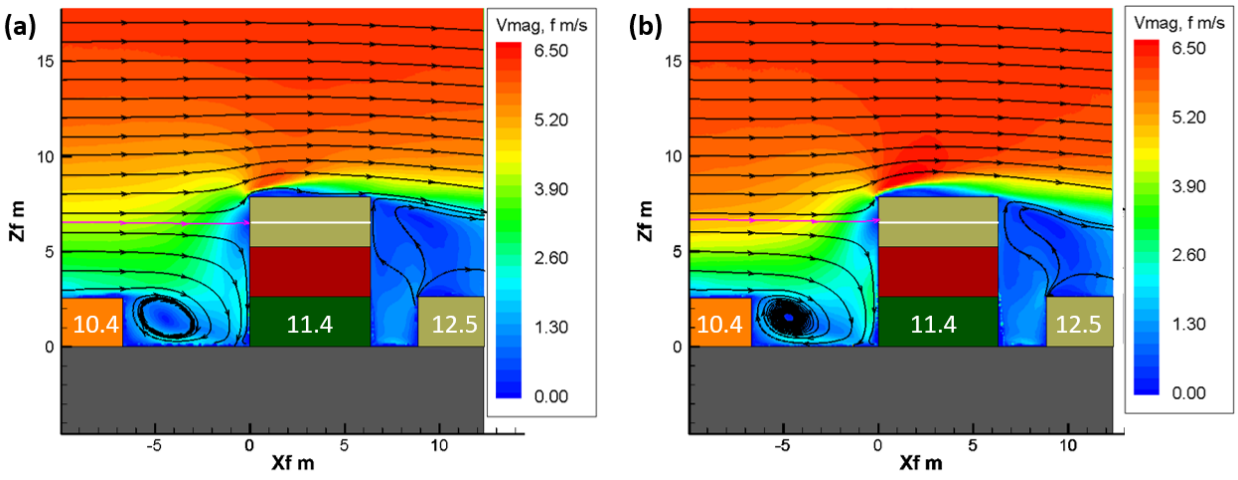

Figure 70 - Streamlines in the XZ plane in Trial 2 conditions for (a) Pre-Release and (b) Simulated chlorine release.

The effect of the release on the vorticity around CONEX 11.4 can also be studied. Figure

71 contrasts the average vorticity in the pre-release (Figure 71a) and release (Figure 71b) cases. As a direct consequence of the added momentum of the release, greater fluid element rotation is observed in the region above CONEX 10.4, but very little changes in the canyon between CONEX containers 10.4 and 11.4. Figure 71b also shows an increase in vorticity at the rooftop of CONEX 11.4, which indicates the release increases the vortex shedding from the leading edge of the mock building. Minor differences can also be observed on the lee side of CONEX 11.4.

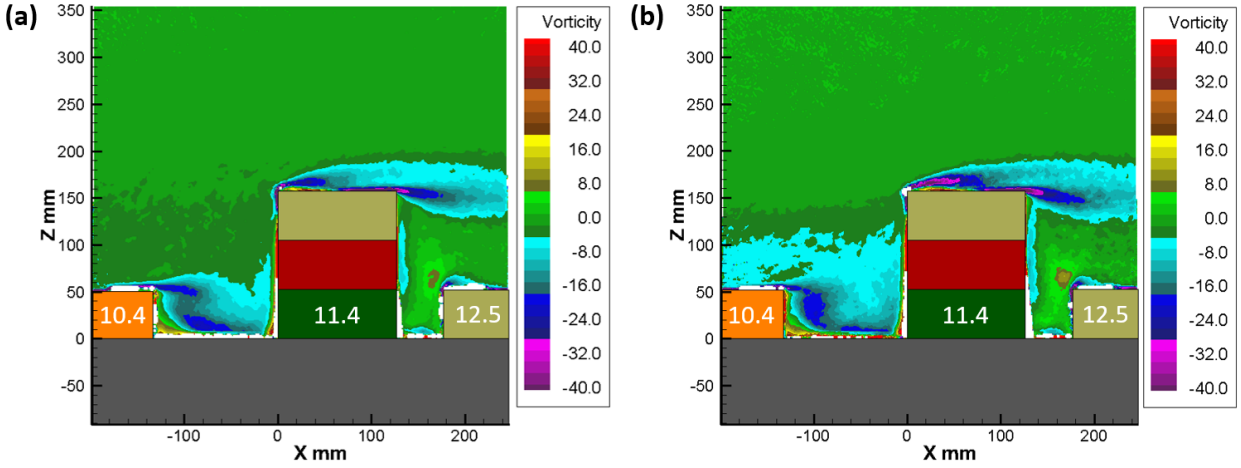

Figure 71 - Average vorticity (s^{-1}) in the XZ plane in Trial 2 conditions for (a) Pre-Release and (b) Simulated chlorine release.

Figure 72c shows the average velocity magnitude after the steady state stage of the release. For comparison, the average velocity in the pre-release and during the steady state phase of the release are shown in Figures 72a and Figure 72b, respectively. In general, the average velocity magnitude after the steady state stage is very similar to the average velocity during the steady state phase of the release. Some of the differences are observed at lower heights, with significant velocity increase just upwind of CONEX 11.4 (green contour). The circulation region in the canyon also changes, with a lower velocity (darker blue) center being well-defined. Little change is observed in the velocities above CONEX 11.4, which are nearly identical to the velocities in the steady state release case. Plots of the along-wind and vertical velocity

components after the steady state phase can be viewed in Appendix H3. The gas after the steady state stage is less dense and has much lower momentum than the gas in the steady state phase of the release, but it has not yet returned to the characteristics of the pre-release stage. After the steady state phase, the flow of the chlorine simulant cloud is no longer dominated by the momentum of the release, being dominated instead by the atmospheric momentum.

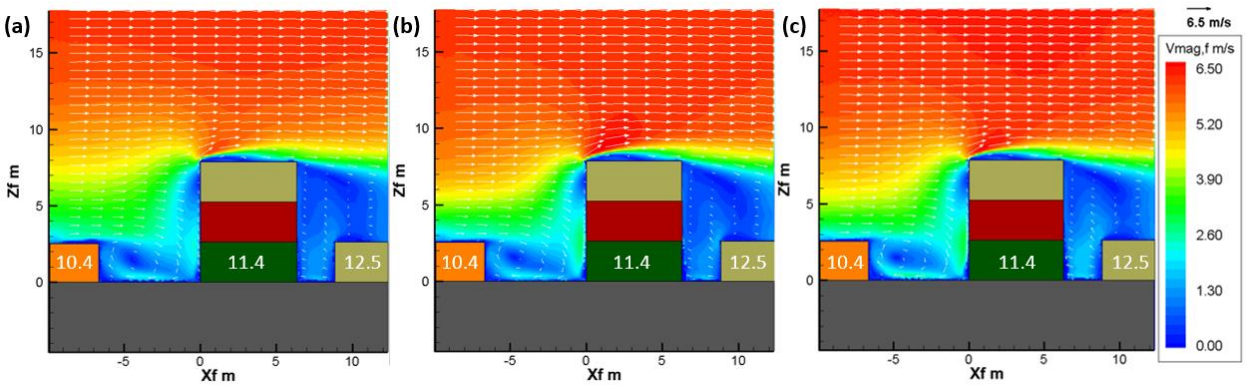

Figure 72 - Average velocity magnitude in the XZ plane in Trial 2 conditions for (a) Pre-Release, (b) Steady state phase and (c) After the steady state phase of the simulated chlorine release.

Figure 73c shows streamlines, with the dividing streamline shown in pink after the steady state phase of the release. The streamlines in the pre-release (Figure 73a) and during the steady state phase (Figure 73b) of the release are shown for comparison. As observed during the steady state stage of the release, the change in height of the dividing streamline is negligible. The height of the dividing streamline was measured at 6.52 m after the steady state stage, versus 6.53 m in the pre-release case and 6.6 m during the steady state phase.

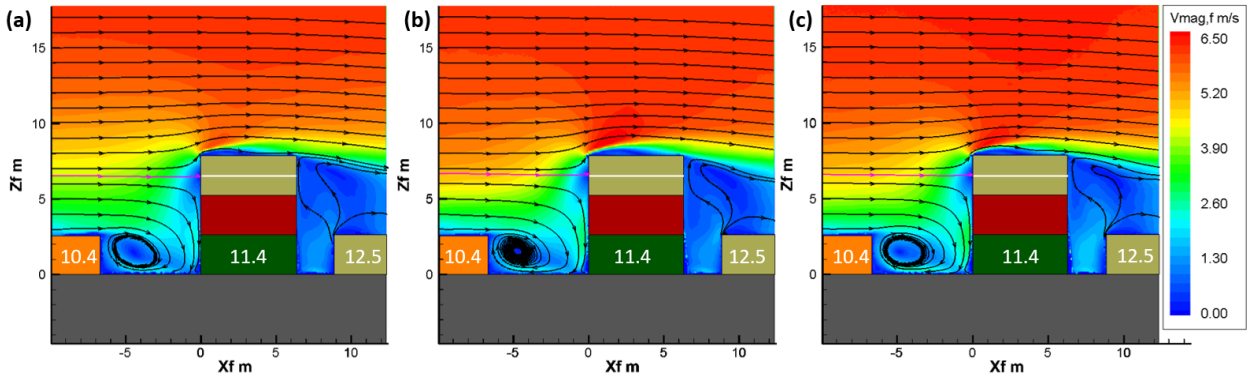

Figure 73 - Streamlines in the XZ plane in Trial 2 conditions for (a) Pre-Release, (b) Steady state phase and (c) After the steady state phase of the simulated chlorine release.

The average vorticity in the region after the steady state phase of the release is shown in Figure 74c. For comparison, the vorticity in the pre-release and during the steady state phase of the release are shown in Figures 74a and Figure 74b, respectively. A significant increase in the vorticity in the canyon is observed, including a center with extremely high vorticity values ($\omega \approx -40\ s^{-1}$), approximately located at the same place as the darker blue center identified in Figure 72c. The remaining vorticity field is similar to what was observed during the steady state phase of the release.

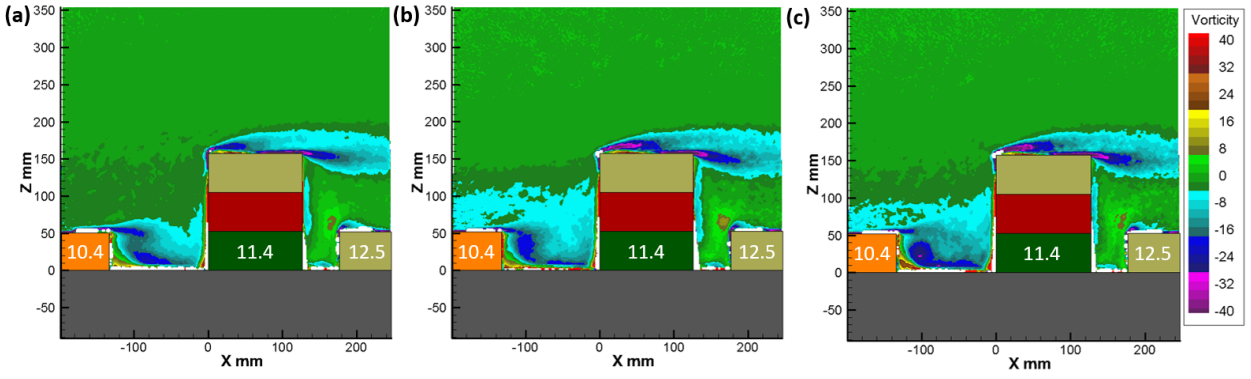

Figure 74 - Average vorticity (s^{-1}) in the XZ plane in Trial 2 conditions for (a) Pre-Release, (b) Steady state phase and (c) After the steady state phase of the simulated chlorine release.

The results shown in this section indicate that the additional momentum from the chlorine release has very little impact on the flow in JR-II Trial 2 conditions, characterized by a relatively high atmospheric momentum. Differences between during and after the steady state phases of the

release are observed only at ground level, which happens because the final phase (after the steady state) is primarily consisted of flow traveling close to the ground, moving downwind by clearing the urban environment. The flow at taller heights after the steady state phase has a significantly lower density, insufficient to affect the release.

5.2.2.1.2 Trial 4 Simulations

Average velocity magnitudes in JR-II Trial 4 conditions are shown in Figure 75. The pre-release case is shown in Figure 75a and the DTA release case is shown in Figure 75b.

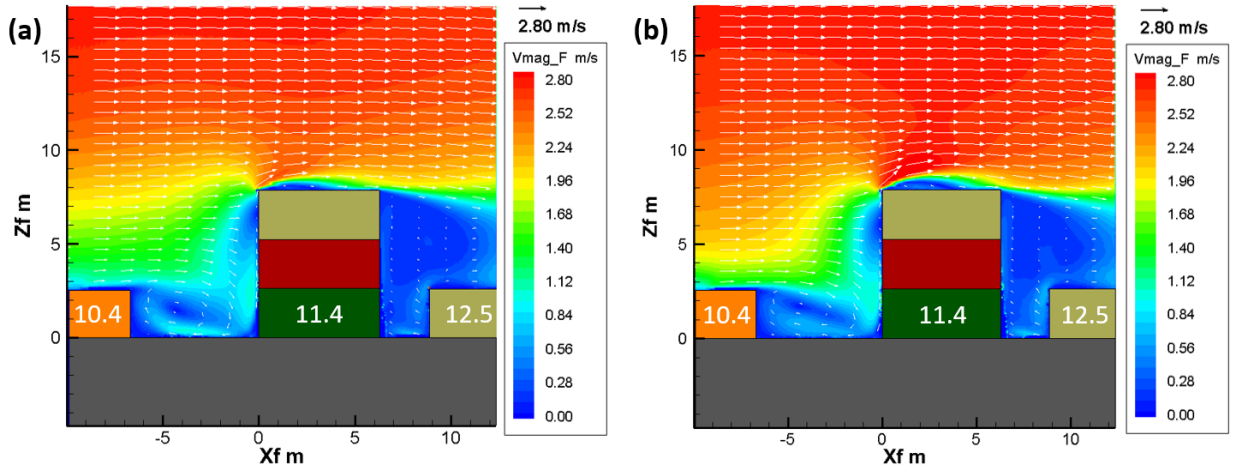

Figure 75 - Average velocity magnitude in the XZ plane in Trial 4 conditions for (a) Pre-Release and (b) Simulated chlorine release.

The release affects the velocity magnitude in Trial 4 conditions in a similar manner as observed in Trial 2. The main changes observed include significantly faster velocities above CONEX 11.4, faster velocities in the canyon between CONEX containers 10.4 and 11.4, and a decrease in height of the mid-high (orange and yellow) velocity contours upwind of CONEX 11.4. The decrease in height of the mid-high velocity contours and the increase in velocity in the upper region (above the leading edge of CONEX 11.4) are more evident in Trial 4, as in this condition the free stream wind velocity is significantly slower than in Trial 2. The momentum of the release is more impactful in the lower atmospheric momentum of Trial 4. Comparisons of the

u and w velocity components are shown in Appendix H4.

Figure 76 compares equally-spaced streamlines in pre-release (Figure 76a) and release (Figure 76b) situations. In contrast to the previous high wind case, there is a decrease in height of the dividing streamline from 6.64 m in the pre-release case to 6.09 m in the release case for Trial 4 conditions, a difference of 55 cm (8%).

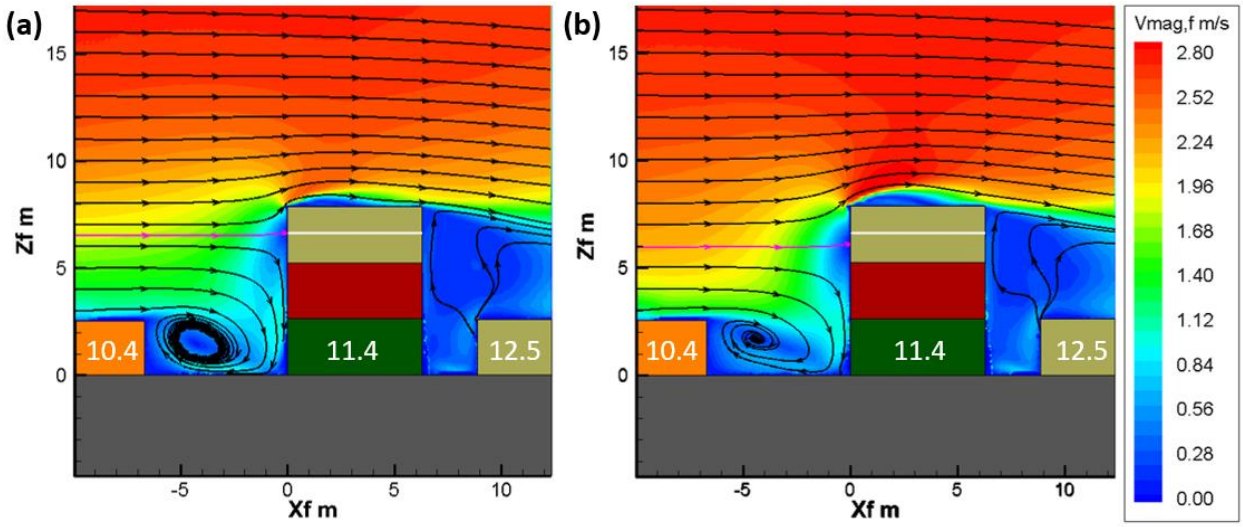

Figure 76 - Streamlines in the XZ plane in Trial 4 conditions for (a) Pre-Release and (b) Simulated chlorine release.

The decrease in height of the dividing streamline implies that flow is closer to the ground, and a higher portion of the total approaching flow is redirected to the rooftop and above CONEX 11.4. This effect, combined with the downward shift in medium-high velocity contours discussed in Figure 76, results in higher velocity regions that extend from lower heights to the top of the tall building, which can carry contaminants to that location. Additionally, the shift in height of the dividing streamline was only observed in Trial 4 conditions, which shows that the added momentum of the release has a bigger effect on the lower wind speed case.

The effect of the release on the vorticity is evaluated in Figure 77. The average vorticity in the pre-release and release cases are shown respectively in Figures 77a and 77b. The impact of

the release on the vorticity is observed mainly in the significant increase at the rooftop level of CONEX 11.4, which again shows an increase in the vortex shedding at the top of the mock building. This effect can also be observed in the average velocity plots (Figures 75 and 76), as the increase of the extremely low average velocity area (dark blue contours) along the roof of CONEX 11.4. Once again, the effect of the added momentum of the release is more evident in Trial 4 conditions than in Trial 2 conditions. Stronger vortex shedding is also observed at the rooftop level of CONEX 10.4, although little change is observed in the canyon between CONEX containers 10.4 and 11.4. Slight increases in vorticity can also be observed in the lee side of CONEX 11.4).

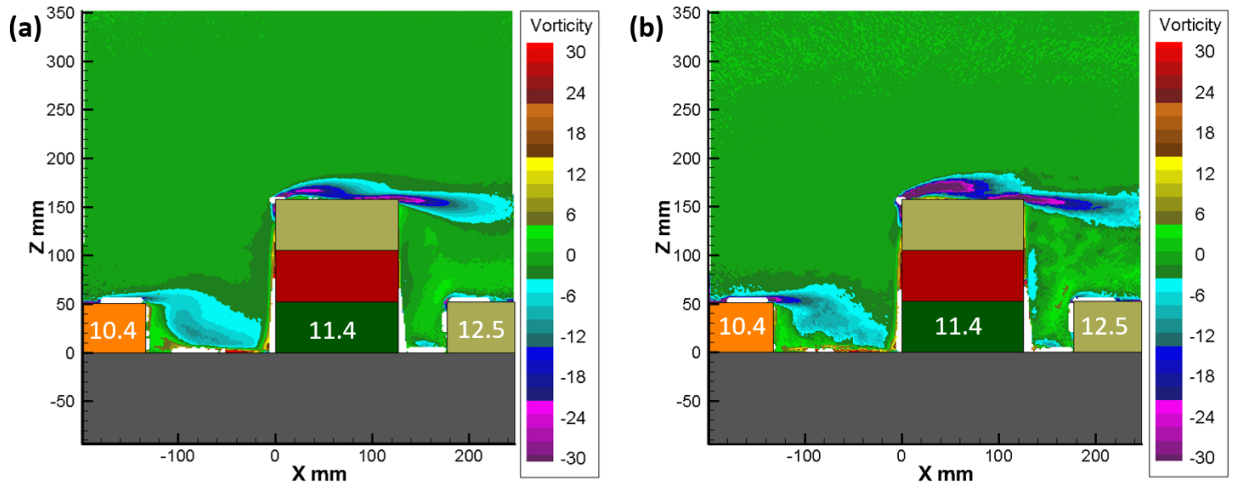

Figure 77 - Average vorticity (s^{-1}) in the XZ plane in Trial 4 conditions for (a) Pre-Release and (b) Simulated chlorine release.

Figure 78c shows the average velocity magnitude after the steady state phase of the release. For comparison, the average velocity in the pre-release (Figure 78a) and during the steady state phase (Figure 78b) are also shown. Several changes in the flow are observed in this final phase condition, mainly near ground level, as expected, since the final phase of the release is composed of gas that has been "trapped" due to entrainment behind other CONEX containers within the model MUE. A larger low velocity contour (dark blue) is present immediately behind

CONEX 10.4 at a lower velocity when compared to the pre-release and steady state release cases. Additionally, there is a significant wind speed increase at ground level immediately upwind of CONEX 11.4 (green contours). These factors combined result in an increase of circulating flow in the canyon, with a well-defined stationary vortex that has moved further downwind within the canyon than in the steady state case. Velocity at the higher levels is similar to the steady state phase. The along-wind and vertical velocity components are shown in Appendix H5.

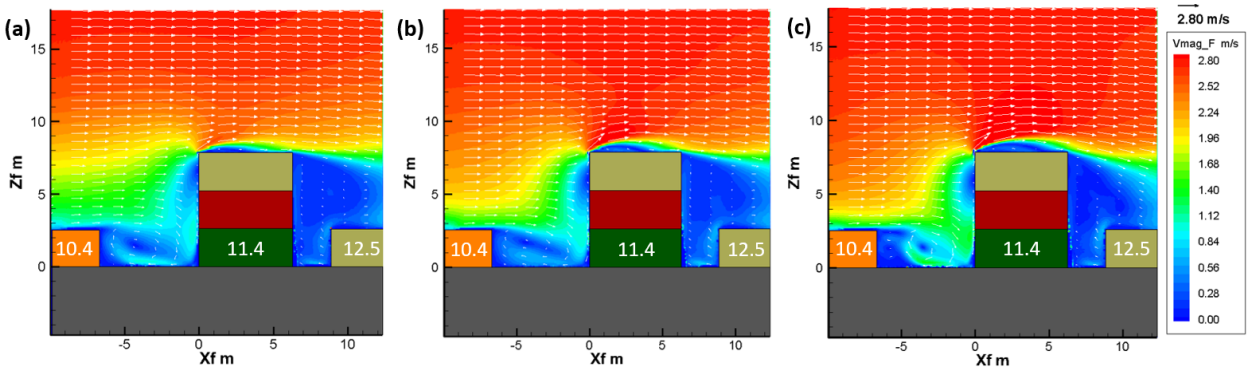

Figure 78 - Average velocity magnitude in the XZ plane in Trial 4 conditions for (a) Pre-Release, (b) Steady state phase and (c) After the steady state phase of the simulated chlorine release.

The streamlines after the steady state phase are shown in Figure 79c. For comparison, the plots of average velocity with streamlines in the pre-release (Figure 79a) and during the steady state phase (Figure 79b) are also shown. The dividing streamline after the steady state phase of the release is located at 6.02 m AGL, a similar height to the steady state case (6.09 m). A major change observed is the presence of a second, smaller vortex in the canyon between CONEX 10.4 and 11.4. The second vortex rotates in the counterclockwise direction, forming a pair of counter-rotating vortices in the canyon. Counter-rotating vortices have been identified as a worst-case scenario in terms of circulation in urban canyons, as the concentration of pollutants at ground level increases significantly when two counter-rotating vortices are present (Xiaomin, Zhen, &

Jiasong, 2006).

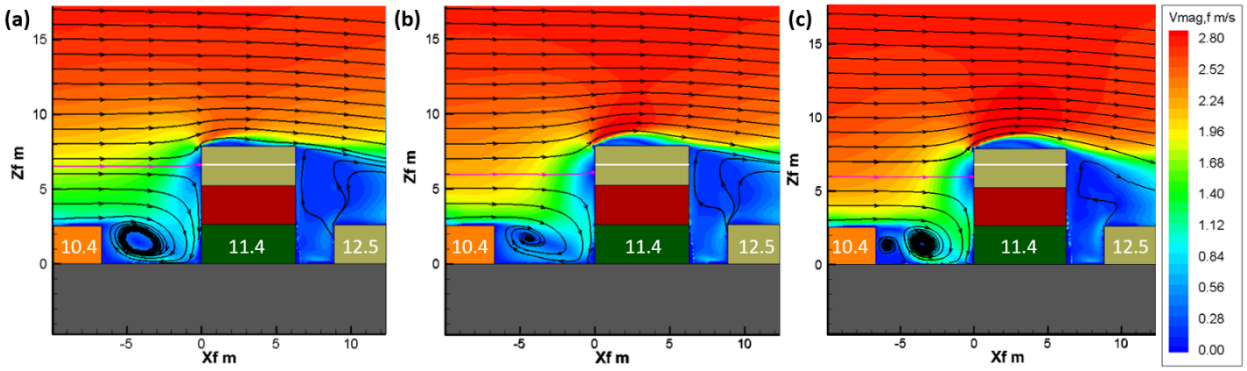

Figure 79 - Streamlines in the XZ plane in Trial 4 conditions for (a) Pre-Release, (b) Steady state phase and (c) After the steady state phase of the simulated chlorine release.

The average vorticity after the steady state stage of the release is shown in Figure 80c. The average vorticity in the pre-release (Figure 80a) and in the steady state phase of the release (Figure 80b) are also shown. As indicated by the velocity magnitude plots in Figure 78c, the main vortex in the canyon between CONEX containers 10.4 and 11.4 is stronger in the final phase when compared to both the pre-release and the steady state phase, consistent with what was discussed previously that the final of the release affects mostly the heights closer to the ground. It is also possible to identify the secondary vortex in the canyon, with a positive (counterclockwise) rotation, consistent with the streamlines in the same region shown in Figure 79c. The vortex shedding from the leading edge of CONEX 11.4 is shown as an intermediate intensity, between the pre-release and steady state releases.

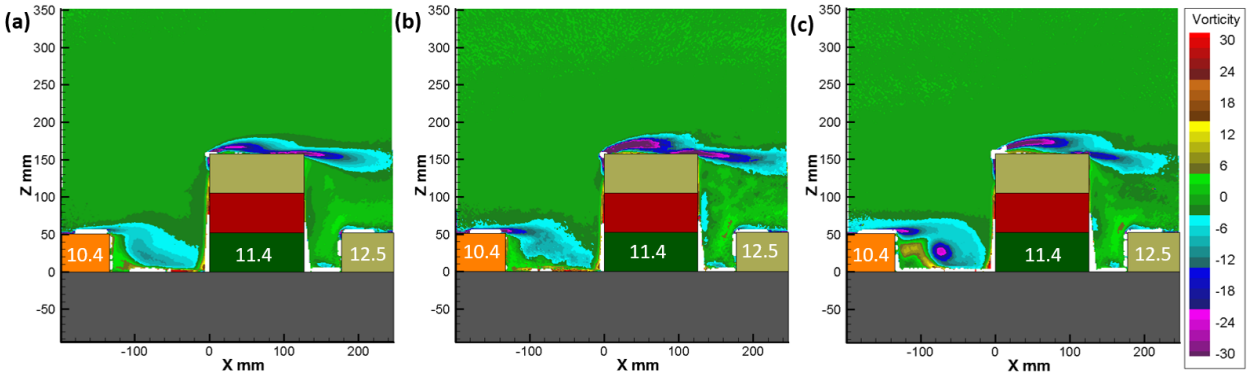

Figure 80 - Average vorticity (s^{-1}) in the XZ plane in Trial 4 conditions for (a) Pre-Release, (b) Steady state phase and (c) After the steady state phase of the simulated chlorine release.

The final set of tests consisted of simulations of neutrally buoyant releases. The dense chlorine gas simulant was replaced with air, while the release flow rate was kept the same (680 L/min). Figure 81c shows the average velocity magnitude in the steady state phase of the neutrally buoyant releases. The average velocity in the pre-release case and in the steady state phase of the DTA release are shown in Figures 81a and 81b, respectively, for comparison. The velocity contours in the neutrally buoyant release case are nearly identical to the ones measured in the pre-release case. The along-wind and vertical velocity plots can be found in Appendix H6.

Comparisons of the three cases pictured in Figure 81 indicate that the changes in the velocity patterns observed in the DTA gas release are much more related to the density of the release than to the velocity of the release. The neutrally buoyant release case had the same release velocity as the DTA case because both releases had the same volumetric flow rate. However, the flow pattern only changed during the DTA release, indicating that the change in the DTA case is due to the density of the gas release.

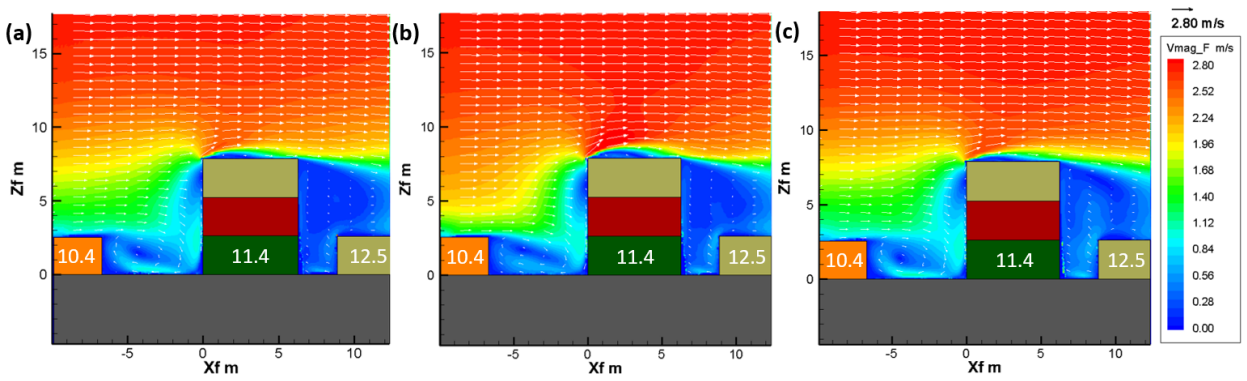

Figure 81 - Average velocity magnitude in the XZ plane in Trial 4 conditions for (a) Pre-Release, (b) DTA release (steady state phase) and (c) Neutrally Buoyant release (steady state phase).

The streamlines in the steady state phase of the neutrally buoyant release case are shown in Figure 82c. For comparison, similar plots in the pre-release (Figure 82a) case and steady state phase of the simulated chlorine release (Figure 82b) are also shown. The dividing streamline for the neutrally buoyant release case is located at 6.56 m AGL, a negligible drop of only 8 cm (1.2%) when compared to the pre-release case. Once again, the results of the neutrally buoyant releases are very similar to the pre-release case.

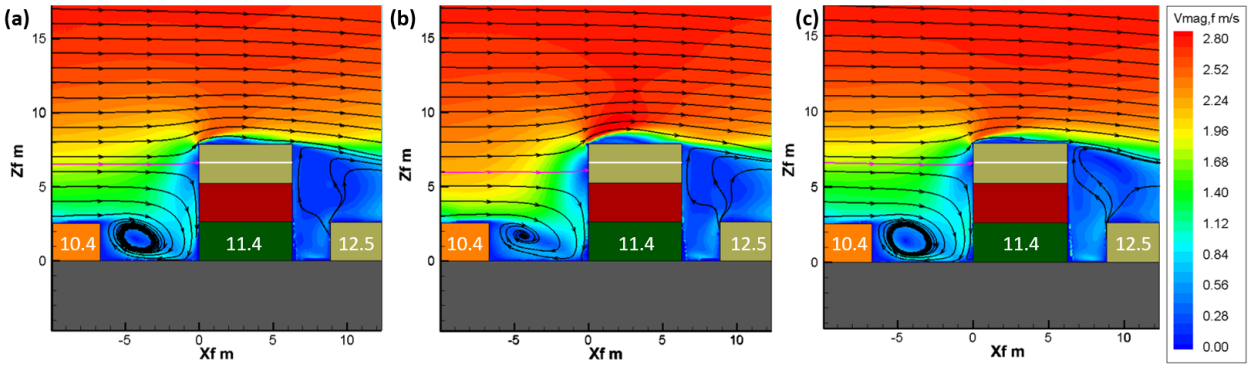

Figure 82 - Streamlines in the XZ plane in Trial 4 conditions for (a) Pre-Release, (b) DTA release (steady state phase) and (c) Neutrally Buoyant release (steady state phase).

Finally, Figure 83c shows the average vorticity in the neutrally buoyant release simulation. The average vorticity in the pre-release (Figure 83a) case and in the steady state phase of the DTA release (Figure 83b) are shown alongside for comparison. The vortex present

in the canyon between CONEX containers 10.4 and 11.4 is nearly identical to the one measured in the pre-release case. The vortex shedding from the leading edge of CONEX 11.4 for the neutrally buoyant release case is less intense than all vortex shedding previously shown for Trial 4 conditions.

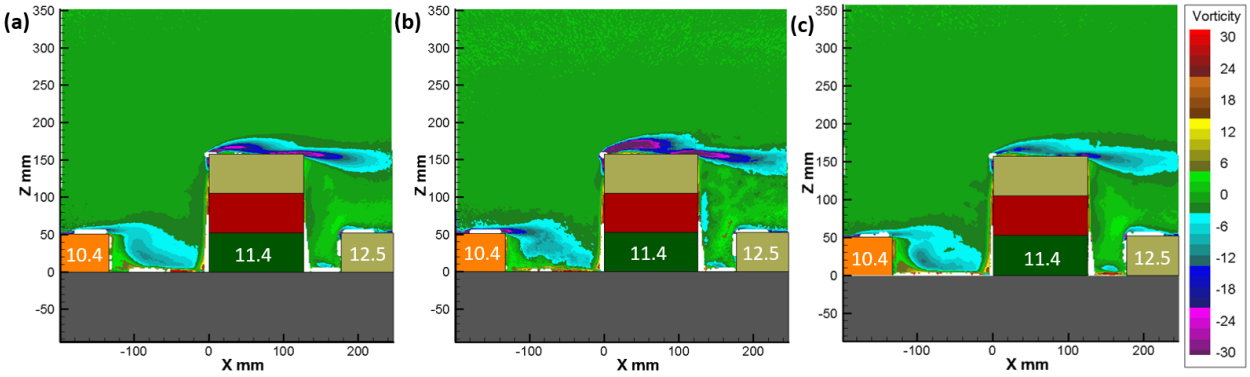

Figure 83 - Average vorticity (s^{-1}) in the XZ plane in Trial 4 conditions for (a) Pre-Release, (b) DTA release (steady state phase) and (c) Neutrally Buoyant release (steady state phase).

The results shown in Figures 81, 82, and 83 indicate little to no change in the flow properties when a neutrally buoyant chemical is released. The addition of the neutrally buoyant flow at this flow rate is insufficient to significantly change the flow in urban environments. Consequently, the changes in flow patterns observed in the DTA gas release cases (during and after the steady state phase) are mainly caused by the added density of the release.

5.2.2.2 Velocity Measurements in the XY plane

PIV measurements were conducted in the XY plane of the tunnel for JR-II Trial 4 conditions at 2 cm above the MUE model pad, which is equivalent to 1 m AGL in field scale. Measurements were taken for pre-release and with a simulated chlorine release to investigate how the added momentum from the release affected the flow around Rows 10, 11, and 12 of the MUE. The approaching wind was directed with a relative angle of 22° with respect to the MUE pad, which corresponds to the average wind direction for the Trial 4 release of the JR-II field

test.

Five special model CONEX containers were constructed with a layer of clear casting epoxy and placed (at locations 11.3, 11.4, 12.4, 12.5, and 12.6). Implementation of the CONEX containers with a layer of clear casting epoxy was largely successful. However, the corners of the clear layers interfered with the laser light, causing small areas with diminished illumination and consequently some loss of data.

It should be noted that reliable PIV results could not be obtained in some areas within the horizontal laser sheet, as those areas had to be removed. The larger zones in black in the figures (see Figure 84, for example) are areas where opaque CONEX containers (10.2, 10.3, 10.4, 10.5, 11.2, 11.5, and 12.3) blocked laser light and prevented PIV measurements. Thin black zones in the figures are areas where corners of the special CONEX containers created shadows that also prevented PIV measurements. In the case of the pre-release measurements, the combined effect of two layers of clear casting epoxy slightly distorted the laser sheet and hindered data acquisition between the containers of Rows 10 and 11, as shown in the plot of instantaneous measurements that contributed to the averaged result for each subregion in Figure 84a. A similar plot for the release case is shown in Figure 84b for comparison. Regions with unreliable data due to low vector count have been covered in dark grey in the figures for the pre-release case. Even though PIV data could not be acquired for some locations, reliable velocity data was obtained for the majority of the measurement areas.

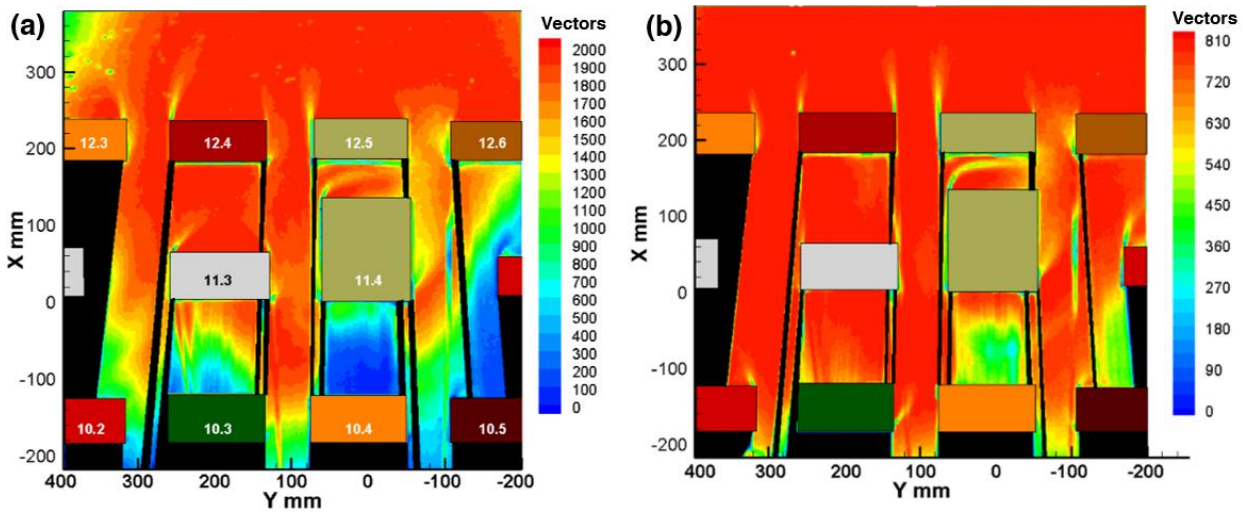

Figure 84 - Plot of vector count per subregion in JR-II Trial 4 conditions for (a) pre-release and (b) Simulated chlorine release.

The average velocity in the XY plane is shown in Figure 85, with the pre-release and the simulated chlorine release cases shown in Figures 85a and 85b, respectively. The major difference observed is the increase in velocity in the channels beside CONEX 11.4, especially in the wider channel (increase in velocity around 30%) between CONEX containers 11.4 and 11.5. This acceleration is likely due to the redirection of the release gas arriving at CONEX 11.4 below the dividing streamline, being then redirected sideways while favoring the wider gap to the right of the tall building. An increase in velocity from the corners of the model buildings is also observed on both sides of CONEX containers 10.4 and 12.5.

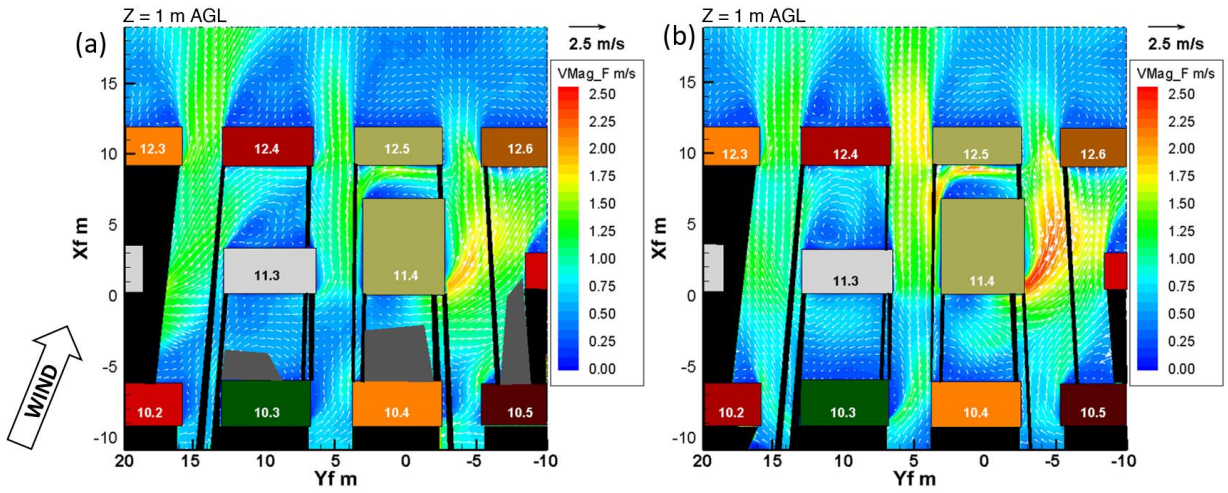

Figure 85 - Average velocity magnitude at 1 m AGL in the XY plane in Trial 4 conditions for (a) pre-release and (b) Simulated chlorine release.

Other differences due to the simulated release are observed in the wake of CONEX containers 11.3 and 11.4. An increase in velocity of around 40% is observed on the side upwind side of CONEX 12.5 as a consequence of the acceleration of flow on the left side of CONEX 11.4, as discussed previously. A decrease in speed of approximately 30% in the canyon between CONEX containers 11.3 and 12.4 is also observed, with an enlargement of the boundary of the clockwise recirculation zone downwind of CONEX 11.3.

Figure 86 shows the average cross-wind velocity component (Vf) in the pre-release (Figure 86a) and the steady state phase of the release (Figure 86b).

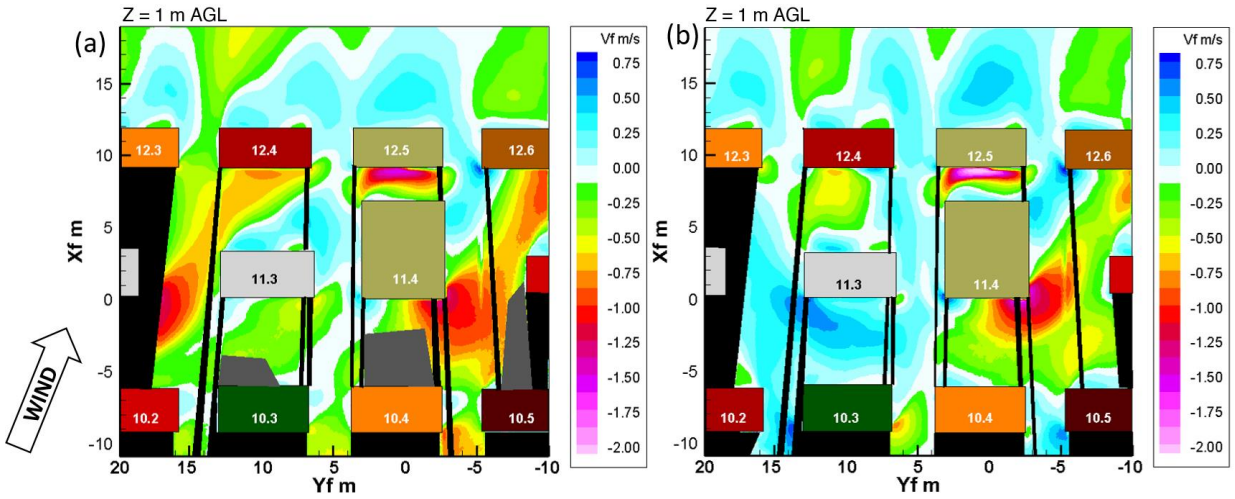

Figure 86 - Average cross-wind velocity component at 1 m AGL in Trial 4 conditions for (a) pre-release and (b) Simulated chlorine release.

As expected, due to the angle of the approaching wind, the flow in the pre-release case is skewed towards the negative y-direction (to the right), with some areas in the wake of several CONEX containers (11.3, 11.4, 12.3, 12.4, ad 12.5) registering flow reversals. As shown in Figure 86b, the momentum of the release suppresses the skewness due to the wind angle that was seen in the pre-release case, causing the flow pattern to behave much more as if the wind angle was 0° (i.e., wind moving straight down the MUE pad). During the release, the flow is split more evenly around the containers, as the momentum of the release overrides the effect of the angle of the approaching wind. In the canyon between CONEX containers 10.3 and 11.3, the cross-wind component is, on average, altered by about 1 m/s (in the positive y-direction flow) in the release case when compared to the pre-release. The change in the velocity just upwind of CONEX 12.5, as mentioned in the discussion of Figure 85, is clearly observed in the cross-wind velocity component plots, increasing by about 0.5 m/s (33%) in the negative y-direction for the release case.

Figure 87 shows the average vorticity (s^{-1}) in the XY plane in the pre-release (Figure 87a) and steady state phase of the release (Figure 87b).

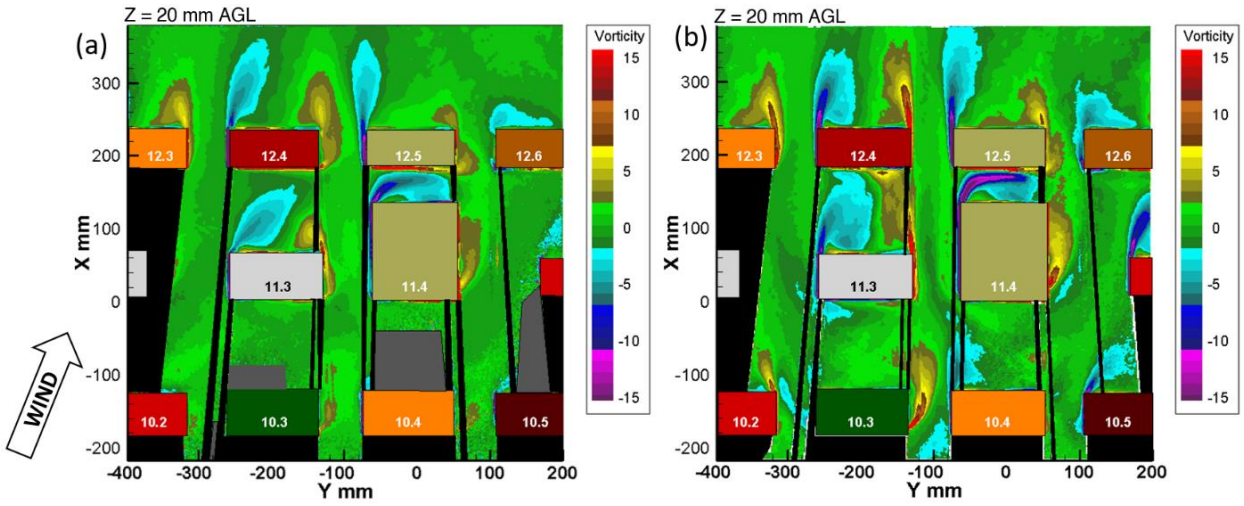

Figure 87 - Average vorticity (s^{-1}) at 1 m AGL in Trial 4 conditions for (a) pre-release and (b) Simulated chlorine release.

As shown in Figure 87a, the pairs of counter-rotating vortices in the wake of CONEX containers are dominated by the negative (counterclockwise) vortex of the pair for the pre-release case, as expected due to the relative direction of the approaching wind. Higher vortex shedding from the edges of CONEX containers is observed in Figure 87b as an effect of the release. Similar to the cross-wind velocity plots, the release suppresses the skewness caused by the angled approaching wind, as many vortex pairs become symmetric as a consequence of the added momentum from the release.

As was observed in the results shown in this section, the added momentum from the release significantly affects the flow in the back rows of the MUE in Trial 4 conditions, with a lower atmospheric momentum. The average velocities in the channels increase significantly as a consequence of the release of a denser-than-air gas. Average cross-wind and vorticity results show that the momentum of the release is enough to overcome the angle of the approach wind, which was skewed in the pre-release case to the right as a consequence of the direction angle of the approaching wind.

Chapter 6 – Conclusions

The industrial sector requires the storage and transportation of hazardous gases in large quantities. An accidental release of an airborne denser-than-air chemical in an urban area is of particular concern due to the impact that urban environments have on wind characteristics, potentially creating areas of high contaminant concentration. Hazard assessment of such accidents can be better understood via field tests, physical models, or computational models. Field tests have been previously completed to better understand the dispersion of toxic chemicals, exemplified by the Jack Rabbit II (JR-II) and the Jack Rabbit II Special Sonic Anemometer Study (JRII-S). Field tests are crucial but cannot provide all necessary information about the behavior of denser-than-air toxic gas releases. Therefore, appropriate wind tunnel and CFD models should be used to supplement the data obtained from field tests. Physical models are widely used due to active control of wind conditions and opportunity for repeated tests with increased statistical confidence. Velocity measurements in models of urban environments using Laser Doppler Velocimetry (LDV) and Particle Image Velocimetry (PIV) have shown the complex flow patterns within such models. However, no simulations of denser-than-air gas releases in a model urban environment have been conducted previously.

The Jack Rabbit II field test was commissioned to evaluate the effect of a chlorine release in a mock urban environment (MUE). Visual recordings, anemometry, and concentration data were taken during the test. Due to the corrosive nature of chlorine, no velocity data was collected within the MUE. The complimentary Special Sonic Anemometry test was conducted to measure the wind patterns around a wide (CONEX 9.4) and a tall mock building (CONEX 11.4). No chlorine releases were conducted during JRII-S. A valid physical model of the JR-II field test would be capable of acquiring velocity measurements within the MUE before and during a

simulated chlorine release. Specifically, such a physical model would allow researchers to quantify the effects of the added momentum of the release in the flow around the model buildings.

Two physical models of the JR-II field test and one computational model of the JRII-S field test have been conducted previously. Unfortunately, only neutrally buoyant releases were conducted in previous physical models, which misses the main purpose of JR-II, namely the release of a DTA chlorine gas and aerosol mixture. No actual DTA releases in a model of JR-II have been conducted previously. The computational study presented two different types of simulations, with conflicting results. Therefore, proper modeling of the JR-II test was still needed to understand the impacts of the release in the flow within the MUE and to help validate CFD models.

The wind tunnel of the Chemical Hazards Research Center (CHRC) at the University of Arkansas is an ultra-low-speed wind tunnel, capable of reproducing the turbulence level found in the atmospheric boundary layer. The wind tunnel is equipped with velocity measurement techniques (Laser Doppler Velocimetry and Particle Image Velocimetry) and an area source for the remote release of gases into the tunnel. A 1:50 scale model of the JR-II field test was constructed in the CHRC wind tunnel. Velocity measurements were taken in the model using LDV, and the agreement was demonstrated between the physical model and data from the field test for wind velocity and turbulence, quantified via friction velocity. Flow visualization experiments in the wind tunnel model also showed the agreement between model and field data. The best visual agreement of the releases was achieved when a mixture of air, sulfur hexafluoride, and carbon dioxide (with added fog for visualization) was released in the tunnel at 680 L/min, with an equivalent density of a mixture of 49% chlorine in (dry) air.

Before further tests were conducted in the model, a fundamental question was investigated: “Is it possible to obtain accurate 3D velocity and turbulence measurements by using only one LDV probe (2D measurements) placed at an angle?”. Extrapolated 3D velocity and turbulence data were obtained from a simplified 2D setup using the relative angle between the LDV probe and the axis of the tunnel. The extrapolated data was compared to actual velocity measurements taken with the full 3D LDV system. In the LDV probe configuration used for this work, the 2D approximation was deemed valid for the measurement of velocity in the vertical direction but failed to provide a good approximation for the velocity in the cross-wind direction, as the perspective from the other LDV probe is needed to accurately resolve the velocity components. The values of the overall turbulence (quantified via turbulent kinetic energy) were always underestimated by approximately a third, due to the missing contribution of the other LDV probe. The simplified 2D setup should only be used if one velocity component is of less importance than the other two, otherwise the full 3D LDV setup is recommended.

Three-dimensional LDV measurements in the MUE showed agreement between the model and Time Frames C and E of the JRII-S field test at locations of the sonic anemometers. Regions of near-stagnant flow on the lee side of CONEX containers were observed. High wind direction variability in the channels between CONEX containers explains some disagreement in wind direction measurements between the model and the field. Future wind tunnel tests may be conducted to demonstrate agreement in the remaining Time Frames from the JRII-S field test.

Two-dimensional PIV measurements were conducted in the wind tunnel model from two different perspectives: side view (measurements in the XZ plane of the tunnel) and top view (measurements in the XY plane). Time Frames C and E from JRII-S and Trials 2 and 4 from JR-II were reproduced in the tunnel for PIV tests in the XZ plane. Time Frames C and D from JRII-

S and Trial 4 from JR-II were reproduced in the tunnel for tests in the XY plane.

Results from the JRII-S simulations in the XZ plane showed a similarity between LDV and PIV measurements. The complete flow field around CONEX 11.4 was measured, showing a region of near-stagnant flow behind the model building, a stationary vortex in the canyon between CONEX containers 10.4 and 11.4, and vortex shedding from the leading edge of the tall building. Results showed that, over the short velocity range of the Time Frames, the height of the dividing streamline barely moved. Future tests may investigate if greater change in height of the dividing streamline is observed over a larger range of approaching wind velocities.

Results from the JRII-S simulations in the XY plane showed a sharp increase in velocity in the channels between CONEX containers and the formation of counter-rotating vortices downwind of CONEX containers. The small relative wind direction in Time Frame D conditions is enough to skew the flow to the right, creating asymmetries in the regions behind buildings. PIV data was used for comparisons with simulations found in the literature for Time Frames C and D. The comparison showed that the simulation overpredicted the velocity in the channels beside CONEX 11.4 in Time Frame C conditions, while also underpredicting the velocity between rows 10 and 11, and downwind of CONEX 11.4. In Time Frame D conditions, the simulation results were sufficiently close to the PIV results in the channels beside CONEX 11.4. However, like in the previous case, the simulation underpredicted the velocity between rows 10 and 11 and behind CONEX 11.4. Future tests can isolate the effect of the wind angle by studying the flow patterns in Time Frame E conditions, which has a characteristic wind aligned with the pad and has a slightly faster approaching wind than Time Frame C.

Results from the JR-II simulations in the XZ plane showed the impact of a DTA release in the flow field. Results showed that the momentum of the release is more impactful for the case

of lower atmospheric momentum of Trial 4, with very little change observed in Trial 2 conditions. Results from Trial 4 showed a drop in the height of the dividing streamline by 8% during the release, which can lead to the transport of pollutants to the roof level of the building. After the steady state phase of the release in Trial 4 conditions, the presence of two counter-rotating vortices in the canyon between CONEX containers 10.4 and 11.4 was observed, a particularly dangerous scenario. Simulations of neutrally buoyant releases conducted in Trial 4 wind conditions showed that the impacts on the flow observed previously were mostly a result of the added density of the chlorine and not from the added velocity of the gas release. Future tests should be conducted to investigate the impact of the release in other wind conditions.

The impact of a DTA release in the flow field was also observed in the results from the JR-II simulations in the XY plane. Increased velocity in the channels beside CONEX 11.4 was observed, along with changes in the recirculation patterns behind CONEX containers 11.3 and 11.4. Results of average cross-wind and vorticity show the influence of the release on the wind direction. It was observed that the momentum of the release was high enough to overcome the skewness in the flow caused by the relative angle of the approaching wind in respect of the pad. Future tests can verify how the momentum of the releases affects other JR-II Trials, especially Trial 2, with a higher average velocity and a smaller relative angle of the approaching wind than that of Trial 4.

Finally, the measurements described here offer the opportunity for comparison with computational models for the purpose of validation of the computational models. Because almost all of the hazard assessments made in the foreseeable future are made using computational models, it will be important to provide data sets that could pose a validation challenge to computational models, and wind tunnel models are an excellent source of such data.

Chapter 7 – References

Adrian, R.J. & Westerweel J. (2011). *Particle Image Velocimetry* (p. 374). Cambridge University Press.

Ahmad, K., Khare, M., & Chaudhry, K.K. (2005). Wind tunnel simulation studies on dispersion at urban street canyons and intersections – a review. *Journal of Wind Engineering and Industrial Aerodynamics*. Vol. 93, 9, 697-717. https://doi.org/10.1016/j.jweia.2005.04.002

Akour, O. (2022, June 27). *Toxic gas released in Jordan port kills 13, injures 250.* Associated Press News. https://apnews.com/article/middle-east-jordan-amman-0302c9ba322321e11a723df3051b18ab

Aliabadi, A.A., Moradi, M., & Byerlay, R.A.E. (2021). The budgets of turbulence kinetic energy and heat in the urban roughness sublayer. *Environmental Fluid Mechanics*. 21, 843-884. https://doi.org/10.1007/s10652-021-09800-x

Allwine, K.J. & Flaherty, J.E. (2006). *Joint Urban 2003: Study Overview and Instrument Locations.* Pacific Northwest National Laboratory. https://doi.org/10.2172/890732

Allwine, K.J. & Flaherty, J.E. (2007). *Urban Dispersion Program Overview and MID05 Field Study Summary*. Pacific Northwest National Laboratory. https://doi.org/10.2172/912723

Allwine, K.J., Shinn, J.H., Streit, G.E., Clawson, K.L., & Brown, M. (2002). Overview of Urban 2000 – A Multiscale Field Study of Dispersion through an Urban Environment. *Bulletin of the American Meteorological Society*, Vol. 83, 4, 521-536. https://doi.org/10.1175/1520-0477(2002)083<0521:OOUAMF>2.3.CO;2

American Chemistry Council, 2020. *Chlorine production in the United States from 1990 to 2019.* Statista. https://www.statista.com/statistics/974614/us-chlorine-production-volume/

Barlow, J.F., Halios, C.H., Lane, S.E., Wood, C.R. (2015). Observations of urban boundary layer structure during a strong urban heat island event. *Environmental Fluid Mechanics*, 15, 373-398. https://doi.org/10.1007/s10652-014-9335-6

Baum, D. (2013, January 17). *How to prevent America's next train crash.* Popular Science. https://www.popsci.com/technology/article/2013-01/how-to-prevent-americas-next-train-crash/

BBC (2021, April 12). *Syrian air force behind 2018 chlorine attack on Saraqeb, OPCW finds.* BBC News – World – Middle East. https://www.bbc.com/news/world-middle-east-56721409

Belcher, S.E. (2005). Mixing and transport in urban areas. *Philosophical Transactions of the Royal Society*, 363, 2947-2968. https://doi.org/10.1098/rsta.2005.1673

Belcher, S.E., Coceal, O., Hunt, J.C.R., Carruthers, D.J., & Robins, A.G. (2012). *A review of*

urban dispersion modeling. Atmospheric Dispersion Modelling Liaison Committee.

Blackman, K., Perret, L., & Mathis, R. (2019). Assessment of inner-outer interactions in the urban boundary layer using a predictive model. *Journal of Fluid Mechanics*, 875, 44-70. https://doi.org/10.1017/jfm.2019.427

Blackman, K., Perret, L., Savory, E., & Piquet, T. (2015). Field and wind tunnel modeling of an idealized street canyon flow. *Atmospheric Environment*, 106, 139-153. https://doi.org/10.1016/j.atmosenv.2015.01.067

Blewitt, D.N., Yohn, J.F., Koopman, R.P., & Brown, T.C. (1987). *Conduct of Anhydrous Hydrofluoric Acid Spill Experiments.* Lawrence-Livermore National Laboratory.

Boddy, J.W.D., Smalley, R.J., Dixon, N.S., Tate, J.E., & Tomlin, A.S. (2005). The spatial variability in concentration of a traffic-related pollutant in two street canyons in York, UK – Part I: The influence of background winds. *Atmospheric Environment*, Vol. 39, No. 17, 3147-3161. https://doi.org/10.1016/j.atmosenv.2005.01.043

Britter, R.E. & Hanna, S.R. (2003). Flow and Dispersion in Urban Areas. *Annual Review of Fluid Mechanics*, 469-96. https://doi.org/10.1146/annurev.fluid.35.101101.161147

Brown, T.C., Cederwall, R.T., Chan, S.T., Ermak, D.L., Koopman, R.P., Lamson, K.C., McClure, J.W., & Morris, L.K. (1990). *Falcon Series Data Report. 1987 LMG Vapor Barrier Verification Field Trials*. Lawrence-Livermore National Laboratory. https://doi.org/10.2172/6633087

Buckley, R.L., Hunter, C.H., Addis, R.P., & Parker, M.J. (2007). Modeling dispersion from toxic gas released after a train collision in Graniteville, SC. *Journal of the Air & Waste Management Association*, 57, 268-278. http://doi.org/10.1080/10473289.2007.10465329

Carissimo, B., Trini Castelli, S., & Tinarelli, G. (2021). JRII special sonic anemometer study: A first comparison of building wakes measurements with different levels of numerical modelling approaches. *Atmospheric Environment*, 244, 117798. https://doi.org/10.1016/j.atmosenv.2020.117798

Carlotti, P. (2015). Urban fluid mechanics: current issues and trends – summary of the special symposium on urban fluid mechanics at the ASME 2014 4th joint US-European fluid engineering division summer meeting. *Environmental Fluid Mechanics*, 15, 483-490. https://doi.org/10.1007/s10652-015-9393-4

Castro, I.P., Cheng, H., & Reynolds, R.T. (2006). Turbulence over Urban-type Roughness: Deductions from Wind-Tunnel Measurements. *Boundary-Layer Meteorology*, 118, 109-131. https://doi.org/10.1007/s10546-005-5747-7

Cave, D. & Fadam, A. (2007, February 22). Iraq insurgents employ chlorine in bomb attacks. *The New York Times*. https://www.nytimes.com/2007/02/22/world/middleeast/22iraq.html

Cermak, J.E. (1975). Applications of Fluid Mechanics to Wind Engineering – A Freeman Scholar Lecture. *Journal of Fluids Engineering*, Vol. 97, 1, 9-38. https://doi.org/10.1115/1.3447225

Cook, N.J. (1985). *The designer's guide to wind loading of building structures – Part 1: Background, damage survey, wind data and structural classification* (pp. 40, 41). Butterworths.

Dauxois, T., Peacock, T., Bauer, P., Caulfield, C.P., Cenedese, C., Gorlé, C., Haller, G., Ivey, G.N., Linden, P.F., Meiburg, E., Pinardi, N., Vriend, N.M., & Woods, A.W. (2021). Confronting Grand Challenges in environmental fluid mechanics. *Physical Review Fluids*, 6, 020501. https://doi.org/10.1103/PhysRevFluids.6.020501

Davidson, M.J, Snyder, W.H., Lawson Jr., R.E., & Hunt, C.R. (1996). Wind tunnel simulations of plume dispersion through groups of obstacles. *Atmospheric Environment*, Vol. 30, No. 22, 3715-3731. https://doi.org/10.1016/1352-2310(96)00103-3

Davies, M.E. & Singh, S. (1985). The Phase II trials: A data set on the effect of obstructions. *Journal of Hazardous Materials*. Vol. 11, 301-323. https://doi.org/10.1016/0304-3894(85)85043-3

EPA (2022, May 18). *Status of Chlorine Product Availability and Pricing.* United States Environmental Protection Agency. https://www.epa.gov/waterutilityresponse/status-chlorine-product-availability-and-pricing

Essel, E.E., Balachandar, R., & Tachie, M.F. (2023). Effects of sheltering on the unsteady wake dynamics of tandem cylinders mounted in a turbulent boundary layer. *Journal of Fluid Mechanics*. Vol. 954, A40. https://doi.org/10.1017/jfm.2022.1029

Fares, S. (2022). Wind Tunnel Modeling of Jack Rabbit II Mock Urban Environment Gas Concentration Measurements. [Master's Thesis, University of Arkansas]. ScholarWorks@UARK.

Fernando, H.J.S., Lee, S.M., Anderson, J., Princevac, M., Pardyjak, E., & Grossman-Clarke, S. (2001). Urban Fluid Mechanics: Air Circulation and Contaminant Dispersion in Cities. *Environmental Fluid Mechanics*, 1, 107-164. https://doi.org/10.1023/A:1011504001479

Fox, S. (2019, July 17). *Jack Rabbit II – Update and Impacts* [PowerPoint slides]. U.S. Department of Homeland Security – Science and Technology Chemical Security Analysis Center.

Fox, S. & Storwold, Jr., D. (2011). *Project Jack Rabbit: Field Tests*. U.S. Department of Homeland Security – Science and Technology Chemical Security Analysis Center.

Gallimore, S. (2023). Wind Tunnel Modeling of the Jack Rabbit II Mock Urban Environment Chlorine Releases Based on Comparison with Field Scale Video Record. [Master's Thesis, University of Arkansas]. ScholarWorks@UARK.

Goldwire, Jr., H.C., McRae, T.G., Johnson, G.W., Hipple, D.L., Koopman, R.P., McClure, J.W., Morris, L.K., & Cederwall, R.T. (1985). *Desert Tortoise Series Data Report. 1983 Pressurized Ammonia Spills*. Lawrence-Livermore National Laboratory. https://doi.org/10.2172/6393901

Goldwire, Jr., H.C., Rodean, H.C., Cederwall, R.T., Kansa, E.J., Koopman, R.P., McClure, J.W., McRae, T.G., Morris, L.K., Kamppinen, L., & Kiefer, R.D. (1983). *Coyote series data report LLNL/NWC 1981 LNG spill tests dispersion, vapor burn, and rapid-phase-transition. Volume 1. [7 experiments with liquefied natural gas, 2 with liquid methane, and one with liquid nitrogen]*. Lawrence-Livermore National Laboratory.

Hall, D.J. & Walker, S. (1997). Scaling rules for reduced-scale field releases of hydrogen fluoride. *Journal of Hazardous Materials*, 54, 89-111. https://doi.org/10.1016/S0304-3894(96)01856-0

Hall, D.J. & Waters, R.A. (1985). Wind tunnel model comparisons with the Thorney Island dense gas release field trials. *Journal of Hazardous Materials*, 11, 209-235. https://doi.org/10.1016/0304-3894(85)85039-1

Hamed, A.M., Peterlein, A.M., & Randle, L.V. (2019). Turbulent boundary layer perturbation by two wall-mounted cylindrical roughness elements arranged in tandem: Effects of spacing and height ratio. *Physics of Fluids*, 31, 065110. https://doi.org/10.1063/1.5099493

Hanna, S. (2020). Meteorological Data Recommendations for Input to Dispersion Models applied to Jack Rabbit II Trials. *Atmospheric Environment*, 235, 117516. https://doi.org/10.1016/j.atmosenv.2020.117516

Hanna, S. & Chang, J. (2015). Skyscraper rooftop tracer concentration observations in Manhattan and comparisons with urban dispersion models. *Atmospheric Environment*, 106, 215-222. https://doi.org/10.1016/j.atmosenv.2015.01.051

Havens, J., Spicer, T., & Walker, H. (1996). *Evaluation of Mitigation Methods for Accidental LNG releases. Volume 1: Wind Tunnel Experiments and Mathematical Model Simulations to Study dispersion of a vapor cloud formed following LNG Spillage into a diked area surrounding a storage tank.* Gas Research Institute.

Health & Safety Laboratory (1985). *Heavy Gas Dispersion Trials, 1980s.* Science Photo Library. https://www.sciencephoto.com/media/664132/view/heavy-gas-dispersion-trials-1980s

Herpin, S., Perret, L., Mathis, R., Tanguy, C., & Lasserre, J.J. (2018). Investigation of the flow inside an urban canopy immersed into an atmospheric boundary layer using laser Doppler anemometry. *Experiments in Fluids*, 59, 80. https://doi.org/10.1007/s00348-018-2532-1

Hist, W.J.S., & Eyre, J.A. (1983). *Maplin Sands Experiments 1980: Combustion of Large LNG and Refrigerated Liquid Propane Spills on the Sea.* Heavy Gas and Risk Assessment – II, 211-224.4. https://doi.org/10.1007/978-94-009-7151-6_12

H'ng, Y.M., Ikegaya, N., Zaki, S.A., Hagishima, A., & Mohammad, A.F. (2022). Wind-tunnel estimation of mean and turbulent wind speeds within canopy layer for urban campus. *Urban Climate*, 41, 101064. https://doi.org/10.1016/j.uclim.2021.101064

JEMS (2008, January 16). *Tacoma Chlorine Plant will pay penalty for leak, donate to F.D.* Journal of Emergency Medical Services. https://www.jems.com/operations/tacoma-chlorine-plant-will-pay/

Kastner-Klein, P. & Rotach, M.W. (2004). Mean Flow and Turbulence Characteristics in an Urban Roughness Sublayer. *Boundary-Layer Meteorology*, 111, 55-84. https://doi.org/10.1023/B:BOUN.0000010994.32240.b1

Keane, R.D. & Adrian, R.J. (1990). Optimization of Particle Image Velocimeters. Part I: Double pulsed systems. *Measurement Science and Technology,* 1(11), 1202-1215. https://doi.org/10.1088/0957-0233/1/11/013

Kim, B., Tse, K.T., Yoshida, A., Tamura, Y., Chen, Z., Phuc, P.V., & Park, H.S. (2019). Statistical analysis of wind-induced pressure fields and PIV measurements on two buildings. *Journal of Wind Engineering & Industrial Aerodynamics*. Vol. 188, 161-174. https://doi.org/10.1016/j.jweia.2019.01.016

Kim, T. & Christensen, K.T. (2018). Flow Interactions Between Streamwise-Aligned Tandem Cylinders in Turbulent Channel Flow. *American Institute of Aeronautics and Astronautics Journal.* Vol. 56, No.4, 1421-1433. https://doi.org/10.2514/1.J056186

König-Langlo, G. & Schaztmann, M. (1991). Wind Tunnel Modeling of Heavy Gas Dispersion. *Atmospheric Environment.* Vol. 25A, No. 7, 1189-1198. https://doi.org/10.1016/0960-1686(91)90230-5

König, G., Schaztmann, M., & Lohmeyer, A. (1987). Measurements of gas concentration fluctuations in wind tunnel simulations. *Proceedings 7th International Conference on Wind Engineering*, Aachen, Federal Republic of Germany.

Koopman, R.P., Cederwall, R.T., Ermak, D.L., Goldwire, Jr., H.C., Hogan, W.J., McClure, J.W., McRae, T.G., Morgan, D.L., Rodean, H.C., & Shinn, J.H. (1982). Analysis of Burro series 40-m^3 LNG spill experiments. *Journal of Hazardous Materials*, Vol. 6, No. 1-2, 43-83. https://doi.org/10.1016/0304-3894(82)80034-4

Louka, P., Belcher S.E., & Harrison, R.G. (1999). Coupling between air flow in streets and the well-developed boundary layer aloft. *Atmospheric Environment*, 34, 2613-2621. https://doi.org/10.1016/S1352-2310(99)00477-X

MacDonald, R.W., Griffiths, R.F., & Hall, D.J. (1998). A comparison of results from scaled field and wind tunnel modelling of dispersion in arrays of obstacles. *Atmospheric Environment*, Vol. 32, No. 22, 3845-3862. https://doi.org/10.1016/S1352-2310(98)80006-X

Mazraawi, K. (2022). *Jordanian forensics experts inspect the site of a toxic gas explosion at the*

Red Sea port of Aqaba on June 28, 2022 [Photograph]. Agence France-Presse. https://thearabweekly.com/chlorine-gas-leak-aqaba-port-causes-13-deaths-250-injuries

McQuaid, J. (1985). Objectives and design of the Phase I Heavy Gas Dispersion Trials. *Journal of Hazardous Materials,* Vol. 11, 1-33. https://doi.org/10.1016/0304-3894(85)85031-7

McRae, T.G., Cederwall, R.T., Ermak, D.L., Goldwire, Jr., H.C., Hipple, D.L., Johnson, G.W., Koopman, R.P., McClure, J.W., & Morris, L.K. (1987). *Eagle Series Data Report: 1983 Nitrogen Tetroxide Spills.* Lawrence-Livermore National Laboratory. https://doi.org/10.2172/6578665

Morris, J. (2018). Experimentation and Modeling of the Effects of Along-Wind Dispersion on Cloud Characteristics of Finite-Duration Contaminant Releases in the Atmosphere. [Doctoral dissertation, University of Arkansas]. ScholarWorks@UARK.

Neff, D.E. & Meroney R.N. (1981). *Wind-Tunnel Simulation of 40 m^3 LNG Spill Tests at China Lake Naval Weapons Center, California.* Gas Research Institute.

Owkes, M., Benson, M., Elkins, C., Wilde, N., & Van Poppel, B. (2020). Three-dimensional velocity and concentration measurements and simulations of a scaled Jack Rabbit II mock urban array. *Atmospheric Environment*, 233, 117520. https://doi.org/10.1016/j.atmosenv.2020.117520

Parsons, C. (2007, February 20). *Chlorine truck blast kills five in Iraq.* Reuters. https://www.reuters.com/article/idUSPAR030640

Paterna, E. (2015). Wind Tunnel Investigation of Turbulent Flow in Urban Configurations. A Time-Resolved PIV Analysis. [Doctoral dissertation, Eidgenössische Technische Hochschule Zürich]. Research Collection ETH Zürich.

Petersen, R.L. & Ratcliff, M.A. (1989). *Vapor Barrier Assessment Program for Delaying and Diluting Heavier-than-air HF Vapor Clouds – A Wind Tunnel Modeling Evaluation. Volume III: Appendices A-G.* The Industry Cooperative HF Mitigation / Assessment Program Vapor Barrier Subcommittee.

Pirhalla, M., Heist, D., Perry, S., Tang, W., & Brouwer, L. (2021). Simulations of dispersion through an irregular urban building array. *Atmospheric Environment*, 258, 118500. https://doi.org/10.1016/j.atmosenv.2021.118500

Pope, S.B. (2000). *Turbulent Flows* (p. 269). Cambridge University Press.

Raffel, M., Willert, C., Wereley, S., & Kompenhans, J. (1998). *Particle Image Velocimetry – A Practical Guide* (2nd ed., pp. 4, 149, 191). Springer.

Reynolds, R.M. (2006). *The Madison Square Garden Dispersion Study (MSG05) Meteorological Data Description.* Environmental Sciences Department. Environmental Research & Technology Division. Brookhaven National Laboratory.

Reynolds, R.M., Sullivan, T.M., Smith, S., & Cassella, V. (2006). *The New York Midtown Dispersion Study (MID-05) Meteorological Data.* Environmental Sciences Department. Environmental Research & Technology Division. Brookhaven National Laboratory.

Reynolds, R.T. & Castro, I.P. (2008). Measurements in an urban-type boundary layer. *Experiments in Fluids*. 45, 141-156. https://doi.org/10.1007/s00348-008-0470-z

Rubin, A.J. (2007, April 7). Chlorine gas attack by truck bomber kills up to 30 in Iraq. *The New York Times*. https://www.nytimes.com/2007/04/07/world/africa/07iht-web-0407-iraq.5182467.html

Semple, K. (2007, March 18). Suicide bombers using chlorine gas kill 2 and sicken hundreds in Western Iraq. *The New York Times.* https://www.nytimes.com/2007/03/18/world/middleeast/18iraq.html?fta=y

Sheppard, P.A. (1956). Airflow over mountains. *Quarterly Journal of the Royal Meteorological Society,* 82, 528-529. https://doi.org/10.1002/QJ.49708235418

Shin, S.H., Meroney, R.N., & Neff, D.E. (1991). *LNG Vapor Barrier and Obstacle Evaluation: Wind Tunnel Simulation of 1987 Falcon Spill Series, Final Report.* Gas Research Institute.

Shirzadi, M., Tominaga, Y., & Mirzaei, P.A. (2019). Wind tunnel experiments on cross-ventilation flow of a generic sheltered building in urban areas. *Building and Environment*, 158, 60-72. https://doi.org/10.1016/j.buildenv.2019.04.057

Snyder, W.H. (1981). *Guideline for Fluid Modeling of Atmospheric Diffusion*. Office of Air Quality Planning and Standards, Environmental Protection Agency. https://www.osti.gov/biblio/5876795

Snyder, W.H., Thompson, R.S., Eskridge, R.E., Lawson, R.E., Castro, I.P., Lee, J.T., Hunt, J.C.R., & Ogawa, Y. (1985). The structure of strongly stratified flow over hills: dividing-streamline concept. *Journal of Fluid Mechanics*, 152, 249-288. https://doi.org/10.1017/S0022112085000684

Song, J., Fan, S., Lin, W., Mottet, L., Woodward, H., & Davies Wykes, M. (2018). Natural ventilation in cities: the implications of fluid mechanics. *Building Research & Information*, Vol. 46, 8, 809-828. https://doi.org/10.1080/09613218.2018.1468158

Sosnowski, M., Gnatowska, R., Grabowska, K., Krzywanski, J., & Jamrozik, A. (2019). Numerical Analysis of Flow in Building Arrangement: Computational Domain Discretization. *Applied Sciences*. 2019; 9(5):941. https://doi.org/10.3390/app9050941

Spicer, T.O. & Havens, J.A. (1985). Modeling the Phase I Thorney Island Experiments. *Journal of Hazardous Materials*, 11, 237-260. https://doi.org/10.1016/0304-3894(85)85040-8

Spicer, T.O. & Tickle, G. (2021). Simplified source description for atmospheric dispersion model comparison of the Jack Rabbit II chlorine field experiments. *Atmospheric*

Environment, 244, 117866. https://doi.org/10.1016/j.atmosenv.2020.117866

Takimoto, H., Sato, A., Barlow, J.F., Moriwaki, R., Inagaki, A., Onomura, S., & Kanda, M. (2011). Particle Image Velocimetry of Turbulent Flow Within Outdoor and Indoor Urban Scale Models and Flushing Motions in Urban Canopy Layers. *Boundary Layer Meteorology.* 140, 295-314. https://doi.org/10.1007/s10546-011-9612-6

The Chlorine Institute. (2022). *Incident Statistics.* The Chlorine Institute. https://www.chlorineinstitute.org/transportation/incident-statistics/

TSI Incorporated. (2020). Insight 4G™ Global Image Acquisition, Analysis, and Display Software – User's Guide. P/N 6004904, Revision F. https://tsi.com/getmedia/a1332d37-89b0-4323-926d-c05c9a019362/Insight4G_US_5001374_Web?ext=.pdf

Varma, R. & Varma, D.R. (2005). The Bhopal Disaster of 1984. Bulletin of Science, *Technology & Society*, Vol. 25, No.1, 37-45. https://doi.org/10.1177/0270467604273822

Venart, J.E.S. (2004). Flixborough: the Explosion and its Aftermath. *Process Safety and Environmental Protection*, 82, 2, 105-127. https://doi.org/10.1205/095758204322972753

Vogel, A.C. (2015, October 5). *Chlorine test concludes safely with five successful trials.* U.S. Army. https://www.army.mil/article/156528/chlorine_test_concludes_safely_with_five_successful_trials

Warner, S., Platt, N., Heagy, J.F., Jordan, J.E., & Bieberbach, G. (2006). Comparisons of Transport and Dispersion Model Predictions of the Mock Urban Setting Test Field Experiment. *Journal of Applied Meteorology and Climatology.* Vol. 45, 10, 1414-1428. https://doi.org/10.1175/JAM2410.1

Xiaomin, X., Zhen, H., & Jiangsong, W. (2006). The impact of urban street layout on local atmospheric environment. *Building and Environment*, Vol. 41, No. 10, 1352-1363. https://doi.org/10.1016/j.buildenv.2005.05.028

Zhao, Y., Li, H., Kubilay, A., & Carmeliet, J. (2021). Buoyancy effects on the flows around flat and steep street canyons in simplified urban settings subject to a neutral approaching boundary layer: Wind tunnel PIV measurements. *Science of The total Environment*, 797, 149067. https://doi.org/10.1016/j.scitotenv.2021.149067

Zhixiang L., Zhixiang Y., Xiaoxiao C., Ruizhou C., & Fu Z. (2020). An investigation on external airflow around low-rise building with various roof types: PIV measurements and LES simulations. *Building and Environment*, 269, 106583. https://doi.org/10.1016/j.buildenv.2019.106583

Appendices

Appendix A – Correlation Between Wind Tunnel Fan Rotation Speed and Wind Speed

Figure A-1 shows the relation between the rotation speed of the wind tunnel fans with the wind velocity measured using 3D LDV at 8 cm above the tunnel floor, at the equivalent location of Tower 3. The experiments taken to establish the relation were taken with one row of Irwin Spires (14 spires, each measuring 93 cm tall and 13.5 cm wide at the base) and surface roughness elements (measuring 1.5 in x 1.5 in each) placed at 2 ft (0.6096 m) apart (referred to as "sparse" configuration).

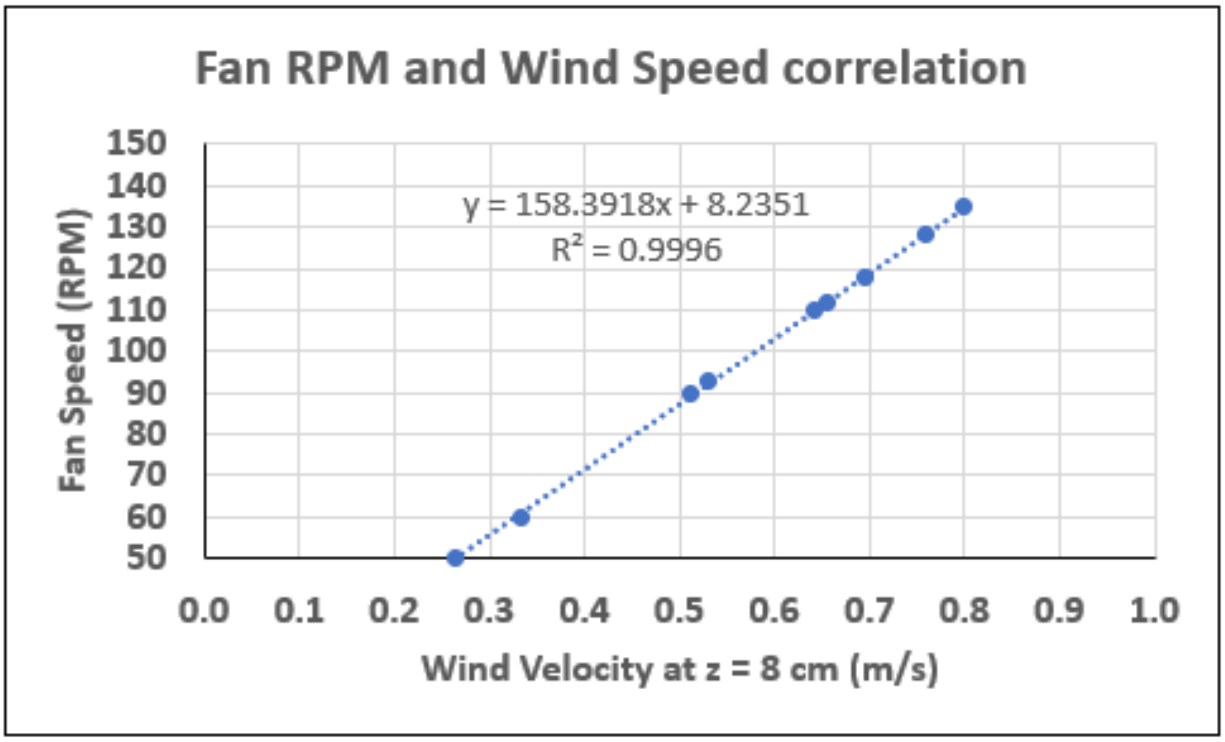

Figure A-1 - Correlation between fan speed and wind velocity at 8 cm above tunnel floor, with one row of spires and sparse surface roughness.

Appendix B – Agreement Between Wind Tunnel and Field Velocity Measurements

All wind tunnel measurements shown in Appendix B were taken at Tower 3 location. Velocity values are scaled up to field scale.

Appendix B1 – Agreement Between approaching wind measurements in the Wind Tunnel and the JR-II Trials Velocity Measurements

Table B-1 - Scaled-up wind tunnel and Field velocity data for JR-II Trial 2.

Trial 2 – 128 RPM			
Height (m)	Wind Tunnel at Full Scale (m/s)	DPG Field Data [PWIDS] Velocity Magnitude (m/s)	Difference (%)
25	6.5432	-	-
16	6.1309	5.90	3.91
10	5.8453	-	-
8	5.7202	5.68	0.71
6	5.5618	-	-
4	5.3691	5.58	3.78
2	4.9987	5.19	3.68

Table B-2 - Scaled-up wind tunnel and Field velocity data for JR-II Trial 3.

Trial 3 – 112 RPM			
Height (m)	Wind Tunnel at Full Scale (m/s)	DPG Field Data [PWIDS] Velocity Magnitude (m/s)	Difference (%)
25	5.7056	-	-
16	5.3261	5.92	10.0
10	5.0397	-	-
8	4.9296	5.10	3.34
6	4.8226	-	-
4	4.6406	4.62	0.44
2	4.2989	3.76	14.3

Table B-3 - Scaled-up wind tunnel and Field velocity data for JR-II Trial 4.

Trial 4 – 60 RPM			
Height (m)	Wind Tunnel at Full Scale (m/s)	DPG Field Data [PWIDS] Velocity Magnitude (m/s)	Difference (%)
25	2.9189	-	-
16	2.7493	2.59	6.15
10	2.5281	-	-
8	2.4963	2.39	4.45
6	2.4175	-	-
4	2.3516	2.35	0.07
2	2.1820	2.22	1.71

Table B-4 - Scaled-up wind tunnel and Field velocity data for JR-II Trial 5.

Trial 5 – 50 RPM			
Height (m)	Wind Tunnel at Full Scale (m/s)	DPG Field Data [PWIDS] Velocity Magnitude (m/s)	Difference (%)
25	2.3240	-	-
16	2.2656	2.10	7.89
10	2.0900	-	-
8	2.0386	2.03	0.42
6	1.9703	-	-
4	1.8655	1.98	5.78
2	1.7151	1.72	0.29

Appendix B2 – Comparison Plots Between Wind Tunnel and Jack Rabbit II Trials Velocity Measurements

Plots for Trials 2 and 4 are shown in the main body (Section 2.5.2).

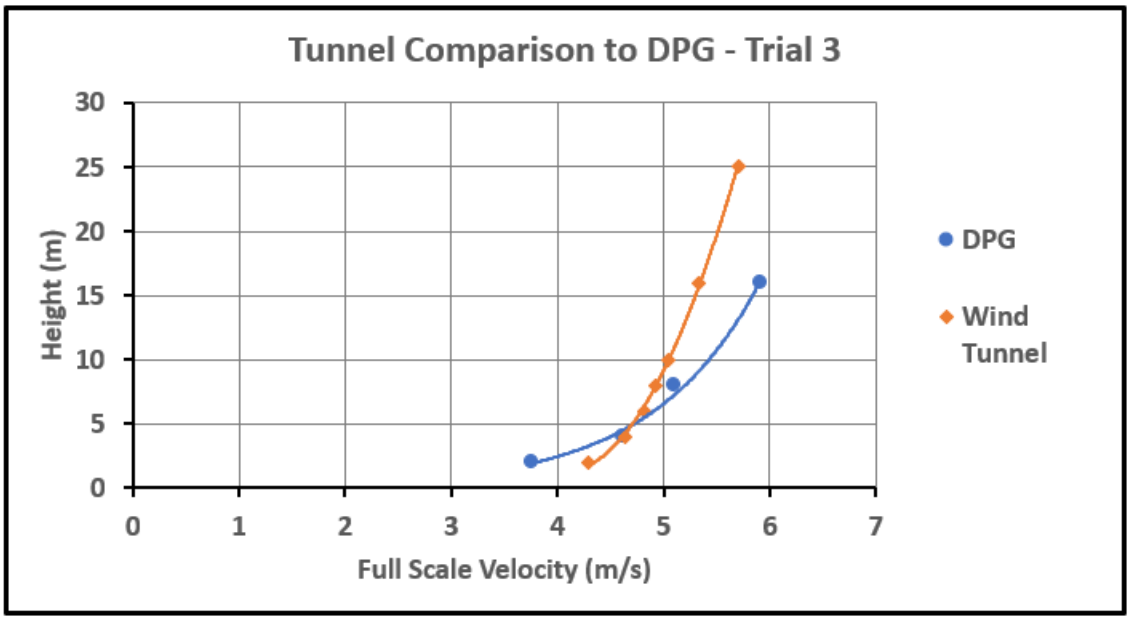

Figure B-1 - Velocity Profile comparisons between field and scale models for JR-II Trial 3.

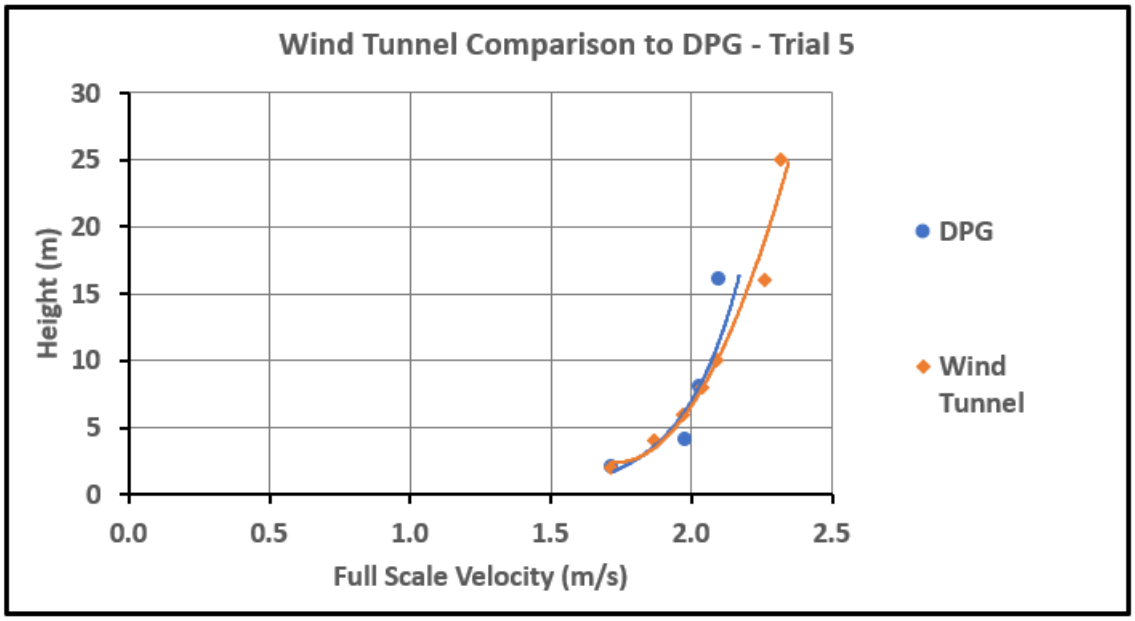

Figure B-2 - Velocity Profile comparisons between field and scale models for JR-II Trial 5.

Appendix B3 – Agreement Between Wind Tunnel and Jack Rabbit II – Special Sonic Anemometer Study Time Frames Velocity Measurements

Table B-5 - Scaled-up wind tunnel and Field velocity data for JRII-S Time Frame A.

Time Frame A – 173 RPM						
Height (m)	Wind Tunnel [at Full Scale]		DPG Field Data		Difference	
	u (m/s)	w (m/s)	u (m/s)	w (m/s)	%	%
25	8.8268	-0.3266	-	-	-	-
16	8.3481	-0.3289	8.44	-0.093	1.13	112
10	8.0165	-0.3018	-	-	-	-
8	7.8312	-0.2650	7.74	-0.405	1.20	41.7
6	7.6700	-0.2496	-	-	-	-
4	7.2846	-0.1807	7.27	-0.055	0.24	106
2	6.6836	-0.1151	6.44	0.109	3.63	7004

Table B-6 - Scaled-up wind tunnel and Field velocity data for JRII-S Time Frame B.

Time Frame B – 184 RPM						
Height (m)	Wind Tunnel [at Full Scale]		DPG Field Data		Difference	
	u (m/s)	w (m/s)	u (m/s)	w (m/s)	%	%
25	9.5304	0.0744	-	-	-	-
16	8.9180	-0.3565	9.16	0.145	2.62	473
10	8.5553	-0.3228	-	-	-	-
8	8.3658	-0.2832	8.33	-0.261	0.40	8.09
6	8.1727	-0.2652	-	-	-	-
4	7.7739	-0.1966	7.79	0.066	0.24	404
2	7.1623	-0.1288	6.89	0.105	3.84	1962

Table B-7 - Scaled-up wind tunnel and Field velocity data for JRII-S Time Frame C.

Time Frame C – 93 RPM						
Height (m)	Wind Tunnel [at Full Scale]		DPG Field Data		Difference	
	u (m/s)	w (m/s)	u (m/s)	w (m/s)	%	%
25	4.6803	-0.1480	-	-	-	-
16	4.4088	-0.1478	4.40	-0.012	0.31	171
10	4.1366	-0.1206	-	-	-	-
8	4.0602	-0.0981	4.01	-0.183	1.35	60.3
6	3.9124	-0.0770	-	-	-	-
4	3.7533	-0.0746	3.79	0.003	1.00	219
2	3.5150	-0.0339	3.36	0.094	4.67	424

Table B-8 - Scaled-up wind tunnel and Field velocity data for JRII-S Time Frame D.

Time Frame D – 112 RPM						
Height (m)	Wind Tunnel [at Full Scale]		DPG Field Data		Difference	
	u (m/s)	w (m/s)	u (m/s)	w (m/s)	%	%
25	5.7027	-0.1796	-	-	-	-
16	5.3242	-0.1439	5.56	0.011	4.29	234
10	5.0384	-0.1158	-	-	-	-
8	4.9287	-0.0935	5.02	-0.226	1.81	83.0
6	4.8212	-0.1139	-	-	-	-
4	4.6397	-0.0903	4.65	0.011	0.32	254
2	4.2988	-0.0245	4.03	0.093	6.47	343

Table B-9 - Scaled-up wind tunnel and Field velocity data for JRII-S Time Frame E.

Time Frame E – 118 RPM						
Height (m)	Wind Tunnel [at Full Scale]		DPG Field Data		Difference	
	u (m/s)	w (m/s)	u (m/s)	w (m/s)	%	%
25	6.0557	-0.2227	-	-	-	-
16	5.6788	-0.1877	5.84	-0.063	2.73	99.4
10	5.3882	-0.1558	-	-	-	-
8	5.2425	-0.1348	5.27	-0.263	0.62	64.5
6	5.0883	-0.1119	-	-	-	-
4	4.9144	-0.0947	4.96	-0.017	0.93	139
2	4.5672	-0.0347	4.38	0.096	4.24	429

Table B-10 - Scaled-up wind tunnel and Field velocity data for JRII-S Time Frame F.

Time Frame F – 135 RPM						
Height (m)	Wind Tunnel [at Full Scale]		DPG Field Data		Difference	
	u (m/s)	w (m/s)	u (m/s)	w (m/s)	%	%
25	6.9111	-0.2101	-	-	-	-
16	6.4538	-0.1781	6.73	-0.149	4.25	18.1
10	6.1760	-0.1590	-	-	-	-
8	6.0346	-0.1279	6.01	-0.360	0.32	95.2
6	5.8769	-0.1183	-	-	-	-
4	5.6578	-0.0894	5.61	-0.071	0.77	22.5
2	5.2897	-0.0340	4.93	0.101	7.05	403

Appendix B4 – Comparison Plots Between Wind Tunnel and Jack Rabbit II – Special Sonic Anemometer Study Time Frames Velocity Measurements

Plots of Time Frames C and E are shown in the main body (Section 2.5.2)

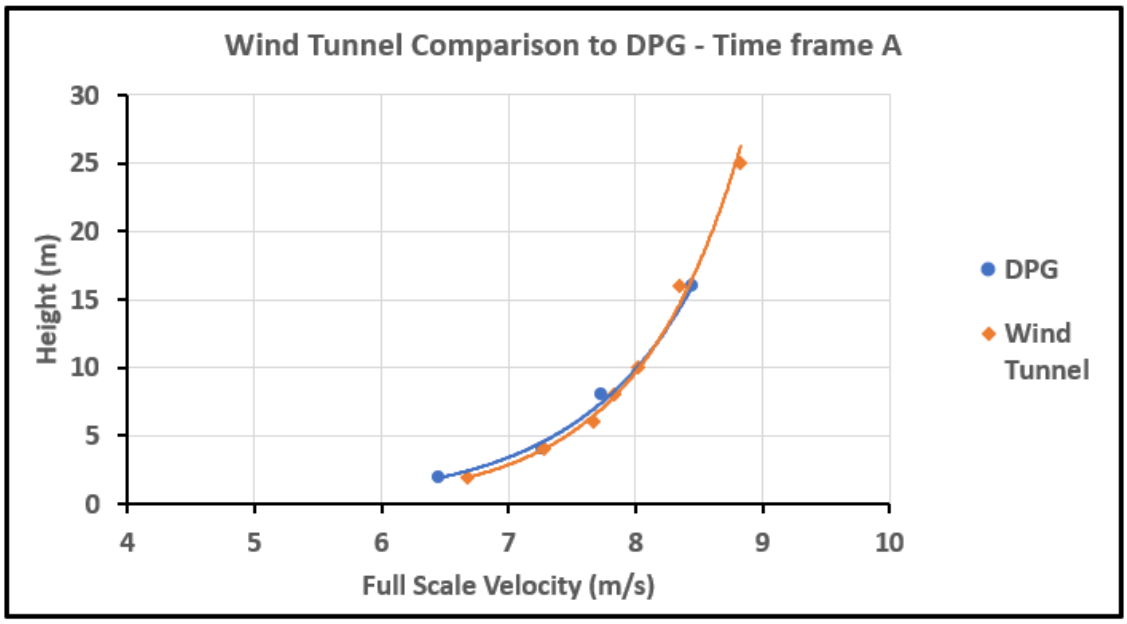

Figure B-3 - Velocity Profile comparisons between field and scale models for JRII-S Time Frame A.

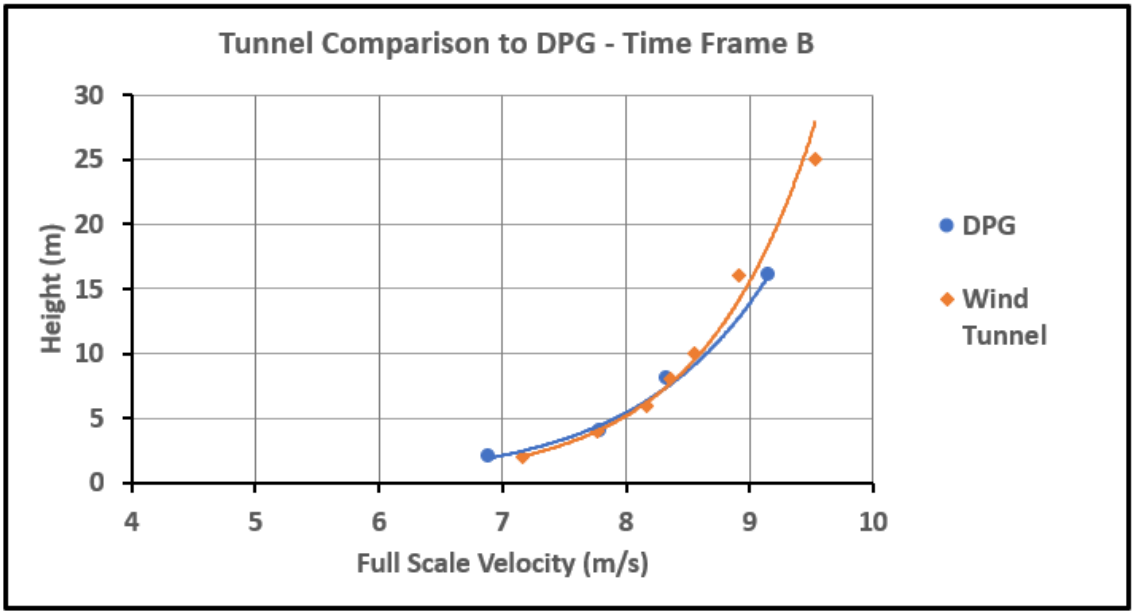

Figure B-4 - Velocity Profile comparisons between field and scale models for JRII-S Time Frame B.

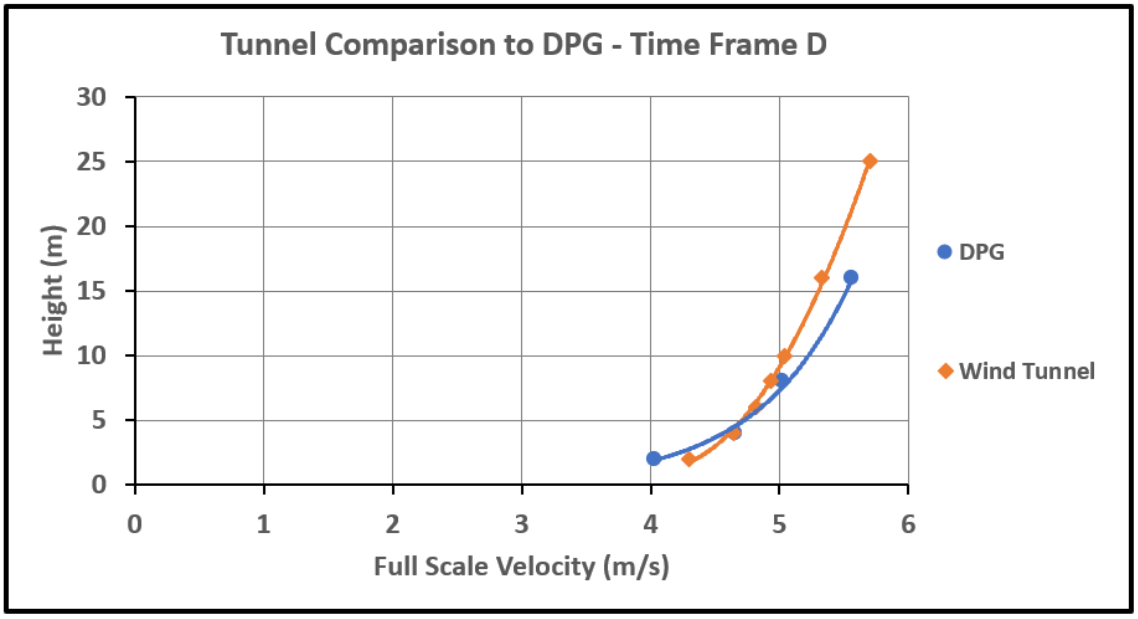

Figure B-5 - Velocity Profile comparisons between field and scale models for JRII-S Time Frame D.

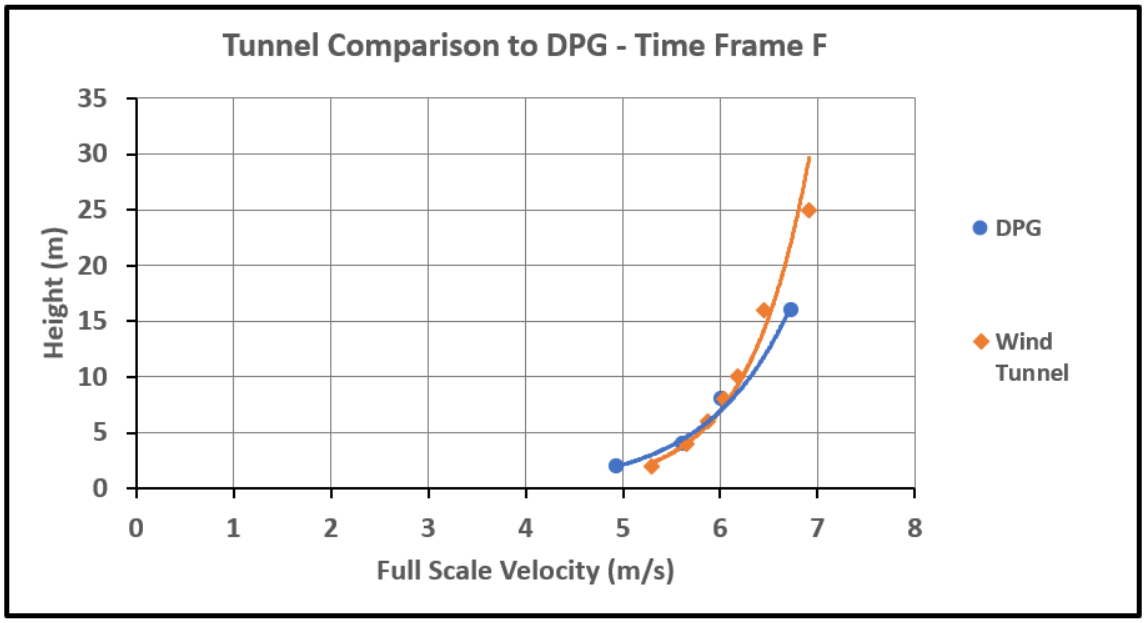

Figure B-6 - Velocity Profile comparisons between field and scale models for JRII-S Time Frame F.

Appendix B5 – Agreement Between Wind Tunnel and Jack Rabbit II – Special Sonic Anemometer Study Time Frames C and E Friction Velocity Measurements

Data shown in Tables B-11 and B-12 were acquired with 3D LDV at Tower 3 location, using one row of Irwin spires and sparse (i.e., 2 ft apart) surface roughness elements.

Table B-11 - Scaled-up wind tunnel and Field friction velocity data for JRII-S Time Frame C.

Time Frame C – 93 RPM			
Height (m)	Wind Tunnel [at Full Scale]	DPG Field Data	Difference
	u* (m/s)	u* (m/s)	%
16	0.1650	0.1854	11.63
10	0.1685	-	-
8	0.1827	0.1963	7.19
6	0.1857	-	-
4	0.1770	0.1626	8.46
2	0.1823	0.1328	31.45
AVERAGE	**0.1769**	**0.1693**	**4.49**

Table B-12 - Scaled-up wind tunnel and Field friction velocity data for JRII-S Time Frame E.

Time Frame E – 188 RPM			
Height (m)	Wind Tunnel [at Full Scale]	DPG Field Data	Difference
	u* (m/s)	u* (m/s)	%
16	0.2040	0.2032	0.35
10	0.2168	-	-
8	0.2387	0.2172	9.42
6	0.2295	-	-
4	0.2439	0.2112	14.35
2	0.2286	0.1687	30.14
AVERAGE	**0.2269**	**0.2001**	**13.40**

Appendix C – Duration of the Open Time of the Area Source for the Release Simulations of the Jack Rabbit II Field Tests

The last column of Table C-1 includes 0.3 sec added to the scaled-down value of the discharge period to account for the delay between opening the area source and the flow exiting the source into the tunnel (Gallimore, 2023). The simulated chlorine release to the tunnel consisted of a mixture of 304 L/min of air, 76 L/min of SF_6, and 300 L/min of CO_2. Commercially available fog fluid (Rosco™ Clear Fog Fluid) was added at 21.4 mL/min (Minimum setting in the Rosco™ fog machine remote control). The disk was placed 7 mm above the pad.

Table C-1 - Duration of chlorine releases during JR-II (Spicer & Tickle, 2021) and duration of simulated releases in the CHRC wind tunnel model.

JR-II Trial	Full-Scale Discharge Period (sec) (Spicer & Tickle, 2021)	Tunnel Scale Discharge Period (sec)	Area Source Open Interval (msec)
Trial 1	20.3	2.87	3170
Trial 2	**30.0**	**4.24**	**4540**
Trial 3	16.6	2.33	2630
Trial 4	**25.9**	**3.66**	**3960**
Trial 5	30.6	4.33	4630

The exit port of the chlorine tank was not placed at the center of the concrete pad. To resolve the forces associated with the release, the exit port of the chlorine tank in the field test was placed 1 m off-center from the vessel (Spicer & Tickle, 2021). This off-center effect was accounted for in the tunnel by covering the top of the area source with an annulus: 50 cm outside diameter covering the outer parts of the area source and 32 cm inner diameter circle to allow the flow to pass through. The inner circle is set off-center by 2 cm in the positive y-direction.

Appendix D – Supplemental PIV Information

Table D-1 - PIV supplemental information for tests in the XZ plane (Vertical laser sheet).

JR-II/JRII-S Wind Condition	Fan Speed (RPM)	Simulated Release?	ΔT (µs)	Average plots sample size
Time Frame C	93	No	1700	1,499
Time Frame E	118	No	1300	1,994
Trial 4	60	No	2500	1,996
Trial 4	60	Yes (Cl_2 simulant)	2500	820 (Steady State) 595 (Final Phase)
Trial 4	60	Yes (Neutrally Buoyant)	2500	820
Trial 2	128	No	1100	1,996
Trial 2	128	Yes (Cl_2 simulant)	1100	1,020 (Steady State) 595 (Final Phase)

Table D-2 - PIV supplemental information for tests in the XY plane (Horizontal laser sheet).

JR-II/JRII-S Wind Condition	Fan Speed (RPM)	Simulated Cl_2 Release?	Wind direction (°)	ΔT (µs)	Average plots sample size
Time Frame C	93	No	0	5500	2,000
Time Frame D	112	No	7	3500	2,000
Trial 4	60	No	22	5000	2,000
Trial 4	60	Yes	22	7000	810

Table D-3 - Global validation set threshold for each experiment condition.

JR-II/JRII-S Wind Condition	Laser Sheet Orientation	Global Validation Threshold (px/sec)	Global Validation Threshold (m/s)
Time Frame C	Vertical	± 11,000	± 1.00
Time Frame E	Vertical	± 13,000	± 1.15
Trial 2	Vertical	± 13,000	± 1.15
Trial 4 (Pre-Release, DTA release)	Vertical	± 8,000	± 0.70
Trial 4 (Neutrally Buoyant Release)	Vertical	± 6,000	± 0.55
Time Frame C	Horizontal	± 4,250	± 0.50
Time Frame D	Horizontal	± 6,800	± 0.80
Trial 4 (Pre-Release)	Horizontal	± 4,300	± 0.50
Trial 4 (DTA Release)	Horizontal	± 6,000	± 0.70

Table D-4 - Additional PIV notes

Category	Notes
Laser Power	Time (μs) after peak power in the Q-Switch settings: High: 280 (both lasers); **Medium: 215 (Laser A) & 210 (Laser B)**; Low 135 (both lasers) All PIV data is this dissertation was captured using the medium setting in both laser cavities
Seeding	Fog was added to the entire tunnel room using the (non-modified) Rosco™ Vapour Fog Machine Fog Machine operated using the remote control at setting 1 (knob position) Tunnel was fogged using a mixture of glycerin and water 50% v/v Operating the fog machine for 5 minutes provides sufficient seeding for PIV
Camera	**Camera will overheat when cords are connected, even if camera is "off"** It is necessary to place a desk fan pointing at the camera when it is not in use to prevent overheating and possible damages
External Trigger	External trigger was used to capture PIV data in the simulated release cases. Details and step-by-step operation instructions for the external trigger mode are available in the PIV procedures at the CHRC
Particle Focusing	Particle focusing works better over a dark, distant background No problems are expected in the particle focusing on the vertical laser sheet (background is the tunnel wall in the positive y-direction, approximately 3 m behind the laser sheet) It can become a problem on the horizontal laser sheet, due to the proximity of the tunnel floor. For focusing, it is recommended to create a dark background by removing tunnel tiles and placing black coverings on the room floor. To verify the focus, it is recommended to take a small sample run (around 20 images) and process with background subtraction

Appendix E – Anemometry Results from the Jack Rabbit II – Special Sonic Anemometry Study Field Test

Velocity data shown are the averages calculated in the 30 min interval of each Time Frame.

Appendix E1 – Time Frame C

Table E-1 - Sonic Anemometer data from JRII-S field test Time Frame C.

Sonic Anemometer Code	u (m/s)	v (m/s)	w (m/s)	Notes
S11L1	0.1626	0.4099	-0.0600	
S11L2	0.8316	0.3331	0.0010	
S11L3	4.5324	-0.4597	3.0330	Values for u and w components are unreasonable
S21	0.5678	0.1408	-0.0060	
S22	0.3309	-0.1715	-0.1240	
S23	1.8250	-0.1205	0.0610	
S24	0.9565	0.2044	0.0830	
S25	0.9058	0.3050	0.0680	
S31L1	-0.2429	0.6272	0.2010	
S31L2	0.1840	-0.0472	0.0900	
S31L3	2.2188	-0.2581	-0.1400	
S41	-0.5087	0.7212	0.0760	
S51	0.1849	0.5975	-0.0760	
S61L1	0.0385	0.3872	-0.3560	
S61L2	0.8048	-0.0914	-0.5050	
S61L3	1.2383	-1.5565	-0.2440	
S61L4	2.1863	-2.1605	0.2320	
S71	2.2052	-0.4325	-0.2320	
S72	1.8424	-0.8477	-0.3930	
S73	2.9262	-0.9487	-0.2290	
S74	1.3968	-0.2811	-0.1160	
S75	1.4003	-0.2800	-0.2770	
S81	1.7400	-0.6153	-0.0700	
S82L1	-0.3893	0.0422	0.0500	
S82L2	-0.3914	0.0076	-22.8240	Value for w component is unreasonable
S82L3	-0.2570	-0.0202	0.0990	
S82L4	3.2277	-0.4456	-0.2400	
S83	1.8106	-0.1704	-0.1790	
S1001	0.0392	0.3705	-0.2100	
S1101	0.5353	0.2013	0.0620	

Appendix E2 – Time Frame E

Table E-2 - Sonic Anemometer data from JRII-S field test Time Frame E.

Sonic Anemometer Code	u (m/s)	v (m/s)	w (m/s)	Notes
S11L1	0.2430	-0.0320	-0.2180	
S11L2	1.2260	-0.2271	-0.1720	
S11L3	6.1839	-1.4789	5.8120	Values for u and w components are unreasonable
S21	0.9250	-0.2530	0.0820	
S22	*NO DATA*	*NO DATA*	*NO DATA*	
S23	2.5924	-0.6605	0.0370	
S24	0.8776	-0.0436	0.0320	
S25	0.9199	-0.0405	0.0800	
S31L1	-0.4001	0.0523	0.3490	
S31L2	-0.0451	-0.0832	0.2310	
S31L3	3.0437	-0.7804	-0.2180	
S41	*NO DATA*	*NO DATA*	*NO DATA*	
S51	*NO DATA*	*NO DATA*	*NO DATA*	
S61L1	-0.3725	0.0356	-0.5600	
S61L2	0.4865	-0.7577	-0.8470	
S61L3	1.3381	-2.0305	-0.3990	
S61L4	2.6633	-3.3246	0.2650	
S71	*NO DATA*	*NO DATA*	*NO DATA*	
S72	*NO DATA*	*NO DATA*	*NO DATA*	
S73	3.8571	-1.7903	-0.2240	
S74	2.4234	-0.6576	-0.3540	
S75	1.7518	-0.2893	-0.2380	
S81	2.2508	-0.6062	-0.1890	
S82L1	-0.5245	0.1985	0.1080	
S82L2	-0.5215	0.1325	-24.0780	Value for w component is unreasonable
S82L3	-0.3562	0.0654	0.1770	
S82L4	4.1847	-1.3170	-0.2930	
S83	*NO DATA*	*NO DATA*	*NO DATA*	
S1001	-0.0943	0.0346	-0.4090	
S1101	0.1810	-0.0237	0.0920	

Appendix F – Anemometry Results from the Scale Model of the Jack Rabbit II – Special Sonic Anemometry Study in the Wind Tunnel

Appendix F1 – Time Frame C

Table F-1 - LDV results in the model at Sonic Anemometer locations in JRII-S Time Frame C conditions, with comparison to JRII-S field data.

Sonic Anemometer Code	u (m/s)	v (m/s)	w (m/s)	Diff u (%)	Diff v (%)	Diff w (%)
S11L1	0.1909	0.8423	-0.4085	16.0	69.1	149
S11L2	1.0308	0.6334	-0.3299	21.4	62.1	201
S11L3	2.6021	-0.0381	-0.0588	54.1	169	208
S21	1.0532	-0.2621	0.0470	59.9	664	258
S22	1.3652	-0.0155	-0.2588	122	167	70.4
S23	2.2330	-0.0044	-0.0416	20.1	186	1,059
S24	1.2898	-0.1826	-0.3555	29.7	3,548	322
S25	1.0568	-0.1598	-0.0831	15.4	641	2,001
S31L1	-0.3308	0.3088	0.2990	30.6	68.1	39.2
S31L2	0.0448	-0.0819	0.2570	122	53.7	96.2
S31L3	2.6499	-0.0080	-0.1239	17.7	188	12.2
S41	-0.1693	0.9370	0.2980	100	26.0	119
S51	0.0580	0.8030	0.0399	104	29.4	643
S61L1	-0.0582	0.3417	-0.9347	982	12.5	89.7
S61L2	0.5665	0.1277	-1.2273	34.8	1,206	83.4
S61L3	1.1951	-0.0712	-0.7329	3.55	183	100
S61L4	3.7511	-0.0147	0.2591	52.7	197	11.0
S71	1.8074	0.1718	0.0395	19.8	464	282
S72	2.0814	-0.1254	-0.5924	12.2	148	40.4
S73	3.9229	0.0429	-0.1380	29.1	219	49.6
S74	2.1245	0.1540	-0.4653	41.3	685	120
S75	1.8881	-0.0595	-0.0164	29.7	130	178
S81	2.0693	-0.0091	-0.2420	17.3	194	110
S82L1	-0.6168	0.0104	0.1040	45.2	121	70.2
S82L2	-0.5304	-0.0035	0.1263	30.2	541	202
S82L3	-0.3602	-0.0012	0.2851	33.5	178	96.9
S82L4	3.9093	-0.0069	-0.2894	19.1	194	18.7
S83	2.0998	0.2427	-0.1779	14.8	1,143	0.61
S1001	-0.6158	-0.0624	0.0324	227	281	273
S1101	0.2015	0.3472	0.0055	90.6	53.2	167

Appendix F2 – Time Frame E

Table F-2 - LDV results in the model at Sonic Anemometer locations in JRII-S Time Frame E conditions, with comparison to JRII-S field data.

Sonic Anemometer Code	u (m/s)	v (m/s)	w (m/s)	Diff u (%)	Diff v (%)	Diff w (%)
S11L1	-0.0260	0.7085	-0.4123	248	219	61.6
S11L2	1.1007	0.3796	-0.3261	10.8	795	61.9
S11L3	3.4447	-0.1064	-0.0643	56.9	173	204
S21	1.3158	-0.3929	0.0161	34.9	43.3	134
S22	1.6592	-0.0913	-0.3151	*NO DATA*	*NO DATA*	*NO DATA*
S23	2.9626	-0.0774	-0.0621	13.3	158	790
S24	1.0961	-0.1532	-0.4008	22.1	111	235
S25	1.1228	-0.2072	-0.1503	19.9	135	655
S31L1	-0.5528	0.1701	0.3078	32.0	106	12.5
S31L2	-0.1606	-0.0188	0.3232	112	126	33.3
S31L3	3.4247	-0.0881	-0.1163	11.8	159	60.8
S41	-0.3540	0.6283	0.2976	*NO DATA*	*NO DATA*	*NO DATA*
S51	0.0276	0.8057	0.0091	*NO DATA*	*NO DATA*	*NO DATA*
S61L1	-0.1665	0.1420	-1.3171	76.4	120	80.7
S61L2	0.6995	0.0581	-1.5660	35.9	233	59.6
S61L3	1.5089	-0.1285	-0.9017	12.0	176	77.3
S61L4	4.8281	-0.0413	0.3354	57.8	195	23.5
S71	2.4244	0.2252	-0.0941	*NO DATA*	*NO DATA*	*NO DATA*
S72	2.9061	-0.1634	-0.8039	*NO DATA*	*NO DATA*	*NO DATA*
S73	5.1135	-0.0471	-0.1840	28.0	190	19.6
S74	2.6122	0.2629	-0.5448	7.50	466	42.5
S75	2.4898	-0.1891	-0.2997	34.8	41.9	22.9
S81	2.6951	-0.0540	-0.2827	18.0	167	39.7
S82L1	-0.7845	0.0393	0.1285	39.7	134	17.3
S82L2	-0.6844	0.0026	0.1603	27.0	192	203
S82L3	-0.5241	-0.0050	0.3943	38.1	233	76.1
S82L4	5.0309	0.0893	-0.3774	18.4	229	25.2
S83	2.5791	0.4136	-0.2157	*NO DATA*	*NO DATA*	*NO DATA*
S1001	-0.6899	0.1758	0.0066	152	134	207
S1101	0.2544	0.4052	-0.0074	33.7	225	235

Appendix G – Supplementary information for the 3D vs. 2D LDV setup study

Appendix G1 – Extrapolated and Actual Values of Turbulence Intensity Components

The turbulence intensity in a given direction (ix, iy, iz) is defined as the ratio between the root mean square of the instantaneous velocity measurements in a given direction and the average velocity in that direction, as shown in Equations G-1 through G-5. Turbulence intensity measurements differ from turbulent kinetic energy (TKE) measurements, as the latter is a more direct measurement of overall turbulence, normalized by unit mass. Turbulence intensities describe the turbulence in each component, normalizing the fluctuation per the average velocity along the same direction.

$$i_x = \frac{\left(\overline{u_{act}'^2}\right)^{1/2}}{u_{act}} \quad \textbf{(G-1)}$$

$$i_{y,act} = \frac{\left(\overline{v_{act}'^2}\right)^{1/2}}{v_{act}} \quad \textbf{(G-2)}$$

$$i_{z,act} = \frac{\left(\overline{w_{act}'^2}\right)^{1/2}}{w_{act}} \quad \textbf{(G-3)}$$

$$i_{y,ext} = \frac{\left(\overline{V2'^2}\right)^{1/2}}{\overline{V2}} \quad \textbf{(G-4)}$$

$$i_{z,ext} = \frac{\left(\overline{V3'^2}\right)^{1/2}}{\overline{V3}} \quad \textbf{(G-5)}$$

The results for the turbulence values for the lower and higher wind cases are shown in Figures G-1 and G-2, respectively. Actual and extrapolated tabulated values of iy and iz are shown in Tables G-1 and G-2, for the low and high wind cases respectively. As the turbulence intensity formula has the average velocity in the denominator, extremely high turbulence

intensity will be found if the average velocity at a specific height is near zero. For this work, this was a particular problem for iy values. Extremely high values of turbulence intensity (iy > 2500%) were discarded and are not shown in Figures G-1b and G-2b.

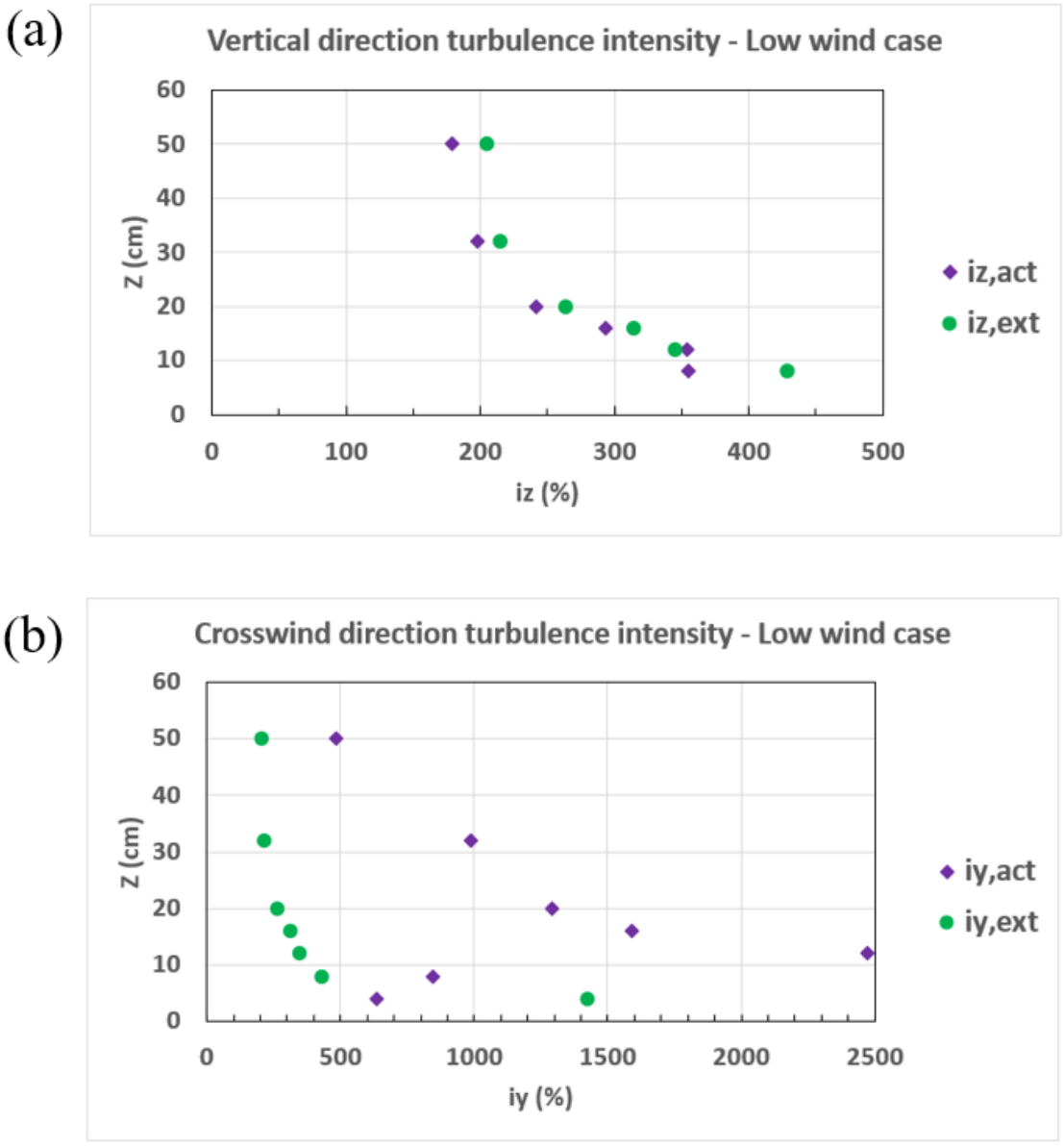

Figure G-1 Comparison between extrapolated 2D and actual 3D LDV measurements of (a) vertical and (b) cross-wind turbulent intensity in Time Frame C conditions.

(a)

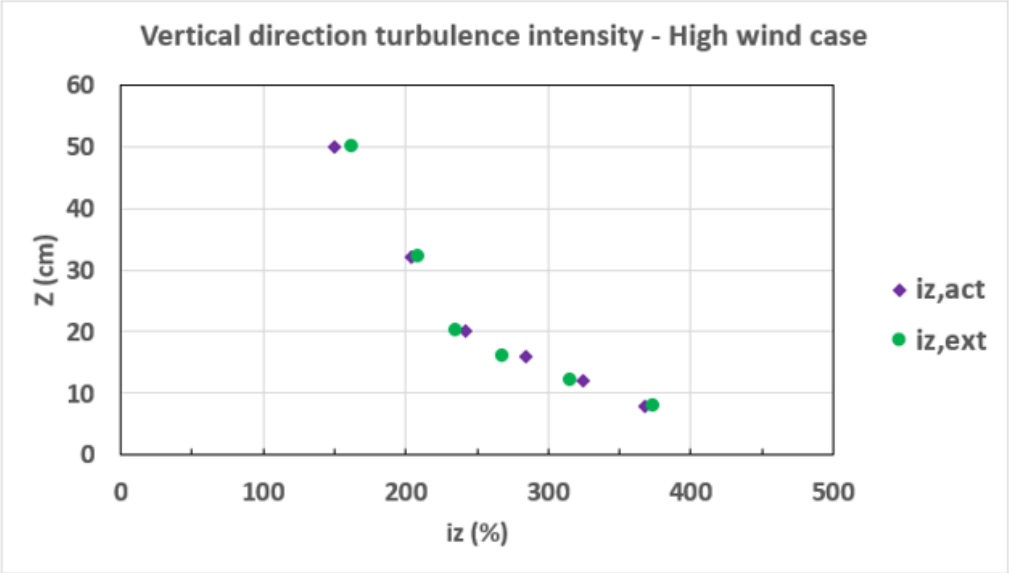

(b)

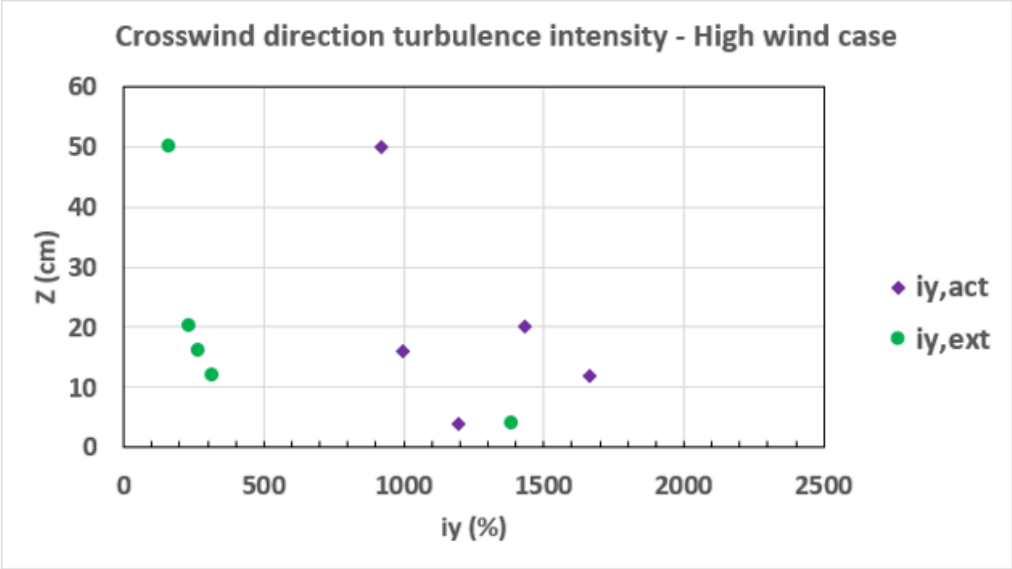

Figure G-2 - Comparison between extrapolated 2D and actual 3D LDV measurements of (a) vertical and (b) cross-wind turbulent intensity in Time Frame E conditions.

Just like observed in the average velocity comparison (as shown in Section 3.3 in the main body), the simplified setup fails to express the correct behavior in the cross-wind direction, showing significantly elevated errors in the values of iy in both wind speed cases, as shown in Figures G-1b and G-2b, averaging at 80% in the low wind case and 75% in the high wind case, across all heights. In the vertical direction, the extrapolated approximation is consistently close

to the actual turbulence intensity values at most heights. However, relatively high errors are observed at the lowest height (95% in the low wind case and 52% in the high wind case), where the turbulence is high, as shown in Figures G-1a and G-2a. The magnitude of the error decreased with height, averaging 10% in the low wind case and 4% in the high wind case, across 8 to 50 cm. Overall, the simplified setup does not yield an adequate approximation for most turbulence indicators, despite correctly showing the decrease of turbulence with height. It is also important to highlight that the extrapolated values of iy and iz had the same values at each height. Since those values start from the same population (V2) of 200,000 vectors, they have the same root mean square.

Table G-1 - Comparison between actual 3D LDV and extrapolated from 2D turbulence intensity in the lower wind speed case.

Lower wind velocity – 93 RPM fan speed							
Height (cm)	i_x (%)	$i_{y,act}$ (%)	$i_{y,ext}$ (%)	Error (%)	$i_{z,act}$ (%)	$i_{z,ext}$ (%)	Error (%)
4	12.0	638	1,424	123	730	1,424	95.1
8	10.2	847	429	49.3	355	429	20.7
12	9.4	2,473	345	86.0	354	345	2.44
16	8.8	1,589	314	80.2	293	314	7.14
20	8.3	1,294	263	79.7	242	263	8.45
32	7.5	987	215	78.2	198	215	8.50
50	6.2	485	205	57.8	179	205	14.5
		Average error (%)		**79.2**	**Average error (%)**		**22.4**

Table G-2 - Comparison between actual 3D LDV and extrapolated from 2D turbulence intensity in the higher wind speed case.

Higher wind velocity – 118 RPM fan speed							
Height (cm)	i_x (%)	$i_{y,act}$ (%)	$i_{y,ext}$ (%)	Error (%)	$i_{z,act}$ (%)	$i_{z,ext}$ (%)	Error (%)
4	11.2	1,193	1,386	16.2	915	1,386	51.6
8	10.2	5,747	374	93.5	368	374	1.59
12	9.3	1,663	316	81.0	324	316	2.62
16	8.7	997	268	73.2	284	268	5.84
20	8.2	1,430	236	83.5	242	236	2.34
32	7.1	12,985	209	98.4	204	209	2.40
50	5.8	922	163	82.3	150	163	8.94
		Average error (%)		**75.44**	**Average error (%)**		**10.8**

Appendix G2 – Study of the dependency of the error magnitude with the relative angle of the probe and the tunnel axis

The results shown in Chapter of the main body and in Appendix G1 indicate that the simplified 2D setup cannot accurately measure velocity and turbulence, especially in the cross-wind direction. The relative angle of the blue probe to the vertical axis causes its measurements to be biased towards the vertical component. A separate investigation is necessary to verify if placing the probe at different angles would fix this biasing.

Starting from the actual velocity components as measured by the full 3D setup (u_{act}, v_{act}, w_{act}), it is possible to predict the values of velocity components (V1, V2, V3) as measured by the probes in different theoretical configurations, with different values of probe angle α. This scenario is possible by using Equation 7 to calculate the (theoretical) measured components (V1, V2, V3) at each relative probe angle. Furthermore, new values of v_{ext} and w_{ext} can then be calculated via Equations 8b and 8c. After that, errors in velocity magnitude are calculated for every theoretical angle situation, as shown in Table G-3 for the high wind case and Table G-4 for the low wind case.

Table G-3 - Effect of the relative angle of the primary probe with the vertical axis in the error of extrapolating 2D LDV data into 3D measurements in Time Frame E conditions.

Higher Wind Velocity – 118 rpm fan speed							
h = 16 cm		**u_{act} = 0.7414 m/s**		**v_{act} = -0.0060 m/s**		**w_{act} = -0.0191 m/s**	
α (°)	V1 (m/s)	V2 (m/s)	V3 (m/s)	w_{ext} (m/s)	Error w (%)	v_{ext} (m/s)	Error v (%)
90	-0.7414	-0.0191	0.0135	-0.0191	0	0.0000	100
75	-0.7414	-0.0200	0.0135	-0.0193	1.15	-0.0052	13.7
60	-0.7414	-0.0195	0.0135	-0.0169	11.4	-0.0098	62.8
45	-0.7414	-0.0177	0.0135	-0.0126	34.3	-0.0126	109
30	-0.7414	-0.0147	0.0135	-0.0074	61.4	-0.0128	113
25	-0.7414	-0.0135	0.0135	-0.0057	70.1	-0.0122	104
10	-0.7414	-0.0092	0.0135	-0.0016	91.6	-0.0091	51.4
0	-0.7414	-0.0060	0.0135	0.0000	100	-0.0060	0

A single height (h = 16 cm) was chosen for this study. In both wind cases, the angle β remained fixed at 25°. V1 is invariant, as the green beams always measure the along-wind component directly. V3 is invariant because it depends only on the theoretical angle β.

Table G-4 - Effect of the relative angle of the primary probe with the vertical axis in the error of extrapolating 2D LDV data into 3D measurements in Time Frame C conditions.

Lower Wind Velocity – 93 rpm fan speed							
h = 16 cm		**u_{act} = 0.5742 m/s**		**v_{act} = 0.0029 m/s**		**w_{act} = -0.0139 m/s**	
α (°)	V1 (m/s)	V2 (m/s)	V3 (m/s)	w_{ext} (m/s)	Error w (%)	v_{ext} (m/s)	Error v (%)
90	-0.5742	-0.0139	0.0032	-0.0139	0	0.0000	100
75	-0.5742	-0.0127	0.0032	-0.0122	11.9	-0.0033	213
60	-0.5742	-0.0106	0.0032	-0.0092	34.0	-0.0053	283
45	-0.5742	-0.0078	0.0032	-0.0055	60.4	-0.0055	290
30	-0.5742	-0.0044	0.0032	-0.0022	84.0	-0.0038	233
25	-0.5742	-0.0032	0.0032	-0.0014	90.1	-0.0029	201
10	-0.5742	0.0004	0.0032	0.0001	101	0.0004	85.0
0	-0.5742	0.0029	0.0032	0.0000	100	0.0029	0

As shown in Tables G-3 and G-4, the minimum error in w_{ext} occurs when the probe is as close as possible to the direct measurement (α = 75°). Placing the probe at 90° would make direct measurements of the vertical velocity component, while completely missing the cross-wind component, while the opposite is valid for placing the probe at 0°. Similar behavior is observed

in v_{ext}, with smaller errors as close as possible to the direct measurement ($\alpha = 10°$) in the lower wind case. In general, the results of the error magnitude in the cross-wind (v-component) direction show that, once again, high errors are observed in the extrapolated values, indicating that it is not reliable to use the simplified LDV setup to obtain that component.

The error magnitudes in the cases above seem to be directly related to the characteristics of the flow field. It is important to notice that, in both wind cases, the vertical (w) velocity component is one order of magnitude larger than the cross-wind (v) component. Therefore, all measurements taken by the probe are skewed towards the larger component. Consequently, an angle position near the direct measurement (i.e., placing the probe horizontally, in which V2 and w_{act} coincide) yields the smallest error in the extrapolation. Therefore, if the velocity components differ vastly, it is preferable to measure them separately and directly.

The same theoretical study can be conducted in a hypothetical flow field, in which the vertical and cross-wind velocity components are the same order of magnitude. Results for such a hypothetical flow field (u_{hyp}, v_{hyp}, w_{hyp}) are shown in Table G-5. The same value of $\beta = 25°$ was used in this study. Since this is not the characteristic flow field of the CHRC wind tunnel, actual 3D LDV velocity measurements in this specific case could not be completed.

Table G-5 - Effect of the relative angle of the primary probe with the vertical axis in the error of extrapolating 2D LDV data into 3D measurements in a hypothetical flow field.

Hypothetical Flow Field							
u_{hyp} = 0.7000 m/s			v_{hyp} = -0.0060 m/s		w_{hyp} = -0.0050 m/s		
α (°)	V1 (m/s)	V2 (m/s)	V3 (m/s)	w_{ext} (m/s)	Error w (%)	v_{ext} (m/s)	Error v (%)
90	-0.7000	-0.0050	0.0076	-0.0050	0	0.0000	100
75	-0.7000	-0.0064	0.0076	-0.0062	23.3	-0.0017	72.5
60	-0.7000	-0.0073	0.0076	-0.0063	27.0	-0.0037	38.9
45	-0.7000	-0.0078	0.0076	-0.0055	10.0	-0.0055	8.3
30	-0.7000	-0.0077	0.0076	-0.0038	23.0	-0.0067	11.1
25	-0.7000	-0.0076	0.0076	-0.0032	36.2	-0.0068	14.1
10	-0.7000	-0.0068	0.0076	-0.0012	76.5	-0.0067	11.2
0	-0.7000	-0.0060	0.0076	0.0000	100	-0.0060	0

As shown in Table G-5, with the vertical and cross-wind velocity components of the same magnitude, placing the primary probe at 45° provides a valid approximation due to the equal contribution to the measurement from both components. This result is as expected, based on geometric considerations.

Appendix G3 – Alternative Setup – Placing the primary probe at angle to measure a vectorial sum

If the full 3D setup is not available, a possible alternative setup consists of placing the main probe at an angle and measuring one component directly using the green beams and a vectorial sum of the other two components using the blue beams. Figure G-3 compares the combined (v + w) vector obtained via 3D setup actual measurement and via 2D extrapolation at both wind speeds.

(a)

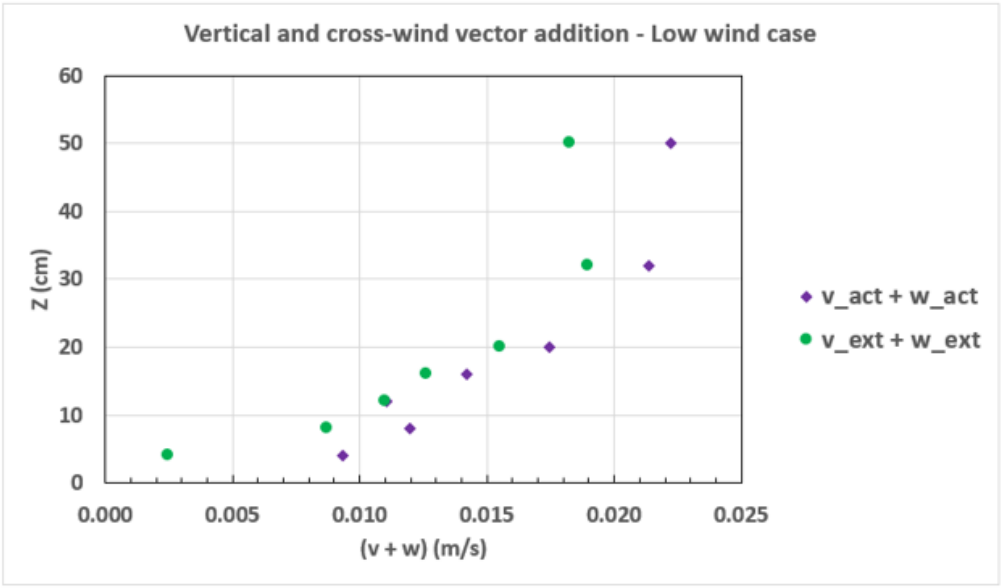

(b)

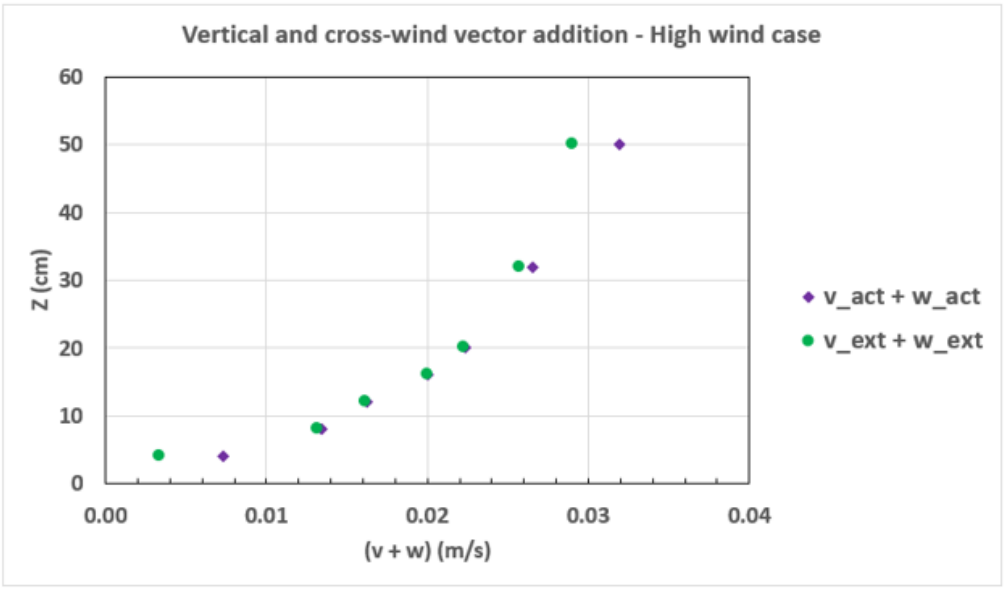

Figure G-3 - Comparison between extrapolated 2D and actual 3D LDV measurements of the combined vertical (w) and cross-wind (v) velocity components in (a) Time Frame C and (b) Time Frame E conditions.

As shown in Figure G-3, the extrapolated values of the (v + w) vectorial sum are sufficiently close to actual values measured by the full 3D setup, except for the lowest height. The error from obtaining the (v + w) vectorial sum from the simplified 2D setup averages 13.5% at the lower speed case and 2.4% in the higher speed case, when averaging the six tallest heights. The difference observed in the error magnitude between high and low speed cases can be

attributed to the difference in magnitude between the v_{act} and w_{act} components. As the values of vertical and cross-wind components are closer in the high wind case, it yields a better approximation for the value of the (v + w) vectorial sum.

Appendix G4 – Extrapolated and Actual Velocity Components Tabulated Data

Table G-6 - Comparison between actual 3D LDV and extrapolated from 2D velocity components in the lower wind speed case.

Lower wind velocity – 93 RPM fan speed							
Height (cm)	u (m/s)	v_{act} (m/s)	v_{ext} (m/s)	Error (%)	w_{act} (m/s)	w_{ext} (m/s)	Error (%)
4	0.4971	0.0080	-0.0007	108	-0.0048	-0.0024	49.6
8	0.5308	0.0056	-0.0023	141	-0.0106	-0.0084	20.6
12	0.5533	-0.0019	-0.0029	55.9	-0.0109	-0.0106	2.62
16	0.5742	0.0029	-0.0033	214	-0.0139	-0.0122	12.3
20	0.5850	0.0035	-0.0041	218	-0.0171	-0.0150	12.2
32	0.6235	0.0044	-0.0050	215	-0.0209	-0.0183	12.3
50	0.6619	0.0075	-0.0048	164	-0.0209	-0.0176	16.2
		Average error (%)		**159.45**	**Average error (%)**		**17.97**

Table G-7 - Comparison between actual 3D LDV and extrapolated from 2D velocity components in the higher wind speed case.

Higher wind velocity – 118 RPM fan speed							
Height (cm)	u (m/s)	v_{act} (m/s)	v_{ext} (m/s)	Error (%)	w_{act} (m/s)	w_{ext} (m/s)	Error (%)
4	0.6459	0.0054	-0.0009	116	-0.0049	-0.0032	35.2
8	0.6950	-0.0011	-0.0035	222	-0.0134	-0.0127	4.92
12	0.7196	-0.0036	-0.0043	18.1	-0.0158	-0.0156	1.14
16	0.7414	-0.0060	-0.0053	11.8	-0.0191	-0.0193	1.01
20	0.7620	-0.0040	-0.0059	46.8	-0.0220	-0.0215	2.34
32	0.8031	-0.0004	-0.0068	1,512	-0.0265	-0.0248	6.57
50	0.8564	0.0051	-0.0077	250	-0.0315	-0.0280	11.1
		Average error (%)		**310.9**	**Average error (%)**		**8.90**

Appendix G5 – Tabulated values of Extrapolated and Actual Measurements of Turbulent Kinetic Energy

Table G-8 - Comparison between actual 3D LDV and extrapolated from 2D turbulent kinetic energy in the lower wind speed case.

Lower wind velocity – 93 RPM fan speed			
Height (cm)	TKE_{act} (m^2/s^2)	TKE_{ext} (m^2/s^2)	Error (%)
4	0.00370	0.00241	34.8
8	0.00332	0.00217	34.5
12	0.00315	0.00207	34.3
16	0.00317	0.00205	35.2
20	0.00303	0.00201	33.7
32	0.00286	0.00192	33.1
50	0.00220	0.00153	30.6
Average error (%)			**33.7**

Table G-9 - Comparison between actual 3D LDV and extrapolated from 2D turbulent kinetic energy in the higher wind speed case.

Higher wind velocity – 118 RPM fan speed			
Height (cm)	TKE_{act} (m^2/s^2)	TKE_{ext} (m^2/s^2)	Error (%)
4	0.00573	0.00366	36.1
8	0.00568	0.00374	34.1
12	0.00535	0.00353	34.0
16	0.00531	0.00349	34.2
20	0.00499	0.00332	33.5
32	0.00461	0.00309	32.9
50	0.00347	0.00237	31.7
Average error (%)			**33.8**

Note how the average error is approximately equal across both wind speeds.

Appendix G6 – Additional Conclusions

Throughout Chapter 3 of the main body and Appendix G, the possibility of obtaining reliable LDV data using a simplified 2D setup, in lieu of using a more complex 3D setup was discussed. The setup of the study, and conclusions regarding the average velocity and overall turbulence measurements are shown in Chapter 3 of the main body.

The error quantification of the directional turbulence intensities showed a similar result to the errors observed in the comparison of the velocity components in the vertical and cross-wind directions, with a reasonable approximation for the vertical turbulence intensity and a poor approximation of the cross-wind velocity component.

Different setups with hypothetical relative angles between the main probe and the vertical axis were also studied. The results show that the error inherent to the extrapolated approximation is not only dependent on the relative angle of the probe, but also on the characteristics of the flow. Unequal velocity components in the vertical and cross-wind axis cause a bias in the measurement towards the faster velocity component.

If it is not possible to use the full three-dimensional setup, alternative setups with only the main probe are possible, but limited to measuring only two components. Or it is possible to measure one component and a vectorial sum of the other two components. The former is recommended if measuring one velocity component is of less importance, while the latter is recommended if all components are equally important and the flow in question has self-similar vertical and cross-wind velocity components.

Appendix H – Supplemental PIV Data

Appendix H1 – PIV Measurements Extracted at the Sonic Anemometer Locations in the Model

Table H-1 - Velocity measurements extracted from PIV data in the XZ plane at the locations of Sonic Anemometers in JRII-S Time Frame C conditions, with comparison to wind tunnel LDV and field data.

Time Frame C – XZ Plane (Vertical laser sheet)						
Sonic Anemometer Code	u [PIV] (m/s)	w [PIV] (m/s)	Diff u [DPG] (%)	Diff w [DPG] (%)	Diff u [LDV] (%)	Diff w [LDV] (%)
S61L1	-0.1628	-1.0861	324	101	94.6	15.0
S61L2	0.4408	-1.2679	58.4	86.1	25.0	3.25
S61L3	1.0368	-0.6092	17.7	85.6	14.1	18.4
S61L4	3.6739	0.3086	50.8	28.3	2.08	17.4
S73	3.9774	-0.0372	30.4	144	1.38	115
S82L1	-0.4569	0.1234	16.0	84.7	29.8	17.1
S82L2	-0.4304	0.1337	9.49	20	20.8	5.66
S82L3	-0.3500	0.2263	30.6	78.3	2.87	23.0
S82L4	3.8944	-0.2581	18.7	7.26	0.38	11.4
S1001	-0.6069	0.1686	228	1,827	1.46	136
S1101	-0.0042	0.1129	203	58.2	208	181

Table H-2 - Velocity measurements extracted from PIV data in the XY plane at the locations of Sonic Anemometers in JRII-S Time Frame C conditions, with comparison to wind tunnel LDV and field data.

Time Frame C – XY Plane (Horizontal laser sheet)						
Sonic Anemometer Code	u [PIV] (m/s)	v [PIV] (m/s)	Diff u [DPG] (%)	Diff v [DPG] (%)	Diff u [LDV] (%)	Diff v [LDV] (%)
S61L1	-0.1566	-0.4782	330	1902	91.6	1201
S71	1.6702	0.0912	27.6	307	7.89	61.3
S72	1.9773	-0.1056	7.06	156	5.13	17.2
S74	1.8502	-0.0927	27.9	101	13.8	804
S75	1.7433	-0.3398	21.8	19.3	7.98	140
S81	1.9516	0.0291	11.5	220	5.86	382
S82L1	-0.3500	0.2242	10.6	137	55.2	182
S83	1.7728	0.1790	2.11	8098	16.9	30.2
S101	-0.4990	-0.0673	234	289	21.0	7.63
S111	-0.0341	0.3036	227	40.5	282	13.4

Table H-3 - Velocity measurements extracted from PIV data in the XZ plane at the locations of Sonic Anemometers in JRII-S Time Frame E conditions, with comparison to wind tunnel LDV and field data.

Time Frame E – XZ Plane (Vertical laser sheet)						
Sonic Anemometer Code	u [PIV] (m/s)	w [PIV] (m/s)	Diff u [DPG] (%)	Diff w [DPG] (%)	Diff u [LDV] (%)	Diff w [LDV] (%)
S61L1	-0.1076	-1.3753	110	84.3	43.0	4.32
S61L2	0.5514	-1.6277	12.5	63.1	23.7	3.87
S61L3	1.3929	-0.7788	4.01	64.5	7.99	14.6
S61L4	4.6954	0.4374	55.2	49.1	2.79	26.4
S73	5.1100	-0.0139	28.0	177	0.07	172
S82L1	-0.6001	0.1514	13.4	33.5	26.6	16.4
S82L2	-0.5357	0.1447	2.68	202	24.4	10.2
S82L3	-0.4174	0.2689	15.8	41.2	22.7	37.8
S82L4	4.9847	-0.3110	17.4	5.97	0.92	19.3
S1001	-0.8083	0.1804	158	516	15.8	186
S1101	0.0060	0.0864	187	6.32	191	237

Appendix H2 – Along-wind and Vertical Velocity Components Plots in JR-II Trial 2 Conditions in the Steady State Phase of the Release

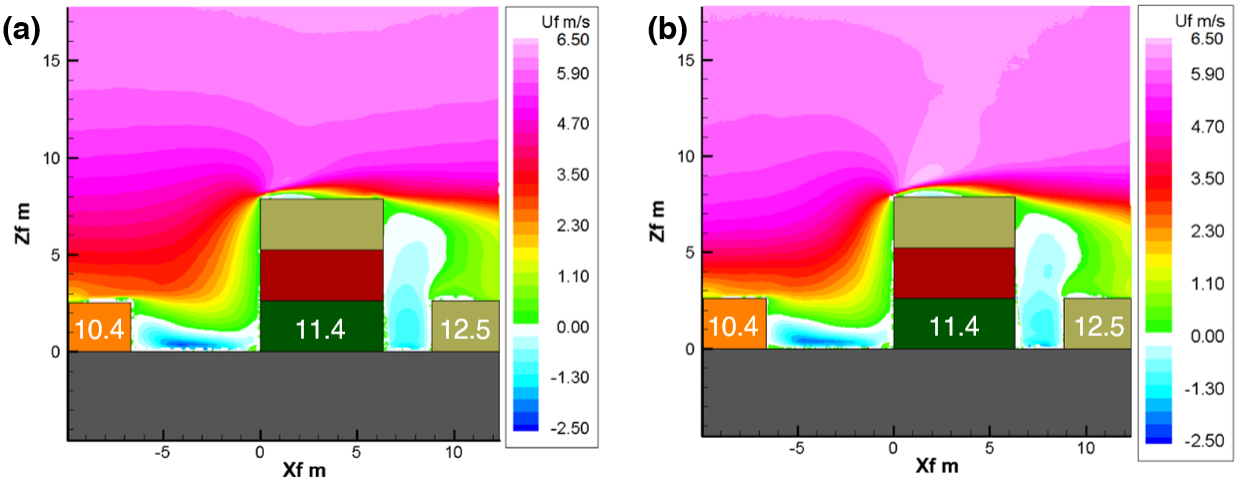

Figure H-1 - Average along-wind velocity component in JR-II Trial 2 conditions for (a) Pre-Release and (b) Steady State Phase of the Simulated chlorine release.

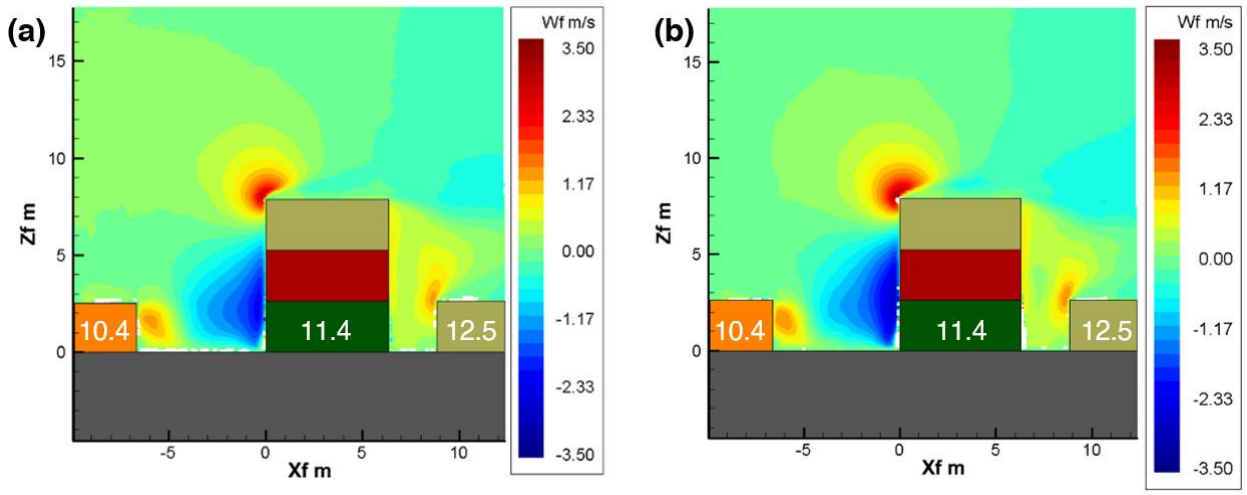

Figure H-2 - Average vertical velocity component in JR-II Trial 2 conditions for (a) Pre-Release and (b) Simulated chlorine release.

Appendix H3 – Along-wind and Vertical Velocity Components Plots in JR-II Trial 2

Conditions after the Steady State Phase of the Release

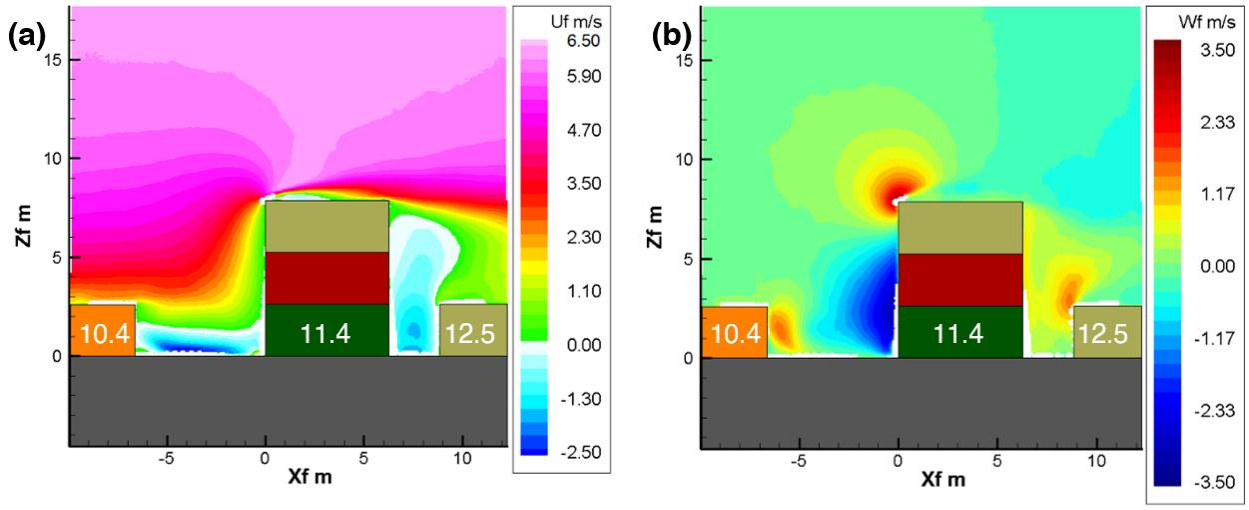

Figure H-3 - Average (a) along-wind and (b) vertical velocity components in JR-II Trial 2 conditions after the steady state phase of the release.

Appendix H4 – Along-wind and Vertical Velocity Components Plots in JR-II Trial 4 Conditions in the Steady State Phase of the Release

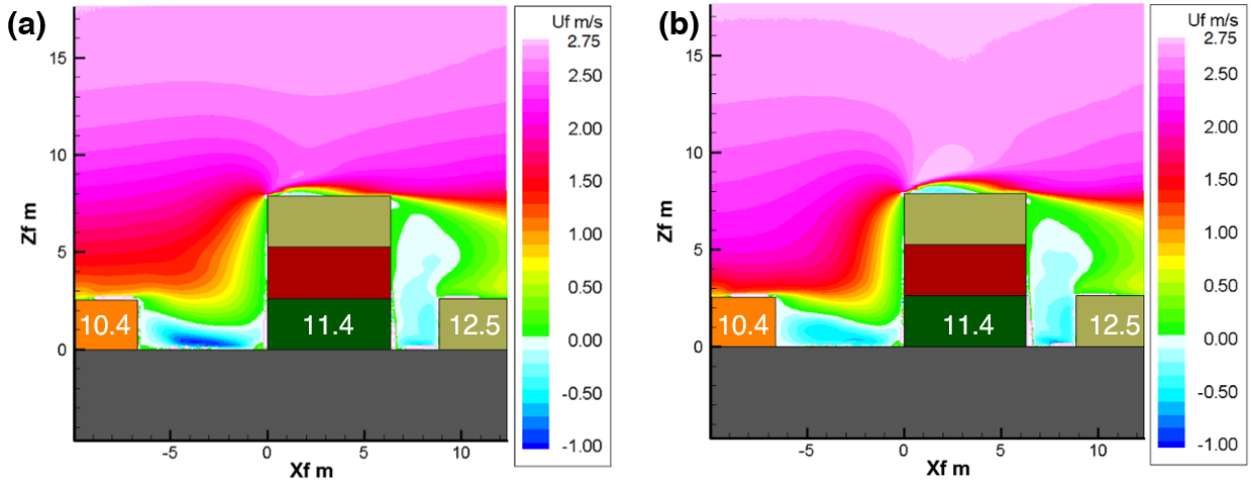

Figure H-4 - Average along-wind velocity component in JR-II Trial 4 conditions for (a) Pre-Release and (b) Simulated chlorine release.

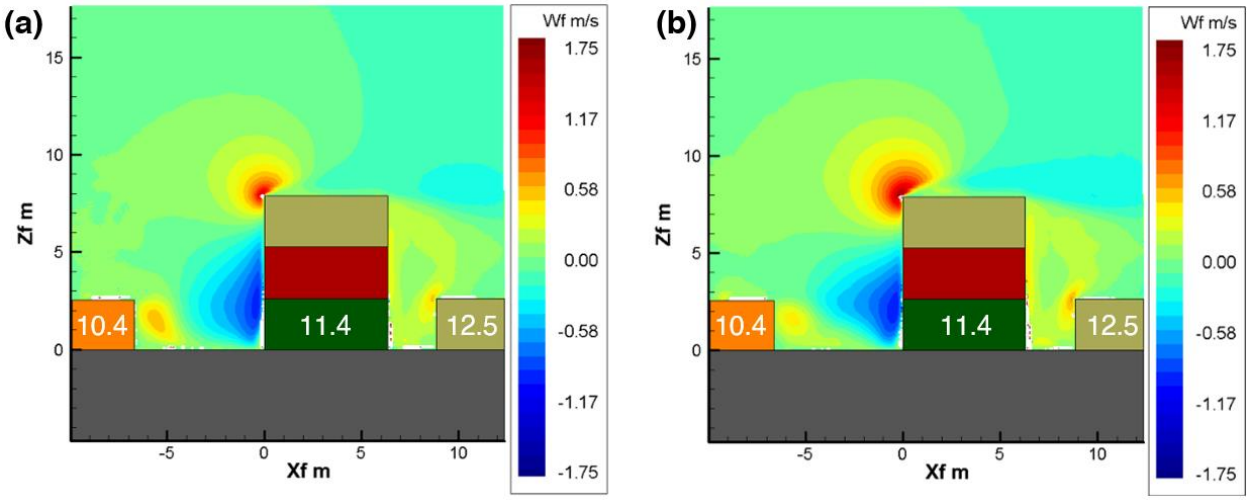

Figure H-5 - Average vertical velocity component in JR-II Trial 2 conditions for (a) Pre-Release and (b) Simulated chlorine release.

Appendix H5 – Along-wind and Vertical Velocity Components Plots in JR-II Trial 4 Conditions after the Steady State Phase of the Release

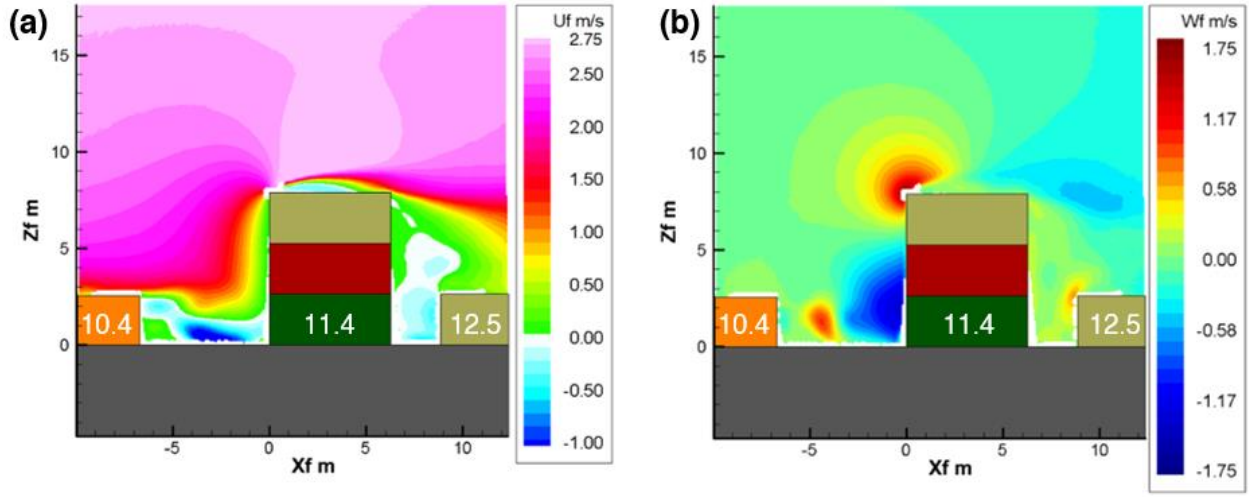

Figure H-6 - Average (a) along-wind and (b) vertical velocity components in JR-II Trial 4 conditions after the steady state phase of the release.

Appendix H6 – Along-wind and Vertical Velocity Components Plots During Neutrally Buoyant Releases in JR-II Trial 4 Conditions

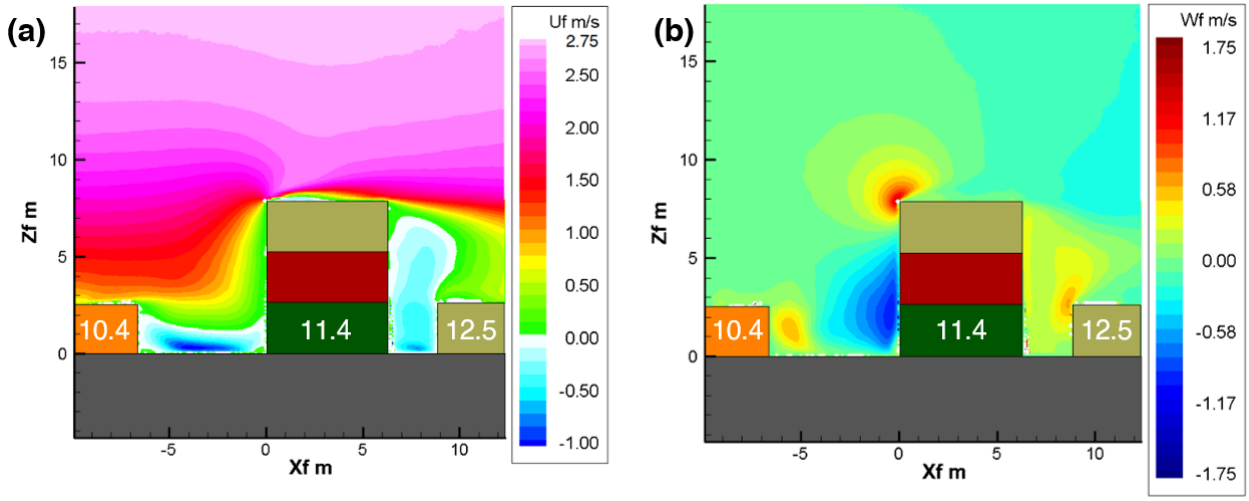

Figure H-7 - Average (a) along-wind and (b) vertical velocity components during neutrally buoyant releases in JR-II Trial 4 wind conditions.

Appendix H7 – Instantaneous Contributions to the Average Results in Each Particle Image Velocimetry Subregion (Vector count)

The average plots shown in this dissertation were calculated in Tecplot® Focus 2013R1 using the available number of measurements per location ("vector count"). Tecplot® Focus 2013R1 calls vector count by "CHC".

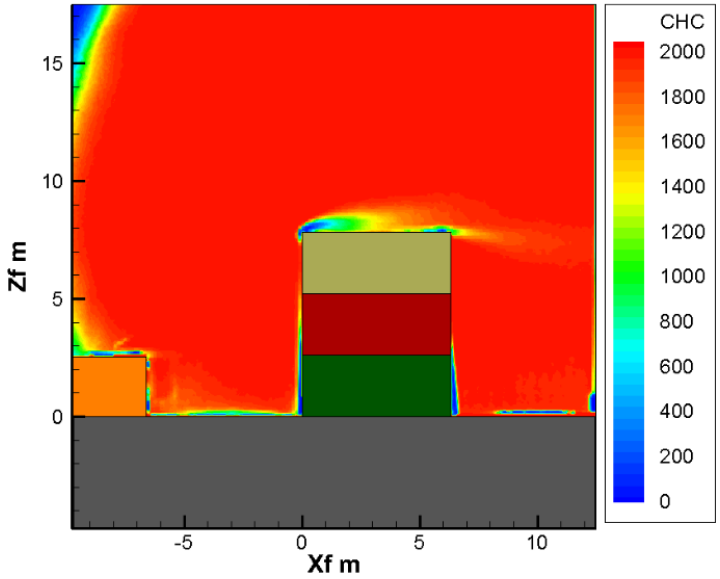

Figure H-8 - Vector count plot in JRII-S Time Frame E conditions in the XZ plane.

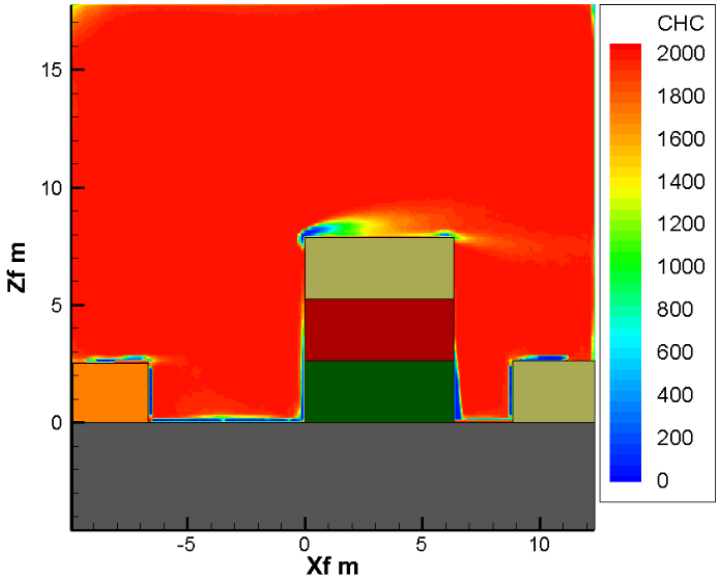

Figure H-9 - Vector count plot in JR-II Trial 2 pre-release conditions in the XZ plane.

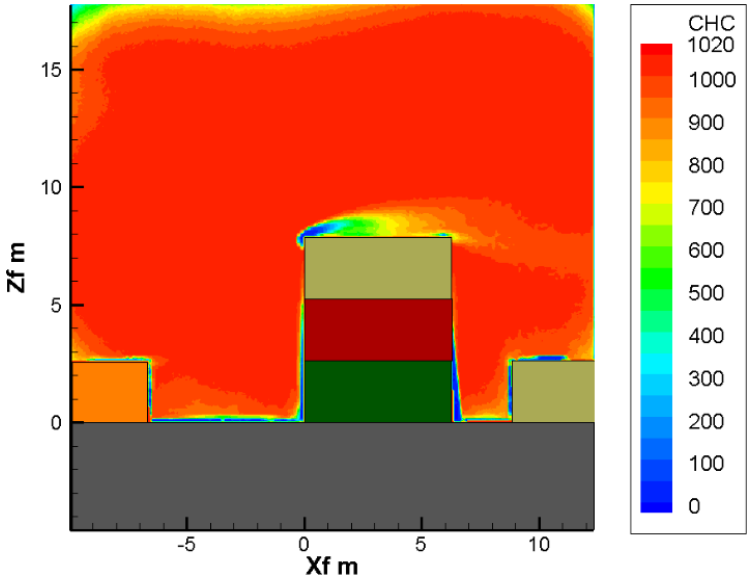

Figure H-10 - Vector count plot in JR-II Trial 2 conditions in the steady state phase of the release in the XZ plane.

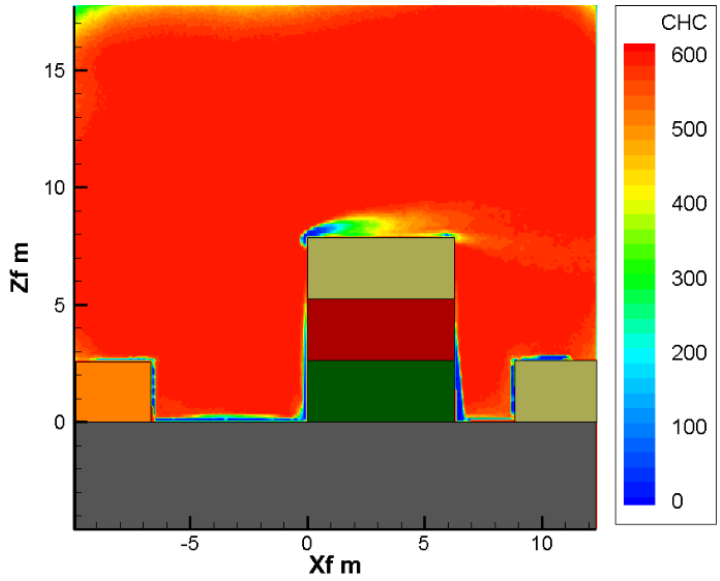

Figure H-11 - Vector count plot in JR-II Trial 2 conditions after the steady state phase of the release in the XZ plane.

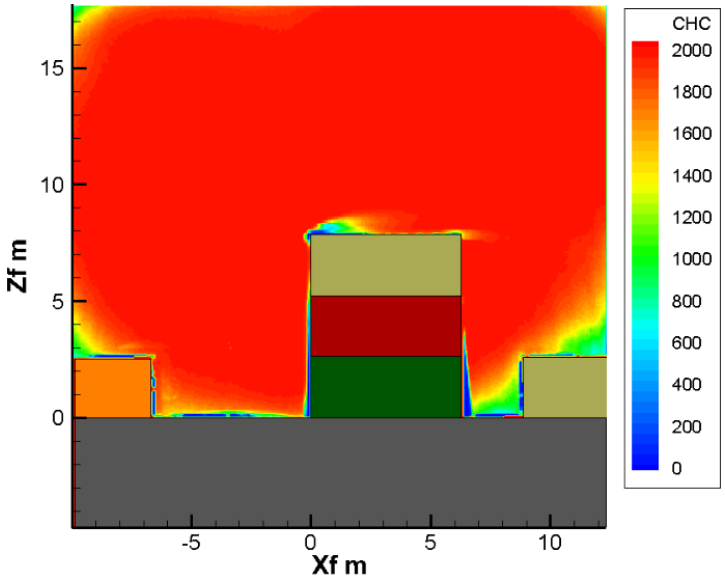

Figure H-12 - Vector count plot in JR-II Trial 4 pre-release conditions in the XZ plane.

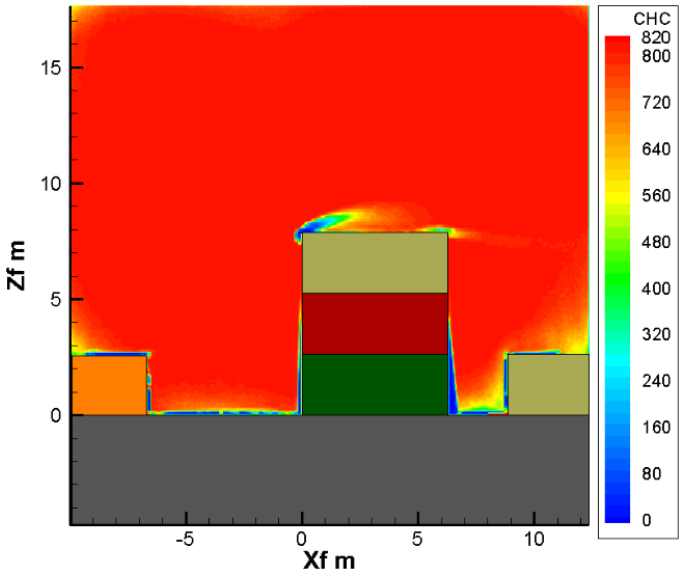

Figure H-13 - Vector count plot in JR-II Trial 4 conditions in the steady state phase of the denser-than-air release in the XZ plane.

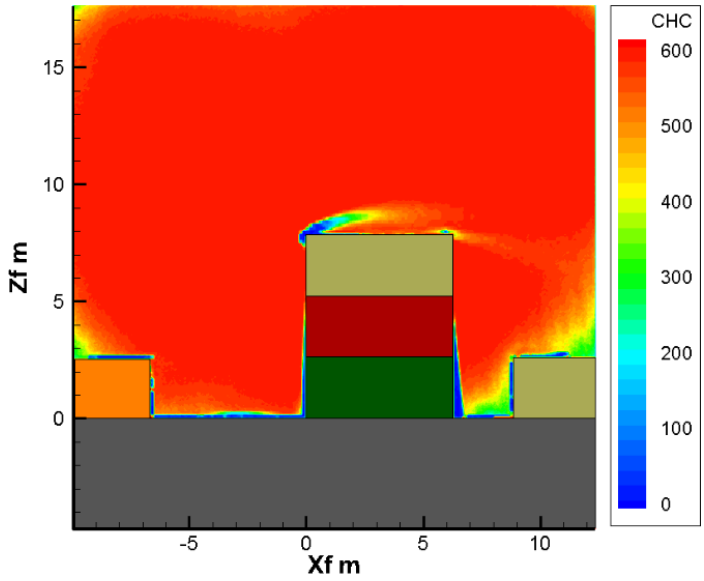

Figure H-14 - Vector count plot in JR-II Trial 4 conditions after the steady state phase of the denser-than-air release in the XZ plane.

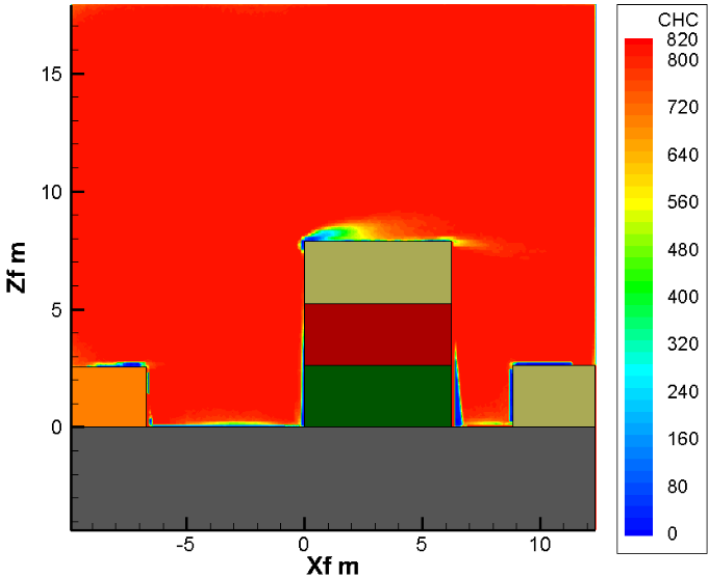

Figure H-15 - Vector count plot in JR-II Trial 4 conditions in the steady state phase of the neutrally buoyant release in the XZ plane.

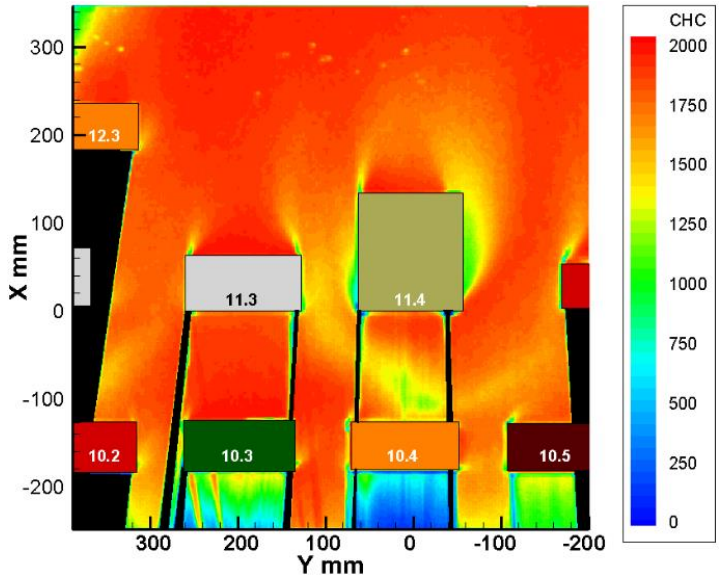

Figure H-16 - Vector count plot in JRII-S Time Frame D conditions in the XY plane.

Appendix H8 – PIV Convergence Study

A sequence of 1,500 PIV instantaneous PIV measurements was conducted in Time Frame C wind conditions. The setup used was the same as described for the PIV measurements in the XZ plane (as discussed in Section 4.2.1). The time interval between pulses was set at 1700 μs. Averages velocities in the XZ plane were calculated with samples sizes of 100, 300, 600, 900, 1200, and 1500 images, as shown in Figure H-17.

Comparison with the average velocity plots at the different sample sizes indicate very little changes in the velocity patterns when the instantaneous count is at 600 measurements and above. It was determined that 600 velocity measurements is an adequate sample size for a representative average. The number of instantaneous results used to calculate the averages in each wind and release conditions is shown in Appendix D, ranging from 600 to 2000.

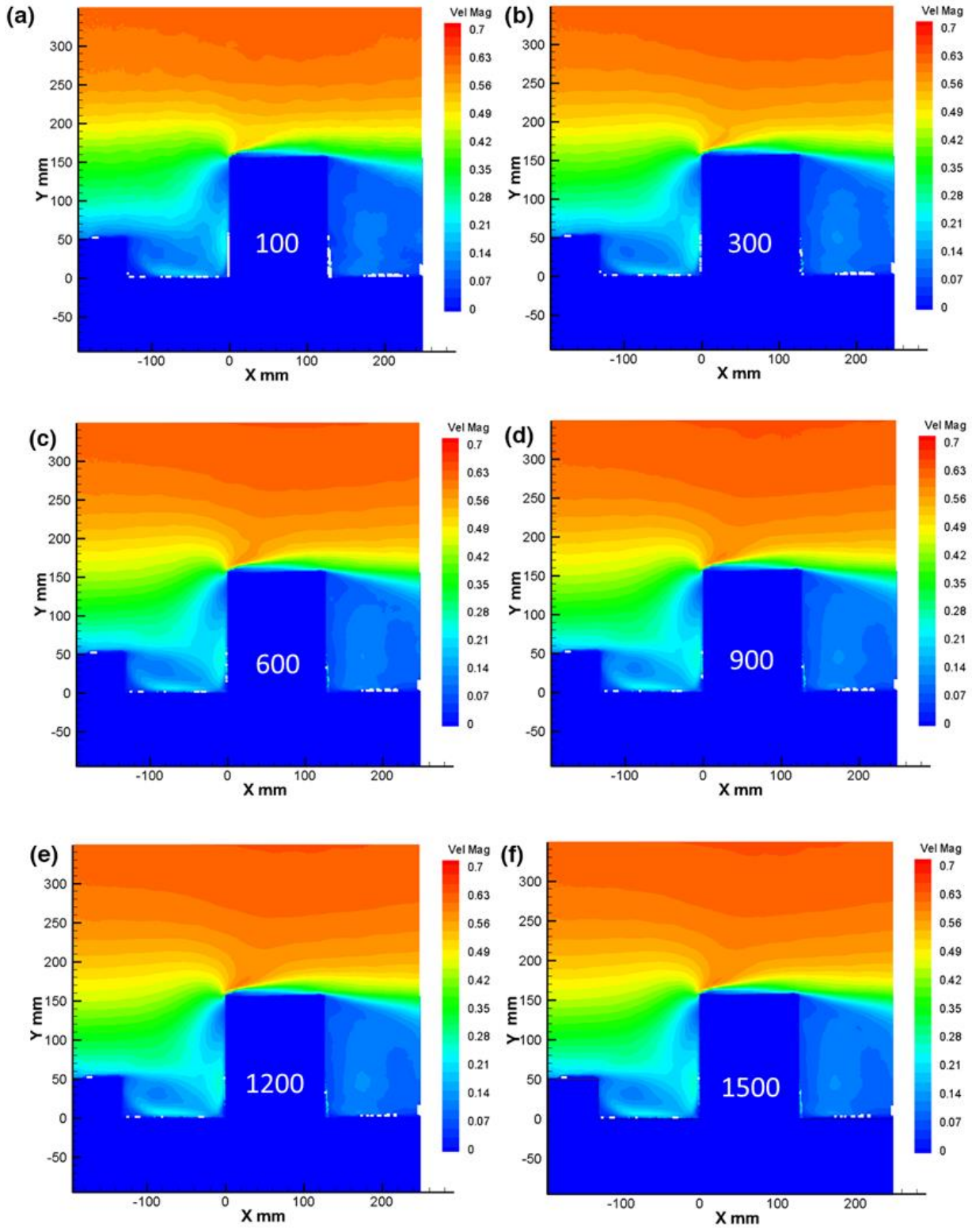

Figure H-17 - Average velocity measurements in the XZ plane with a sample size of (a) 100, (b) 300, (c) 600, (d) 900, (e) 1200 and (f) 1500 instantaneous PIV measurements in Time Frame C conditions.

Appendix I – Supplemental LDV Information

Appendix I1 – How velocity data is calculated

The LDV probes capture light intensity scattered by the particles that travel with the flow. The light signal travels through fiber optics to the signal processor, which converts light intensity to an electronic signal using a photomultiplier tube. The electronic signal is processed using software (TSI FlowSizer 64™) that performs statistical analysis to determine the flow velocity. The software also allows the user to optimize settings, improving the acquired data quality. These settings are subdivided into two categories:

1. Quality of the returning light signal
    a. Voltage of the photomultiplier tubes
    b. Burst Threshold
2. Quality of the frequency data
    a. Band Pass Filter
    b. Signal-to-noise ratio
    c. Downmix Frequency

Typical values for the settings are shown in Table I-3 (in Appendix I-2). The downmix frequency is used by the software to convert frequency data into velocity measurements, as shown in Equation I-1. For LDV measurements, one beam in each pair has its frequency shifted by 40 MHz. A stationary particle generates a 40 MHz frequency signal. Some of the added frequency can be removed as the "Downmixing Frequency" setting. Downmix Frequency allows the user to optimize the Doppler frequency to increase the accuracy of the LDV technique in the velocity range being measured.

$$[Velocity] = ([Frequency\ Data] + [Downmix\ Frequency] - 40) * [Fringe\ Spacing] \quad \textbf{(I-1)}$$

The optimal value of downmix frequency changes linearly with the measured velocity in each channel, as shown in Figure I-1 for the 30 to 300 kHz band pass filter range.

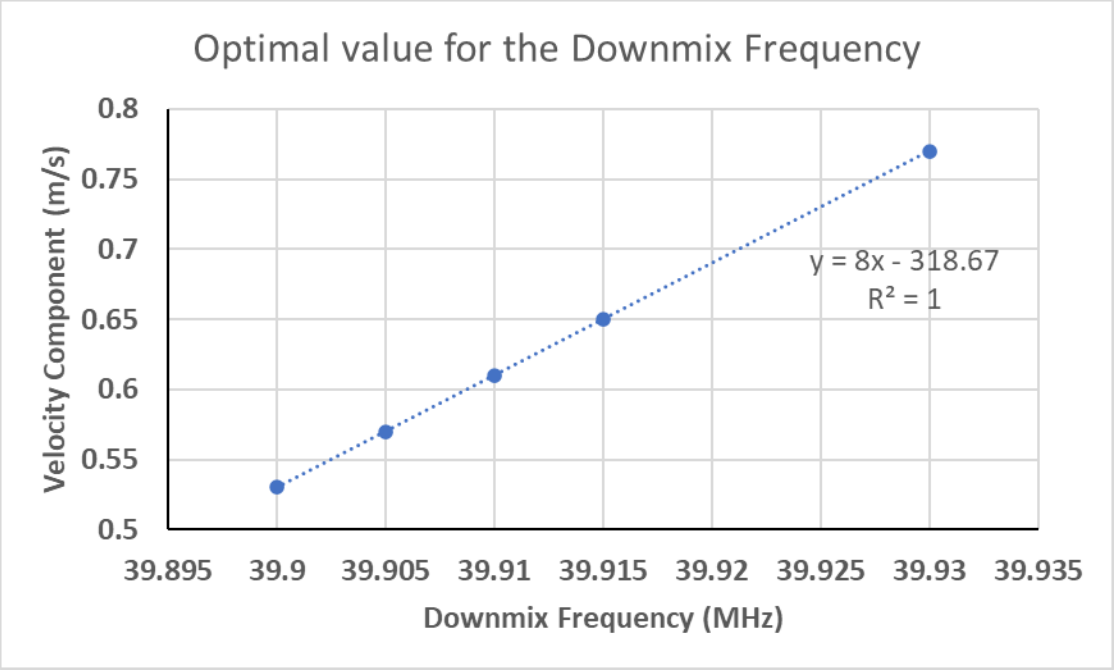

Figure I-1 - Optimal curve for the Downmix Frequency per measured velocity component for the 30 to 300 kHz band pass filter range.

The mathematical relation between the optimal value of the downmix frequency and the target velocity component for the 30 to 300 kHz band pass filter range is expressed in Equation I-2.

$$[Downmix\ Frequency] = \frac{[Velocity] + 318.67}{8} \quad \textbf{(I-2)}$$

Fringe spacing (δf) is intrinsic to each wavelength, calculated via Equation I-3, in which λ is the wavelength and 2κ is the angle between the beams.

$$\delta_f = \frac{\lambda}{\sin(2\kappa)} \quad \textbf{(I-3)}$$

Values for wavelength, angle of the beams, and fringe spacing for the three pairs of LDV beams used in this dissertation are shown in Table I-1.

Table I-1 - Characteristic parameters of each pair of laser beams in the LDV system.

Color	λ (nm)	2κ (rad)	δf (μm)
Green (Channel 1)	514.4	0.068	7.5695
Blue (Channel 2)	488	0.068	7.1810
Violet (Channel 3)	476.5	0.125	3.8194

Appendix I2 – Additional LDV notes

Table I-2 - Additional LDV notes

Category	Notes
Focal Length	Primary probe (blue/green) f = 110.3 mm Secondary probe (violet) f = 60 mm
Fringe Motion	Fringe motion determines the direction of the measured vectors (V1, V2, V3) Positive velocity direction points against the motion of the fringes. Fringe motion is from shifted to unshifted beam (as verified **before** the crossing volume)
Alignment	Alignment of 3D LDV via the pinhole method is cumbersome Procedure for the alignment process can be found in the CHRC files The pinhole used in this dissertation has an opening of 100 μm
Seeding	Fog was added to the entire tunnel room using the (non-modified) Rosco™ Vapour Fog Machine Fog Machine operated using the remote control at setting 1 (knob position) Tunnel was fogged using a mixture of glycerin and water 50% v/v Operating the fog machine for 10 minutes provides sufficient seeding for LDV
"Chopped" Histogram	Sometimes a velocity histogram can appear to be incomplete, suddenly "chopped" before completing the bell shape. Data acquisition *should* be normal, but the histogram display settings need to be adjusted to show complete bell curve.

Table I-3 - Typical setup parameters for LDV measurements in the wind tunnel

Parameter	Channel 1 (Green)	Channel 2 (Blue)	Channel 3 (Violet)
Photomultiplier Tube (PMT) Voltage (V)	610	600	600
Burst Threshold (mV)	30	30	30
Band Pass Filter Range (kHz)	30 - 300	30 - 300	30 -300
Signal-to-noise Ratio	Medium	Medium	Medium
Downmix Frequency	Changes with wind speed and measurement location. Check Figure I-1 and Equation I-2		

Appendix I3 – LDV convergence study

A set of 300,000 instantaneous LDV captures was acquired in the wind tunnel at the equivalent Tower 3 location at 4 cm AGL. The fan speed was set at 104 rpm. Along-wind velocity averages and root mean square (RMS) were calculated sequentially, starting at a population of 10,000 instantaneous acquisitions and increasing by 10,000 acquisitions in each new attempt.

The calculated average and RMS in each population step were compared with the final (300,000 instantaneous measurements sample size) calculated value. Changes in errors of velocity and RMS values per population step are shown in Figures I-1a and I-1b, respectively.

Tabulated values are presented in Table I-2. Results from the study showed that average velocity converged (error < 0.5%) at a population size of 120,000. The higher-order statistic of RMS required a larger number of instantaneous measurements. RMS values converged (error < 1.0%) at a population size of 190,000. It was determined that 200,000 velocity measurements suffice both parameters. Averages for LDV experiments in this dissertation were taken from a population size of 200,000 instantaneous measurements.

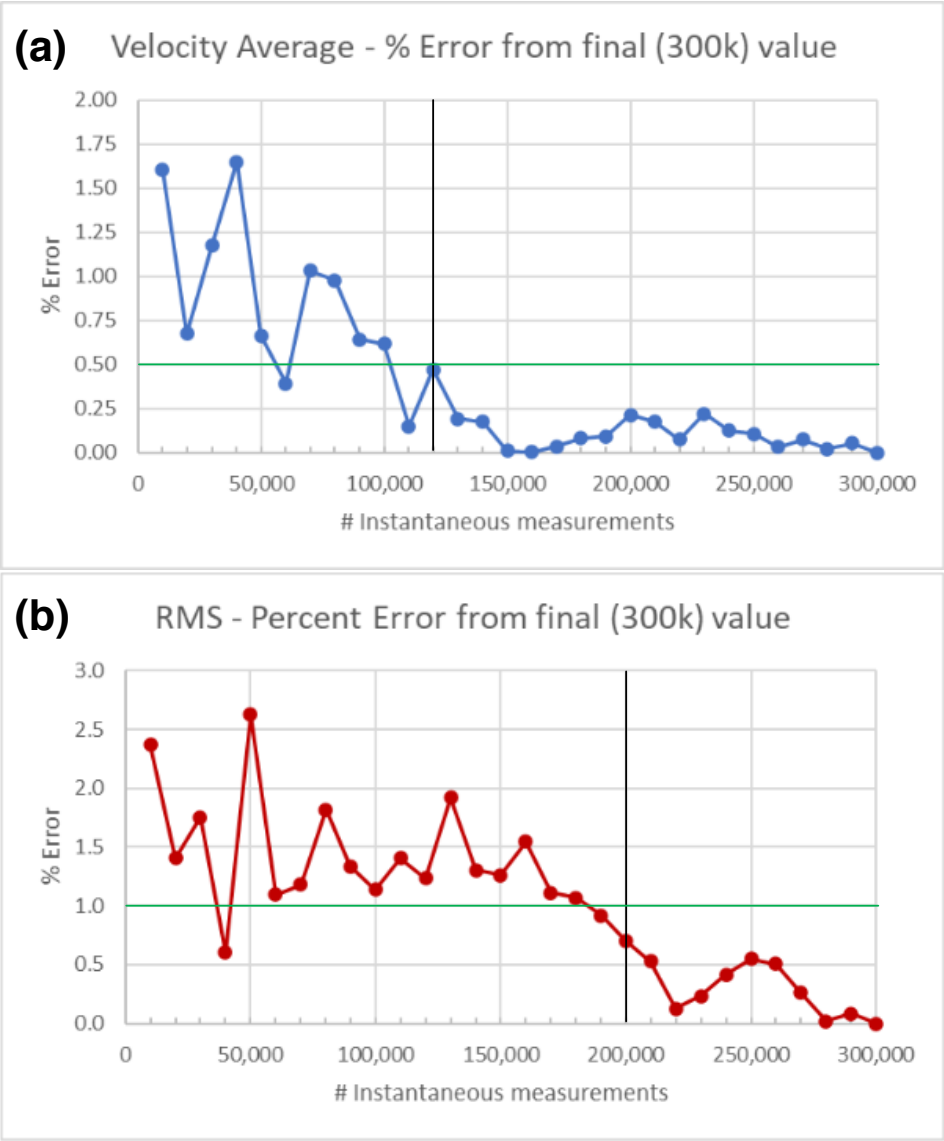

Figure I-2 - Comparison of (a) velocity and (b) RMS data calculated at different population sizes with final values calculated from a population of 300,000 measurements for the convergence study of LDV data.

Table I-4 - Calculated average and RMS values at different sample sizes, with comparisons to final (300,000 population size) data.

Sample Size	Average u velocity (m/s)	Error (%)	RMS u (m/s)	Error (%)
10,000	0.4830	1.60	0.0821	2.37
20,000	0.4876	0.67	0.0853	1.41
30,000	0.4851	1.17	0.0856	1.76
40,000	0.4828	1.65	0.0846	0.60
50,000	0.4876	0.66	0.0863	2.62
60,000	0.4890	0.39	0.0850	1.10
70,000	0.4858	1.03	0.0851	1.18
80,000	0.4861	0.98	0.0857	1.82
90,000	0.4877	0.64	0.0852	1.34
100,000	0.4878	0.62	0.0851	1.14
110,000	0.4901	0.15	0.0853	1.41
120,000	0.4886	0.47	0.0852	1.23
130,000	0.4899	0.19	0.0857	1.92
140,000	0.4900	0.18	0.0852	1.31
150,000	0.4908	0.01	0.0852	1.26
160,000	0.4909	0.00	0.0854	1.55
170,000	0.4907	0.04	0.0851	1.11
180,000	0.4913	0.08	0.0850	1.07
190,000	0.4913	0.09	0.0849	0.92
200,000	0.4919	0.22	0.0847	0.71
210,000	0.4917	0.17	0.0846	0.53
220,000	0.4913	0.08	0.0842	0.13
230,000	0.4920	0.22	0.0843	0.23
240,000	0.4915	0.13	0.0845	0.41
250,000	0.4904	0.11	0.0846	0.55
260,000	0.4907	0.03	0.0845	0.51
270,000	0.4905	0.07	0.0843	0.26
280,000	0.4908	0.02	0.0841	0.02
290,000	0.4906	0.05	0.0840	0.09
300,000	0.4909	0.00	0.0841	0.00